UNIVERSITÀ DI PARMA

UNIVERSITÀ DEGLI STUDI DI PARMA

DOTTORATO DI RICERCA IN

SCIENZE DELLA TERRA

CICLO XXXVI

Development of analysis techniques for Electromagnetic and Electrical methods

Coordinatore:
Chiar.mo Prof. Fabrizio Balsamo

Tutore:
Chiar.mo Prof. Roberto Francese

Dottorando:
Oziel Souza de Araújo

Anni Accademici 2020/2021 – 2022/2023

Development of analysis techniques for Electrical and Electromagnetic methods

by

Oziel S. Araújo

Submitted to the Department of Chemical, Life, and Environmental Sustainability Sciences (SCVSA)
on 31 July 2024, in partial fulfillment of the
requirements for the Degree of Doctor of Philosophy in
Earth Sciences

Abstract

The thesis stands as a pivotal contribution in the development of analysis techniques within the realm of Electromagnetic and Electrical methods, specifically delving into geological risks like landslides and levees. The urgency of this research is underscored by recent catastrophic events, including landslides and levee failures during floods, intensified by unforeseen and intense rainfall events that have raised concerns about the impacts of climate change. At its core, the thesis aims to comprehensively address and illuminate various facets of geophysics. Each chapter within the thesis serves a distinct purpose in advancing knowledge in the field. The methodological foundation of this thesis is multi-layered. One crucial facet involves the meticulous calibration of electromagnetic (EMI) data, a process specifically applied to segments of a levee subjected to multiarray EMI surveys. This calibration process is not merely a technical step but a strategic one, as it enables the transposition of the entire survey onto "ERT-like" images. This transposition is integral, enhancing the identification of vulnerabilities in river embankments, a critical aspect for averting potential failures that could have cascading consequences. Another pivotal aspect of the research involves the development of innovative self-potential (SP) survey techniques. This encompasses both conventional (Fixed-Base and Leapfrog) and non-conventional (Sparse Gradient and Full Sparse Gradient) arrays, reflecting a nuanced approach to data acquisition and analysis. Such an approach acknowledges the complexity of geological structures and strives to capture a comprehensive understanding through diverse survey techniques. The research unfolds with noteworthy findings that extend beyond the mere application of methodologies. It becomes evident that the use of new-concept instrumentations like FullWaver serves as a catalyst, facilitating detailed SP surveys with both conventional and unconventional arrays. The breakthrough realization emerges that meaningful SP values can be derived, even in scenarios involving stainless-steel electrodes. This finding is particularly significant, broadening the potential application of SP surveys, including data obtained from electrical resistivity tomography surveys. Moreover, the recoverable SP signal is showcased as not just a data point but a qualitatively useful insight. The exploration of the Amplitude Signal Analytic technique, when applied to the Sparse Gradient array, further enhances the arsenal of tools available for reconnaissance of the source of SP anomalies, marking a significant stride in the interpretative capabilities of SP data. In drawing conclusions, the ramifications of this study extend far beyond the academic realm. The thesis promises real-world impact with practical solutions and insights, addressing vulnerability identification, preventing river embankment failures, which might guide proactive measures against geological hazards.

Acknowledgements

Thank God for renewing my faith every day.

I would like to express my gratitude to the University of Parma for providing me with this great opportunity to pursue my Ph.D. alongside individuals of great value.

I extend my deepest thanks to my advisor, Prof. Roberto Francese. He has helped me stay immersed in this significant cycle of continuous learning, not only limited to geophysics but also extending to my personal development. Through his altruism, I have achieved personal and professional milestones that were reserved in the deepest recesses of my being, and now I have experienced them intensely. It is through "Prof." that I have also met and made great friends around the world, which is invaluable. Friends enrich our lives with genuine connections. Grazie, Prof.!

Among these connections, I also express my immense gratitude to my friend Federico Bocchia, manolo Fede. I am immensely grateful for his constant and selfless kindness, not only towards me but to everyone around him.

My sincere thanks go to Massimo Giorgi for his remarkable leadership. His attention to detail and ability to listen make a significant difference in every conversation, along with his skill in choosing excellent restaurants.

Similarly, I extend my thanks to Stefano Picotti, who has exceptionally helped me develop my scientific writing skills in recent years.

To Federico Fischanger, who assisted us with the initial insights of the research, my gratitude.

Thanks to the friends from the Department for the great moments of discussion during lunch, especially to the Pizzati brothers (Mattia and Vani), Nico, and Alessio.

I thank Mara Rossi, who has always been so helpful and accommodating in assisting me with numerous field activities.

Speaking of the field, I appreciate the friends from Geo-Energizers, Francesco Fiera, and Massimo Perini, pioneers who believed in my professional development and taught me a lot about seismic methods in 2013.

I also appreciate the numerous field opportunities provided by Progea Consulting s.r.l, represented by Giancarlo Ceresoli and Cristina.

Likewise, I thank Adastra Engineering s.r.l, represented by Prof. Aldino Bondesan, who provided numerous field activities and often made geophysical instrumentation available.

Heartfelt thanks to Geostudi Astier for enabling the development of this research by providing all the FullWaver instrumentation. Without this University-Industry partnership, my research would not have been possible.

A big thank you to my friends from Canada: Rafael Gonzalez, Mojtaba Abdolahnezhad, Lavie Nguyen, Leo Cheung, and Janvier Uwanyirigira, who welcomed me with such kindness and care during the development of this research there. And not least, Prof. Sam Butler and Prof. Igor Morozov, who helped me significantly with the modeling used in this thesis, and beyond.

I am very grateful to the Rigoti family at Geodecon Geologia e Geofisica (Fabio and Augustinho), who have encouraged and inspired me in all aspects of my life over the past 10 years, especially by immersing me in the world of Applied Geophysics. Even from afar, in Brazil, they continue to be present in my professional and personal life. Thanks, papas.

All my thanks and dedication to my great childhood friend/brother, Iuri, who was a turning point in my life!

Many thanks to my friends from Unipampa: Charles Lima, Daniele Martins, Jean de Carli, Shaiely Fernandes, and Victor Macedo.

Thanks: Gilvan Pereira & Noely Liberato!

Thanks: Santa, Papis, Thelves, Laurinha, Micula, Negas, Zezinho, and Cocas!

Thanks: Lenira, my oteba do CAPS!

Thank you very much to everyone because it was worth it.

“vanità delle vanità, tutto è vanità”

Contents

List of Figures

List of Tables

CHAPTER 1

1. INTRODUCTION

1.1 BACKGROUND AND CONTEXT

1.1.1 Research Area

Geological risks refer to threats or dangers arising from natural geological processes on Earth. These processes include events such as earthquakes, volcanic activity, landslides, floods, tsunami activity, and other phenomena related to the dynamics of the Earth's crust. These geological events can pose significant threats to human safety, infrastructure, and the environment.

In addition to natural events, geological risks can also be influenced or exacerbated by human activities, such as improper land use in landslide-prone areas, inadequate exploitation of natural resources, and the construction of infrastructure in seismic zones, among others. Assessing and managing geological risks involves understanding geological dynamics, identifying areas prone to adverse events, and implementing preventive or mitigating measures to reduce the negative impacts of these risks.

Landslides and levee failures during floods have proven to be catastrophic, causing extensive damage to agriculture, industry, infrastructure, and communities. Recent years have witnessed unexpected and intense rainfall events, with rainfall intensities surpassing hundreds of millimeters within mere hours (Jongman et al., 2014). A striking example occurred during the May 2023 flood in the Emilia-Romagna region in northern Italy, where rainfall peaked at over 250 mm in less than 24 hours. This deluge triggered more than 20 levee failures, resulting in devastating consequences, including numerous casualties and billions of Euros in damages. The alarming social costs incurred by such events, especially when exacerbated by climate change, pose a significant concern for the future.

According to Peruccacci et al., (2023), Italy has a long history of landslides triggered by various factors, including natural elements and human activities. Rainfall-induced landslides are widespread, causing severe consequences for people and property

nationwide. Over nearly five decades (1972–2021), landslides displaced 145548 individuals and caused 2504 casualties. From 2017 to 2020, 645 "major landslide events" were recorded by the Italian Institute for Environmental Protection and Research (ISPRA), impacting lives, buildings, and infrastructure (Trigila et al., 2021).

To address this risk, the ongoing challenge involves understanding and mitigating these frequent and impactful geological events to protect lives and infrastructure, integrating geophysical and geotechnical data is essential for a comprehensive understanding of river embankment structures and landslides. While geotechnical investigations offer precise but localized data, they are time-consuming, invasive, and costly compared to noninvasive geophysical methods (Cosenza et al., 2006). Geophysical surveys, such as Electrical Resistivity Tomography (ERT), Self-Potential (SP), Induced Polarization (IP), and Electromagnetic Induction (EMI), provide rapid and nondestructive insights over large areas, making them pivotal in identifying potential critical segments. However, geotechnical testing validates the geophysical results, highlighting the complementary nature of these methods in mapping levees and landslides, being crucial for assessing their vulnerability and instability, thereby preventing catastrophic failures.

1.1.2 Research Problem

The use of electrical resistivity methods for exploring the subsurface at large depths (known as Deep Electrical Resistivity Tomography - DERT) is rapidly increasing. This trend is bringing about significant changes to the field, as numerous datasets of electrical resistivity data are now available for a variety of geological conditions (Carrier et al., 2019; Lajaunie et al., 2019; Troiano et al., 2019; Rizzo et al., 2020; Bocchia et al., 2021). DERT surveying boosted the development of multichannel and distributed systems based on loggers capable of sampling the electrical potentials in continuous using several couples of electrodes inserted into the ground.

ERT monitoring also became popular (Chambers et al., 2015) for studying water content changes and water flow movements in landslides (Kukemilks & Wagner, 2021), aquifers, levees, and other areas. The SP method has tremendous potential for those applications (Gallipoli et al., 2000; Perrone et al., 2004; Revil et al., 2006; Jouniaux et al., 2009; Kukemilks & Wagner, 2021), but this capability to be fully exploited, requires

specific field procedures and data processing techniques (Barde-Cabusson et al., 2021; Eppelbaum, 2021). The hardware for single-channel SP measurements is relatively cheap, and some developments are mandatory to switch from single to multi-channel SP. New-generation georesistivimeters like the Fullwaver (Gance et al., 2018) and the Multisource (LaBrecque et al., 2013; Bocchia et al., 2021) already log potentials at high frequency. However, the SP voltages in these instruments are considered noise rather than signals, and they are logged with the sole purpose of separating artificial and site-related potentials.

In general, traditional and new-generation georesistivimeters have automatic SP compensation features that zero out or remove the influences of natural voltages on the ERT data. This means that in the datalogger instruments, the meaningful information from natural voltages is not fully exploited or utilized.

As most ERT surveys use stainless steel rather than non-polarizing electrodes, the first question that arose in this study was:

I. *Is it possible to obtain meaningful SP information from the FullWaver even when it is using stainless steel electrodes?*

This question arose because SP surveys require the use of non-polarizing electrodes for several key reasons related to the nature of the measurements and the need for accuracy and reliability.

Another question was:

II. *Is it possible to retrieve the natural voltage from the ERT records dataloggers and provide useful information?*

The idea is similar to that observed in seismic acquisitions. In the past, environmental signals, considered noise in seismic reflection data, used to be filtered or eliminated from the data and not exploited as meaningful signals. Later, new acquisition types and processing techniques emerged, which started using the "noise" as a signal to extract useful information.

Although, when compared to traditional systems, the new-generation of georesistivimeters tend to have higher costs for SP monitoring acquisitions, it becomes

relevant to retrieve or extract the SP data that would traditionally be discarded from the ERT acquisitions using such instrumentations. One of the major drawbacks in utilizing such SP data relates to the array used in the acquisition, considering that these georesistivimeters employ a new modality in electrode layout (non-conventional arrays). So far, a practical method for the analysis and interpretation of these SP data with non-conventional arrays has not been observed in the literature, which brings another question:

III. How to interpret maps of non-conventional arrays?

Numerous geophysical investigations have been applied to levee and landslide monitoring (Dunbar et al., 2007; Perrone et al., 2014; Radzicki et al., 2021; Adams et al., 2021), as is the focus of this thesis, most of them use Electromagnetic methods (EMI) and ERT techniques for subsurface conductivity mapping. EMI is renowned for its rapid data acquisition capabilities and efficiency in covering extensive survey areas, making it one of the fastest geophysical mapping techniques available (Doll et al., 2014). Conversely, ERT is celebrated for its high accuracy in correlating geophysical data with geotechnical and hydraulic properties (Weller et al., 2006; Hen-Jones et al., 2017), although its application is limited by higher costs and logistical challenges, restricting its use to smaller segments of levees.

Despite the fundamental differences in the physical principles underlying EMI (induction) and ERT (galvanic phenomena), both methods can yield comparable measurements of electrical conductivity under certain conditions, particularly at low frequencies ($f < 105$ Hz) and in the absence of metallic objects in the subsurface. However, discrepancies arise due to the distinct sensitivities of the methods: ERT is more responsive to resistive features, while EMI is more attuned to conductive anomalies.

Popular EMI systems like DUALEM (DUALEM Inc, 2008) and CMD-Explorer (GF Instruments, 2011), known for their multi-array configurations, offer effective solutions for investigating river levees (Monteiro Santos et al., 2010). Nevertheless, the apparent conductivity values provided by EMI represent cumulative resistivity distributions over specific depth ranges and are influenced by various factors, including ground coupling,

thermal drifts, and EM noise. These factors complicate the direct comparison of resistivity fields obtained from ERT and EMI data inversions.

A reliable quantitative approach to reconcile these differences necessitates the calibration of EMI measurements against ERT data. This calibration process, involving the simultaneous acquisition of EMI and ERT data, is crucial for obtaining accurate and comparable conductivity values (Lavoué et al., 2010; von Hebel et al., 2019; McLachlan et al., 2021).

Based on this, the primary question that emerged was:

IV. *How can EMI and ERT techniques be effectively integrated and calibrated to provide accurate and comparable subsurface conductivity measurements for river levee investigations?*

1.2 OBJECTIVES AND SCOPE

1.2.1 General Objetive

This thesis focuses on introducing a novel geophysical survey technique, with a detailed exploration of its development and application. It situates this method within the broader context of geology and natural hazards, emphasizing its potential contributions to advancing geophysical survey capabilities and enhancing understanding and mitigation strategies for natural hazards.

1.2.2 Specific Objectives

The specific objectives of this work regarding to the development of analysis techniques for Electrical and Electromagnetic methods are:

a) Compare the response of different types of field SP arrays.
b) Implement and assess non-conventional SP arrays by using different electrode patterns with independent units to log the potential difference.
c) Evaluate the effectiveness and suitability of new-generation georesistivimeters in reconstructing different sources of anomalies using SP analysis based on the Analytical Signal Amplitude algorithm.

d) Investigate the feasibility of obtaining meaningful SP information from FullWaver georesistivimeters using stainless steel electrodes.
e) Determine the possibility of retrieving natural voltage from ERT records dataloggers to provide useful information.
f) Present practical methods for analyzing and interpreting SP data from non-conventional arrays.
g) Establish a procedure for correcting multi-array EMI data to obtain cost-effective information comparable to standard ERT imaging.

1.2.3 Scope

This thesis focuses on the development, implementation, and assessment of non-conventional geophysical survey techniques, with particular emphasis on electrical resistivity and electromagnetic methods. The research highlights the use of non-invasive geophysical methods, including ERT, IP, SP, and Frequency Domain Electromagnetic methods, due to their rapid and extensive data coverage capabilities. Key components of the study include comparing different types of SP field arrays, assessing new electrode patterns, and evaluating the effectiveness of new-generation georesistivimeters such as the FullWaver. Additionally, the thesis aims to establish procedures for correcting multi-array EMI data, making it comparable to standard ERT imaging for detailed subsurface investigations.

While geotechnical investigations provide crucial localized data, this research prioritizes geophysical surveys for their non-invasive nature and broader area coverage. The practical applications of these techniques are demonstrated through multiple case studies. However, the study does not delve into detailed climate change modeling or the impacts of other geological hazards beyond landslides and levee failures. Furthermore, the SP techniques explored are limited to qualitative analysis and do not directly address the theoretical background or origin of SP, nor different types of SP inversion.

1.3 SIGNIFICANCE AND CONTRIBUTION

1.3.1 Significance

The research presented in this thesis is significant for several reasons. Firstly, it addresses indirectly the critical issue of geological risks, which pose severe threats to human safety, infrastructure, and the environment. With natural disasters such as landslides and levee failures becoming increasingly frequent and intense due to climate change, there is an urgent need for effective monitoring and mitigation strategies. This thesis contributes to this need by advancing non-invasive geophysical survey techniques, particularly focusing on geoelectrical methods. These techniques offer rapid and extensive data coverage, enabling better identification and assessment of vulnerable areas.

Secondly, the study highlights the complementary nature of geophysical and geotechnical investigations. While geotechnical methods provide detailed, localized data, they are often time-consuming, invasive, and costly. In contrast, the geophysical methods explored in this research, such as Electrical Resistivity Tomography (ERT), Induced Polarization (IP), Self-Potential (SP), and Electromagnetic Induction (EMI), are non-invasive and capable of covering large areas quickly. This makes them invaluable for initial surveys and continuous monitoring, particularly in identifying critical segments of levees and landslides.

Furthermore, this research introduces innovative procedures for correcting multi-array EMI data and integrating it with standard ERT imaging, enhancing the reliability and cost-effectiveness of subsurface investigations. By focusing on the practical applications of these methods through case studies, the thesis demonstrates their real-world relevance and potential to prevent catastrophic failures in river embankments and landslide-prone areas.

1.3.2 Contribution

This thesis makes several key contributions to the field of geophysical survey techniques and their application to geological risk assessment and mitigation:

- The study explores new acquisition types and processing techniques.

- The research evaluates the effectiveness of new electrode patterns and assesses the feasibility of obtaining meaningful SP information using stainless steel electrodes in FullWaver georesistivimeters. This innovation addresses the challenge of SP data acquisition with non-polarizing and stainless-steel electrodes, enhancing the applicability of SP methods.
- The thesis establishes procedures for correcting multi-array EMI data, making it comparable to standard ERT imaging. This advancement is crucial for accurately interpreting subsurface materials, particularly in river levee investigations, where identifying textural anomalies can prevent water filtration and potential failures.
- By demonstrating the complementary nature of geophysical and geotechnical investigations, the research highlights the importance of integrating these methods for a comprehensive understanding of subsurface conditions. This integration is vital for assessing the vulnerability and instability of levees and landslides.
- Through multiple case studies, the thesis showcases the practical applications of the developed techniques in real-world scenarios. These examples illustrate the effectiveness of the methods in identifying and mitigating geological risks, providing valuable insights for future research and implementation.

1.4 OUTLINE OF THESIS

The chapters of this thesis are independent of each other and are produced in manuscript format for journals; therefore, each chapter has its own references. The current introduction chapter, for example, outlines the thesis, discusses the motivations and relevance of the topic, and includes relevant references.

Chapter 2, entitled "Innovative Survey Approaches for Self-Potential Investigation", involves numerical simulations of self-potential using COMSOL software. The chapter constitutes a feasibility study of both conventional and unconventional SP arrays. Various models were created with spherical and cylindrical targets positioned under different orientations. In the same approach, it became evident that valuable information could be obtained by applying the Hilbert transform to SP data, thereby revealing the location of primary SP anomalies even in environments with a low signal-

to-noise ratio. The chapter, bearing the same title, is currently in the submission phase for a Journal.

Chapter 3, entitled "SPViewer: A Tool for SP Processing and Visualization of Data from FullWaver Instrument," addresses the SPViewer, a free and open tool designed for extracting and processing temporal series of SP signals from V-FullWaver systems and visualizing their time-lapse maps. The step-by-step usage and its significance in the development of new geo-electrical analysis techniques are discussed. A levee in San Martino di Venezze is taken as a field example to analyze electrokinetic processes associated with water infiltration. Also written in an article-style format, the chapter will be submitted as a manuscript to a Journal within the geosciences and software field.

Chapter 4, titled "Analysis of Spontaneous Potential at Adige River, Northern Italy," is a short case study comparing the use of non-polarizing electrodes and stainless-steel electrodes for monitoring levees. This real-world application evaluates conventional and non-conventional SP arrays. The chapter highlights the efficacy of SP monitoring alongside advanced instrumentation in evaluating levees stability and hydrogeological risks without invasive methods. It significantly improves understanding of fluid distribution, identifies potential structural integrity issues, and facilitates proactive measures against water infiltration and erosion. SP analysis, incorporating temporal and ASA techniques, accurately pinpoints critical anomaly zones, enabling prompt interventions to safeguard infrastructure. These findings advocate for wider implementation of SP monitoring in civil engineering and environmental management to enhance resilient infrastructure planning and mitigate risks effectively.

Chapter 5, entitled "Self-Potential Signal Analysis to Recognize Sources of Primary Anomaly in a Landslide: A Novel Approach" explores the use of the Sparse Gradient array in studying a landslide in Cazzaso, Italy, demonstrating that even with the use of steel electrodes, meaningful SP values can be obtained in certain circumstances, including data obtained from electrical resistivity tomography surveys. The SP signal can be recovered and qualitatively utilized. Furthermore, it is shown that the Amplitude Signal Analytic technique applied to the Sparse Gradient array can be useful as a preliminary approach for delineating the source of SP anomalies on a regional scale.

The chapter is written in the form of an article and is in the preparation phase for submission to a Journal in the field.

Chapter 6, entitled "Deep Electrical Resistivity Tomography and Unconventional Self-Potential Technique Applied to Landslide" The chapter presents results from electrical resistivity tomography, induced polarization, and self-potential for monitoring landslides in Tizzano Val Parma, Italy. Time-lapse SP acquisitions were conducted in two consecutive years with long-duration recordings using the FullWaver system employing two techniques or arrays: Fixed-Base and Sparse Gradient. The application of these techniques significantly contributes to a more effective approach in managing areas prone to landslides, promoting safety and sustainability in land use planning. The chapter is written in the form of an article and is in the preparation phase for submission to a Journal in the field.

Chapter 7, entitled "Frequency Domain Electromagnetic Calibration for Improved Detection of Sand Intrusions in River Embankments," presents the development of a procedure capable of correcting multiarray Electromagnetic method (EMI) data to obtain information similar to standard Electrical Resistivity Tomography (ERT) imaging in a cost-effective manner. Calibration can be applied to one or more segments of the levees investigated with multiarray EMI, and then the entire survey can be transposed onto "ERT-like" images, enhancing the reliability of textural anomaly interpretation. The chapter was also published in the Journal Leading Edge in 2023 with the same title:

- Araujo, O. S; Picotti, S., Francese, R.G., Bocchia, F., Monteiro Santos. A.F., Giorgi, M., Tessarollo, A., (2023). Frequency domain electromagnetic calibration for improved detection of sand intrusions in river embankments: The Leading edge, 42(9),615-624.

Chapter 8, provides conclusions and future research directions.

In addition to the chapters currently in the preparation and submission phase, this thesis has led to six other publications:

Araujo, O. S.; Butler, S.; Francese, R. G. (2023). Insights of self-potential array technique for primary anomaly reconnaissance. In BeGEO2023 – The 2nd

Conference of Young Geoscientists, Sustainability and Risks: BeGEO Scientists on the road to the future, Naples, Italy.

Araujo, O. S.; Butler, S.; Francese, R. G. , Picotti, S. (2023). Innovative approaches to geological structure characterization: self-potential insights. In 4th SEG Latin American Virtual Student Conference 2023, Latin America Regional Advisory Committee.

Araujo, O. S; Picotti, S., Francese, R.G., Bocchia, F., Monteiro Santos. A.F., Giorgi, M., Tessarollo, A., (2023). Frequency domain electromagnetic calibration for improved detection of sand intrusions in river embankments: The Leading edge, 42(9),615-624.

Araujo, O.S.; Bocchia, F.; Francese, R.G.; Rossi, M.; Picotti, S.; Giorgi, M. (2023). Calibration and comparison of electromagnetic data based on electrical resistivity tomography in levee context. 41st National Conference, Bologna, Italy.

Araujo, O. S.; Rossi, M.; Giorgi, M.; Picotti, S.; Bratus, A.; Francese, R. G. (2023). Improving Self-Potential methodology for a better understanding of subsurface flow patterns in an active landslide. In 6th World Landslide Forum, Florence, Italy.

Araujo, O. S.; Rossi, M.; Giorgi, M.; Picotti, S.; Pellinghelli, N.; Francese, R. G. (2023). Sparse Gradient array: a new approach to Self-Potential landslide monitoring. In 6th World Landslide Forum, Florence, Italy.

REFERENCES

Adams, R. F., Miller, B. V., Kress, W. H., Ikard, S. J., Payne, J. D., & Killion, W. H. (2021). Evaluation of Electrical and Electromagnetic Geophysical Techniques to Inspect Earthen Dam and Levee Structures in Arkansas. *Journal of Environmental and Engineering*.

Barde-Cabusson, S., Finizola, A., & Grobbe, N. (2021). A practical approach for self-potential data acquisition, processing, and visualization. Interpretation, 9(1), T123-T143.

Bocchia, F., Francese, R. G., Giorgi, M., Fischanger, F., & Picotti, S. (2021). The impact of multiple transmitters on the signal strength in Deep Electrical Resistivity Tomography data: an experiment in the Vajont valley (north-eastern Italy). Bollettino di Geofisica Teorica e Applicata. Forthcoming.

Carrier, A., Fischanger, F., Gance, J., Cocchiararo, G., Morelli, G., & Lupi, M. (2019). Deep electrical resistivity tomography for the prospection of low-to medium-enthalpy geothermal resources. Geophysical journal international, 219(3), 2056-2072.

Chambers, J. E., Meldrum, P. I., Wilkinson, P. B., Ward, W., Jackson, C., Matthews, B., ... & Gunn, D. (2015). Spatial monitoring of groundwater drawdown and rebound associated with quarry dewatering using automated time-lapse electrical resistivity tomography and distribution guided clustering. Engineering Geology, 193, 412–420.

Cosenza, P., E. Marmet, F. Rejiba, Y. J. Cui, A. Tabbagh, A., and Y. Charlery. (2006). *Correlations between geotechnical and electrical data: A case study at Garchy in France*. Journal of Applied Geophysics, 60, 3-4, 165-178.

Dunbar, J. B., Smullen, S., & Stefanov, J. E. (2007, January). The use of geophysics in levee assessment. In *Symposium on the Application of Geophysics to Engineering and Environmental Problems 2007* (pp. 61-68). Society of Exploration Geophysicists.

Eppelbaum, L. V. (2021). Review of processing and interpretation of self-potential anomalies: Transfer of methodologies developed in magnetic prospecting. Geosciences, 11(5), 194.

Gallipoli, M. R., Lapenna, V., Lorenzo, P., Mucciarelli, M., Perrone, A., Piscitelli, S., & Sdao, F. (2000). Comparison of geological and geophysical prospecting techniques in the study of a landslide in Southern Italy.

Gance, J., Leite, O., Texier, B., Bernard, J. & Truffert, C., (2018). The Fullwaver systems: distributed network of autonomous devices for deep 3D electrical resistivity and induced polarization survey, in EGU General Assembly Conference Abstracts, Vol. 20 of EGU General Assembly Conference Abstracts, p. 12569

Jongman, B., S. Hochrainer-Stigler, L. Feyen, J. C. J. H Aerts, R. Mechler, W. J. W. Botzen, L. M. Bouwer, G. Pflug, R. Rojas, and P.J. Ward. (2014). *Increasing stress on disaster-risk finance due to large floods*. Nat. Clim. Change, 4, 264–268.

Jouniaux, L., Maineult, A., Naudet, V., Pessel, M., & Sailhac, P. (2009). Review of self-potential methods in hydrogeophysics. Comptes Rendus Geoscience, 341(10-11), 928-936.

Kukemilks, K., & Wagner, J. F. (2021). Detection of Preferential Water Flow by Electrical Resistivity Tomography and Self-Potential Method. Applied Sciences, 11(9), 4224.

LaBrecque, D. J., Morelli, G., Fischanger, F., Lamoureux, P., & Brigham, R. (2013, December). Field trials of the multi-source approach for resistivity and induced polarization data acquisition. In AGU Fall Meeting Abstracts (Vol. 2013, pp. NS34A-03).

Lajaunie, M., Gance, J., Nevers, P., Malet, J. P., Bertrand, C., Garin, T., & Ferhat, G. (2019). Structure of the Séchilienne unstable slope from large-scale 3D electrical tomography using a Resistivity Distributed Automated System (R-DAS). Geophysical Journal International, 219(1), 129–147, doi:10.1093/gji/ggz259

Perrone, A., Iannuzzi, A., Lapenna, V., Lorenzo, P., Piscitelli, S., Rizzo, E., & Sdao, F. (2004). High-resolution electrical imaging of the Varco d'Izzo earthflow (southern Italy). Journal of Applied Geophysics, 56(1), 17-29.

Perrone, A., Lapenna, V., & Piscitelli, S. (2014). Electrical resistivity tomography technique for landslide investigation: A review. *Earth-Science Reviews*, *135*, 65-82.*Geophysics*, *26*(4), 287-303.

Peruccacci, S., Gariano, S. L., Melillo, M., Solimano, M., Guzzetti, F., & Brunetti, M. T. (2023). The ITAlian rainfall-induced LandslIdes CAtalogue, an extensive and accurate spatio-temporal catalogue of rainfall-induced landslides in Italy. *Earth System Science Data*, *15*(7), 2863-2877.

Radzicki, K., Gołębiowski, T., Ćwiklik, M., & Stoliński, M. (2021). A new levee control system based on geotechnical and geophysical surveys including active thermal sensing: A case study from Poland. *Engineering Geology*, *293*, 106316.

Revil, A., Titov, K., Doussan, C., & Lapenna, V. (2006). Applications of the self-potential method to hydrological problems. In Applied hydrogeophysics (pp. 255-292). Springer, Dordrecht.

Rizzo, E., Capozzoli, L., De Martino, G., Piscitelli, S., Bellanova, J., Caputo, R., ... & Fischanger, F. (2020). Deep geophysical investigation in urban area: Ferrara city example (No. EGU2020-9294). Copernicus Meetings.

Trigila, A., Iadanza, C., Lastoria, B., Bussettini, M., and Barbano, A.: Dissesto idrogeologico in Italia: pericolosità e indicatori di rischio – Edizione 2021, Rapporti 356/2021, ISPRA, 2021 (in Italian).

Troiano, A., Isaia, R., Di Giuseppe, M. G., Tramparulo, F. D. A., & Vitale, S. (2019). Deep electrical resistivity tomography for a 3D picture of the most active sector of Campi Flegrei caldera. Scientific reports, 9(1), 1-10.

CHAPTER 2

2. INNOVATIVE SURVEY APPROACHES FOR SELF-POTENTIAL INVESTIGATION

2.1 INTRODUCTION

The Self-Potential (SP) method is a passive geoelectrical technique that is particularly sensitive to the presence of ore bodies (Mehanee, 2014; Rakoto et al., 2019, Su et al., 2022; Zhu et al., 2023, Revil et al., 2023) and to the movement of fluids in the subsurface (Poldini, 1938; Sill, 1983; Jouniaux et al., 2009; Valois et al., 2018; Ahmed et al., 2020; Kukemilks & Wagner, 2021). There are several examples in the literature describing the application of the SP method like hydrogeophysics (Revil et al., 2006; Jouniaux et al., 2009), mineral exploration (Biswas, 2017), dikes and embankments (Song et al., 2021), quantitative analysis (Eppelbaum, 2021), hydrothermal systems (Finizola et al., 2004; Revil et al., 2023) and marine exploration (Xie et al., 2023). Although collecting SP data is quite simple, its systematic use has been fairly limited by lack of a quantitative approach and uncertainties in data interpretation (Nyquist & Corry, 2002; Revil & Jardani, 2013; Barde-Cabusson et al., 2021). Further limitations depend on the absence of a definitive consensus on data inversion procedures.

This scenario has been partly changed because of the recent growing use of electrical resistivity methods to explore the subsurface at large depths (Deep Electrical Resistivity Tomography – DERT), in a variety of geological conditions (Carrier et al., 2019; Lajaunie et al., 2019; Troiano et al., 2019; Rizzo et al., 2020). DERT surveying boosted the use and the development of distributed systems as an effective alternative to traditional resistivity-meters. Distributed systems are based on the separation of transmitting and receiving units (Lajaunie et al., 2019; Bocchia et al., 2021) and they use powerful or multiple transmitters to increase the signal-to-noise ratio at large depths. The receivers are often comprised of recorders capable of continuously sampling, at high frequency, the natural and artificial electric potentials. The FullWaver (Gance et al., 2018) and the Multisource (LaBrecque et al., 2013; Bocchia et al., 2021; Picotti et al., 2017) are among these new generation resistivity-meters and they allow

for the deployment of complicated patterns of receiving electrodes and also for the permanent storage of long time series of electric potentials. Following the standard DERT procedure, the natural SP values in these datasets are treated as noise rather than signal and they are filtered out to retrieve the artificial potentials. Contrarily, these SP data, when adequately processed, represent a valuable geophysical signal useful to map specific geological features in the subsurface. The lack of logistical constraints while deploying the distributed systems for DERT purposes enables to adopt a non-conventional type of SP array, herein referred to as the Sparse Gradient (SG) array, which is explained in the following sections. This uncommon type of array consists of several sparse dipoles with independent units logging the potential difference (p.d.) between couples of electrodes. In order to evaluate the SG technique, we thus consider a base-measuring pattern consisting of two-channel recorders connected to three electrodes that simultaneously sample two values of p.d. There are numerous studies in the literature adopting multi-channel self-potential measurements in offshore surveys (Zhu et al., 2021; Ikard et al., 2021; Song et al., 2022; Su et al., 2022; Zhu et al., 2023; Jiang et al., 2024). In contrast, the SG technique represents a significantly different approach, as there are no common reference electrodes for all measurements, and the acquisition is performed onshore. The "star network" approach presented by Revil & Jardani (2013) is somewhat similar to the Full SG approach, because it exploits the p.d. between electrodes controlled by a set of base stations deployed in an "L-shaped form," with the units separated by several hundred meters. To our knowledge, in the literature there are no other examples regarding the employment of the SG technique, as well as on the data interpretation, for SP studies.

Several studies in the literature applied numerical, analytical and graphical methods to generate synthetic SP data, with the purpose of interpreting SP anomalies (Paul, 1965; Rao et al., 1970; Meiser, 1962; Monteiro Santos, 2010; Roudsari & Beitollahi, 2013; Xie et al., 2020). Some of these works adopted the COMSOL Multiphysics package, which is a computational modeling software based on the finite-element methods to solve partial differential equations (e.g., Boleve et al., 2007; Troiano et al., 2017; Soueid Ahmed et al., 2016; Ahmed et al., 2020; Kang et al., 2020). Among the analytical and graphical methods, the Analytic Signal Amplitude (ASA) algorithm uses gradients and the Fast Fourier Transform (FFT) to generate potential field maps (Abdelrahman et al.,

2003; Abdelrahman et al., 2009), which contributes to better estimate the source location. This technique has been commonly applied (e.g., Sundararajan & Srinivas, 1996; Sundararajan et al., 2000) to effectively locate source anomalies for geophysical methods based on potential fields (e.g., Magnetic and Gravimetric). ASA approach, for SP surveying, has been successfully applied in many studies (e.g., Agarwal, 1984; Atchuta Rao & Ram Babu, 1983; Sundararajan & Srinivas, 1996; Agarwal & Srivastava, 2009; Mehanee et al., 2023). The Normalized Full Gradient technique has been also utilized (Sundararajan et al., 1998; Sindirgi et al., 2008; Abedi et al., 2012; Sindirgi & Ozyalin, 2019) integrating ASA with the downward continuation.

Two standard single-channel techniques have been widely reported in the literature for SP data acquisition: the Potential or Fixed-Base and the Gradient (Leapfrog). Theoretically, under some circumstances, they are somewhat equivalent but, from the practical point of view, they are rather different (Orellana, 1972). Unfortunately, over large scales these standard approaches are not cost-effective. Data quality is generally high, but site logistics and acquisition time often result in expensive surveys and poor subsurface coverage.

The SG technique could take advantage of the multi-channel capability of the new generation resistivity-meters. However, most SP surveys still use the standard techniques rather than the SG ones, because the hardware for single-channel SP measurements is relatively cheap. For this reason, to our knowledge, SG arrays has not been sufficiently explored for SP surveys, although current technology is sufficiently mature to switch from single to multi-channel measurements. New-generation multi-channel resistivity-meters could noticeably speed up the recording, facilitating the deployment also in the case of complicate acquisition geometry.

Initial attempts to invert SP measurements similarly to resistivity data was based on the calculation of the charge occurrence probability function (Patella, 1997). Other authors solve for the SP after calculating the distribution of streaming current sources in specific hydraulic settings using the Poisson's equations (Jardani et al., 2006; Sheffer and Oldenburg, 2007; Minsley et al., 2007). Many others devised similar or alternative approaches (Mendonça, 2008; Revil & Jardani, 2013) and it appears that a robust

procedure (Gibert & Sailhac, 2008; Revil et al., 2008; Jouniaux et al., 2010; Auken et al., 2010; Revil ,2010) was not yet developed.

In this contribution, we provide a qualitative analysis of SP techniques through synthetic modeling, showing how meaningful can be the information extracted from data obtained using both conventional and non-conventional arrays, i.e., the SG array. We also report here about SP forward modeling based on finite-element numerical methods, to compare the responses of different arrays. We also present an SP analysis, based on the ASA algorithm, to evaluate the effectiveness and suitability of new-generation resistivity meters employing SG arrays to reconstruct different sources of anomalies.

2.1 BASIC THEORY

2.1.1 Brief overview of Self-Potential method

The electroencephalogram (EEG) is a widely recognized medical technique that involves the passive measurement of electrical potential fields on a person's scalp, which fluctuate due to brain activity. The main goal of interpreting EEG data is to pinpoint the sources of electrical activity within the brain, providing valuable insights into areas activated by external stimuli or medical conditions like epilepsy (Michel et al., 2004). If we change the target of the EEG from a person's scalp to the surface of the ground or well logs, the method could be referred to as Self-Potential or Spontaneous Potential (SP) as used in geophysics. The similarity between these methods is so great that many of the concepts and data processing techniques are the same, which may provide useful insights from one to the other (Sheffer, 2007). That's why Geophysicists are often considered the "doctors of the Earth", as we diagnose and study the physical properties and processes of our planet.

The SP method comprises the passive measurement of electric potential at the ground surface and in boreholes (Jackson, 2015). Originating in the early 19th century (Fox, 1830), this method has found applications in mineral exploration (Biswas, 2017; Biswas, 2019), oil well logging (Segesman, 1980), geothermal and volcanic systems (Finizola, 2004; Revil et al., 2023), hydrogeological (Fournier, 1989; Darnet & Marquis,

2004; Revil et al., 2006; Jouniaux et al., 2009), environmental (Naudet et al., 2003; Revil & Jardani, 2013), and engineering investigations (Oliveti & Cardarelli, 2019).

SP data consist of voltage fluctuations measured using sets or arrays of non-polarizing electrodes and high input-impedance measurement instruments. However, the wider acceptance of the SP method has been somewhat constrained by a lack of comprehensive understanding of the mechanisms that generate SP responses (Sheffer, 2007), lack of a quantitative approach and uncertainties in data interpretation (Nyquist & Corry, 2002; Revil & Jardani, 2013; Barde-Cabusson et al., 2021). Many studies have been conducted to establish quantitative approaches for SP (e.g., Di Maio & Patella, 1994; Patella 1997; Iuliano et al., 2001; Iuliano et al., 2002; Jardani et al., 2006; Sheffer and Oldenburg, 2007; Mendonça, 2008; Monteiro Santos, 2010; Revil & Jardani, 2013, Oliveti & Cardarelli, 2019; Sungkono, 2020), there is no definitive consensus on the theoretical inversion (Gibert & Sailhac, 2008; Revil et al., 2008; Jouniaux et al., 2010; Auken et al., 2010; Revil, 2010).

SP have two parts: one that is steady and unidirectional, and another that changes over time. The fluctuating part is influenced by various factors, from alternating currents caused by thunderstorms, changes in the Earth's magnetic field, to the effect of heavy rainfall, etc (Reynolds, 2011).

The mechanisms that generate SP responses involve the accumulation of electrical charge within the subsurface, necessitating a comprehensive understanding for effective interpretation of SP data to extract practical subsurface information (Sheffer, 2007). These mechanisms are associated with electrokinetic, electrochemical, thermoelectric, redox, and piezometric effects, as described by Jouniaux et al., (2009), and Revil & Jardani (2013):

1. thermo-potential and natural potential related to the difference of temperature;
2. electrochemical, as a source of different potential caused by chemical reaction;
3. geobattery, which explains about the difference of potential caused by biotic and abiotic to redox reaction;
4. streaming potential or electrokinetic.

Streaming potential can be used in the field to characterize preferential ground water flow paths (Wilt and Butler, 1990; Panthulu et al.,2001; Darnet et al., 2003; Wilt and Corwin, 2005; Jardani et al., 2009). The electrokinetic phenomenon of streaming potential is the result from the coupling between fluid flow and electric conduction in porous media (Overbeek, 1952), and it is the main mechanism of interest for this research (Gallipoli et al., 2000; Perrone et al., 2004). All study cases herein are assumed that the primary source is due to electrokinetic phenomenon. The concept is that as a fluid moves through a porous medium, it generates an electric potential gradient along its pathway. This occurs due to the interaction between the fluid movement within the pores and the electric double layer on the pore surfaces, a process known as electrokinetic coupling (Gallas, 2020).

The general equation for coupled flows can be written as:

$$\boldsymbol{J_i} = \sum_j L_{ij} X_j \tag{2.1}$$

where the fluxes $\boldsymbol{J_i}$ (of charges, matter, heat, etc) are related to the various forces X_j (gradients of electrical potential, pressure, temperature, etc) through the phenomenological coefficients or conductivities (coupling coefficients) L_{ij}.

Following Jouniaux et al., (2009), in steady-state, and under isothermal conditions, the electric flow ($\boldsymbol{J_e}$, in A/m^3) is related to the pressure gradient (∇P) and to the electric potential gradient (∇V) by the following coupling equation:

$$\boldsymbol{J_e} = L_{\boldsymbol{22}} \nabla V + L_{21} \nabla P \tag{2.2}$$

The first term on the right-hand side in equation 2.2 represents Ohm's law. The coefficient $L_{\boldsymbol{22}}$ is the rock conductivity σ_r. The coupling coefficient L_{21} could be measured by applying a fluid flow (ΔP) and by measuring the induced electric potential (ΔV) in order to find the electrokinetic coefficient C_s:

$$C_s = \frac{\Delta P}{\Delta V} = \frac{\varepsilon \zeta}{n \sigma_f} \tag{2.3}$$

where σ_f and ε are the fluid conductivity and the dielectric constant of the fluid, ζ is the zeta potential (within the double-layer at the interface between the rock and the fluid), and n the dynamic viscosity of the fluid. Then, the eq.2.2 becomes:

$$\boldsymbol{J_e} = \sigma_r \nabla V - C_s \sigma_r \nabla P \tag{2.4}$$

In many earth sciences applications, electrokinetic coefficients typically exhibit negative values, indicating that positive ions move in the direction of flow (Jouniaux et al., 2009). As water flows, potentials tend to become more positive along the direction of flow, while electric charge moves in the opposite direction. Therefore, negative charge moves against the gradient, leading to SP anomalies at higher elevations. This phenomenon occurs due to the higher concentration of cations in water, ensuring that flow always moves from lower to higher potentials (Reynolds, 2011; Jouniaux et al. 2009; Gallas, 2020).

2.1.2 Self-Potential forward modeling

We assume a homogeneous medium, under the hypothesis of the stationarity of currents. Since the charge is conserved, in the low-frequency limit the total current density $\boldsymbol{J}$ (A/m^2) must satisfy the continuity equation

$$\nabla \cdot \boldsymbol{J} = 0, \tag{2.5}$$

(e.g., Griffiths, 1999). Moreover, the following two equations hold

$$\boldsymbol{J} = \sigma \boldsymbol{E} + \boldsymbol{J}_s, \tag{2.6}$$

$$\boldsymbol{E} = \left(E_x, E_y, E_z\right) = -\nabla V, \tag{2.7}$$

where σ is the electric conductivity (S/m), $\boldsymbol{E}$ (V/m) is the quasi-static electric field and V is the electric potential (V). Furthermore, $\boldsymbol{J_c} = \sigma \boldsymbol{E}$ represents the conduction current density in the material, while $\boldsymbol{J_s}$ denotes the source current density. Therefore, the continuity equation (2.1) implies

$$\nabla \cdot \sigma \nabla V = \nabla \cdot \boldsymbol{J}_s = Q_s\,, \tag{2.8}$$

(e.g., Zhu et al., 2023), where Q_s represents the current source in the unit volume (in A/m^3). Equation (2.8) is the equation governing the self-potential forward modeling.

The outer boundaries are insulating and so have no net flux, i.e., the sum of all point current sources must be zero, as required by the stationary condition. The distance of

the model boundaries from the area of interest is assumed large enough that it does not affect the numerical solution.

To find numerical solutions of the above problem, we used the COMSOL Multiphysics package (AB COMSOL, 2017), which is a computational modeling software based on the finite-element methods to solve partial differential equations. In COMSOL, the simulation domain is discretized into a grid of finite elements. The software uses a series of predetermined form functions for most finite elements that describe how the values vary within each element. They are mathematical functions aiding in the numerical approximation of solutions to the equations within the finite element method. By defining the nodes and using the functions, COMSOL is able to interpolate the intermediate values within each finite element.

2.1.3 Some sources of noise

The phenomena of charge polarization arise from natural geological processes, including groundwater flow, changes in solute concentration, temperature fluctuations, and alterations in redox conditions. While these processes are fundamental to SP surveys and monitoring, they can also introduce unwanted "background potentials" or "noise," potentially complicating data interpretation depending on the SP survey's purpose (Jackson, 2015).

In SP surveys, a clear distinction exists between "error" and "noise." Error is generally understood as the non-repeatable aspect of an SP reading, stemming from the data acquisition process. On the other hand, noise refers to a potential arising from sources that are unrelated to the investigation's goals.

Various transient sources can generate noise in SP mapping. These sources encompass the induction of telluric currents within the Earth's conductive layers due to transient current flow in the ionosphere, lightning strikes, large cumulus clouds, and induction from power lines. Examples of SP signals from human activities include the corrosion of metallic casings in piezometers and interference from cathodic protection systems (Corwin & Hoover, 1979). These transient signals can be filtered by using a fixed dipole to record electrical signals during mapping or employing a magnetometer to detect correlated magnetic signals.

Spatial noise can also arise from significant heterogeneity in the resistivity distribution in the shallow subsurface, ranging from a few centimeters to several meters deep. This heterogeneity can be caused by dry conditions or the presence of resistive objects like stones within a more conductive clayey matrix, such as fine-grained soil with higher moisture content (Revil & Jardani, 2013). Generally, Fourier or wavelet-based filters can be used to remove such a noise in a SP maps.

Temperature changes also impact conductivity, affecting both the ground and the electrodes, thus introducing potential noise into the measurements. In effect, the potential of the electrodes is always temperature dependent. Revil & Jardani (2013) have shown that the potential of the electrodes is always temperature dependent and comprised in the range 0.2 $mV^{o}C^{-1}$ to 2 $mV^{o}C^{-1}$ for non-polarizing electrodes. They observed how a difference in temperature of 10°C causes a drift in the SP measurement of 2mV.

Another source of noise, as described by Jackson (2015), is stray currents. These currents originate from anthropogenic sources such as power lines and grounded electric machinery, and they are prevalent in developed areas. Stray currents from power lines typically have a frequency of 50–60 Hz and can be effectively eliminated using band-pass filters.

Not often mentioned in the literature, wind over the electrodes also plays a significant role as a source of noise in SP measurements. Figure 2.1 shows a comparison of SP measurements taken in a test site at the University of Saskatchewan (Canada) during the Field School in 2023. The red line represents (Fig.2.1a) data acquired with the reference electrode unprotected against strong winds, while the black line represents the same data acquisition with the electrode protected, and filtered in (Fig.2.1b). The electrodes $Cu/CuSO_4$, and the target is a buried vertical metal sheet.

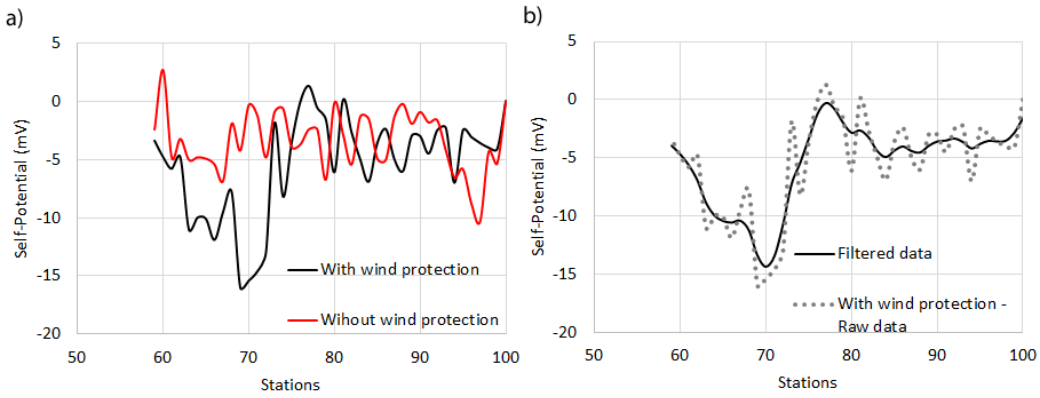

Figure 2.1 - Comparison of SP measurements with and without electrode wind protection (a), filtered data (b).

For more analysis of disturbances in SP observations refer to Revil & Jardani (2013); Jackson (2015); Eppelbaum (2021).

2.1.4 Analytical Signal Amplitude (ASA)

The ASA technique, commonly used in Magnetic and Gravimetric methods, can help to identify the primary source of SP. Following Nabighian (1972), Roest et al., (1992), Biswas (2019), and Sindirgi & Ozyalin (2019), the 3D analytic signal (or ASA) of a potential field is defined as:

$$ASA = \left[\left(\frac{\partial V}{\partial x}\right)^2 + \left(\frac{\partial V}{\partial y}\right)^2 + \left(\frac{\partial V}{\partial z}\right)^2\right]^{1/2}, \tag{2.9}$$

where V represents either the simulated (or measured) potential or p.d. at the surface. In the case of electric potential field, as defined in equation (2.7), the three derivatives in (2.9) coincide with the three components E_x , E_y and E_z , i.e., the ASA is the modulus of the electric field $\boldsymbol{E}$ or the total gradient magnitude V of the SP anomaly. Since our data are computed at a flat surface, E_z in (2.9) is zero. The potential derivatives in (2.9) can be computed numerically by using the FFT technique. The ASA technique first calculates the analytic signal of the input profile using a Hilbert transform. Then, local peaks in the analytic signal profile are interpreted as corners of source bodies, and the shape of the peak contains information about the depth of the corner (Li, 2006; Beiki, 2010; Sunny, 2018). The ASA tends to show a single peak centered over the source

anomaly. In absence of aliasing with a sufficient signal-to-noise ratio, ASA allows for an accurate horizontal localization of anomalies.

2.2 NUMERICAL EXAMPLES

Our study considers conductive anomalies of different geometry embedded in a uniform medium with background resistivity of 50 Ohm.m. The total volume, discretized by a tetrahedral mesh, is a 400 m high parallelepiped, with a base area of 1 km^2 (Fig. 2.2a).

Cylindrical, spherical or blocky anomalies were all tested. The cylindrical body, with a radius of 5 m, is 40 m long. It has a resistivity of 10 Ohm.m and can be vertical, dipping 35° to the positive X direction or dipping 35° to the negative Y direction (Fig. 2.2b). The spherical body, with a resistivity of 10 Ohm.m, has either a radius of 10 m or 40 m (Fig. 2.2c). The cylinder and the sphere are centered at (X, Y, Z) = (0, 0, 170). Then five 8 m^3 blocks, with a resistivity of 90 Ohm.m, were placed at 5 m and 10 m depth, as shown in Fig. 2.2d. A total of 180 survey points (i.e., electrode positions) are deployed at the surface along ten lines. Each line comprises six sets of acquisition units, 30 m spaced and labeled from A to F, as shown in Fig. 2.2d. Each unit has two channels and it controls three electrodes (i.e., two dipoles), 20 m spaced (Fig. 2.2d). All array techniques presented here adopt the same electrode deployment However, as will be seen in the following sections, the arrangement in triplets applies only to the unconventional arrays that will be presented, such as the SG technique, which comprises three electrodes or two dipoles for each unit of measurement.

The spherical anomaly is divided into eight equally spaced longitudes and two lines of constant latitude (Fig. 2.2c). We placed a negative and a positive point source of 50 mA at the poles (top and bottom, respectively), and eight negative point sources of -25 mA on the top line of constant latitude, and other eight positive point sources of 25 mA on the bottom line of constant latitude. Regarding the cubic blocks, a point source of 5 mA (absolute value) was added at each corner, i.e., four negative point sources at top and four positive point sources at the bottom for each block. The cylindrical body is divided into two parts, with 4 equally spaced point sources of -50 mA at the top face and +50 mA at the bottom face. At a distance of 20 m from the top and the bottom,

other eight equally spaced positive and eight negative point sources of 25 mA were placed around the cylinder, as shown in Fig. 2.2b. In all models, the current sources summation is 0.

The mesh was built with a maximum element size of 10 m, minimum element size of 0.2 m, and a curvature factor of 0.2 m. The mesh was refined around every point source and every electrode position at surface, thus increasing the resolution in the regions of interest (Fig. 2.2a)

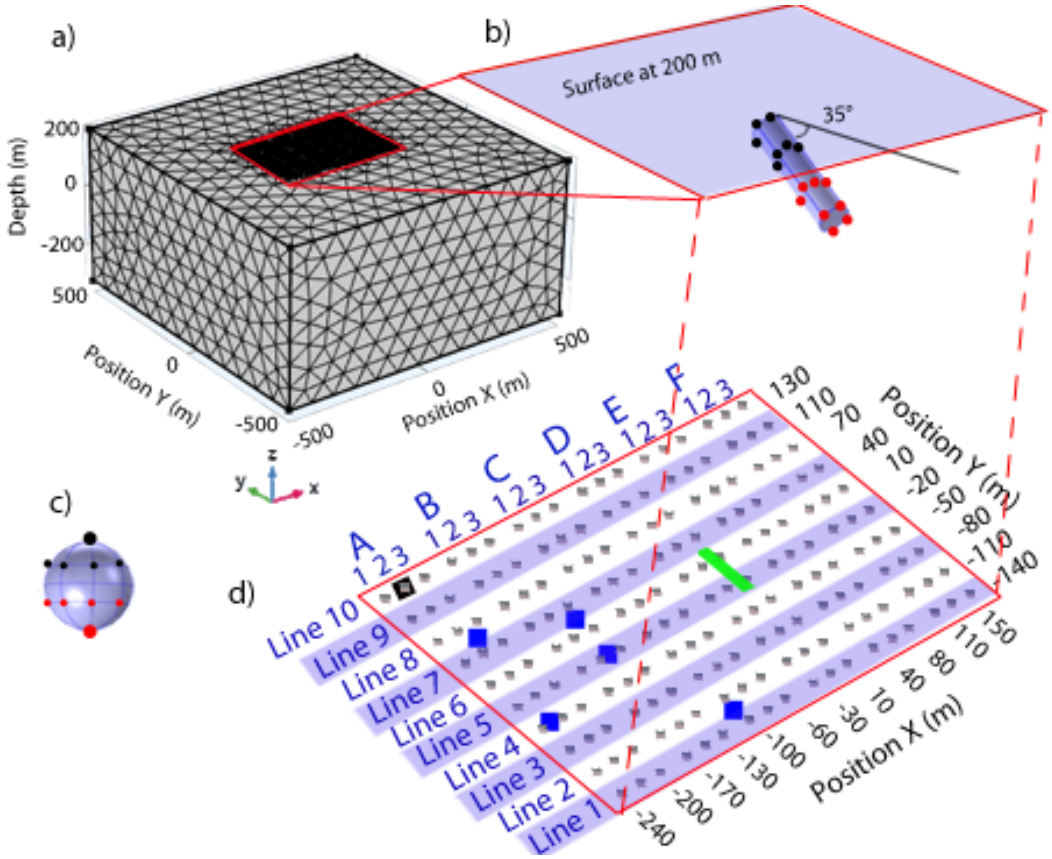

Figure 2.2 - a) discretized COMSOL model; b) cylindrical conductive anomaly dipping 35° to the negative Y direction, where black and red dots are negative and positive current sources, respectively; c) spherical conductive anomaly with corresponding current sources; d) acquisition pattern with 180 electrodes separated by 10 lines (30 m spaced along Y) and six acquisition units (from A to F, 70 m spaced along X). Each unit controls 3 electrodes (2 channels), 20 m spaced. The black square in unit A2 is a reference electrode, labelled as L10A2, meaning "Line 10", position A2. The blue squares are blocky conductive anomalies. The green rectangle is the projection of the cylindrical conductive anomaly on the surface.

2.2.1 Fixed-Base Technique

The Fixed-Base technique consists in computing the p.d. with respect to a fixed reference electrode. Fig. 1d shows a reference electrode (labelled as L10A2) located away from the cylindrical anomaly, giving a sequence of p.d. shown in TABLE 2.1.

Table 2.1 - Sequential p.d. in the Fixed-Based technique, using the reference electrode L10A2, for Lines 10 and 9 labelled as L10 and L9, respectively.

Potential Difference	Potentials
V1	L10A1 - L10A2
V2	L10A2 - L10A2
V3	L10A3 – L10A2
V4	L10B1 - L10A2
V5	L10B2 - L10A2
V6	L10B3 - L10A2
...	...
V19	L10F3 - L10A2
V20	L9A1 - L10A2
V21	L9A2 - L10A2
V22	L9A3 - L10A2
V23	L9B1 - L10A2

V24	L9B2 - L10A2
...	...

Considering the electric potential in L10A2 at ground level (0 mV), the electric potential of the other electrodes is equal to the measured p.d. In other words, the L10A2 point is taken as reference electrode in all Fixed-Base simulations.

2.2.2 Leapfrog Technique

The Gradient or Leapfrog technique is displayed in Fig.2.3, and corresponds to a sequential p.d. for each dipole as shown in Table 2.2.

Table 2.2 - Sequential p.d. in the Gradient (or Leapfrog) technique for Lines 10 and 9, labelled as L10 and L9, respectively.

Potential Difference	Potentials
V1	L10A2 - L10A1
V2	L10A3 - L10A2
V3	L10B1 - L10A3
V4	L10B2 - L10B1
V5	L10B3 - L10B2
...	...
V18	L9F3 - L10F3
V19	L9F2 - L9F3

... ...

A modified Leapfrog technique is obtained by setting the potential at position L10A2 at ground level (0 mV), and referring all the p.d. to this reference electrode. This means that the potential at point A1 in Line 10 (L10A1) equals the measured p.d. V1. Then, the p.d. V2 is equal to the potential at point A3 in Line 10 (L10A3), which implies:

$$V3 = L10B1 - V2, \tag{2.10}$$

$$L10B1 = V2 + V3, \tag{2.11}$$

$$V4 = L10B2 - L10B1. \tag{2.12}$$

Substituting equation (2.11) in (2.12):

$$L10B2 = V4 + L10B1 = V2 + V3 + V4, \tag{2.13}$$

and so on. In other words, in the Leapfrog technique we can sum successive p.d. to infer the electric potential in each point. For this reason, this technique is referred to as "Leapfrog with summation".

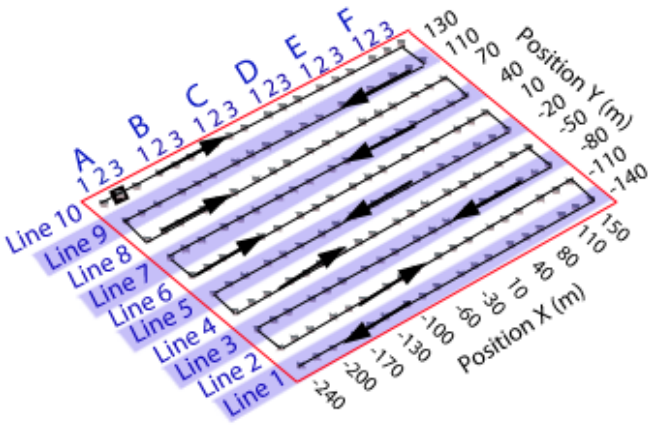

Figure 2.3 - Sequence of dipoles for the measurements of p.d. in the Gradient (or Leapfrog) and Leapfrog with summation techniques. The black square in unit A2 is a reference electrode, labelled as L10A2, meaning "Line 10", position A2, and the arrows indicate the survey orientation.

2.2.3 The SG Technique

As introduced above, the SG technique shown in Fig.2.4 has several units, each comprising three electrodes or two dipoles. The electrodes are collinear for the same line, and the lines are parallel. The main difference between the SG and the Leapfrog is that there is no common reference electrode among different units. For this reason, the summation procedure present in the Leapfrog technique cannot be performed in this case. However, it's important to consider that while the SG technique may have limitations, it also offers advantages in terms of simplicity and efficiency, particularly in scenarios where the conventional techniques may not be feasible. Moreover, it is possible to integrate DERT and SP data simultaneously acquired using the new-generation of resistivity-meters, with a consequent improvement in the localization of the SP source anomaly. Here we assume that every unit is independent, but all the units simultaneously measure the p.d. In Fig.2.4, 60 acquisition units are represented. In a real field acquisition, this would be equivalent to 2 voltmeters per acquisition unit, so 120 voltmeters measure the self-potential simultaneously. Considering the X direction in Fig. 2.4, the p.d. was always computed, in the order, between the larger electrode index and the lower electrode index of the same unit, i.e., 2 – 1, 3 – 2. For example, in the case of Line 10 and positions A and B:

$$V1 = L10A2 - L10A1, \tag{2.14}$$

$$V2 = L10A3 - L10A2, \tag{2.15}$$

$$V3 = L10B2 - L10B1, \tag{2.16}$$

$$V4 = L10B3 - L10B2 \tag{2.17}$$

and so on. Note that, for the SG technique, only the p.d. can be determined, not the electric potential.

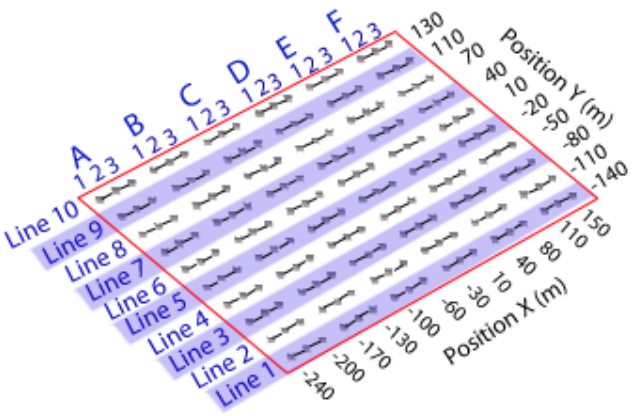

Figure 2.4 - SG technique, including 6 different acquisition units labeled from A to F, each unit controlling 3 electrodes (i.e., two dipoles per acquisition unit), and ten parallel lines.

2.2.4 Full SG Technique

The Full SG technique employs an "L" shaped electrode pattern layout, and allows for two horizontal components of the electric field to be measured. As shown in Fig.2.5, we adopted both "L" and "reversed L" shaped patterns to optimize the spatial resolution.

Considering the Y direction, the p.d. was always computed, in the order, between the larger line index and the lower line index, as shown in Table 2.3. In the X direction, we adopted the same rule of the previous technique, as shown in Table 2.4.

Table 2.3 - Sequential p.d. in the Full SG technique – Y direction for Lines 10, 9, 5, 4, and 3 (labelled as L10, …, L3).

Potential Difference	Potentials
V1y	L9A1 – L10A1
V2y	L7A1 – L8A1
V3y	L5A1 – L6A1
...	…

Vny	L4F3 – L3F3
...	...

Table 2.4 -Sequential p.d. in the Full SG technique – X direction for Lines 10, 9, 5, and 4 (labelled as L10, …, L4).

Potential Difference	Potentials
V1x	L9A2 – L9A1
V2x	L10A3 – L10A2
V3x	L5A2 – L5A1
...	…
Vnx	L4F3 – L4F2
...	...

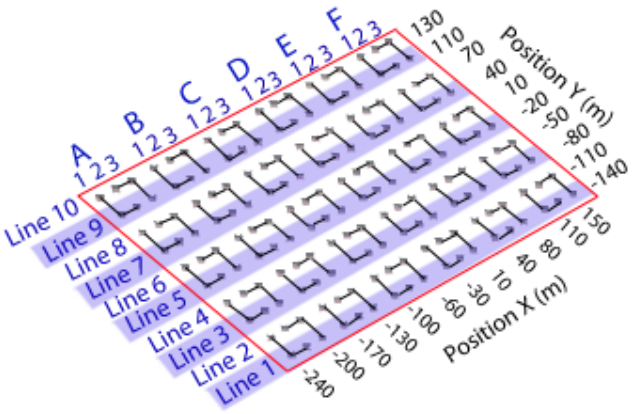

Figure 2.5 - Full SG technique, including orthogonal dipoles for different acquisition units labeled from A to F (direction X) , comprising three electrodes each. The sequential p.d. in the Y direction for Lines 10, 9, …, to 1 (also labelled as L10, …, L1).

2.3 RESULTS

After modelling in COMSOL, the SP at surface were interpolated over the entire survey area shown in Fig. 2.2a using the minimum curvature interpolation method, for all the adopted arrays. Fig. 2.6 shows the results obtained with a homogeneous background medium and a spherical target with a 10 m radius. The simulated SP shown in Fig. 2.6a are obtained adopting a regular distribution of measurement points (monopoles) spaced by 1 m, i.e., it is equivalent to a Fixed-Base array with the reference electrode placed at very large (theoretically infinite) distance. The Fixed-Base technique (Fig. 2.6b) and the Leapfrog technique with summation (Fig. 2.6c) show the same monopolar anomaly, which is similar to that of Fig. 2.6a. This is a consequence of the definition of potential, whose analytical expression is equation (2.7). The two potential fields (i.e., Fig. 2.6a and Fig. 2.6b) differ by a constant value, because both the distribution of measurement points and the reference electrode positions are different. The Leapfrog technique without summation (Fig. 2.6d) and the SG technique (Fig. 2.6e) show a dipolar anomaly, while the Full SG technique (Fig. 2.6f) presented a composition of dipolar response in both directions, X and Y. The Leapfrog technique shows larger SP absolute values than the SG techniques. The SP values of the Full SG technique are smaller than those of all the other techniques.

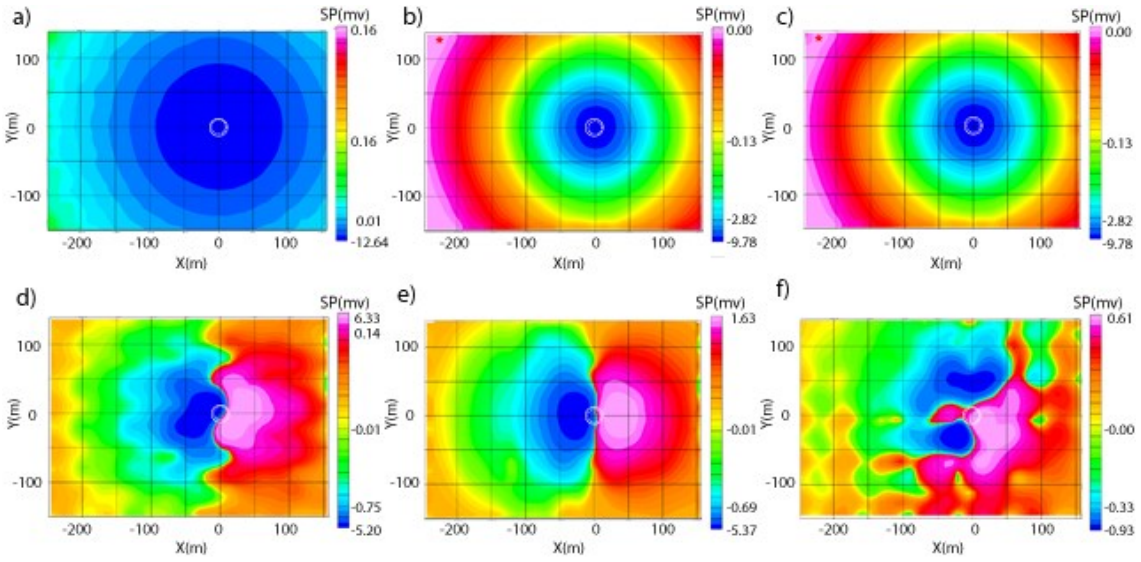

Figure 2.6 - Results obtained using a spherical target anomaly with radius 10 m (white circle), for different SP techniques: a) monopolar anomaly at the surface from the forward modelling, representing the real potential field; b) Fixed-base; c) Leapfrog with summation; d) Leapfrog without summation; e) SG; and f) Full SG. The white circles are the sphere projection at the surface. The red dots in b) and c) indicate the reference electrode, while the white circle is the sphere projection at the surface.

Next, it is computed the response of a spherical target of radius 40 m at 150 m depth, adding the five blocky heterogeneities at 5 m depth, as shown in Fig. 2.2d. Again, the monopole forward model (Fig. 2.7a), the Fixed-Base (Fig. 2.7b) and the Leapfrog with summation techniques (Fig. 2.7c) are in agreement with each other, producing a monopole anomaly. In contrast, the Leapfrog without summation (Fig. 2.7d) and the SG techniques (Fig. 2.7e) show a dipole anomaly. Moreover, the Full SG technique shows a composition of two dipoles in different directions. The spatial resolution is sufficient to locate the blocky heterogeneities (black squares in Fig. 2.7a, Fig. 2.7b and Fig. 2.7c), also those close to the target (white circle in Fig. 2.7). However, the resolution in Figs. 2.7d, 2.7e, and 2.7f is lower due to spatial aliasing. The reduction of measurement points compared to the blocky heterogeneities' discrepancy leads to spatial aliasing, hiding the accurate representation of smaller variations at the surface shown in the Fig. 2.7.

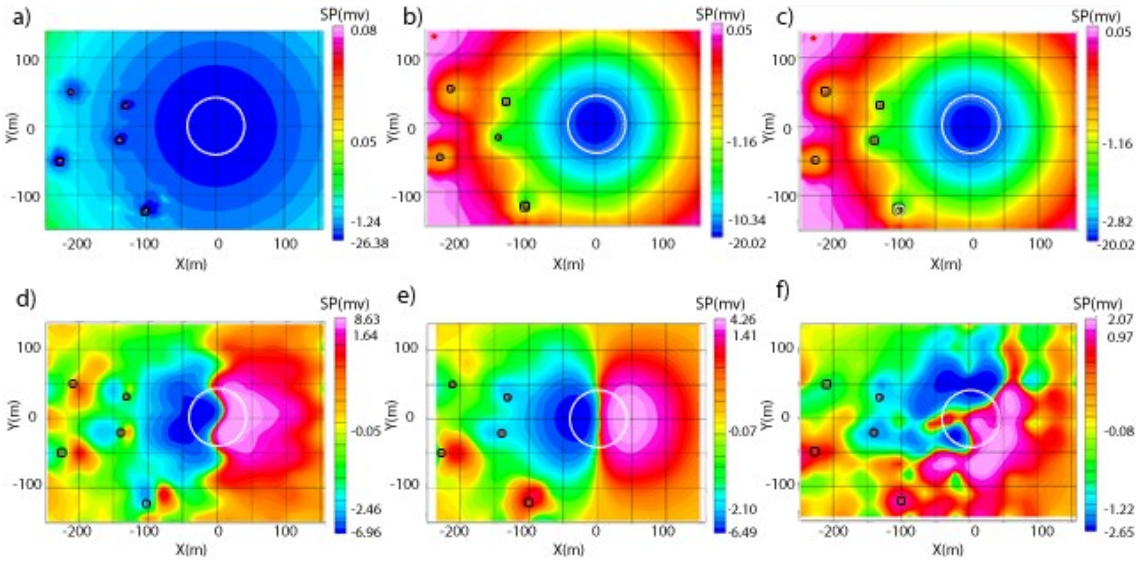

Figure 2.7 - Results obtained using a spherical target anomaly with radius 40 m (white circle) and five blocky heterogeneities, for different SP techniques: a) monopolar anomaly at the surface from the forward modelling representing the real potential field; b) Fixed-base; c) Leapfrog with summation; d) Leapfrog without summation; e) SG; and f) Full SG. The red dots in b) and c) indicate the reference electrode, while the white circle is the sphere projection at the surface. Moreover, the black squares indicate the blocky heterogeneities.

Note that for the Fixed-Base, Leapfrog with summation and Full SG techniques it can appreciate the variation of potential (or p.d.) in the two directions, while this is not the case for the Leapfrog without summation and the SG. For the spherical target radius of 40 m, it is plotted in Fig. 2.8a and 2.8b the p.d. of the Full SG technique acquired in the X and Y directions, respectively. In both cases, the blocky heterogeneities are not visible (black squares Fig. 2.8). Although the spherical target generates a monopole anomaly at the surface (Fig. 2.6a and 2.7a), the Full SG technique represents the source anomaly as dipolar in the two perpendicular directions. The dipole orientation is the same as the acquisition direction, i.e., the same as the single electrode dipoles. Then, the composition of the two maps (Fig. 2.7f) is noisier than the separate plots (Fig. 2.8). It is important, for the Full SG technique, to interpret the SP maps by plotting the computed p.d. in both directions of acquisition.

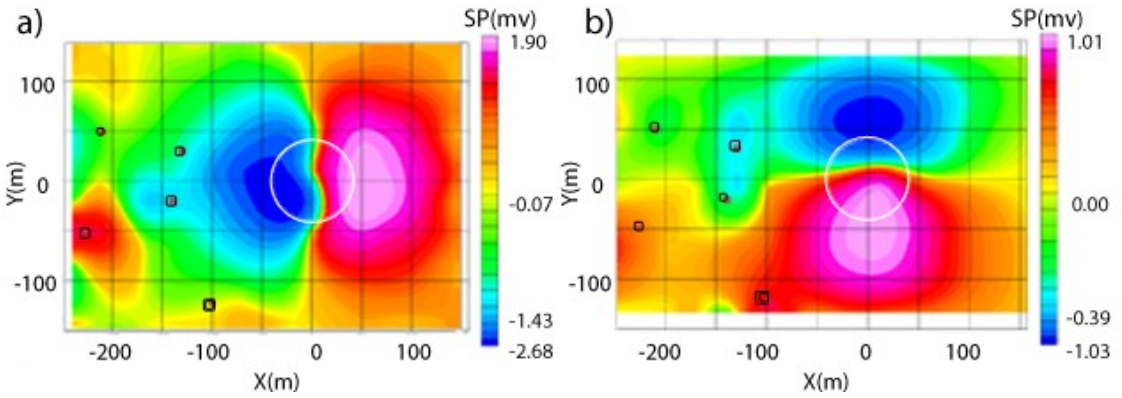

Figure 2.8 - Results obtained using a spherical target anomaly with radius 40 m (white circle) and five blocky heterogeneities, for the Full SG technique. a) dipole measurements acquired in the X direction. b) dipole measurements acquired in the Y direction. The white circle is the sphere projection at the surface, while the black squares indicate the blocky heterogeneities.

Then, it is computed the response of the vertical cylinder with sparse blocky heterogeneities. The Fixed-Base technique (Fig. 2.9b) agree with the monopole forward modelling (Fig. 2.9a) but with lower SP magnitude, mainly due to the different spatial distribution of measurement points (denser in Fig. 2.9a). The resolution is sufficient to distinguish both the deep primary source anomaly and the shallow heterogeneities. As in the previous case, the Fixed-base and the Leapfrog with summation (not shown in Fig. 2.9) are the same. Instead, the Leapfrog technique without summation (Fig. 2.9c) and the SG technique (Fig. 2.9d) shows a dipolar anomaly and the resolution is not sufficient to distinguish the blocky heterogeneities. In the meantime, the Full SG technique is a composite of a dipolar anomaly in the X (Fig. 2.9e) and Y (Fig. 2.9f) directions. The response was similar to the spherical model but with a larger magnitude.

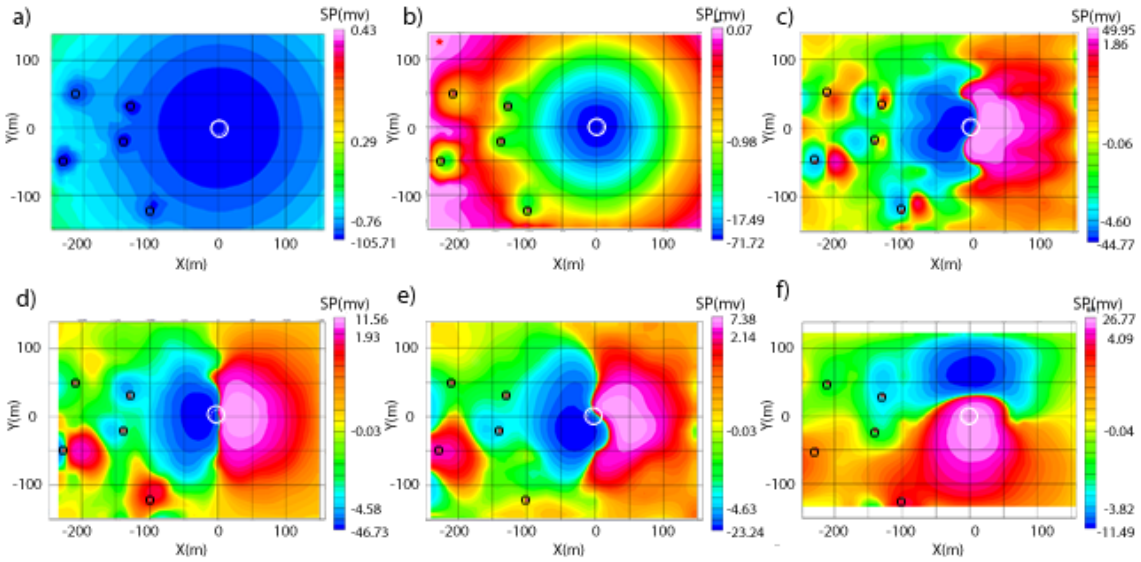

Figure 2.9 - Results obtained using a vertical cylinder with radius 10 m (white circle) and five blocky heterogeneities, for different SP techniques: a) monopole forward modelling representing the real potential field; b) Fixed-base; c) Leapfrog without summation; d) SG; e) Full SG in the X direction; and f) Full SG in the Y direction. The red dot in b) indicates the reference electrode, while the white circle is the cylinder projection at the surface. Moreover, the black squares indicate the blocky heterogeneities.

For the cylinder dipping 35° in the negative Y direction it is obtained a dipole response for the monopole forward modeling (Fig. 2.10a), the Fixed-Base technique (Fig. 2.10b), and the Leapfrog technique with a summation (Fig. 2.10c). Again, the responses were in agreement with each other and with a good resolution. As in the previous cases, the monopole forward modelling exhibits higher SP magnitude, due to the different spatial distribution of measurements points. The Leapfrog without summation (Fig. 2.10d) and the SG technique (Fig. 2.10e) show a quadrupole response and a low resolution.

On the other hand, the Full SG responses in the X and Y directions resemble a quadrupole and two dipoles (of opposite polarities) in series, respectively, while their composition is unclear. In all cases, the center of the dipoles or the quadrupoles do not match the exact center of the cylinder. Only in Fig. 2.10a, Fig. 2.10b Fig. 2.10c the resolution is sufficient to image the shallow resistive heterogeneities.

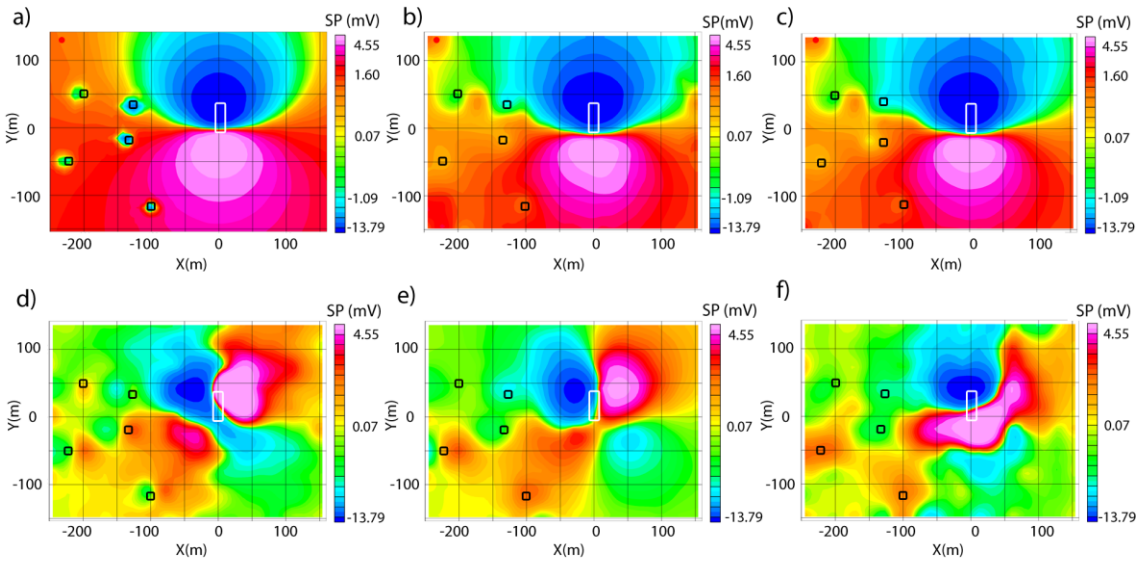

Figure 2.10 - Results obtained using a 35° dipping cylinder (in the negative Y direction) with radius 10 m and five blocky heterogeneities, for different SP techniques: a) monopole forward modelling representing the real potential field; b) Fixed-base; c) Leapfrog without summation; d) SG; e) Full SG in the X direction; and f) Full SG in the Y direction. The red dot in b) indicates the reference electrode, while the white rectangle is the cylinder projection at the surface. Moreover, the black squares indicate the blocky heterogeneities.

For a dipping cylinder 35° toward the negative X direction, the monopolar forward modelling (Fig. 2.11a), the Leapfrog with summation technique (Fig. 2.11b) and the Fixed-Base technique (Fig. 2.11c) exhibit dipolar anomalies with a positive lobe in the negative X direction, i.e., rotated 90° with respect to the previous case. Although the techniques' responses provided different values related to the forward model, their magnitudes are equivalent.

The other techniques provided complicated responses resembling a composition of dipoles with opposite polarities in series.

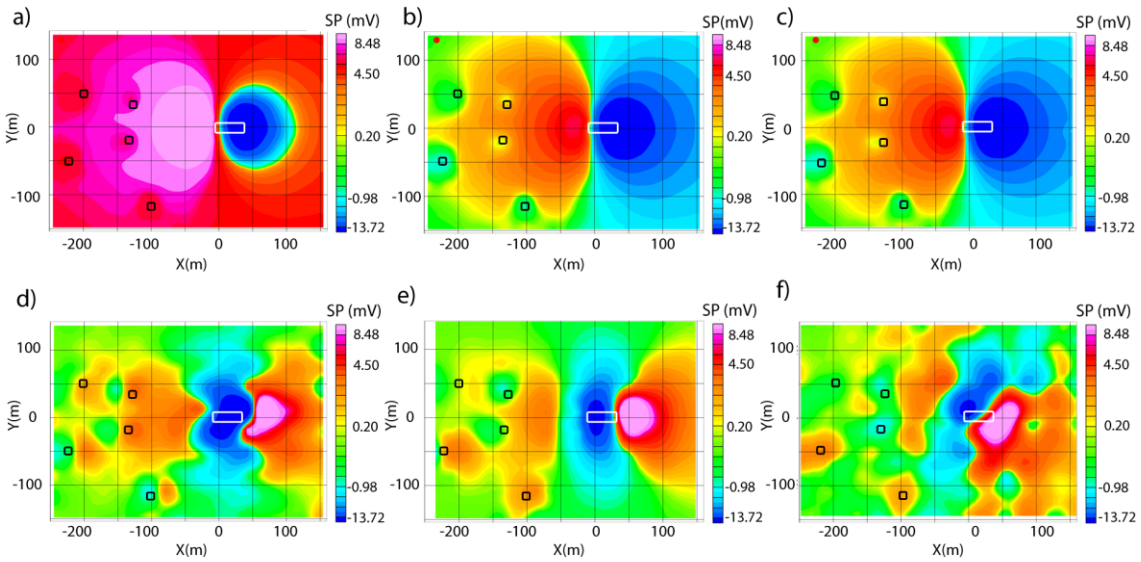

Figure 2.11 - Results obtained using a 35° dipping cylinder (in the negative X direction) with radius 10 m and five blocky heterogeneities, for different SP techniques: a) monopole forward modelling representing the real potential field; b) Fixed-base; c) Leapfrog with summation; d) Leapfrog without summation; e) SG; f) Full SG. The red dots in a), b) and c) indicate the reference electrode, while the white rectangle is the cylinder projection at the surface. Moreover, the black squares indicate the blocky heterogeneities.

Gaussian random noise was added to the numerical modeling to obtain more realistic responses. The noise level ranges from 0% to 90%. In the cases described, at a noise level of about 50-60% the results no longer exhibit a clear and distinguishable dipolar (or quadrupolar) anomaly. In the dipping cylinder case, the SG techniques show a loss of resolution in distinguishing the quadrupole anomaly at even lower noise levels of approximately 40%, except that in the dipping direction, which loses its resolution at 70%.

Fig. 2.12 shows the results adding 30% Gaussian noise, in the case of dipping cylinder in the Y direction). The Leapfrog with summation and Fixed-base techniques no longer produce the same response in the presence of random noise. Moreover, the lateral shallow heterogeneities are no longer visible also for the traditional techniques. The Leapfrog technique without summation (Fig. 2.12d) and the SG technique exhibit the worst results and the responses of the Full SG technique are unclear, which could lead to misinterpretation of the source anomaly. Therefore, one must be cautious when interpreting results using these techniques in high-noise areas.

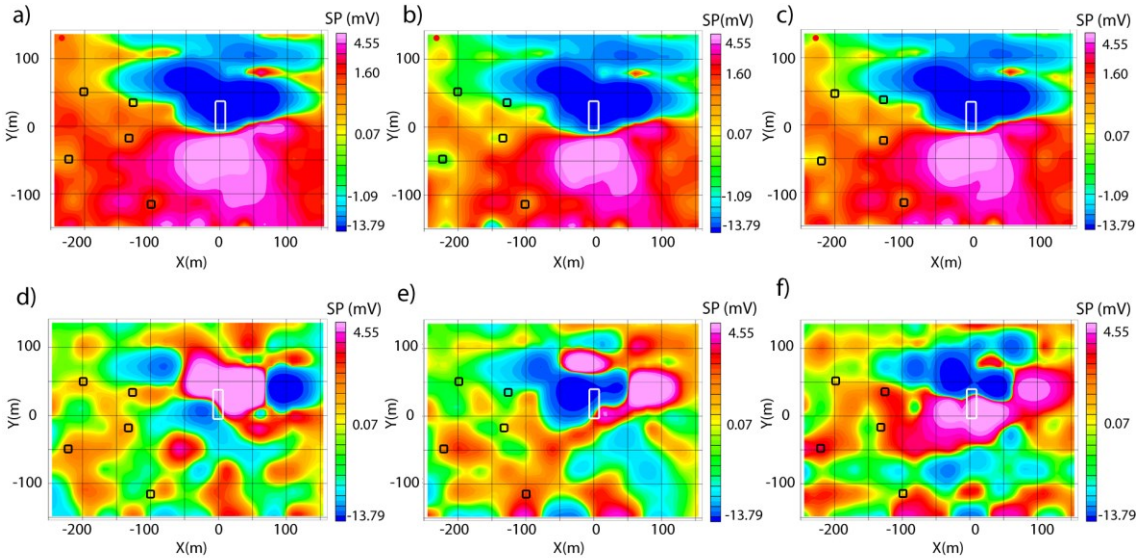

Figure 2.12 - Results obtained in presence of 30% random noise, using a 35° dipping cylinder (in the negative Y direction) with radius 10 m and five blocky heterogeneities, for different SP techniques: a) monopole forward modelling representing the real potential field; b) Fixed-base; c) Leapfrog with summation; d) Leapfrog without summation; e) SG; and f) Full SG for both X and Y components. The red dots in a), b) and c) indicate the reference electrode, while the white rectangle is the cylinder projection at the surface. Moreover, the black squares indicate the blocky heterogeneities.

In general, when the reference electrode is placed away from the source anomaly at ground potential, the Fixed-Base and Leapfrog with summation techniques provide the best results.

2.3.1 Analytical Signal Amplitude Approaches

In the following examples show how the ASA can help identify the source anomaly. It is shown the results of a monopole forward model for a dipping cylinder with a radius of 10 m. As in the previous cases, it is adopted a regular distribution of measurement points (monopoles) spaced by 1 m for the plot interpolation, and a reference electrode placed at very large (theoretically infinite) distance. Fig. 2.13a and 2.13b show the amplitude of the electric field, which is calculated by the magnitude of the electric field vector simulated at the surface, while Fig. 2.13c and 2.13d show the ASA computed from the simulated potentials using equation (2.9). In both cases, the electric field is well represented by a positive peak centered on the source anomalies (Fig. 2.13a and 2.13b). The ASA and electric field maps are in a good agreement, showing similar amplitudes and local differences related to numerical issues around the blocky heterogeneities.

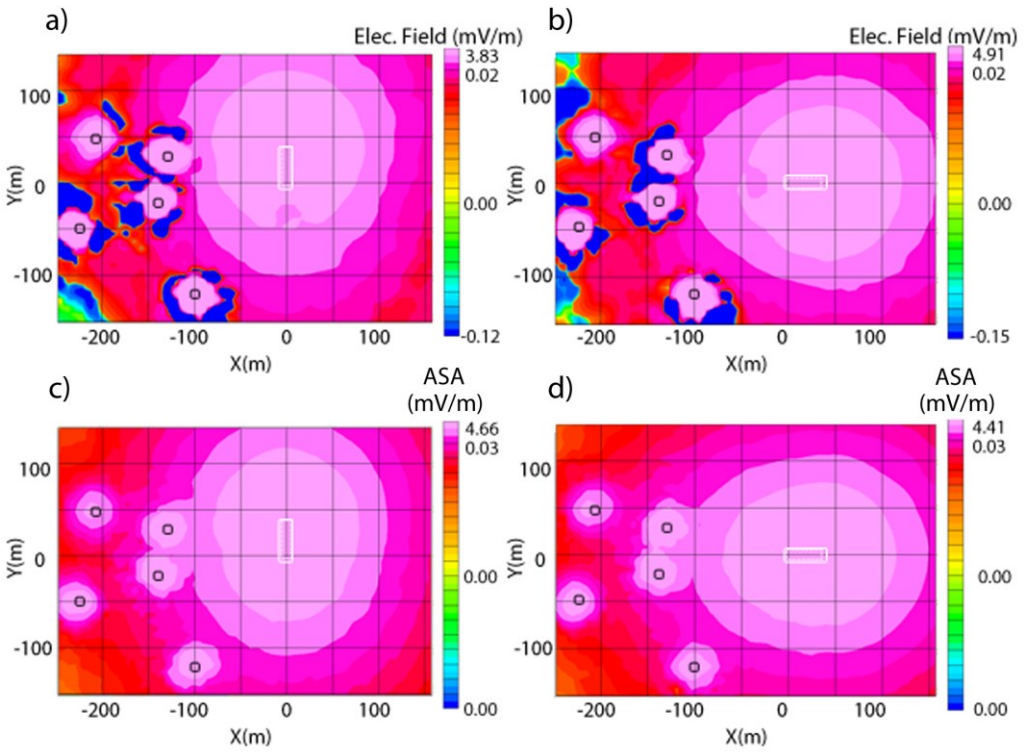

Figure 2.13 - Normalized electric field (a,b) and ASA (c,d) maps obtained from a monopole forward modelling with a regular distribution of measurement points spaced by 1 m. The target anomaly is a 10 m radius cylinder, dipping 35° toward negative Y direction (a,c) and toward the negative X direction (b,d). The white rectangles are the cylinder projections at the surface, while the black squares indicate blocky heterogeneities.

Fig. 2.14 displays the ASA responses of the different arrays in the case of the cylinder dipping to the negative Y direction. All the techniques successfully delimited the primary source anomaly, except a slight shift in the SG array. Good results were obtained for the cylinder dipping to the negative X direction (Fig. 2.15) as well as, except a slight mismatch for the Full SG technique. In both cylindrical cases, Fixed-Base and Leapfrog with summation techniques provide responses very similar to those of the monopole forward modelling, because the ASA is exactly the electric field modulus when V is the potential field in equation (2.9). Although the SG is the noisier approach in measuring the p.d, the ASA enables for a great improvement of the response of this array technique (e.g., Fig. 2.14e). Moreover, the traditional SP arrays undoubtedly provided the best results using ASA as well.

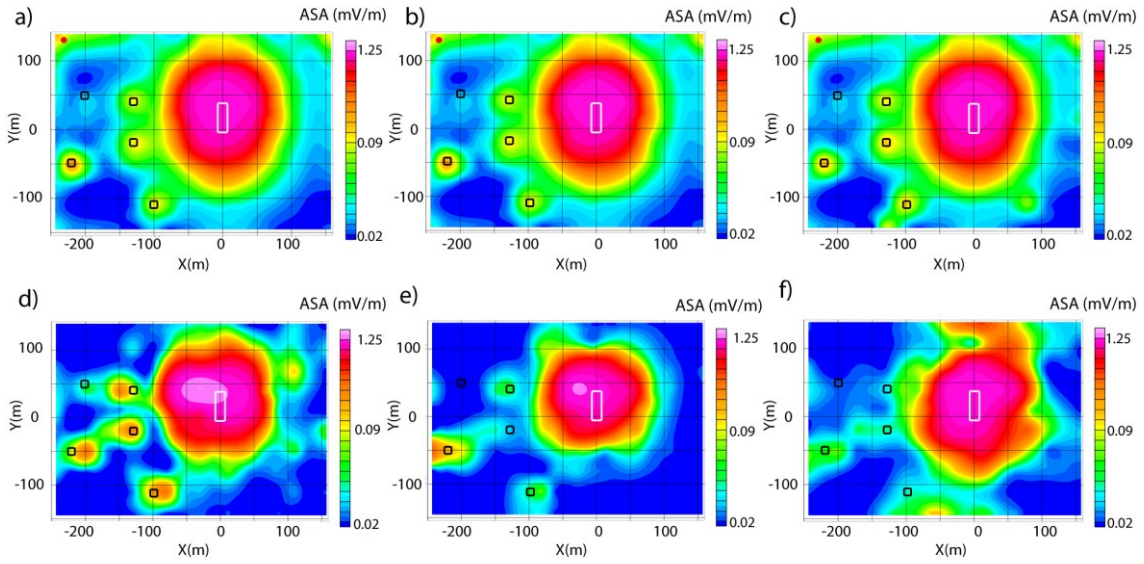

Figure 2.14 - ASA maps for the cylinder dipping to the negative Y direction, for different SP techniques: a) forward model; b) Fixed-Base; c) Leapfrog with summation; d) Leapfrog without summation; e) SG; f) Full SG. The red dots in a), b) and c) indicate the reference electrodes, while the white rectangle is the cylinder projection at the surface. Moreover, the black squares indicate the blocky heterogeneities.

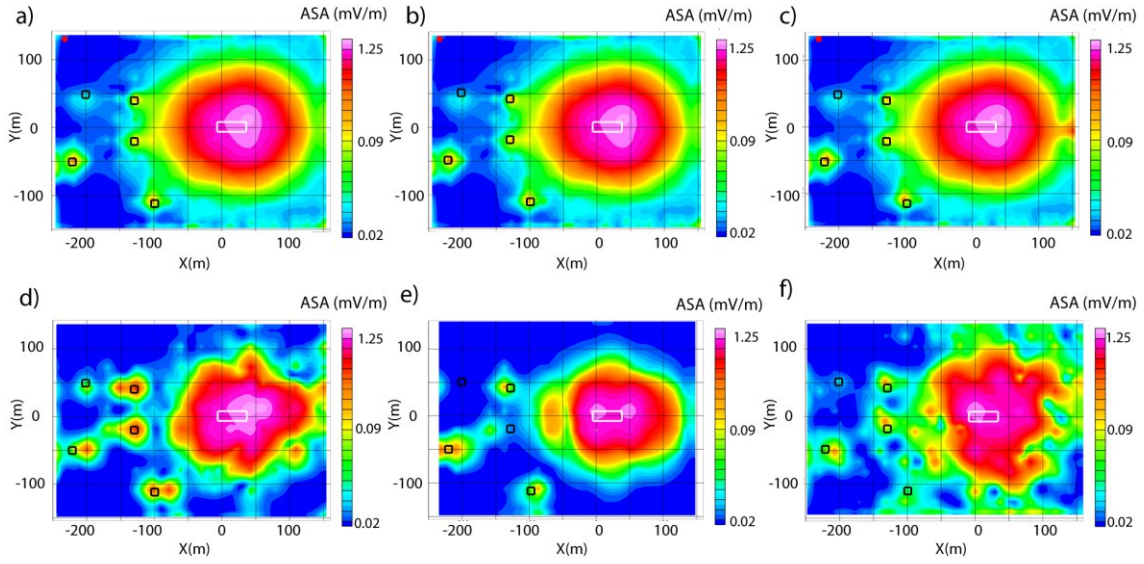

Figure 2.15 - ASA maps for the cylinder dipping to the negative X direction, for different SP techniques: a) forward model; b) Fixed-Base; c) Leapfrog with summation; d) Leapfrog without summation; e) SG; f) Full SG. The red dots in a), b) and c) indicate the reference electrode, while the white rectangle is the cylinder projection at the surface. Moreover, the black squares indicate the blocky heterogeneities.

The results of the ASA analysis in the presence of random noise are displayed in Fig. 2.16, where a 30% noise level has been adopted. The Fixed-base and Leapfrog with summation techniques show the best performance in terms of source delimitation (Fig. 2.16b, 2.16c). In general, the application of the ASA technique improved the results,

even if showing some spatial aliasing, related to the rarefaction of measurement points in the case of the Leapfrog technique with summation (Fig. 2.16c). Furthermore, for the Leapfrog without summation (Fig. 2.16d) and SG (Fig. 2.16e) techniques the acquisition orientation influenced the ASA estimation in the X direction. On the other hand, the Full SG technique employed simultaneously in X and Y directions, enabled to estimate the source anomaly location and its orientation both in noisy (30% noise level) and noise-free simulations. Even with some spatial aliasing (as in precedent cases) in the noisy data, all techniques could still identify and delineate the source anomaly using the ASA. With a noise level higher than 30%, the blocky heterogeneities are hardly detectable.

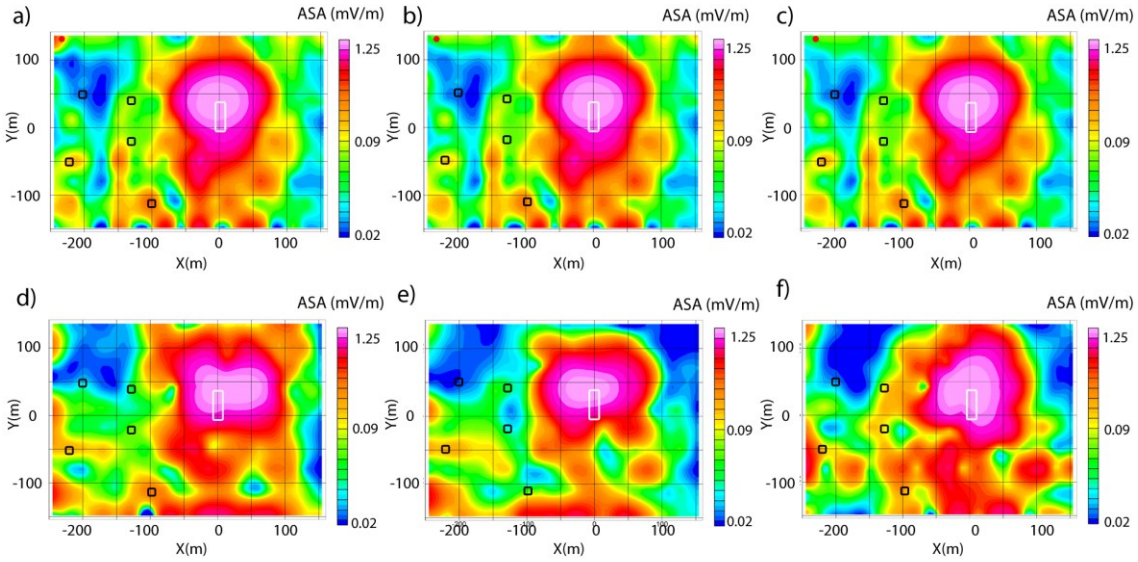

Figure 2.16 - ASA maps with 30% random noise for the cylinder dipping to the negative Y direction, for different SP techniques: a) monopole forward modelling; b) Fixed-Base; c) Leapfrog with summation; d) Leapfrog without summation; e) SG; f) Full SG. The red dots in a), b) and c) indicate the reference electrode, while the white rectangle is the cylinder projection at the surface. Moreover, the black squares indicate the blocky heterogeneities.

2.4 DISCUSSION

It was performed a numerical modelling, using the COMSOL package, to compute the SP response of different geological structures and adopting different acquisition techniques. The model was a homogeneous medium with embedded spherical, cylindrical and small blocky heterogeneities.

The results showed that the Fixed-Base and the Leapfrog with summation techniques are comparable with the monopole forward modelling in all the cases considered,

showing responses of higher quality with respect to the other techniques. In the spherical and vertical cylinder cases, a monopolar anomaly was generated at the surface. The Leapfrog without summation and the SG techniques provided dipolar response, while the Full SG technique presented a composition of dipoles.

In presence of random noise, the Fixed-Base and the Leapfrog techniques show the best performance in resolving shallow resistive heterogeneities. However, adopting the ASA algorithm, also the SG techniques could resolve the blocky resistive bodies until a 30% noise threshold level.

To analyze the influence of different array techniques and target structures, we considered also a dipping cylindrical body. In this case, a dipolar anomaly was observed in the Fixed-Base and Leapfrog with summation techniques, while in the other techniques, a quadrupole or two combined dipoles were observed. When the acquisition direction is parallel to the cylinder axis, the results of the SG, Leapfrog without summation, and Full SG techniques are a composition of dipoles in series. However, when the acquisition direction is orthogonal to the cylinder axis, the results are quadrupoles.

Table 2.5 presents the Root Mean Square Error (RMSE) for the SP and ASA results, both in noise-free conditions and with 30% noise added. It was calculated the individual squared errors for each SP and ASA results. Then, it was computed the square root of the average of the squared errors (RMSE). The Fixed-Base and Leapfrog with summation techniques are equivalent and represent the optimal choices for obtaining high-resolution SP maps and accurately locating primary and shallow source anomalies. However, excellent results can also be achieved using the SG and Full SG arrays with the support of the ASA methodology, allows to obtain valuable additional SP information that would otherwise be discarded in standard DERT processing procedures.

The application of ASA on Fixed-Base and Leapfrog with summation techniques reduced the error from 0.83 to 0.15 for the noise free case. Similarly, for the Leapfrog without summation technique, the error decreased from 8.30 to 0.44, while for the SG technique decreased from 6.56 to 0.42. The ASA error for the Full SG technique was

approximately 0.46. For the cases with 30% added noise, the values changed as follows: from 1.65 to 0.04 for Fixed-Base, from 14.31 to 0.37 for Leapfrog without summation, from 1.55 to 0.03 for Leapfrog with summation, from 10.87 to 0.29 for Sparse Gradient, and from 9.66 to 0.22 for Full Sparse Gradient. These findings show that the ASA procedure considerably improved the reliability of the information regarding source anomalies delimitation.

Table 2.5 - RMSE of the SP (Fig.2.9 and Fig. 2.11) and ASA (Fig. 2.13 and Fig. 2.15) using different arrays, in comparison with the forward model. The noise-free and noisy conditions, with 30% noise added, are considered.

SP (mV)						
Arrays		Fixed-Base	Leapfrog without sum	Leapfrog with sum	SG	Full SG
Noise free	RMSE	0.83	8.30	0.84	6.56	4.93
Noise 30%	RMSE	1.65	14.31	1.55	10.87	9.66
ASA (mV/m)						
Arrays		Fixed-Base	Leapfrog without sum	Leapfrog with sum	SG	Full SG
Noise free	RMSE	0.15	0.44	0.16	0.42	0.46
Noise 30%	RMSE	0.04	0.37	0.03	0.29	0.22

Regardless of the performance of the individual array, new-generation resistivity-meters allow to speed up the acquisition time and to adopt multiple acquisition techniques in

the same SP survey, increasing the information content of SP data. These instruments usually employ SG arrays, but can be adapted also to the traditional arrays. For example, the Fixed-Base and Leapfrog with summation techniques can be easily employed, with some precautions, using the new generation resistivity-meters. This development leads to a significant improvement in the estimate of the electric fields and in a more reliable definition of source anomalies. However, most of DERT acquisitions utilize stainless steel electrodes rather than non-polarizing electrodes.

It is worth mentioning that in many industrial DERT systems (e.g. the FullWaver) there is a physical separation between the transmission and reception components. In this configuration the receiving electrodes are not used to inject the current. Therefore, the polarization effect is much lower even in case of stainless-steel electrodes.

In field experiments, a scaling of SP amplitude was observed when stainless steel electrodes were used instead of non-polarizable electrodes but the overall SP maps appeared to be comparable despite the scaling factor. In addition, in both cases (stainless steel and non-polarizing as the PbCl2/Pb electrodes), when applying the ASA approach, the primary source anomaly can be still recognized, but although with different amplitudes.

2.5 CONCLUSIONS

It was carried out a series of finite-element numerical simulations, using the COMSOL software package, to calculate SP maps in different settings and with various acquisition techniques. Spherical, cylindrical and blocky targets were included in a homogeneous background, thus creating several subsurface models. Modeling results clearly show that the Fixed-Base and the Leapfrog summation techniques are equivalent and they outline different sources of anomaly with a high degree of resolution. Contrarily, the responses of the Leapfrog without summation and of the SG techniques are not straightforward to interpret, in particular in cases with noisy data. For this reason, the summation procedure, in the Leapfrog technique, is highly recommended as it provides more reliable results leading to a better interpretation. The ASA maps, showing a single peak centered over the targets, can significantly help in identifying the source anomalies for all the analyzed array techniques. In particular, the application of ASA

greatly improved the SG responses for all the considered cases, providing reliable information about the electric field generated by the anomaly sources and delimitating the target position at the surface, also in presence of random noise.

As expected, the Fixed-Base and the Leapfrog techniques with summation are the best survey choice for self-potential mapping due to their better accuracy and to their higher resolution in outlining the anomaly sources. However, the SG techniques also provided excellent and interpretable responses when adopting the ASA algorithm, comparable to the results obtained with traditional arrays. This is a relevant breakthrough as it paves the way to a systematic use of SP maps in DERT surveys. This is particularly true in case of separation between the transmission line and the receivers. The typical 3D layout, when collecting DERT data, could be assumed as a non-conventional array and it could be exploited to obtain additional information on the SP maps, enabling a comprehensive electrical characterization of the subsurface. A careful design of DERT field geometry allows for this novel integrated exploration approach especially in cases of large deployments of new-generation distributed systems with several potential-logging units. This approach is cost-effective in terms of both time and logistical effort and, as proved in this study, it could provide additional insight in imaging the subsurface.

REFERENCES

AB COMSOL (2017). COMSOL Multiphysics® v. 5.3. www.comsol.com. COMSOL AB, Stockholm, Sweden.

Abdelrahman, E. S. M., El-Araby, H. M., Hassaneen, A. R. G., & Hafez, M. A. (2003). New methods for shape and depth determinations from SP data. Geophysics, 68(4), 1202-1210.

Abdelrahman, E. M., El-Araby, T. M., & Essa, K. S. (2009). Shape and depth determinations from second moving average residual self-potential anomalies. Journal of Geophysics and Engineering, 6(1), 43-52.

Abedi, M., Hafizi, M. K., & Norouzi, G. H. (2012). 2D interpretation of self-potential data using Normalized Full Gradient, a case study: galena deposit. Bollettino di Geofisica Teorica ed Applicata, 53(2).

Agarwal, B. N. P. (1984). Quantitative interpretation of self-potential anomalies. In SEG Technical Program Expanded Abstracts 1984 (pp. 154-157). Society of Exploration Geophysicists.

Agarwal, B. N. P., & Srivastava, S. (2009). Analyses of self-potential anomalies by conventional and extended Euler deconvolution techniques. Computers & Geosciences, 35(11), 2231-2238.

Ahmed, A. S., Revil, A., Steck, B., Vergniault, C., Jardani, A., & Vinceslas, G. (2019). Self-potential signals associated with localized leaks in embankment dams and dikes. Engineering geology, 253, 229-239.

Ahmed, A. S., Revil, A., Bolève, A., Steck, B., Vergniault, C., Courivaud, J. R., ... & Abbas, M. (2020). Determination of the permeability of seepage flow paths in dams from self-potential measurements. Engineering Geology, 268, 105514.

Atchuta Rao, D., & Ram Babu, H. V. (1983). Quantitative interpretation of self-potential anomalies due to two-dimensional sheet-like bodies. Geophysics, 48(12), 1659-1664.

Auken, E., Guérin, R., de Marsily, G., & Sailhac, P. (2010). Comment on "Review of self-potential methods in hydrogeophysics" by L. Jouniaux et al.[CR Geoscience 341 (2009) 928–936]. Comptes Rendus. Géoscience, 342(10), 806.

Barde-Cabusson, S., Finizola, A., & Grobbe, N. (2021). A practical approach for self-potential data acquisition, processing, and visualization. Interpretation, 9(1), T123-T143.

Beiki, M. (2010). Analytic signals of gravity gradient tensor and their application to estimate source location. Geophysics, 75(6), I59-I74.

Biswas, A. (2017). A review on modeling, inversion and interpretation of self-potential in mineral exploration and tracing paleo-shear zones. Ore Geology Reviews, 91, 21-56.

Biswas, A. (2019). Inversion of Amplitude from the 2-D Analytic Signal of Self-Potential Anomalies. Minerals. doi:10.5772/intechopen.79111

Bocchia, F., Francese, R. G., Giorgi, M., Fischanger, F., & Picotti, S. (2021). The impact of multiple transmitters on the signal strength in Deep Electrical Resistivity Tomography data: an experiment in the Vajont valley (north-eastern Italy). Bollettino di Geofisica Teorica e Applicata. Forthcoming.

Bolève, A., Revil, A., Janod, F., Mattiuzzo, J. L., & Jardani, A. (2007). Forward modeling and validation of a new formulation to compute self-potential signals associated with ground water flow. Hydrology and Earth System Sciences, 11(5), 1661-1671.

Carrier, A., Fischanger, F., Gance, J., Cocchiararo, G., Morelli, G., & Lupi, M. (2019). Deep electrical resistivity tomography for the prospection of low-to medium-enthalpy geothermal resources. Geophysical journal international, 219(3), 2056-2072.

Darnet, M., & Marquis, G. (2004). Modelling streaming potential (SP) signals induced by water movement in the vadose zone. *Journal of hydrology*, *285*(1-4), 114-124.

Darnet, M., Marquis, G., & Sailhac, P. (2003). Estimating aquifer hydraulic properties from the inversion of surface streaming potential (SP) anomalies. *Geophysical research letters*, *30*(13).

Di Maio, R., & Patella, D. (1994). Self-potential anomaly generation in volcanic areas. The Mt. Etna case-history. *Acta Vulcanologica*, *4*, 119-124.

Eppelbaum, L. V. (2021). Quantitative analysis of self-potential anomalies: Review of case studies from various SP applications.

Finizola, A., Lénat, J. F., Macedo, O., Ramos, D., Thouret, J. C., & Sortino, F. (2004). Fluid circulation and structural discontinuities inside Misti volcano (Peru) inferred from self-potential measurements. Journal of Volcanology and Geothermal Research, 135(4), 343-360.

Fournier, C. (1989). Spontaneous Potentials And Resistivity Surveys Applied To Hydrogeology In A Volcanic Area: Case History Of The Chaîne Des Puys (Puy-De-Dôme, France) 1. *Geophysical Prospecting*, *37*(6), 647-668.

Fox, R. W. (1830). On the electro-magnetic properties of metalliferous veins in the mines of Cornwall. *Philosophical Transactions of the Royal Society of London*, 399-414.

Gallas, J. D. F. (2020). Self-potential (SP) generated by electrokinesis–Efficiency and low cost dam safety. *Journal of Applied Geophysics*, *180*, 104122.

Gallipoli, M. R., Lapenna, V. I. N. C. E. N. Z. O., Lorenzo, P. I. E. T. R. O., Mucciarelli, M., Perrone, A., Piscitelli, S., & Sdao, F. (2000). Comparision of geological and geophysical prospecting techniques in the study of a landslide in Southern Italy. *European Journal of Environmental and Engineering Geophysics*, *4*, 117-128.

Gance, J., Leite, O., Texier, B., Bernard, J. & Truffert, C., (2018). The Fullwaver systems: distributed network of autonomous devices for deep 3D electrical resistivity and induced polarization survey, in EGU General Assembly Conference Abstracts, Vol. 20 of EGU General Assembly Conference Abstracts, p. 12569.

Gibert, D., & Sailhac, P. (2008). Comment on" Self-potential signals associated with preferential groundwater flow pathways in sinkholes by A. Jardani, JP Dupont, and A. Revil. Journal of Geophysical Research: Solid Earth, 113(3), B03210.

Griffiths, D.J., (1999). Introduction to Electrodynamics (3rd ed.). Pearson/Addison-Wesley. p. 213.

Ikard, S. J., Briggs, M. A., & Lane, J. W. (2021). Investigation of Scale-Dependent Groundwater/Surface-water Exchange in Rivers by Gradient Self-Potential

Logging: Numerical Modeling and Field Experiments. Journal of Environmental and Engineering Geophysics, 26(2), 83–98.

Iuliano, T., Mauriello, P., & Patella, D. (2001). A probability tomography approach to the analysis of potential field data in the Campi Flegrei caldera (Italy).

Iuliano, T., Mauriello, P., & Patella, D. (2002). Looking inside Mount Vesuvius by potential fields integrated probability tomographies. *Journal of Volcanology and Geothermal Research*, *113*(3-4), 363-378.

Jackson, M. D. (2015). Tools and techniques: Self-potential methods. In G. Schubert (Ed.), *Treatise on geophysics* (2nd ed., Vol. 11, pp. 261–293). Amsterdam: Elsevier.

Jardani, A., Revil, A., & Dupont, J. P. (2006). Self-potential tomography applied to the determination of cavities. Geophysical research letters, 33(13).

Jiang, K., Zheng, P., Chen, M., Xiao, B., Zhang, C., & Chen, K. (2024). Low-noise multi-channel underwater electric field measurement and analysis system for a ship model. Review of Scientific Instruments, 95(1).

Jouniaux, L., Maineult, A., Naudet, V., Pessel, M., & Sailhac, P. (2009). Review of self-potential methods in hydrogeophysics. Comptes Rendus Geoscience, 341(10-11), 928-936.

Jouniaux, L., Maineult, A., Naudet, V., Pessel, M., & Sailhac, P. (2010). Reply to the comment by A. Revil on "Review of Self-potential methods in Hydrogeophysics" by L. Jouniaux et al.[CR Geoscience 341 (2009) 928–936]. Comptes Rendus. Géoscience, 342(10), 810-813.

Kang, X., Kokkinaki, A., Kitanidis, P. K., Shi, X., Revil, A., Lee, J., ... & Wu, J. (2020). Improved characterization of DNAPL source zones via sequential hydrogeophysical inversion of hydraulic-head, self-potential and partitioning tracer data. Water Resources Research, 56(8), e2020WR027627.

Kukemilks, K., & Wagner, J. F. (2021). Detection of Preferential Water Flow by Electrical Resistivity Tomography and Self-Potential Method. Applied Sciences, 11(9), 4224.

LaBrecque, D. J., Morelli, G., Fischanger, F., Lamoureux, P., & Brigham, R. (2013, December). Field trials of the multi-source approach for resistivity and induced polarization data acquisition. In AGU Fall Meeting Abstracts (Vol. 2013, pp. NS34A-03).

Lajaunie, M., Gance, J., Nevers, P., Malet, J. P., Bertrand, C., Garin, T., & Ferhat, G. (2019). Structure of the Séchilienne unstable slope from large-scale 3D electrical tomography using a Resistivity Distributed Automated System (R-DAS). Geophysical Journal International, 219(1), 129–147, doi:10.1093/gji/ggz259

Li, X. (2006). Understanding 3D analytic signal amplitude. Geophysics, 71(2), L13-L16.

Mehanee, S.A. (2014). An efficient regularized inversion approach for self-potential data interpretation of ore exploration using a mix of logarithmic and non-logarithmic model parameters. Ore Geology Reviews, 57, 87-115.

Mendonça, C. A. (2008). Forward and inverse self-potential modeling in mineral exploration. Geophysics, 73(1), F33-F43.

Meiser, P. (1962). A method for quantitative interpretation of self-potential measurements. Geophysical Prospecting, 10(2), 203-218.

Michel, C. M., Murray, M. M., Lantz, G., Gonzalez, S., Spinelli, L., & De Peralta, R. G. (2004). EEG source imaging. *Clinical neurophysiology*, *115*(10), 2195-2222.

Minsley, B.J., Sogade, J., Morgan, F.D., 2007. Three-dimensional source inversion of self-potential data. Journal of Geophysical Research: Solid Earth 112. https://doi.org/10.1029/2006JB004262

Monteiro Santos, F. A. (2010). Inversion of self-potential of idealized bodies' anomalies using particle swarm optimization. Computers & Geosciences, 36(9), 1185-1190.

Nabighian M.N. (1972). The analytic signal of two-dimensional magnetic bodies with polygonal cross-section, its properties and use for automated anomaly interpretation. Geophysics, 37,507-517.

Naudet, V., Revil, A., Bottero, J. Y., & Bégassat, P. (2003). Relationship between self-potential (SP) signals and redox conditions in contaminated groundwater. *Geophysical research letters*, *30*(21).

Nyquist, J. E., & Corry, C. E. (2002). Self-potential: The ugly duckling of environmental geophysics. The Leading Edge, 21(5), 446–451.

Oliveti, I., & Cardarelli, E. (2019). Self-potential data inversion for environmental and hydrogeological investigations. *Pure and Applied Geophysics*, *176*(8), 3607-3628.

Orellana, E. (1972). Prospección geoeléctrica en corriente continua (Vol. 1). Madrid: Paraninfo.

Overbeek, J. T. G. (1952). Electrochemistry of the double layer. *Irreversible Systems. Colloid Science*, *1*, 115-193.

Panthulu, T. V., Krishnaiah, C., & Shirke, J. M. (2001). Detection of seepage paths in earth dams using self-potential and electrical resistivity methods. *Engineering Geology*, *59*(3-4), 281-295.

Patella, D. (1997). Introduction to ground surface self-potential tomography. Geophysical Prospecting, 45(4), 653-681. https://doi.org/10.1046/j.1365-2478.1997.430277.x

Paul, M. K. (1965). Direct interpretation of self-potential anomalies caused by inclined sheets of infinite horizontal extensions. Geophysics, 30(3), 418-423.

Perrone, A., Iannuzzi, A., Lapenna, V., Lorenzo, P., Piscitelli, S., Rizzo, E., & Sdao, F. (2004). High-resolution electrical imaging of the Varco d'Izzo earthflow (southern Italy). *Journal of Applied Geophysics*, *56*(1), 17-29.

Picotti S., Francese R., Giorgi M., Pettenati F. and, Carcione J. M. (2017). Estimation of glaciers thicknesses and basal properties using the horizontal-to-vertical component spectral ratio (HVSR) technique from passive seismic data, Journal of Glaciology, 63, 229-248, DOI: 10.1017/jog.2016.135.

Poldini, E. (1938). Geophysical exploration by spontaneous polarization methods. Mining magazine, 3–22.

Rao, B. S. R., Murthy, I. R., & Reddy, S. J. (1970). Interpretation of self-potential anomalies of some simple geometric bodies. Pure and Applied Geophysics, 78, 66-77.

Rakoto, H.A., Rajaomahefasoa, R., Razafiarisera, R., & Razafindrakoto, B., (2019). Evaluation of flake graphite ore using self-potential (SP), electrical resistivity tomography (ERT) and induced polarization (IP) methods in east coast of Madagascar, Journal of Applied Geophysics, 169, 134-141.

Revil, A. (2010). Comment on "Review of self-potential methods in hydrogeophysics" by L. Jouniaux et al.[CR Geoscience 341 (2009) 928–936]. Comptes Rendus. Géoscience, 342(10), 807-809.

Revil, A., Finizola, A., & Gresse, M. (2023). Self-potential as a tool to assess groundwater flow in hydrothermal systems: A review. Journal of Volcanology and Geothermal Research, 107788.

Revil, A., Jardani, A., (2013). The Self-Potential Method: Theory and Applications in Environmental Geosciences. Cambridge University Press, Cambridge. https://doi.org/10.1017/CBO9781139094252

Revil, A., Jardani, A., & Dupont, J. P. (2008). Reply to comment by D. Gibert and P. Sailhac on "Self-potential signals associated with preferential groundwater flow pathways in sinkholes. Journal of geophysical research, 113, B03205.

Revil, A., Su, Z., Zhu, Z., & Maineult, A. (2023). Self-Potential as a Tool to Monitor Redox Reactions at an Ore Body: A Sandbox Experiment. Minerals, 13(6), 716.

Revil, A., Titov, K., Doussan, C., Lapenna, V. (2006). Applications of the self-potential method to hydrological problems. In: Vereecken, H., Binley, A., Cassiani, G., Revil, A., Titov, K. (eds) Applied Hydrogeophysics. NATO Science Series, vol 71. Springer, Dordrecht. https://doi.org/10.1007/978-1-4020-4912-5_9

Reynolds, J. M. (2011). *An introduction to applied and environmental geophysics*. John Wiley & Sons.

Rizzo, E., Capozzoli, L., De Martino, G., Piscitelli, S., Bellanova, J., Caputo, R., ... & Fischanger, F. (2020). Deep geophysical investigation in urban area: Ferrara city example (No. EGU2020-9294). Copernicus Meetings.

Roudsari, M. S., & Beitollahi, A. (2013). Forward modelling and inversion of self-potential anomalies caused by 2D inclined sheets. Exploration Geophysics, 44(3), 176-184.

Roest, W. R., Verhoef, J., & Pilkington, M. (1992). Magnetic interpretation using the 3-D analytic signal. Geophysics, 57(1), 116-125.

Segesman, F. F. (1980). Well-logging method. *Geophysics*, *45*(11), 1667-1684.

Sheffer, M. R. (2007). *Forward modelling and inversion of streaming potential for the interpretation of hydraulic conditions from self-potential data* (Doctoral dissertation, University of British Columbia).

Sheffer, M.R., Oldenburg, D.W., (2007). Three-dimensional modelling of streaming potential. Geophysical Journal International 169, 839–848. https://doi.org/10.1111/j.1365-246X.2007.03397.x

Sill, W. R. (1983). Self-potential modeling from primary flows. Geophysics, 48(1), 76-86.

Sindirgi, P., Pamukçu, O., & Özyalın, Ş. (2008). Application of normalized full gradient method to self-potential (SP) data. Pure and applied geophysics, 165, 409-427.

Sindirgi, P., & Özyalin, Ş. (2019). Estimating the location of a causative body from a self-potential anomaly using 2D and3D normalized full gradient and Euler deconvolution. Turkish Journal of Earth Sciences, 28(4), 640-659.

Song, S. Y., Cho, A., Kang, P. K., & Nam, M. J. (2021). A Review on Past Cases of Self-potential Surveys for Dikes and Embankments Considering Streaming Potential. Journal of Soil and Groundwater Environment, 26(6), 1-17.

Song, S., Deng, X., Su, Z., Deng, M., & Chen, K. (2022). Marine self-potential measurement tool for autonomous underwater vehicle. Review of Scientific Instruments, 93(11).

Soueid Ahmed, A., Jardani, A., Revil, A., & Dupont, J. P. (2016). Joint inversion of hydraulic head and self-potential data associated with harmonic pumping tests. Water Resources Research, 52(9), 6769-6791.

Su, Z., Tao, C., Shen, J., Revil, A., Zhu, Z., Deng, X., ... & Chen, D. (2022). 3D self-potential tomography of seafloor massive sulfide deposits using an autonomous underwater vehicle. Geophysics, 87(4), B255-B267.

Sundararajan, N., & Srinivas, Y. (1996). A modified Hilbert transform and its application to self-potential interpretation. Journal of Applied Geophysics, 36(2-3), 137-143.

Sundararajan, N., Srinivas, Y., & Rao, T. L. (2000). Sundararajan Transform-A tool to interpret potential field anomalies. Exploration Geophysics, 31(4), 622-628.

Sundararajan, N., Srinivasa Rao, P., & Sunitha, V. (1998). An analytical method to interpret self-potential anomalies caused by 2-D inclined sheets. Geophysics, 63(5), 1551-1555.

Sungkono. (2020). An efficient global optimization method for self-potential data inversion using micro-differential evolution. *Journal of Earth System Science*, *129*(1), 178.

Sunny, A. A. (2018). Derivatives And Analytic Signals: Improved Techniques for Lithostructural Classification. Malaysian Journal of Geosciences, 2(1), 01-08.

Troiano, A., Di Giuseppe, M. G., Monetti, A., Patella, D., Troise, C., & De Natale, G. (2017). Fluid injection in Enhanced Geothermal Systems: a study on the detectability of self-potential effects and on their correlation with induced seismicity. Geothermics, 65, 280-294.

Troiano, A., Isaia, R., Di Giuseppe, M. G., Tramparulo, F. D. A., & Vitale, S. (2019). Deep electrical resistivity tomography for a 3D picture of the most active sector of Campi Flegrei caldera. Scientific reports, 9(1), 1-10.

Valois, R., Cousquer, Y., Schmutz, M., Pryet, A., Delbart, C., & Dupuy, A. (2018). Characterizing stream-aquifer exchanges with self-potential measurements. Groundwater, 56(3), 437-450.

Xie, J., Cui, Y. A., Guo, Y., Zhang, L., Fanidi, M., & Liu, J. (2020). 2.5 D self-potential forward modeling by natural-infinite element coupling method. Journal of Applied Geophysics, 179, 104077.

Xie, J., Cui, Y. A., Liu, J. X., Guo, Y. J., Zhang, L. J., Luo, Y. J., & Zhang, P. F. (2023). A review on theory, modeling, inversion, and application of self-potential in marine mineral exploration. Transactions of Nonferrous Metals Society of China, 33(4), 1214-1232.

Wilt, M. J., & Butler, D. K. (1990). *Geotechnical Applications Of The Self Potential (Sp) Method; Report 4: Numerical Modeling Of Sp Anomalies: Documentation Of Program SPPC And Applications* (No. Tech Rept REMR-GT-6).

Wilt, M. J., & Corwin, R. F. (2005). Numerical modeling of self-potential anomalies due to leaky dams: Model and field examples. In *Detection of subsurface flow phenomena* (pp. 73-89). Berlin, Heidelberg: Springer Berlin Heidelberg.

Zhu, Z., Shen, J., Tao, C., Deng, X., Wu, T., Nie, Z., ... & Su, Z. (2021). Autonomous-underwater-vehicle-based marine multicomponent self-potential method: Observation scheme and navigational correction. Geoscientific Instrumentation, Methods and Data Systems, 10(1), 35-43.

Zhu, Z., Tao, C., Shan, Z., Revil, A., Su, Z., Nie, Z., ... & Zhou, J. (2023). 3D Multicomponent Self-Potential Inversion: Theory and Application to the Exploration of Seafloor Massive Sulfide Deposits on Mid-Ocean Ridges. Minerals, 13(8), 1098.

CHAPTER 3

3. SPVIEWER: A TOOL FOR SP PROCESSING AND VISUALIZATION OF DATA FROM FULLWAVER INSTRUMENT

3.1 INTRODUCTION

In geophysics, understanding self-potential (SP) is pivotal, especially when exploring the underground composition and structure. Revil and Jardani (2013) have described the sources of the SP anomalies, including (1) thermo-potential and natural potential related to the difference of temperature; (2) electrochemical, as a source of different potential caused by chemical reaction; (3) streaming potential or electrokinetic; (4) geobattery, which explains about the difference of potential caused by biotic and abiotic to redox reaction. SP offers crucial insights into underground properties, aiding in fluid distribution comprehension, mineral deposit identification, and geological mapping. This phenomenon directly exposes electrochemical occurrences, vital for interpreting regional geology and natural resources.

Contributing to the development landscape of geoelectrical data acquisition techniques, new-generation of georesistivimeters have been made available in the industry. The FullWaver system is one of these new instruments, which is a distributed network of autonomous devices designed for deep 3D electrical resistivity and induced polarization surveys. These systems, composed of multiple autonomous units (V-FullWaver), about 20 to 50 in number, continuously record the electrical field across two channels between three electrodes (P1-P2 and P2-P3). Typically positioned perpendicular to ensure consistent signal measurement, these dipoles are arranged in either a regular or adapted irregular layout based on field conditions like topography, roads, buildings, and vegetation. By employing such a setup, the system effectively eliminates common drawbacks associated with extensive cable arrangements in large 3D areas, including time consumption, limited accessibility, weight, and electromagnetic induction (Gance et al., 2018).

The V-FullWaver is a dual channel Induced Polarization (IP), Electrical Resistivity Tomography (ERT) and SP receiver. Continually recording at 10ms sample rate provides a full waveform record. It can be synchronized on the GPS PPS signal, allowing an easy process of the signal. Data on the memory can be downloaded directly on a simple USB stick from all the FullWavers (IRIS Instruments - https://www.iris-instruments.com/) . In ERT and IP surveys using these new-generation georesistivimeters, the SP voltages are typically regarded as noise rather than signals, logged solely for the purpose of distinguishing artificial from site-related potentials.

Opposite to that, we have written a tool in MATLAB for extracting and retrieving the self-potential data available in those active electric surveys, as well as for passive acquisitions. The SPViewer is a free-open tool for extracting and processing temporal series of SP signal from FullWaver systems, and visualizing their time-lapse maps. This tool is essential for processing intricate signals, eliminating unwanted noise, and accurately interpreting anomaly sources. Without this specialized tool, analyzing data would be time-consuming, error-prone, and incapable of generating precise SP maps.

3.2 SPVIEWER

The SPViewer consist of 13 script files compiled in MATLAB 2022. It can be installed on a portable computer even without a MATLAB license.

3.2.1 Data Conversion

Before data acquisition, the V-FullWaver receivers (Rx units or box units) need to be sequentially numbered, and the electrode positions P1(x,y), P2(x,y), and P3(x,y) should receive a fictitious coordinate x and y. For instance, for Rx unit 9, the coordinates should be configured as P1(9,1), P2(9,2), and P3(9,3). The data recorded for each V-FullWaver box is stored in binary files with the extension '.VMN' and must be named and organized in sequential order according to each FullWaver "box unit".

The receiver unit should provide a file named according the following form "VPBoxID@UTC_mmddyy_hhmmss", which mmddyy corresponds respectively month, day and year, as well as hhmmss is hour, minute and second that starts the acquisition of that receiver unit. For example, 30th November 2022 at 16h10min15s

for the receiver unit 2, the named file must be organized as “VP002@113022_ 161015.VMN”.

Before organizing the file names, all file must be insert in a single folder inside the folder of the SPViewer folder. On MATLAB is required to add the folders and subfolders to the path directory. Opening the tool, the first step is to select the VMN Data file in order to convert the binary data into temporal series of “csv” extension (Figure 3.1).

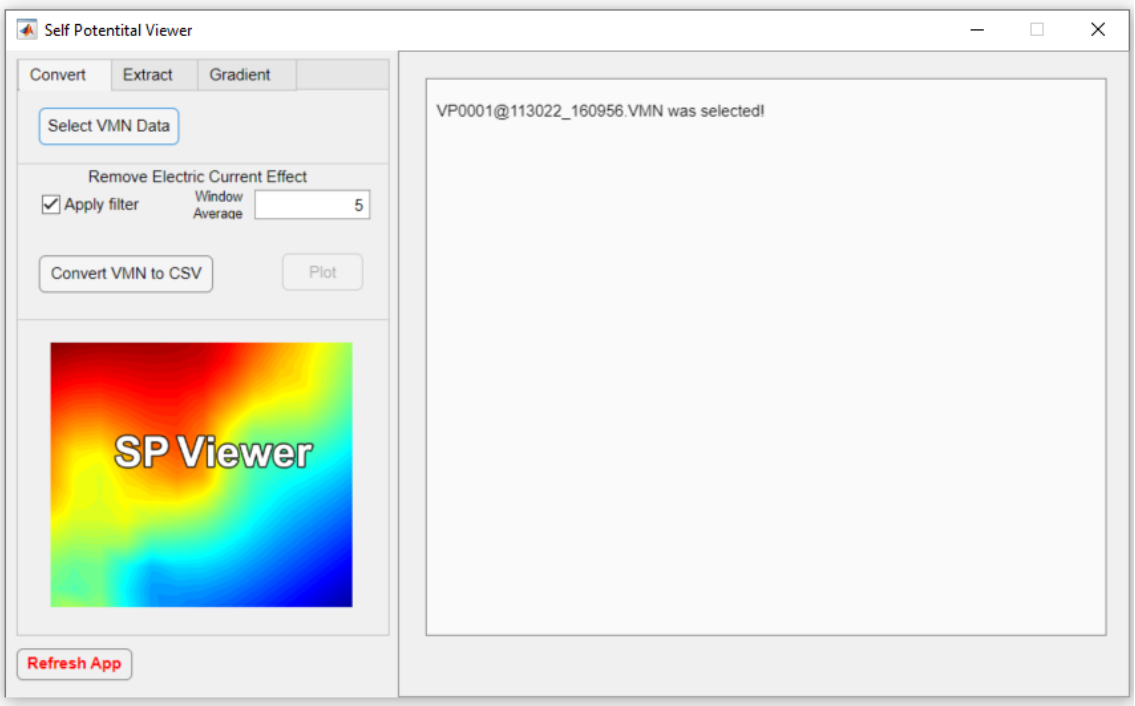

Figure 3.1 – Convert tab of the SP Viewer with window average filter selected.

Depending on how long is the monitoring, the conversion can be taking a while, and will be put in the same directory selected on MATLAB. In case of artificial voltage being present in the data, the electric current effect can be removed applying the window average filter. Figure 3.2a and Figure 3.2c show the recorded voltage of the channel 1 and 2 respectively, and the strong signals correspond to the artificial voltage generated by the electric current injections, while Figure 3.2b and Figure 3.2d are the filtered data.

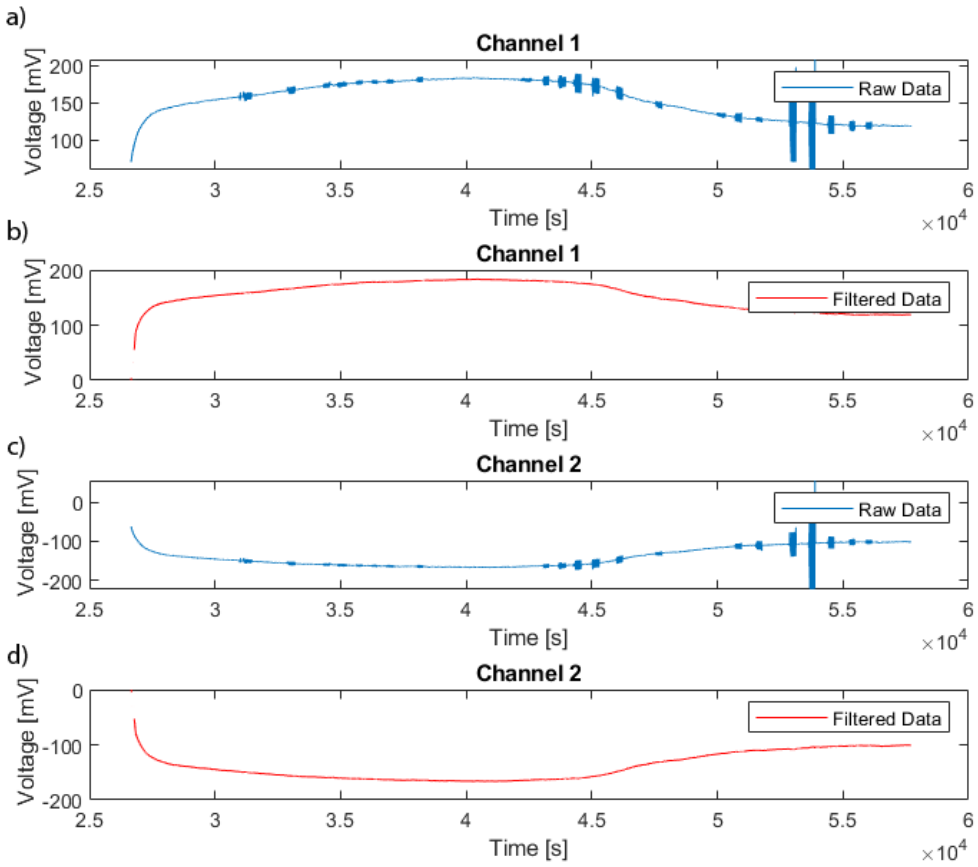

Figure 3.2 - a) and c) display the recorded voltage for channels 1 and 2, respectively, with strong signals representing the artificial voltage from electric current injections. b) and d) showcase the corresponding filtered data.

3.2.2 Data Extraction

The second step is to extract the temporal series selecting the "csv" generated by the conversion step. Sometimes during the field acquisition is possible to swap the electrodes in another port, but this can be easily corrected changing the channel polarities on the tab extraction.

The extraction can be subsampled in 100 milliseconds, 1 second, 1 minute and 10 minutes. A folder called "extracted" will be created on the same directory selected on MATLAB, and the extracted data will be put on that. Figure 3.3 shows the extraction subsampled in 1 s from the 7:40 AM to 4 PM

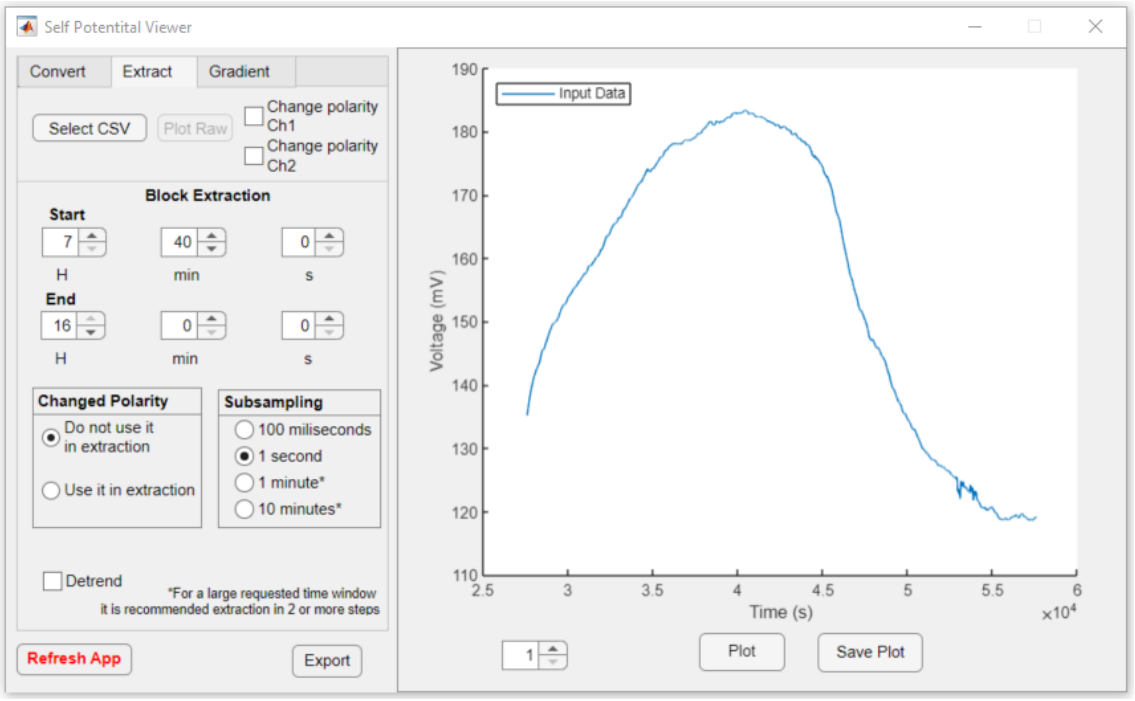

Figure 3.3 - Extract tab with subsampling the data in 1 s.

After selecting the "Extract" tab, the "Convert" tab becomes inactive for processing. To use it again, the user will need to refresh the tool.

4.2.3 Gradient and SP plots

The Gradient tab has the purpose of adding the real coordinates to the "extracted files", generating a file with ". grad" extension. Each extracted file must to be loaded separately in "Time Serie" button. First it is necessary to load the coordinate file in ".txt" format configured in 8 rows as shown in Figure 3.4. The last two lines in the row "ID_box" must be finished by 0. A file for the surface also is required at this step (Figure 3.5). It is also possible to use coordinates that are not coincident to the "ID_box" row.

ID_box	ID_elettrodo	x_dummy	y_dummy	z_dummy	x_UTM(m)	y_UTM(m)	z_(m)
1	1	1	0	595454.84	4930370.66	824.001	
1	2	1	2	0	595473.38	4930364.37	819.871
1	3	1	3	0	595492.38	4930358.32	818.597
2	1	2	1	0	595459.82	4930389.28	820.915
2	2	2	2	0	595478.58	4930383.45	817.961
2	3	2	3	0	595497.35	4930377.28	816.008
3	1	3	1	0	595464.62	4930408.69	817.718
3	2	3	2	0	595483.22	4930402.85	816.209
3	3	3	3	0	595502.15	4930396.68	814.202
4	1	4	1	0	595469.74	4930427.98	816.888
4	2	4	2	0	595488.27	4930421.92	813.539
4	3	4	3	0	595507.12	4930415.53	811.619
5	1	5	1	0	595474.7	4930447.5	816.795
5	2	5	2	0	595492.92	4930440.99	814.317
5	3	5	3	0	595511.76	4930435.04	811.188
6	1	6	1	0	595478.95	4930466.67	815.658
6	2	6	2	0	595498.04	4930460.51	813.181
6	3	6	3	0	595517.04	4930454.34	812.041
7	1	7	1	0	595525.98	4930409.14	808.936
7	2	7	2	0	595530.69	4930428.77	808.538
7	3	7	3	0	595535.74	4930448.06	808.949
8	1	8	1	0	595436.32	4930376.5	825.728
8	2	8	2	0	595441.28	4930395.9	824.788
8	3	8	3	0	595446.09	4930414.97	822.875
0							
0							

Figure 3.4 – Example format of the load "Coordinate file".

ID_box	x_UTM(m)	y_UTM(m)	z_(m)
1	595454.84	4930370.66	824.001
1	595473.38	4930364.37	819.871
1	595492.38	4930358.32	818.597
2	595459.82	4930389.28	820.915
2	595478.58	4930383.45	817.961
2	595497.35	4930377.28	816.008
3	595464.62	4930408.69	817.718
3	595483.22	4930402.85	816.209
3	595502.15	4930396.68	814.202
4	595469.74	4930427.98	816.888
4	595488.27	4930421.92	813.539
4	595507.12	4930415.53	811.619
5	595474.7	4930447.5	816.795
5	595492.92	4930440.99	814.317
5	595511.76	4930435.04	811.188
6	595478.95	4930466.67	815.658
6	595498.04	4930460.51	813.181
6	595517.04	4930454.34	812.041
7	595525.98	4930409.14	808.936
7	595530.69	4930428.77	808.538
7	595535.74	4930448.06	808.949
8	595436.32	4930376.5	825.728
8	595441.28	4930395.9	824.788
8	595446.09	4930414.97	822.875
0			
0			

Figure 3.5 - Example format of the load "Surface file".

On the section "Grad Format Data" the user must select the type of subsampled grad data that will be imported before to load the "Surface file". The button "Grad store" will be activated and pushing it, all subsampled ". grad" will be imported (Figure 3.6). In this step is also possible to generate automatic time-lapse maps on SPViewer or use specific time (Figure 3.7) for plotting the data in other external software.

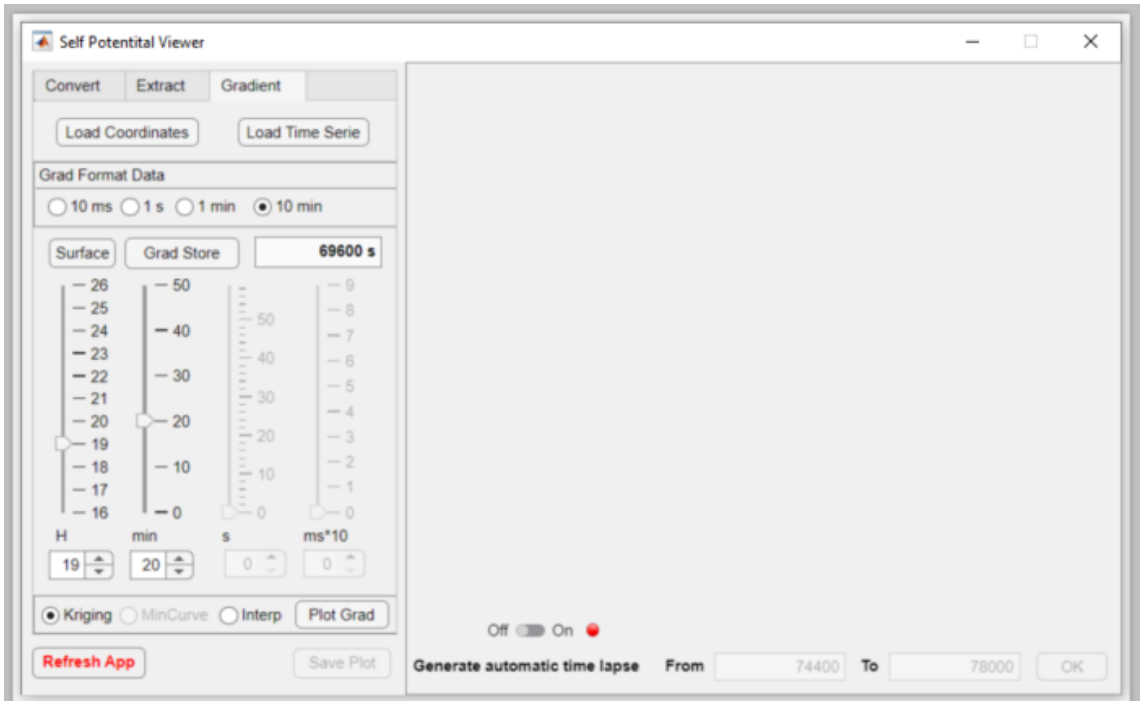

Figure 3.6 – Gradient tab.

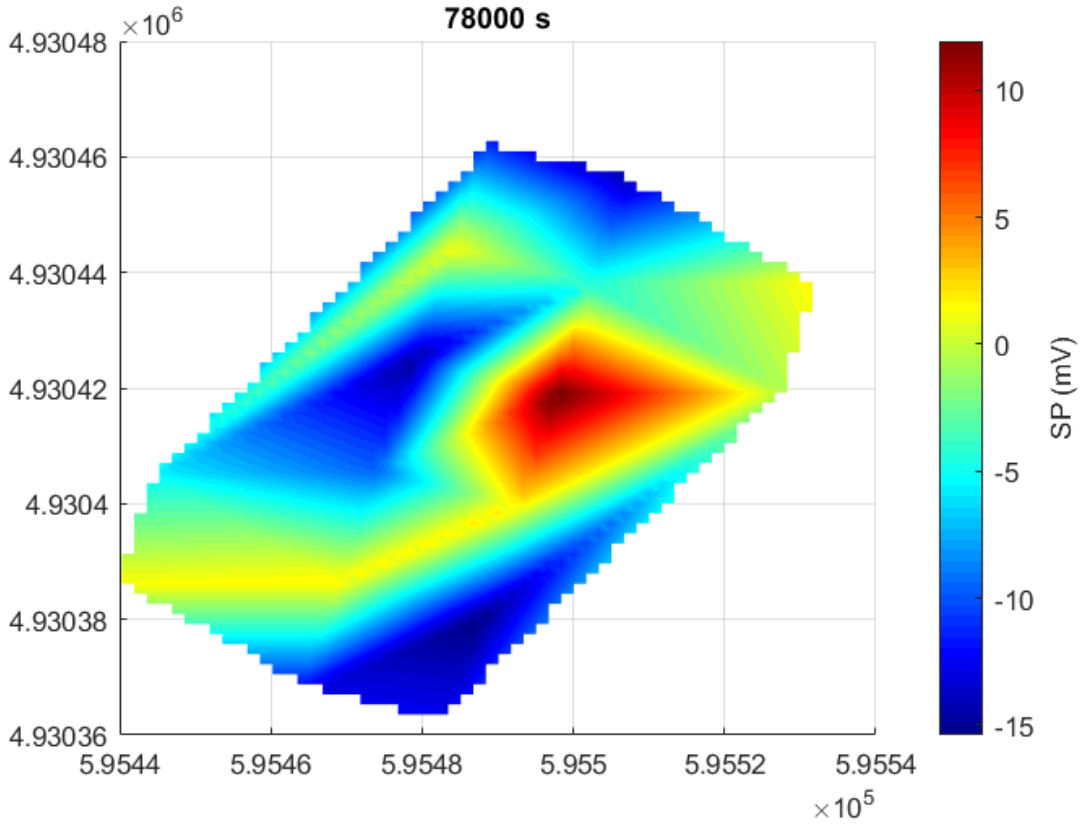

Figure 3.7 – SP map interpolated for a specific time window.

3.3 DRAWBACKS AND SOLUTIONS

Unlike traditional SP acquisitions that feature reference electrodes, the arrays provided by the FullWaver system lacks a common electrode for all channels. Consequently, the resulting map might be inadequate and misinterpreted. An alternative solution involves conducting an analysis of the electric field rather than the potential field.

Another drawback concerning time-lapse plots occurs when the anomaly range, often associated with subsurface water flow variation, is smaller than the absolute value caused by map interpolation. This masks the anomaly due to subtle variations in the maps. A better identification of the transient anomaly can be achieved by analyzing the curves of each channel separately. These transient variations related to water flow exhibit a characteristic shape, allowing the identification of a potentially interesting zone.

When SP data is extracted from ERT surveys, it becomes easier to identify possible electrode swaps by utilizing the quality control methods inherent in ERT. However, if

SP signals from the FullWaver system are not sourced from ERT surveys, alternative strategies must be implemented, as identifying potential electrode swaps becomes increasingly challenging.

3.4 FIELD EXAMPLE

We used the SPViewer tool in a field data sets to examine the transient curve associated to groundwater flow.

3.4.1 San Martino di Venezze anomaly

We conducted a Self-Potential monitoring using the Full Sparse Gradient array with 7 V-FullWwaver units (electrode distance about 20 m apart) shortly after a period of heavy rainfall in an area with notable water seepage and localized infiltration in San Martino di Venezze levee (Figure 3.8). This levee is situated in the Veneto region of Italy and it is part of the Po Valley, characterized by its extensive alluvial plains formed by the Po River. Levees in this region play a crucial role in managing the river's floods and shaping the local landscape. The area's levees are predominantly composed of sedimentary deposits brought and deposited by the Po River over time. These deposits consist of layers of clay, silt, sand, and gravel carried by the river during floods (Piovan et al., 2012). The continuous deposition of these sediments during flooding events has contributed as source material to the levee construction. During periods of flooding, the Po River inundates its banks, depositing sediment. Over time, this continuous deposition builds up the levees, forming raised banks along the river's course. The levees act as natural barriers, confining the river within its channel during normal flows and reducing the risk of flooding for surrounding areas.

The results of the SP monitoring in San Martino di Venezze are analyzed in three different ways. The first step is a temporal analysis, where the variation of the electrical potential is examined separately for each channel of the FullWaver units. In the second step, the signals are plotted in terms of the midpoint of the measurements and then interpolated. However, the interpretation of this unconventional technique is not done directly with the SP map. Instead, in the third step, it is done using the signal analytical signal analysis (ASA) map, which represents the electric field and delineates areas where anomaly sources are observed. The ASA technique first calculates the analytical

signal of the input profile using a Hilbert transform. Subsequently, local peaks in the analytical signal profile are interpreted as the angles of the anomaly sources. ASA tends to show a single peak centered on the anomaly source.

1 hour and 30 minute monitoring session was conducted using non-polarizable electrodes (PbCl2/Pb) and the Full Sparse Gradient array with 7 V-FullWaver units (with electrode distances of approximately 20 m). This took place shortly after a period of heavy rainfall in an area with evident water infiltration, located on the top of the embankment in San Martino di Venezze.

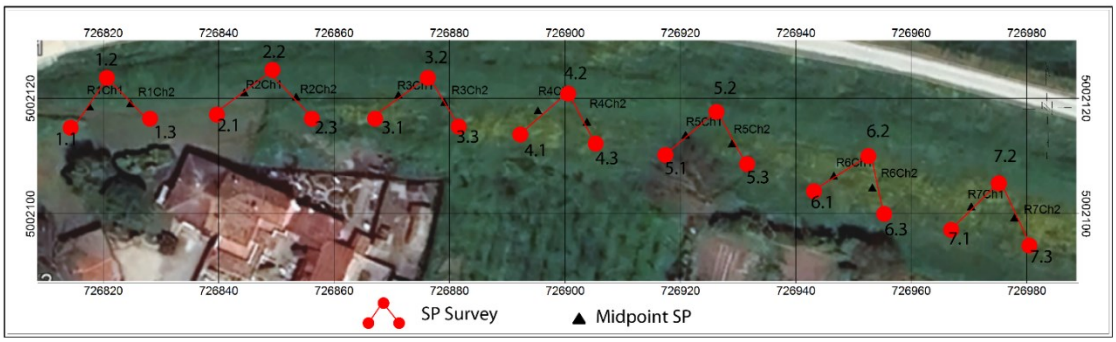

Figure 3.8 - Survey SP in San Martino di Venezze. The red dots represent the SP measurement points, and the black triangles indicate the central points of the measurements on a single channel (Ch1 and Ch2) for each V-FullWaver unit (from #1 to #7).

Figure 3.9 shows the SP anomaly obtained in the San Martino di Venezze levee. The curves represent a SP monitoring of 1h30 min. Standard shape anomaly related to infiltration process are observed in Rx1 Channel 1, Rx1Channel 2, Rx2 Channel 1, Rx4 Channel 2, Rx6 Channel 1. Typical examples associated with infiltration or percolation of water as can be observed in Jardani et al. (2009); and Ikard et al. (2012).

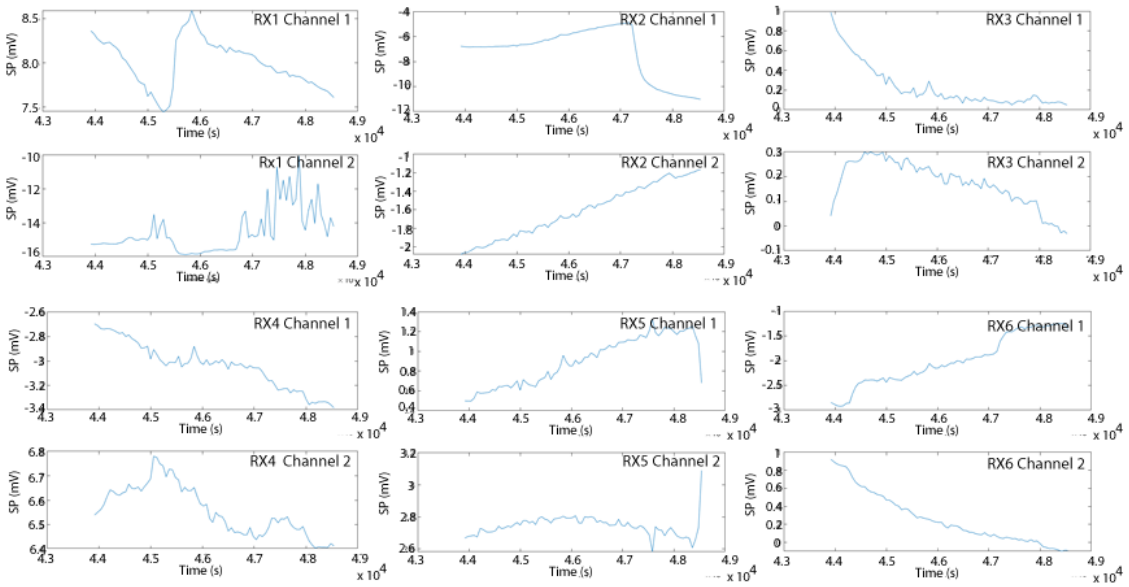

Figure 3.9 - SP monitoring curves of 1h30 min for 6 V-Fullwaver units.

Note that Channel 2 of each FullWaver unit provides SP values with inverted or opposite polarity compared to Channel 1. Figure 3.10 shows the plot of the SP signal interpolated with minimal curvature and with the polarity of Channel 2 already corrected, overlaid on Figure 3.8. Although the typical shape anomaly is observed in channel two of the RX4 unit, its range varies by 0.4mV, which is a negligible value if observed in interpolated time-lapse maps. Instead, temporal curve analysis suggests that such variation exists between electrodes 4.2 and 4.3. The ambiguity in this case revolves around whether the percolation produces a weak signal with a small spatial anomaly, or if both electrodes are situated in very close potential lines, indicating a potentially large spatial anomaly. Field inspection has proven the water percolation at the orange zone in Figure 3.8.

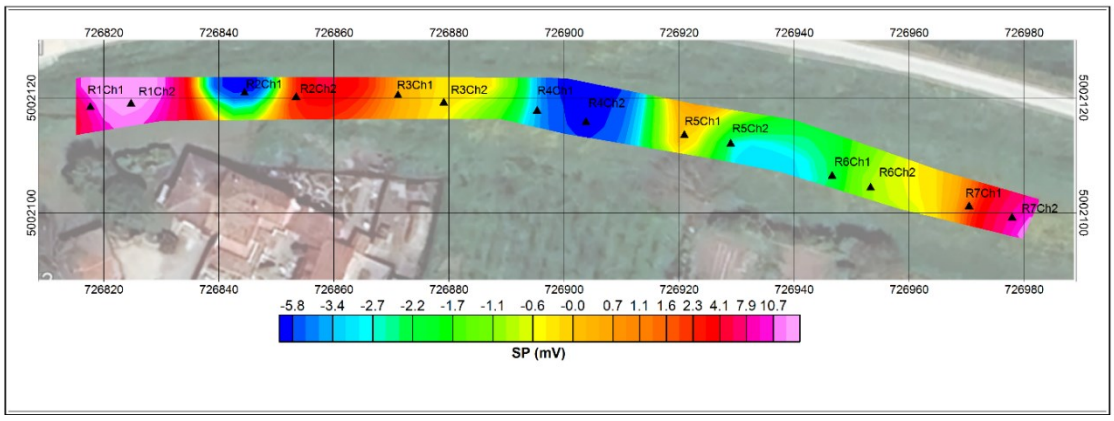

Figure 3.10 - SP anomaly overlaid on Figure 3.8

With ASA (Fig. 3.4), at least three distinct critical zones are observed in pink. The first occurs between Channels 1 and 2 of unit Rx1, and Channel 1 of unit Rx2. Then, in the central area of the map corresponding to unit Rx4, and also near unit Rx7.

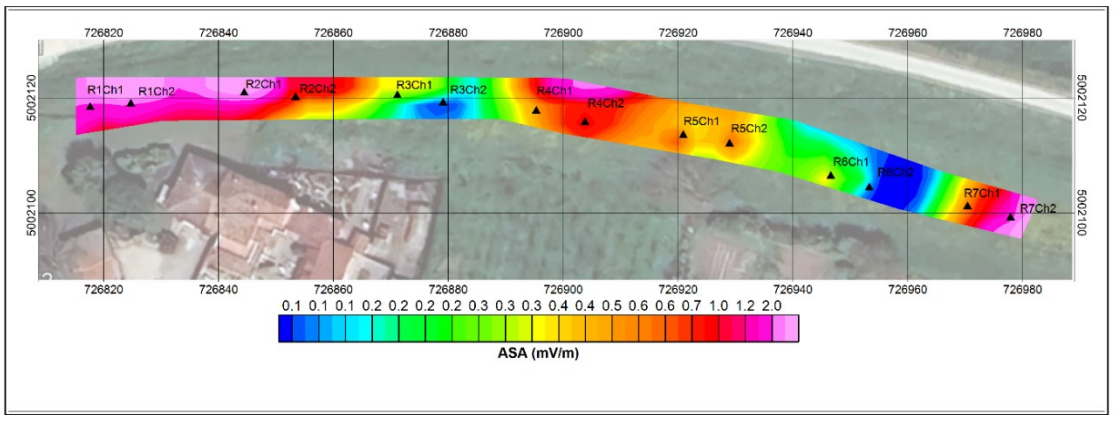

Figure 3.11 - ASA anomaly overlaid on Figure 3.8

3.5 CONCLUSIONS

The introduction of innovative technologies like the FullWaver system presents significant advancements in geoelectrical data acquisition, offering improved efficiency and reduced limitations associated with traditional methods. However, challenges persist in accurately interpreting SP anomalies, especially in cases where electrode configurations lack uniformity or when anomaly ranges are smaller than interpolated values. The development and utilization of specialized tools, such as the SPViewer presented here, stand as critical assets in streamlining data analysis, eliminating noise, and enabling precise anomaly identification. The field example provided from San

Martino di Venezze emphasizes the practical implications of SP monitoring, showcasing its effectiveness in detecting infiltration-related anomalies and emphasizing the need for nuanced interpretation methods to address varying signal complexities. Overall, this paper contributes to enhancing the understanding and application of SP data analysis in geophysical studies, acknowledging both its advancements and the complexities that demand further research and methodological refinement for comprehensive and accurate interpretations.

REFERENCES

Gance, J., Leite, O., Texier, B., Bernard, J. & Truffert, C., (2018). The Fullwaver systems: distributed network of autonomous devices for deep 3D electrical resistivity and induced polarization survey, in EGU General Assembly Conference Abstracts, Vol. 20 of EGU General Assembly Conference Abstracts, p. 12569.

Ikard, S. J., Revil, A., Jardani, A., Woodruff, W. F., Parekh, M., & Mooney, M. (2012). Saline pulse test monitoring with the self-potential method to non-intrusively determine the velocity of the pore water in leaking areas of earth dams and embankments. Water Resources Research, 48(4).

Jardani, A., Revil, A., Barrash, W., Crespy, A., Rizzo, E., Straface, S., ... & Johnson, T. (2009). Reconstruction of the water table from self-potential data: A Bayesian approach. Groundwater, 47(2), 213–227.

Piovan, S., Mozzi, P., & Zecchin, M. (2012). The interplay between adjacent Adige and Po alluvial systems and deltas in the late Holocene (Northern Italy). *Géomorphologie: relief, processus, environnement*, *18*(4), 427-440.

Revil, A., & Jardani, A. (2013). The self-potential method: Theory and applications in environmental geosciences. Cambridge University Press.

CHAPTER 4

4. ANALYSIS OF SELF-POTENTIAL AT ADIGE RIVER, NORTHERN ITALY

4.1 INTRODUCTION

In geophysics, understanding Spontaneous Potential (SP) is crucial, especially in exploring subsurface composition and structure. Revil and Jardani (2013) described sources of SP anomalies, including:

- Thermo-potential and natural potential: linked to temperature differences;
- Electrochemical: arising from different potentials due to chemical reactions;
- Geobattery: explaining potential differences from biotic and abiotic redox reactions;
- Flow potential or electrokinetic potential.

SP provides crucial information about subsurface properties, helping understand fluid distribution (Poldini, 1938; Jouniaux et al., 2009) and identify mineral deposits (Biswas, 2017; Biswas, 2019). This phenomenon directly reveals flow potential, essential for monitoring embankments and providing valuable insights into subsurface conditions. Additionally, it identifies potential risks associated with water infiltration, erosion, and structural stability.

Water infiltrations through embankments can be identified by detecting SP anomalies (Steck et al., 2018; Ahmed et al., 2019; Bouchedda et al., 2019). An increase in electrokinetic potential may indicate the presence of preferential water flow paths, while SP variations can reveal areas with eroded or compacted materials, indicating structural weaknesses in the embankment. SP data can be integrated with other geophysical techniques such as Electrical Resistivity Tomography (ERT) and seismic surveys to obtain a comprehensive assessment of embankment conditions (Busato et al., 2016; Wiejacz et al., 2018; Adetokunbo et al., 2024). The use of SP technique offers advantages as it is non-invasive and does not require drilling or destructive interventions on the embankment. It also allows continuous monitoring over time, providing updated

data on the embankment's condition. Another benefit is early detection capability, enabling proactive interventions before issues become visible or critical.

While Electrical Resistivity Tomography (ERT) applies a potential difference and consequently a current in the subsurface between two electrodes, for instance, to measure a second potential difference between other electrodes, the SP method measures a natural potential difference. Physical and chemical processes, always present to a greater or lesser extent, are responsible for the observed electrical potential differences at any position of a ground electrode pair (Sheffer, 2007; Jackson, 2015).

Certain geological conditions give rise to a larger SP, such as bodies with electronic conductivity (metallic sulfides and graphite), variations in electrical conductivity within geological structures or contacts, and, notably for this study, electrokinetic origin potential.

Historically, electrokinetic potential generated by water movement in soil and rock has been used to map preferred water pathways to address geotechnical and environmental issues (Jardani et al., 2006; Jardani et al., 2007; Goto et al., 2012; Kukemilks & Wagner, 2021). Groundwater, commonly found as a solution with dissolved minerals (electrolytes), causes changes in natural electrical voltage as it moves.

4.2 MATERIALS AND METHODS

4.2.1 New instruments for geoelectrical data acquisitions

Contributing to the advancement of geoelectrical data acquisition techniques, next-generation georesistivimeters have been introduced in the industry. The FullWaver system is one of these new instruments: a distributed network of autonomous devices designed for 3D deep electrical resistivity and induced polarization surveys. These systems, comprising multiple autonomous units (V-FullWaver), continuously record electric potential fields across two channels between three electrodes (P1-P2 and P2-P3). Typically positioned orthogonally to ensure consistent signal measurement, these dipoles are arranged in either a regular or adaptive configuration based on field conditions such as topography, roads, buildings, and vegetation.

Using this configuration, the system effectively eliminates common drawbacks associated with extensive ERT cable arrangements in large 3D areas, including time consumption, limited accessibility, weight, and electromagnetic induction (Gance et al., 2018).

The V-FullWaver (Figure 4.1) is a dual-channel receiver for Induced Polarization (IP), Electrical Resistivity Tomography (ERT), and SP. Recording continuously at a sampling frequency of 10 ms, it provides a comprehensive waveform record. It can synchronize with GPS PPS signal, streamlining signal processing. Stored data can be directly downloaded via a standard USB drive from all FullWaver units.

Figure 4.1 - Single unit of the FullWaver system (iris-instruments.com, 2024).

4.3 SP SURVEY AT ADIGE RIVER

The Boara Polesine embankment is a hydraulic defense structure located in the municipality of Rovigo situated along the Adige River, in the Veneto region, Italy. The embankments are crucial for protecting inhabited and agricultural areas from floods of

the Adige River, which can be particularly dangerous during periods of heavy rainfall or spring thaw. The embankment serves to contain the Adige River during high water levels, preventing water from overflowing and inundating surrounding areas.

The geology and stratigraphy of the Boara Polesine embankment and its surroundings are closely tied to the characteristics of the Adige River and the alluvial plain in which it resides. Its stability is critical and depends on material composition, compaction, and the presence of potential water infiltrations.

On June 13, 2024, a 4-hour monitoring session was conducted using 7 units of V-FullWaver (electrode spacing approximately 10 meters), connected to non-polarizable electrodes (PbCl/Pb), and another 7 units of V-FullWaver connected to stainless-steel electrodes, both utilizing the Full Sparse Gradient array (Figure 4.2). Additionally, 83 conventional SP measurement points were acquired using non-polarizable electrodes on the Boara Polesine embankment (Figure 4.3).

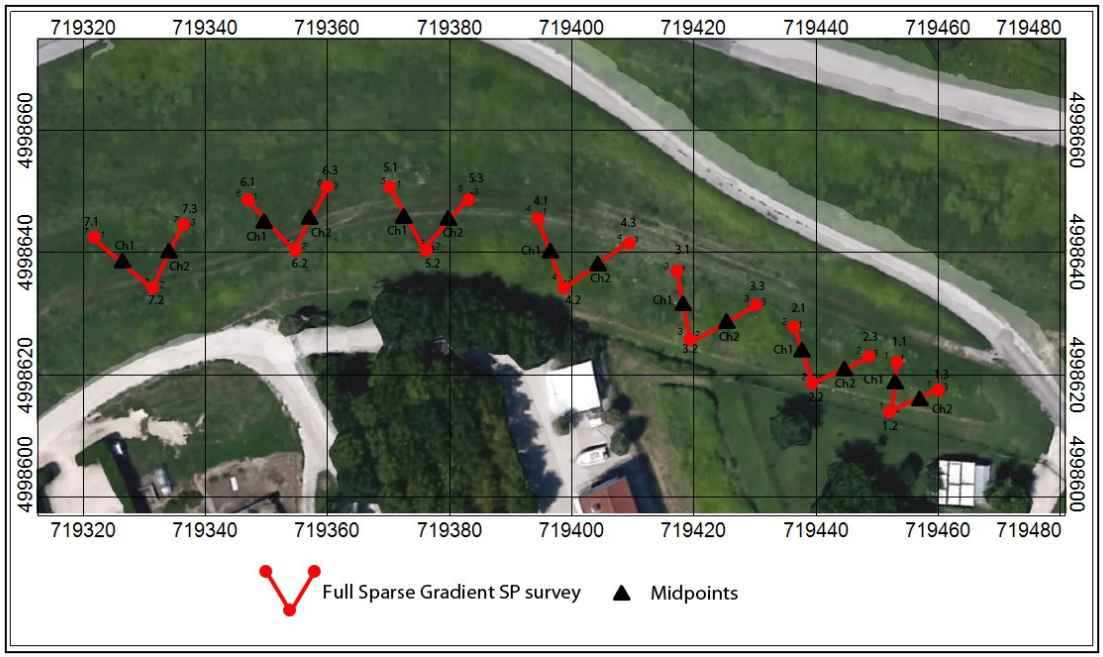

Figure 4.2 - SP Survey at Boara Polesine. The red dots represent SP measurement points using the non-conventional technique, Full Sparse Gradient. The black triangles denote central points of measurements on single channels (Ch1 and Ch2) of each V-FullWaver unit (from #1 to #7).

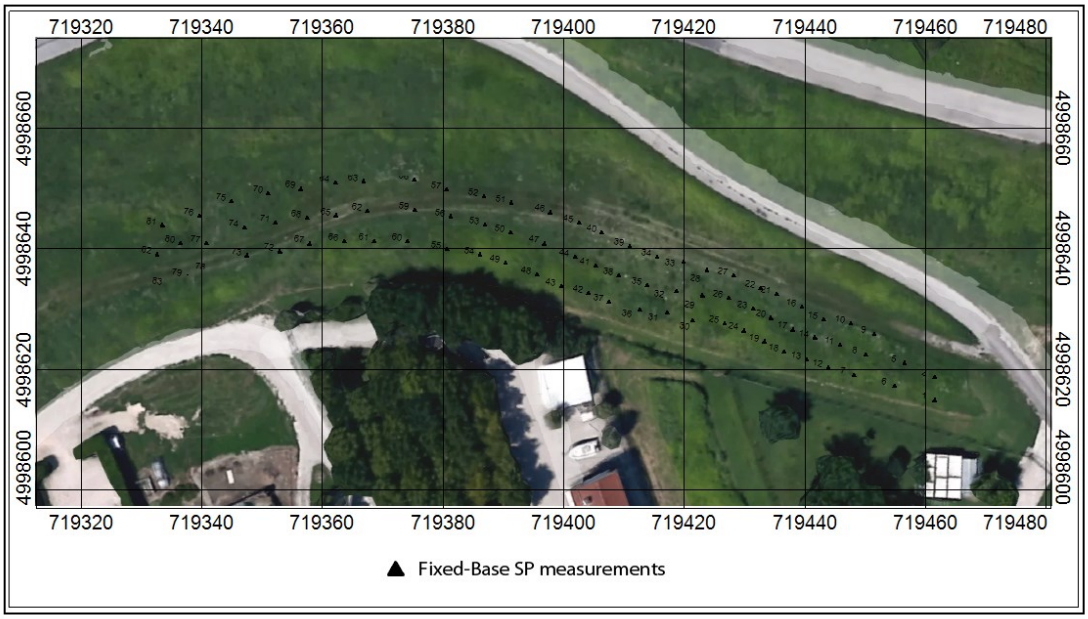

Figure 4.3 - SP Survey at Boara Polesine. The black triangles represent points measured using the conventional SP technique.

4.4 RESULTS AND DISCUSSIONS

The results of the SP monitoring at Boara Polesine are analyzed in three different ways. Firstly, a temporal analysis examines the variation of electrical potential separately in each channel of the FullWaver units. Secondly, signals are plotted in terms of the midpoint of measurements and interpolated. However, the interpretation of the non-conventional technique as a map is not directly performed with the SP map. Instead, under the third step, the Analytical Signal Analysis (ASA) map, which represents the electric field and delineates zones where anomaly sources are observed, is utilized. The ASA technique first computes the analytical signal of the input profile using a Hilbert transform. Subsequently, local peaks in the analytical signal profile are interpreted as anomaly source zones. ASA typically displays a single peak centered on the anomaly source.

Figures 4 and 5 show SP curves with a temporal variation of about 6 hours. Standard-shaped anomalies correlated with the infiltration process are observed on units 1, 4, 5, and 7. Typical examples associated with water infiltration or percolation can be observed in Jardani et al. (2009) and Ikard et al. (2012).

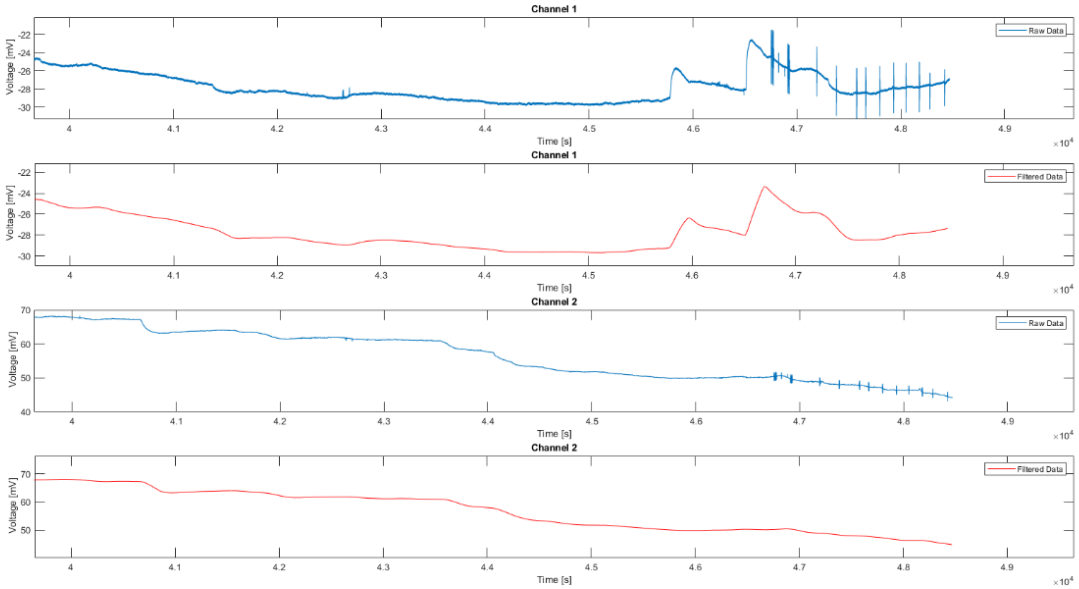

Figure 4.4 - SP monitoring curves for channels Ch1 and Ch2 of unit number 1 from 10:00 AM to 1:00 PM using the Full Sparse Gradient technique with non-polarizable electrodes. Raw data are shown in blue, while filtered data are shown in red.

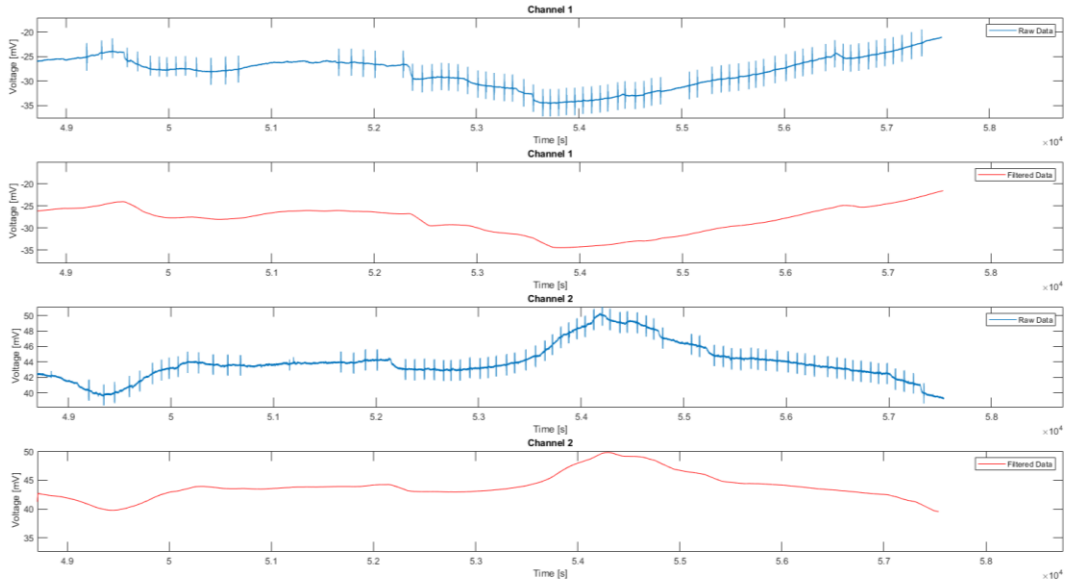

Figure 4.5 - SP monitoring curves for channels Ch1 and Ch2 of unit number 1 from 1:30 PM to 4:00 PM using the Full Sparse Gradient technique with non-polarizable electrodes. Raw data are shown in blue, while filtered data are shown in red.

Figure 4.6 depicts the temporal variation of SP on unit 1 using stainless-steel electrodes. The spatial-temporal variations of SP anomalies with the Full Sparse Gradient technique can be better visualized in Figure 4.7 and Figure 4.8.

Figure 4.7 shows the interpolated result for 12:00 PM using non-polarizable electrodes, while Figure 4.8 presents the same configuration at 10:50 AM, 11:50 AM, 12:50 PM, 1:50 PM, 2:50 PM, and 3:50 PM.

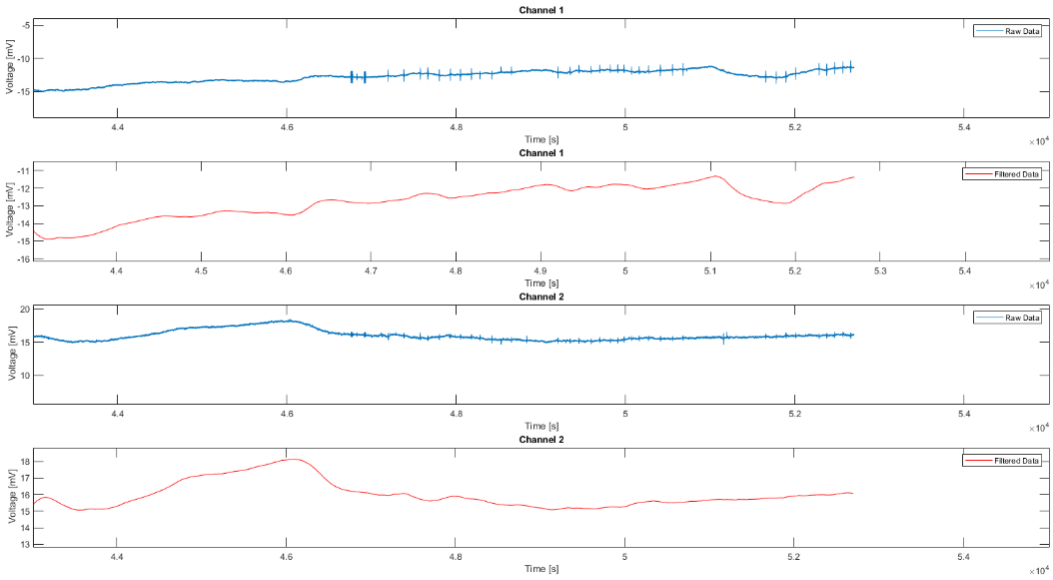

Figure 4.6 - SP monitoring curves for channels Ch1 and Ch2 of unit number 1, from 11:50 AM to 2:10 PM, using the Full Sparse Gradient technique with steel electrodes. Raw data are shown in blue, while filtered data are shown in red.

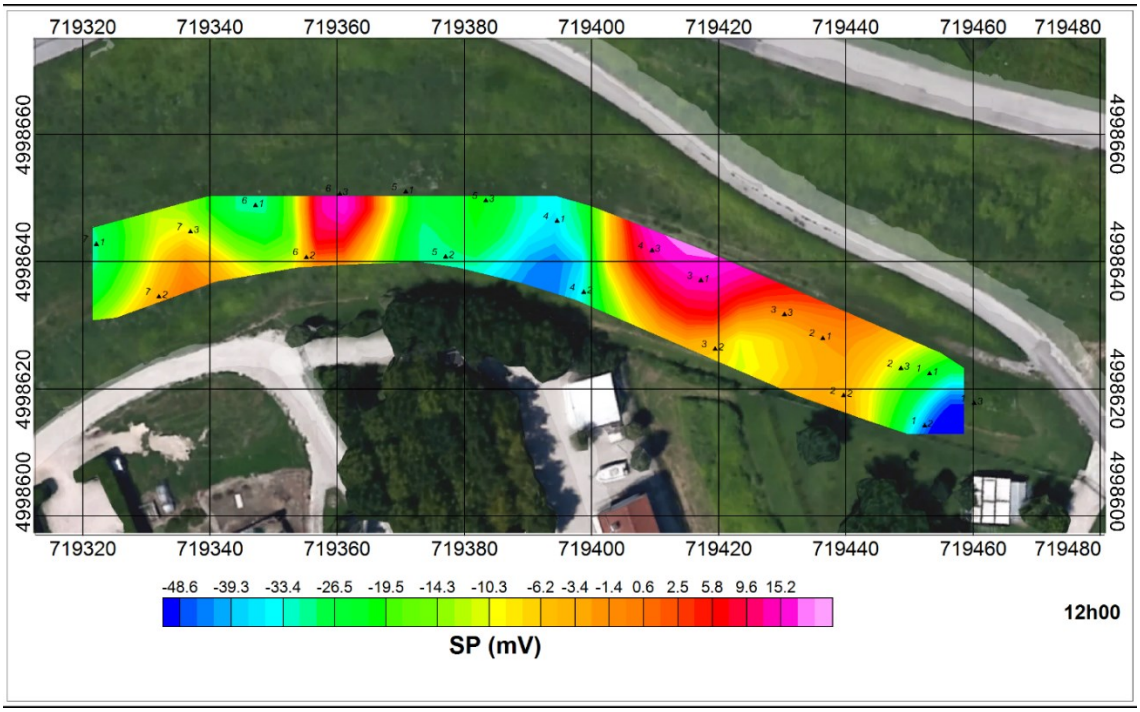

Figure 4.7 - Full Sparse Gradient using non-polarizable electrodes with monitoring at 12:00 PM.

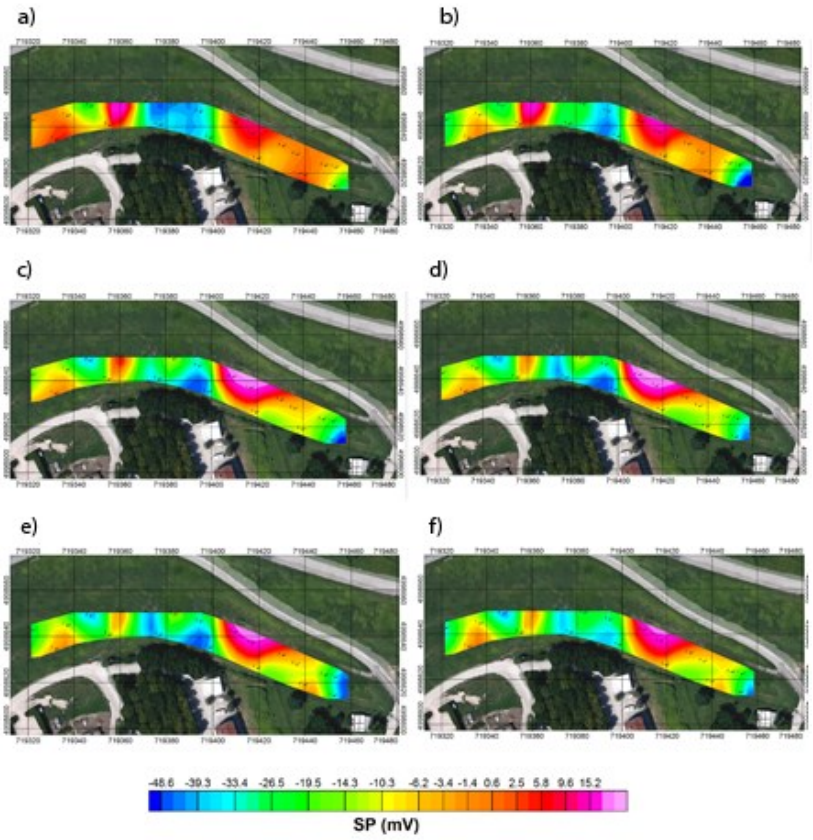

Figure 4.8 - Full Sparse Gradient using non-polarizable electrodes. a) Monitoring at 10:50 AM; b) Monitoring at 11:50 AM; c) Monitoring at 12:50 PM; d) Monitoring at 1:50 PM; e) Monitoring at 2:50 PM; f) Monitoring at 3:50 PM.

The spatial-temporal variations in Figure 4.8 highlight anomaly zones primarily on units 6, 5, 4, and 1. This indicates significant electrical potential variation likely correlated with water filtration or percolation processes in these areas. Similar results can be observed in monitoring with stainless-steel electrodes (Figure 4.9 and Figure 4.10).

However, for some units, the measured values appear negligible where negative SP values were expected; instead, they are positive or show amplitude shifts. Despite providing qualitative information, these variations using stainless-steel electrodes underscore the main zones of SP anomaly

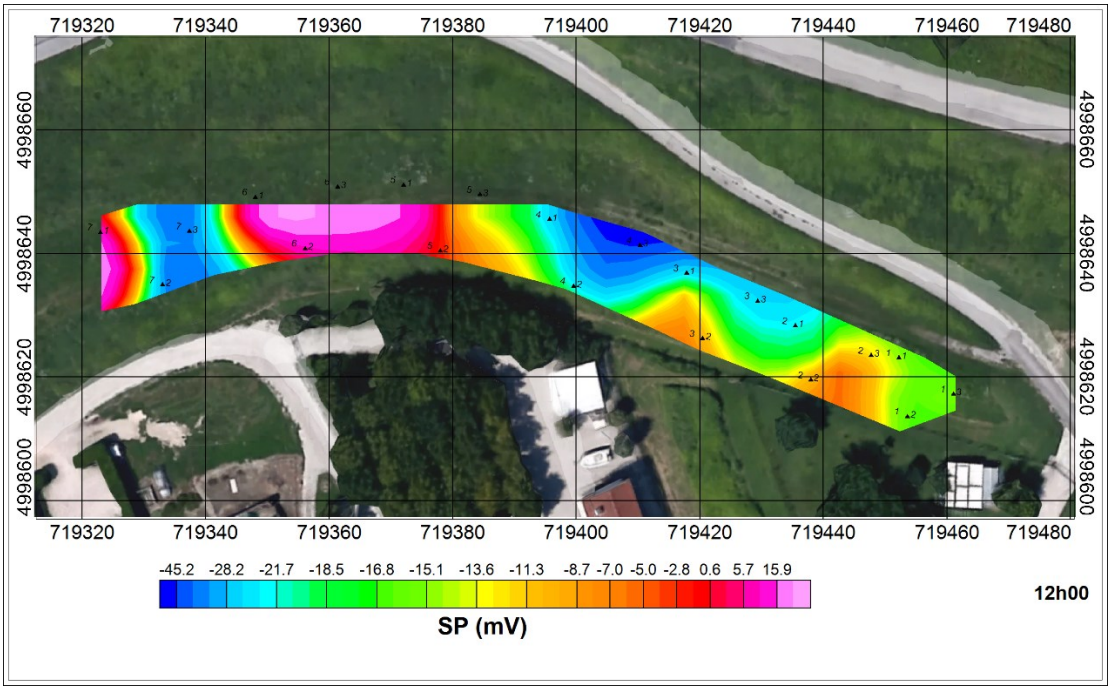

Figure 4.9 - Full Sparse Gradient using steel electrodes with monitoring at 12:00 PM.

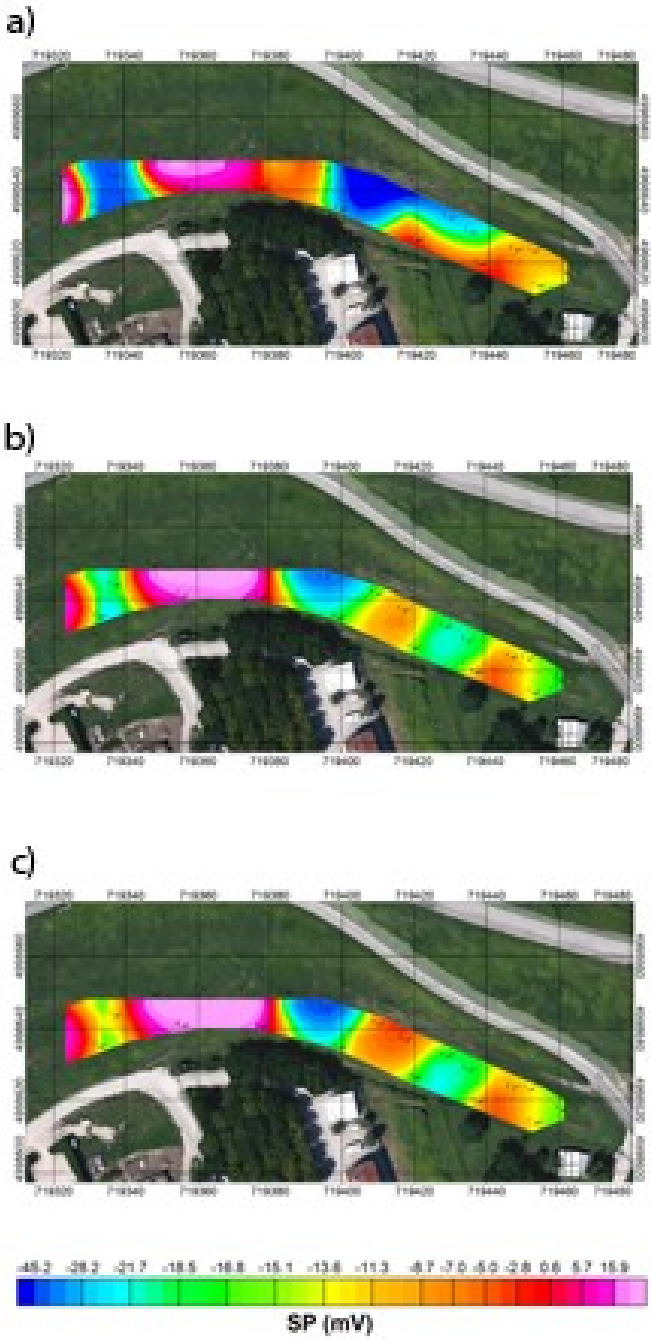

Figure 4.10 - Full Sparse Gradient using steel electrodes. a) Monitoring at 11:50 AM; b) Monitoring at 12:50 PM; c) Monitoring at 1:50 PM.

With ASA, shown in Figures 4.11 and 4.12, at least 3 distinct critical zones are observed in pink color. The first occurs around unit 6, followed by central zones on the map

corresponding to units 4 and 5, and in the area corresponding to unit 1. This indicates electrical field anomalies in these areas, likely stemming from electrokinetic processes.

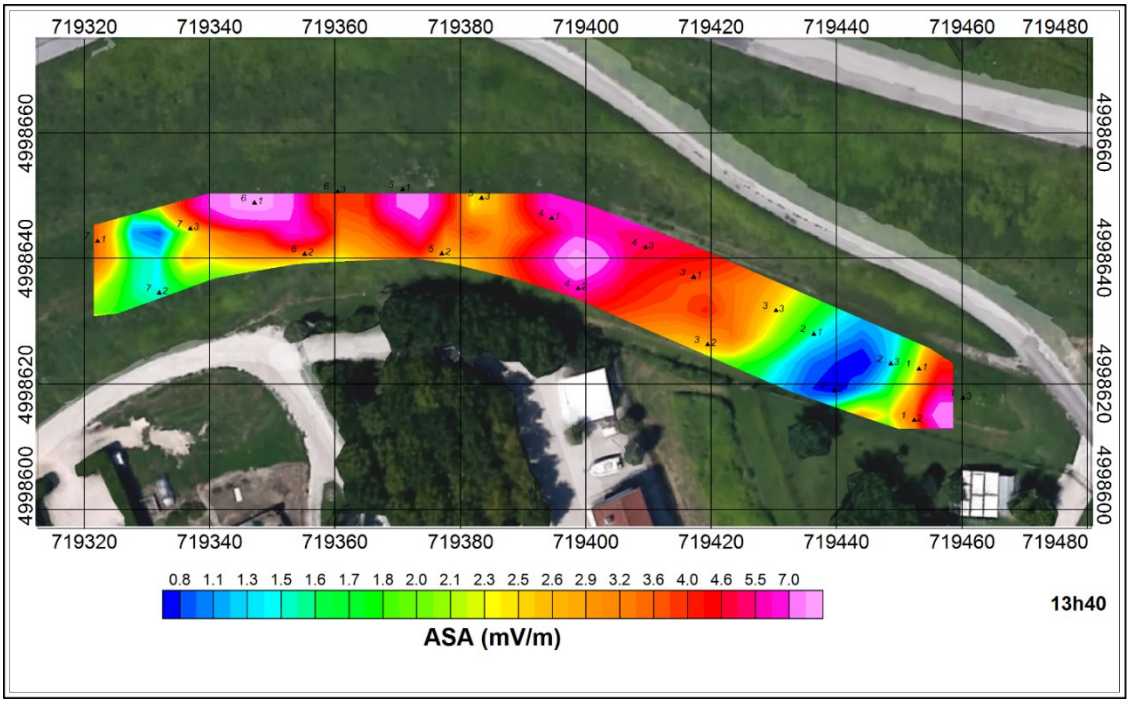

Figure 4.11 - ASA anomaly using the Full Sparse Gradient technique with non-polarizable electrodes.

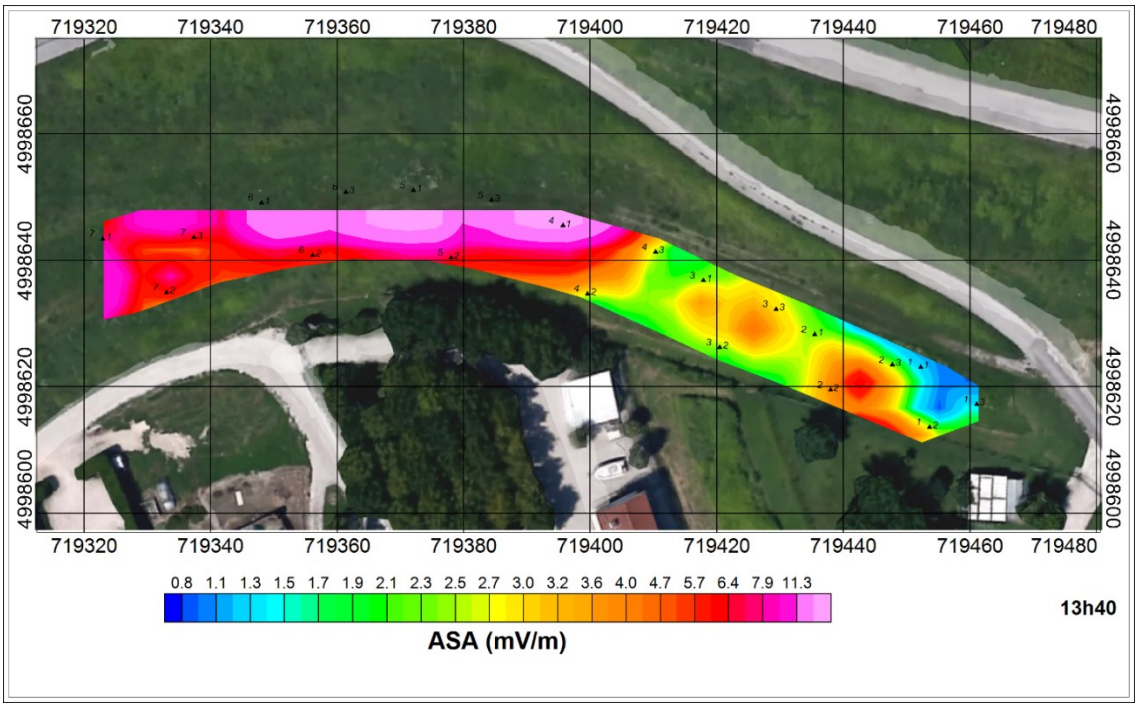

Figure 4.12 - ASA anomaly using the Full Sparse Gradient technique with stainless-steel electrodes.

Validating the unconventional technique (Full Sparse Gradient), the following figures present results using the conventional technique (Fixed-Base).

In the first case, Figure 4.13 displays interpolated raw data, showing significant negative anomalies from point 70 to 83 and from 51 to 59. Additionally, a strong negative anomaly is observed from point 1 to 18. The electric field represented by arrows in black indicates a preferential secondary flow from west to east, and in the central zone (719380 m, 4998640 m) from North to South. ASA on the raw data (Figure 4.14) delineates this central zone as an area of strong electrical field anomaly.

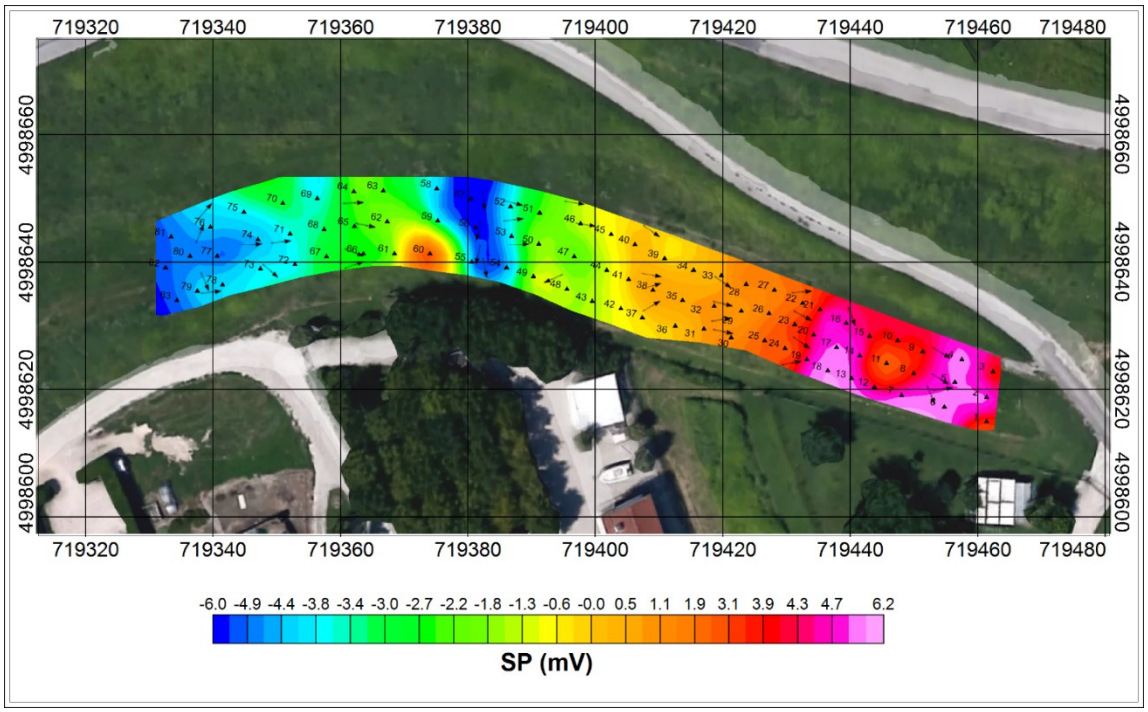

Figure 4.13 - Fixed-Base technique with raw data.

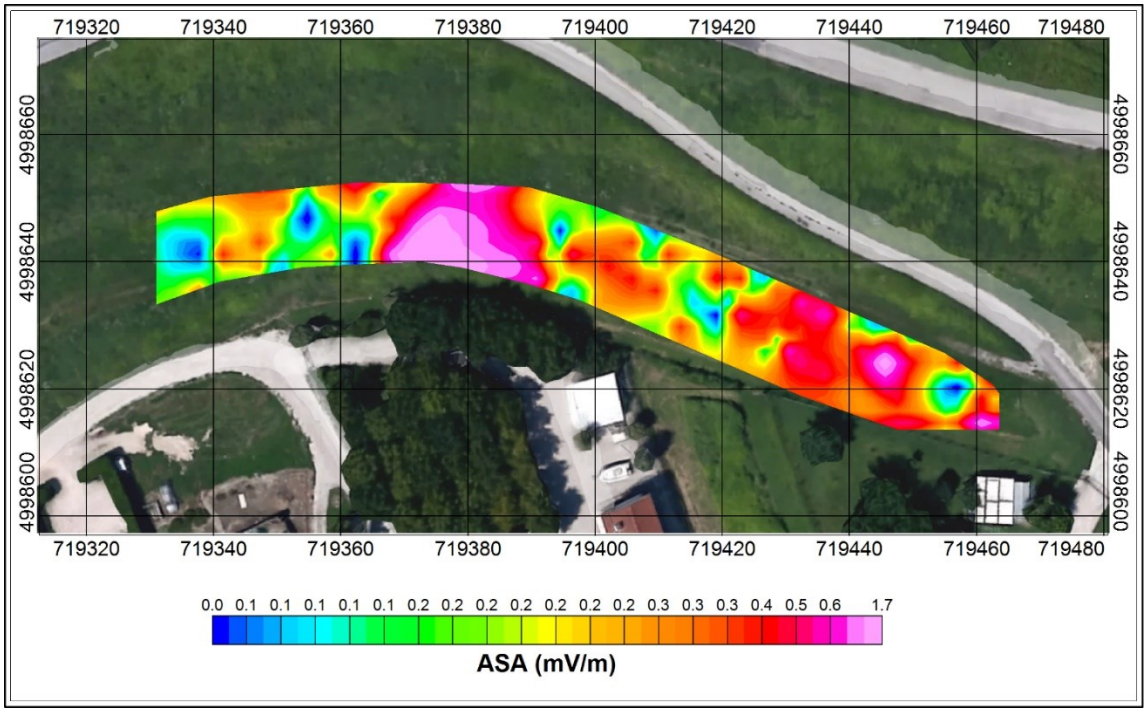

Figure 4.14 - ASA anomaly with the Fixed-Base technique on raw data.

After correcting the raw data for temporal drift (Figure 4.15), the same secondary flows can be observed, and the ASA (Figure 4.16) highlights the same central anomaly zone.

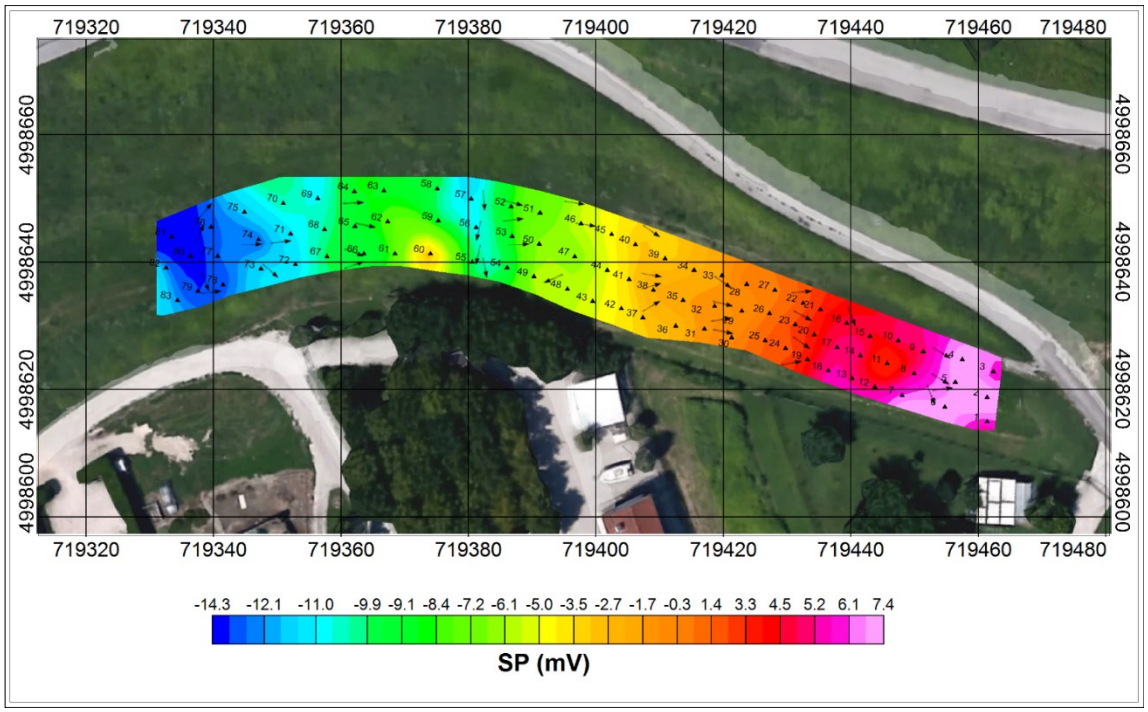

Figure 4.15 - Fixed-Base technique with drift correction.

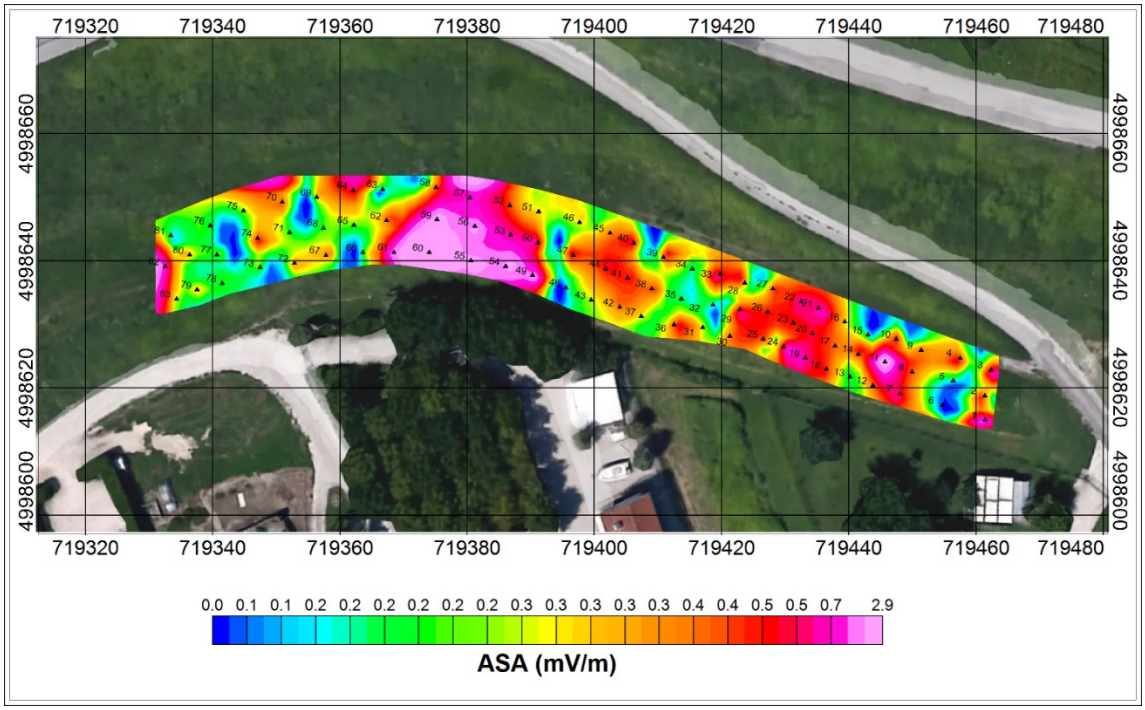

Figure 4.16 - ASA anomaly with the Fixed-Base technique on processed data.

Figure 4.17 presents the final interpretation of the overlap between both SP techniques.

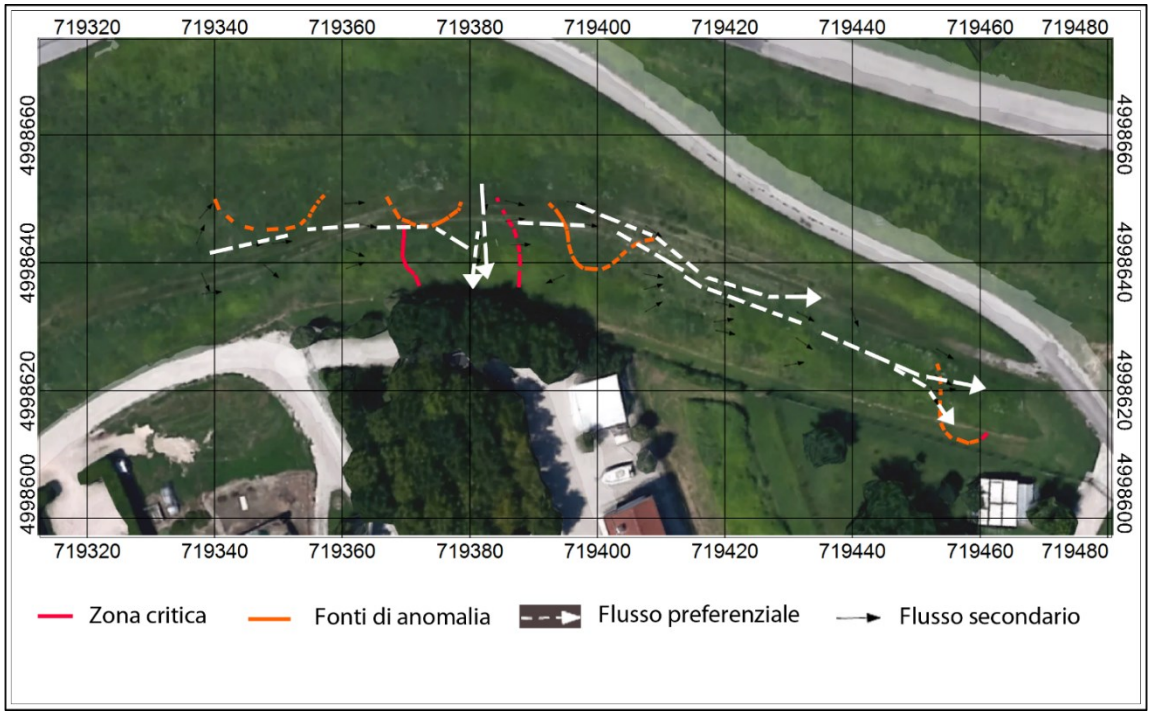

Figure 4.17 - Interpretation.

Field inspections evidenced "sand boils" at the central zone (Figure 4.18).

Figure 4.18 - Sand boil related to water infiltration.

4.5 CONCLUSION

The study conducted on self-potential (SP) analysis in the geophysical context highlights the importance of this technique in understanding subsurface structures. Studying SP anomalies provides valuable insights into soil properties, including fluid distribution. Specifically, using SP to monitor embankments offers a non-invasive and effective method to detect potential risks associated with water infiltration and erosion, enabling timely preventive measures.

The results presented clearly demonstrate the effectiveness of SP monitoring in identifying water infiltration anomalies along embankments, as evidenced in the investigation conducted in Boara Polesine. Through temporal analysis and the use of the Analytic Signal Analysis (ASA) technique, critical risk zones were accurately pinpointed. Early identification of such anomalies provides a significant advantage in embankment management and maintenance, facilitating timely interventions to prevent major damages.

In conclusion, the findings affirm the importance of SP monitoring as an effective tool in assessing embankment stability and managing hydrogeological risks. Apart from the

central zone (719380 m, 4998640 m) identified as critical, attention should also be paid to the area around coordinates 719460 m, 4998620 m.

REFERENCES

Adetokunbo, P., Ismail, A., Mewafy, F., & Sanuade, O. (2024). Geophysical Characterization and Seepage Detection of the Chimney Rock Dam Embankment Near Salina, Oklahoma. *Water*, *16*(9), 1224.

Ahmed, A. S., Revil, A., Steck, B., Vergniault, C., Jardani, A., & Vinceslas, G. (2019). Self-potential signals associated with localized leaks in embankment dams and dikes. *Engineering geology*, *253*, 229-239.

Biswas, A. (2017). A review on modeling, inversion and interpretation of self-potential in mineral exploration and tracing paleo-shear zones. Ore Geology Reviews, 91, 21-56.

Biswas, A. (2019). Inversion of Amplitude from the 2-D Analytic Signal of Self-Potential Anomalies. Minerals. doi:10.5772/intechopen.79111

Bouchedda, A., Chouteau, M., Coté, A., Kaveh, S., & Rivard, P. (2019). Self-potential Imaging of Seepage in an Embankment Dam. *Levees and Dams: Advances in Geophysical Monitoring and Characterization*, 69-90.

Busato, L., Boaga, J., Peruzzo, L., Himi, M., Cola, S., Bersan, S., & Cassiani, G. (2016). Combined geophysical surveys for the characterization of a reconstructed river embankment. *Engineering Geology*, *211*, 74-84.

Gance, J., Leite, O., Texier, B., Bernard, J. & Truffert, C., (2018). The Fullwaver systems: distributed network of autonomous devices for deep 3D electrical resistivity and induced polarization survey, in EGU General Assembly Conference Abstracts, Vol. 20 of EGU General Assembly Conference Abstracts, p. 12569.

Goto, T. N., Kondo, K., Ito, R., Esaki, K., Oouchi, Y., Abe, Y., & Tsujimura, M. (2012). Implications of self-potential distribution for groundwater flow system in a nonvolcanic mountain slope. International Journal of Geophysics, 2012.

Ikard, S. J., Revil, A., Jardani, A., Woodruff, W. F., Parekh, M., & Mooney, M. (2012). Saline pulse test monitoring with the self-potential method to non-intrusively determine the velocity of the pore water in leaking areas of earth dams and embankments. Water Resources Research, 48(4).

Jackson, M. D. (2015). Tools and techniques: Self-potential methods. In G. Schubert (Ed.), *Treatise on geophysics* (2nd ed., Vol. 11, pp. 261–293). Amsterdam: Elsevier.

Jardani, A., Dupont, J. P., & Revil, A. (2006). Self-potential signals associated with preferential groundwater flow pathways in sinkholes. Journal of Geophysical Research: Solid Earth, 111(B9).

Jardani, A., Revil, A., Santos, F., Fauchard, C., & Dupont, J. P. (2007). Detection of preferential infiltration pathways in sinkholes using joint inversion of self-potential and EM-34 conductivity data. Geophysical Prospecting, 55(5), 749-760.

Jardani, A., Revil, A., Barrash, W., Crespy, A., Rizzo, E., Straface, S., ... & Johnson, T. (2009). Reconstruction of the water table from self-potential data: A Bayesian approach. Groundwater, 47(2), 213–227.

Jouniaux, L., Maineult, A., Naudet, V., Pessel, M., & Sailhac, P. (2009). Review of self-potential methods in hydrogeophysics. Comptes Rendus Geoscience, 341(10-11), 928-936.

Kukemilks, K., & Wagner, J. F. (2021). Detection of Preferential Water Flow by Electrical Resistivity Tomography and Self-Potential Method. Applied Sciences, 11(9), 4224.

Poldini, E. (1938). Geophysical exploration by spontaneous polarization methods. Mining magazine, 3–22.

Revil, A., & Jardani, A. (2013). The self-potential method: Theory and applications in environmental geosciences. Cambridge University Press.

Sheffer, M. R. (2007). *Forward modelling and inversion of streaming potential for the interpretation of hydraulic conditions from self-potential data* (Doctoral dissertation, University of British Columbia).

Steck, B., D'Urso, G., Vautrin, D., Sabor, K., Vergniault, C., Courivaud, J. R., ... & Revil, A. (2018, October). Validation of geophysical methods for internal erosion detection on earth embankments. In *Scour and Erosion IX: Proceedings of the 9th International Conference on Scour and Erosion (ICSE 2018), November 5-8, 2018, Taipei, Taiwan* (p. 51). CRC Press.

Wiejacz, P. (2018). Application of Geophysical Methods to Earth River Embankments in Poland. In *Twenty-Sixth International Congress on Large Dams/Vingt-Sixième Congrès International des Grands Barrages* (pp. Q103_725-Q103_735). CRC Press.

CHAPTER 5

5. SELF-POTENTIAL SIGNAL ANALYSIS TO RECOGNIZE SOURCES OF PRIMARY ANOMALY IN A LANDSLIDE: A NOVEL APPROACH

5.1 INTRODUCTION

The so-called Self-Potential (SP) method is a passive geoelectrical method sensitive to underground fluid flows (Poldini, 1938; Jouniaux et al., 2009). Collecting SP data is generally quite simple, but systematic use of this technique, since a few years ago, was limited by insufficient theoretical background and limitations in reliable data interpretation (Nyquist & Corry, 2002; Revil & Jardani, 2013; Barde-Cabusson et al., 2021). The use of electrical resistivity methods for exploring the subsurface at large depths (known as Deep Electrical Resistivity Tomography - DERT) is rapidly increasing. This trend is bringing about significant changes to the field, as numerous datasets of electrical resistivity data are now available for a variety of geological conditions (Carrier et al., 2019; Lajaunie et al., 2019; Troiano et al., 2019; Rizzo et al., 2020; Bocchia et al., 2021). DERT surveying boosted the development of multichannel and distributed systems based on loggers capable of sampling the electrical potentials in continuous using several couples of electrodes inserted into the ground.

Electrical Resistivity Tomography (ERT) monitoring also became popular (Chambers et al., 2015) for studying water content changes and water flow movements in landslides (Kukemilks & Wagner, 2021), aquifers, levees, and other areas. The SP method has tremendous potential for those applications (Gallipoli et al., 2000; Perrone et al., 2004; Revil et al., 2006; Jouniaux et al., 2009; Kukemilks & Wagner, 2021), but this capability to be fully exploited, requires specific field procedures and data processing techniques (Barde-Cabusson et al., 2021; Eppelbaum, 2021). The hardware for single-channel SP measurements is relatively cheap, and some developments are mandatory to switch from single to multi-channel SP. New-generation georesistivimeters like the FullWaver (Gance et al., 2018) and the Multisource (LaBrecque et al., 2013; Bocchia et al., 2021) already log potentials at high frequency. However, the SP voltages in these instruments

are considered noise rather than signals, and they are logged with the sole purpose of separating artificial and site-related potentials.

In the case of ERT/DERT surveys, an external artificial source generates electric fields that propagate in the subsurface. The electric field in SP surveys is from natural sources, and often it is measured between couples of non-polarizing electrodes. Physicochemical processes, always present with variable degrees of intensity, are known to be the cause for the electrical potential observed at any couple of electrodes inserted into the ground.

Revil and Jardani (2013) have described the sources of the SP method, including (1) thermo-potential and natural potential related to the difference of temperature; (2) streaming potential or electrokinetic; (3) electrochemical, chemical reactions can generate variations in potential; (4) geobattery, which explains about the difference of potential caused by biotic and abiotic to redox reaction.

High-amplitude SP is generally to be measured in various geologic settings: metal bodies with electronic conductivity like sulfide and graphite (Sato & Mooney, 1960); sudden changes in electrical conductivity occurring within geological structures or at geological boundaries (Anderson & Johnson, 1976); presence of potentials of electrokinetic origin. Due to the electrokinetic origin, the corresponding SP signal is sometimes called streaming potential (Jouniaux et al., 2009). Some SP studies have been focused on the potential of electrokinetic origin, which is associated with groundwater flow used for mapping its preferential pattern (Jardani et al., 2006; Jardani et al., 2007; Goto et al., 2012; Kukemilks & Wagner, 2021).

Two techniques are widely spread for SP data acquisition: the potential or Fixed-Base and gradient techniques. Theoretically, both approaches are equivalent, but in practical terms, they are distinct (Orellana, 1972).

Barde-Cabusson et al., (2021) showed an excellent practical approach for SP data acquisition using the Fixed-Base technique, which consists in measuring the difference in the electrical potential between a reference base electrode that remains fixed during the survey and a rover electrode.

The gradient technique or leapfrog involves taking measurements while moving forward both electrodes with constant aperture along the survey profile. The SP measurement value of each point is obtained by the cumulative sum of the previous ones (Gallas, 2020). Very little researches have been published on the SP gradient technique (Thanassoulas, 1989; Minsley, 1997; Ikard et al., 2021, Embeng et al., 2022). This is mostly because this technique, when performed with traditional instruments, involves some practical drawbacks like high susceptibility to spurious anomalies generated by cumulative errors from effects of contact resistance, electrode polarization, electrode drift, and electrode-polarity swap. However, we noticed that new-generation data loggers could easily overcome some of these limitations.

Self-potential signals were retrieved while collecting data during a 3D – DERT survey targeting an active landslide. Resistivity data were collected using new-generation distributed georesistivimeters. Results represent significant progress in the SP methodology and time-lapse applied to groundwater flow pattern recognition as a first approach or large scale because every unit FW is an independent station logging the SP continuously. As independent stations and sparse separation between the units, in the acquisition, there are no reference electrodes as in the Fixed-Base and leapfrog techniques. In this case, this uncommon array we call as Sparse Gradient technique.

In effect, in traditional SP techniques, the non-use of non-polarizing electrodes tends to present no meaningful SP values due to electrochemical contacts between the metallic electrode and the ground causing a strong potential. For didactic purposes and a qualitative approach, we use stainless-steel electrodes in this study, showing that meaningful SP values can also be observed in this type of survey in certain circumstances.

The experiment results in several outcomes: usable SP signals collected with data loggers and non-traditional arrays could be retrieved and successfully processed using stainless-steel electrodes instead of non-polarizing electrodes in case of qualitative approach; specific procedures have been devised to process and analyze SP data; time-lapse SP maps clearly outline the electrical signature of groundwater flow; time-lapse mapping allows for the recognition of typical patterns that could be spatially correlated.

5.2 SITE LOCATION

The study area is located in the Carnic Alps, forming part of the eastern sector of the Alps (Pondrelli et al., 2020; Zuliani et al., 2022). An active landslide threatens the village of Cazzaso (Municipality of Tolmezzo, Udine, Italy). The active landslide is the reactivation of a portion of a large paleo-landslide, probably dating to past-LGM (Last Glacial Maximum). The geophysical survey (Figure 5.1) mostly covered the Paleo-landslide. The slope is composed of glacial, fluvioglacial, lacustrine, and fluvial deposits (Colucci et al., 2014; Zuliani et al., 2022). The slope has been affected by movements since the second half of the 19th century (CNR-GNDCI, 1992). The landslide exhibits a composite behavior. A slow rotational movement occurring mountain-side evolves into an earth flow valley-side (Carlini et al., 2018). The active landslide mostly develops within the Quaternary coverage. This near-surface layer is characterized by inhomogeneous permeability, with spatial rain drainage and the absence of water springs (Zuliani et al., 2022). The region has a temperate climate characterized by cold winters (Marchi et al., 2021). January experiences the lowest average monthly temperature at -3.7 °C, while the highest monthly average maximum temperature peaks at 26.6° C. Additionally, there is abundant precipitation throughout all seasons (2500 – 3000 mm/year).

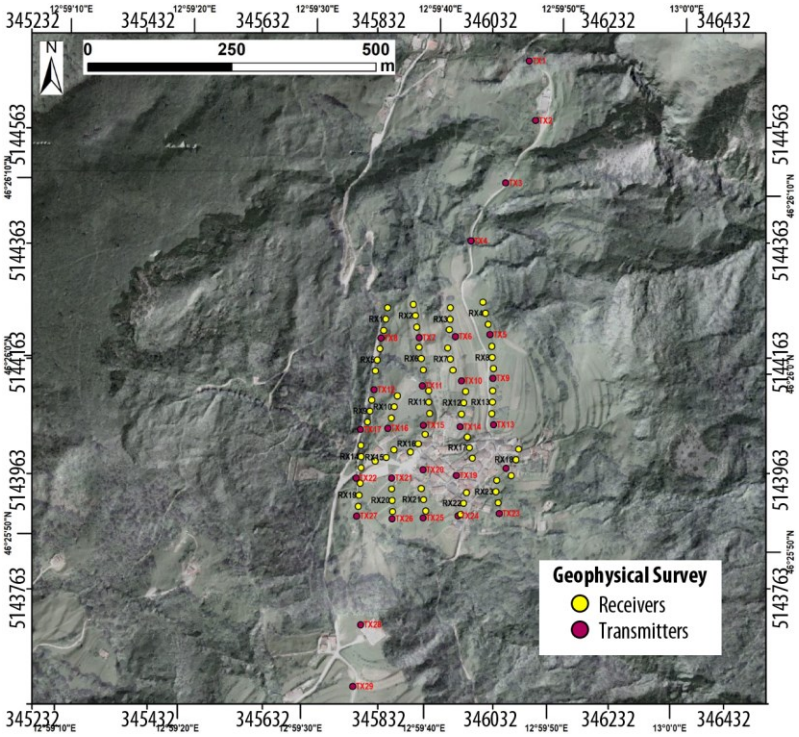

Figure 5.1 - Map of the study area showing the layout of the 3D-DERT geophysical survey.

5.3 MATERIAL AND METHODS

5.3.1 Self-Potential Survey

3D – DERT data were collected on two consecutive days (February 8 and 9- 2022) using 23 FW recording units, a passive system capable of logging artificial and self-potentials, with a frequency of 100 Hz, between multiple couples of electrodes. The FW system comprises several autonomous receivers (V-FullWaver) and one independent current recorder (I-FullWaver) connected to a high-power transmitter. The receivers and the transmitter combination form a Resistivity - Devices and Acquisition Setup (R-DAS) (Gance et al., 2018; Lajaunie et al., 2019). The measurements are time-stamped to the Global Navigation Satellite System (GNSS) clock as the transmitter and receivers are spaced apart.

The field layout was organized in four parallel lines (Figure 5.2). Each line is comprised of five "Rx" units numbered from 1 to 23. Three units (Rx10, Rx15, and Rx20) were positioned between "Line 1" and "Line 2". Each unit was connected to 3 electrodes resulting in two dipoles of 20 m of aperture. The difference of potential $Vmn_{1,2}$ and

$Vmn_{2,3}$ correspond to the electrodes 1 – 2 and 2 – 3, respectively. SP was recorded for about 20 minutes prior to injecting the electrical current in the subsurface.

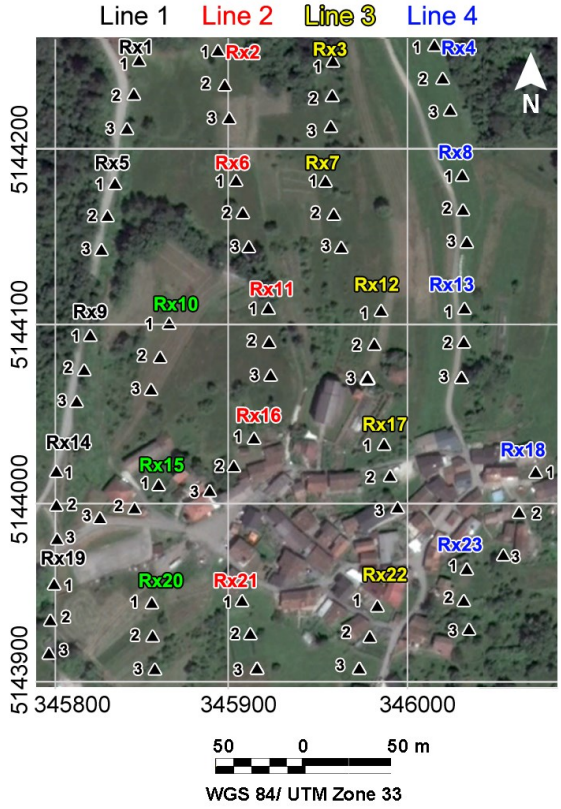

Figure 5.2 - 3D-DERT setup. The black triangles represent the electrodes gathered in groups of three and spaced approximately 20 m (within each gather).

Receiving units were coupled to the ground using stainless-steel electrodes. The artificial potentials were generated by a high-power transmitter capable of delivering voltages up to 3KV. The current injection was performed in time-domain transmitting a waveform of 2s comprised of several turn-on/turn-off pulses for a comprehensive duration of 150s. The transmitted current was around 2150 mA during the first run (25 injections) and about 2500 mA during the second run (28 injections). During the survey, all contact resistances were below 1.5 KOhm avoiding the need to improve coupling watering the electrodes with salty brine. Electrode station locations were surveyed using a differential GPS device.

Revil & Jardani (2013) have shown that the potential of the electrodes is always temperature dependent and comprised in the range 0.2 mV^oC^{-1} to 2 mV^oC^{-1} for non-

polarizing electrodes. They observed how a difference in temperature of 10°C causes a drift in the SP measurement of 2mV. In the present case, data were collected in wintertime with minimal daily temperature changes. The continuous potential sampling allows for observing possible influences of the stainless-steel electrodes on the SP measurements. The electrode positions were carefully selected in order to minimize possible electrochemical processes generated by the contact between the electrode and the ground. On the first day, the temperature changed from a minimum of 8.5°C to a maximum of 11.5°C, while on the second day, the daily temperature oscillation was comprised between 10.8°C and 12°C. This range is minimal enough to be neglected even in the case of the use of stainless-steel electrodes providing qualitative SP maps. Extrapolating the temperature-dependence of the non-polarizing electrodes as compared to stainless-steel electrodes results in a quintupled function with a maximum range of 10 $mV^{o}C^{-1}$. In our data, this represents a few percentages, less than 25% of the probability density function around 80%.

Data collected during day 1 (from 11:20 AM to 12:30 AM) show a Gaussian distribution (Figure 5.3a) in the interval comprised between -126 mV and 104 mV with a probability density of about 80% from -65 mV to 73 mV. During day 2 in the same time interval, the distribution is similar (Figure 5.3b) in the interval comprised between -137 mV and 127 mV with a probability density of about 80% from -66 mV to 74 mV. However, from feasibility studies, we have noticed that this kind of sparse SP array tends to present a small amplitude than the other ones. In this case, the large observed SP range is correlated to the use of stainless-steel electrodes, in the case of using non-polarizing electrodes this range could be smaller.

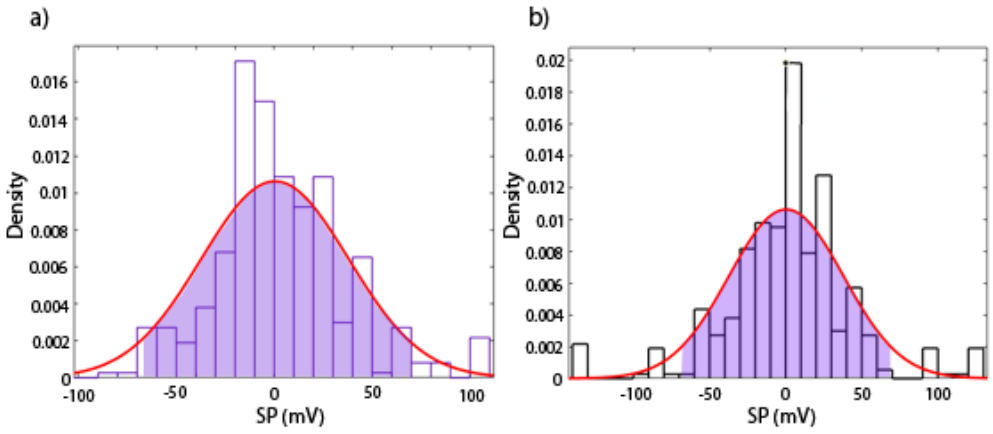

Figure 5.3 - Statistical analysis of SP values. a) SP averaged on a 60 s interval: distribution from 11:20 AM to 12:30 AM of day 1. b) SP averaged on a 60 s interval: distribution from 11:20 AM to 12:30 AM of day 2. The filled areas below the Gaussian curves represent the probability density function around 80%.

A series of MATLAB (The Mathworks, 2020) tools were implemented to analyze and process the potential time series. The suite of codes performs the following tasks: extract specific time windows; perform signal processing; insert geometry; generate the time-lapse maps.

5.4 DATA PROCESSING

Data quality control performed in DERT (Lajaunie et al., 2019; Carrier et al., 2019) also benefits from the analysis of SP data, mainly for detecting electrode swaps. Considering a simple array and a single measure with a positive geometric factor, current and voltage waveforms should be recorded in-phase. In the case of out-phase waveforms, an electrode swap could have occurred. Figure 5.4 shows an example of an electrode swap that occurred at unit Rx13. Channel 1 is in-phase while channel 2 is out-phase indicating the swap of electrodes 2 and 3.

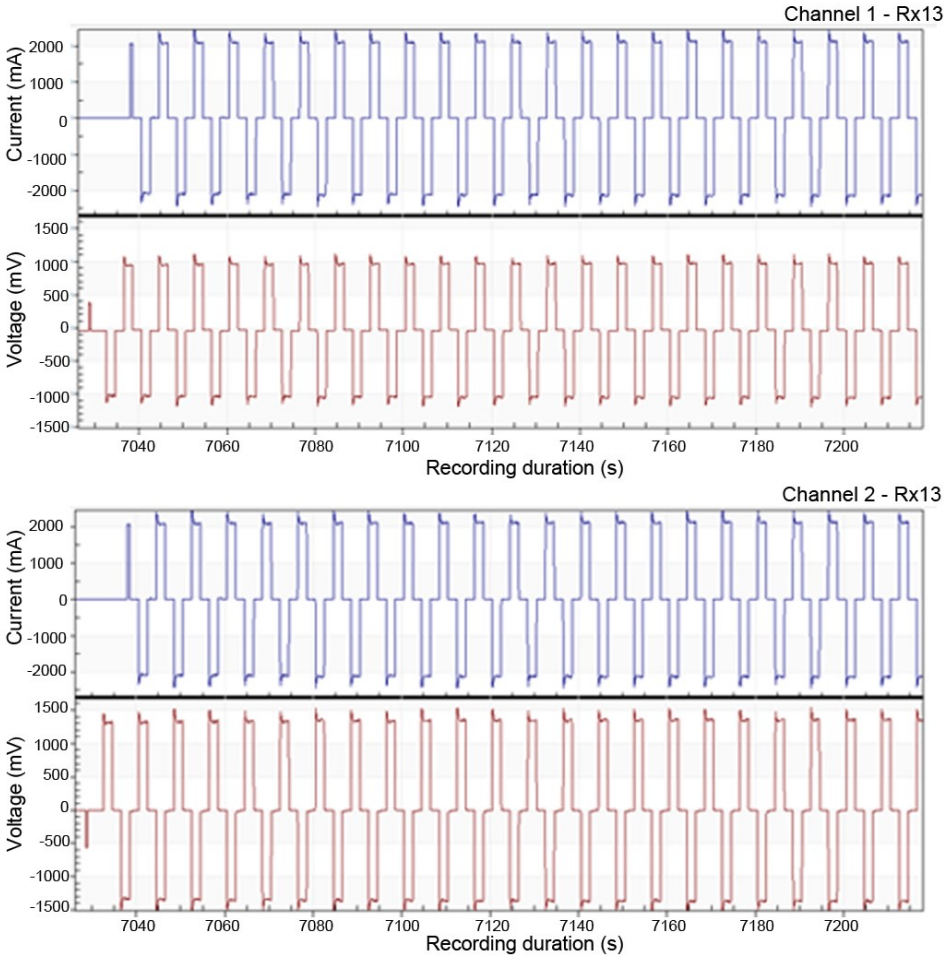

Figure 5.4 - Out-phase voltage (mV) and current (mA) recorded at unit Rx13. Channel #1 (electrodes 1-2): top. Channel #2 (electrodes 2-3): bottom.

Daily SP time series from unit Rx14 (second day) are presented in Figure 5.5 recording of the DERT survey during the second acquisition day and the potential difference of the dipole between electrodes 1 and 2 (channel 1) and 2 and 3 (channel 2). The blue line is the SP signal measured, and the vertical blue spikes are the turn-on and turn-off time of the artificial transmission of the electric current on the ground. The pink window is the interval from 9:00 to 9:20 AM before the transmission of electric current, where there are no artificial voltages. By choosing the same time window for each unit Rx, it is possible to generate time-lapse SP maps of 10 ms sample rate.

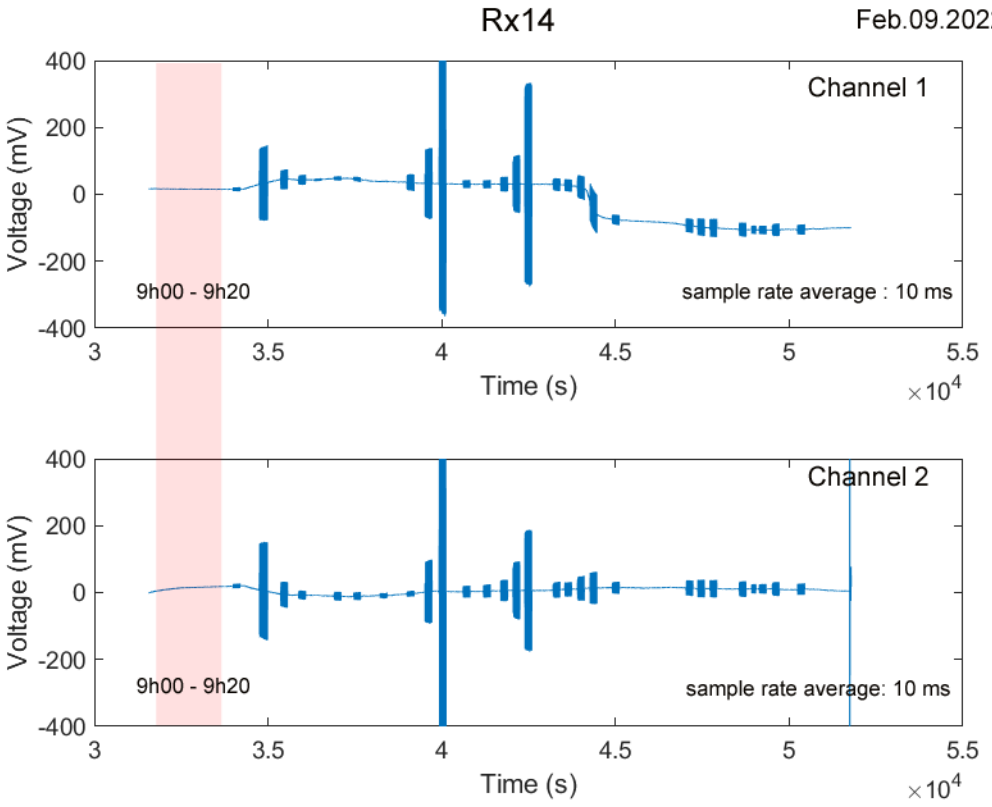

Figure 5.5 - Daily SP as recorded at unit Rx14 for dipoles 1-2 (channel 1) and 2-3 (channel 2). The pink time window is the recording period of the natural electric potential before the injection of electric current. The thin blue windows are the turn-on and turn-off time of the artificial current injection. The sampling interval is 10 ms.

Figure 5.6 shows the application of an anti-spike filter to remove the artificial voltages from the SP time series. Data have been further processed averaging the potentials over a time window of 60 s. The process was fairly effective and just some residual noises are still visible.

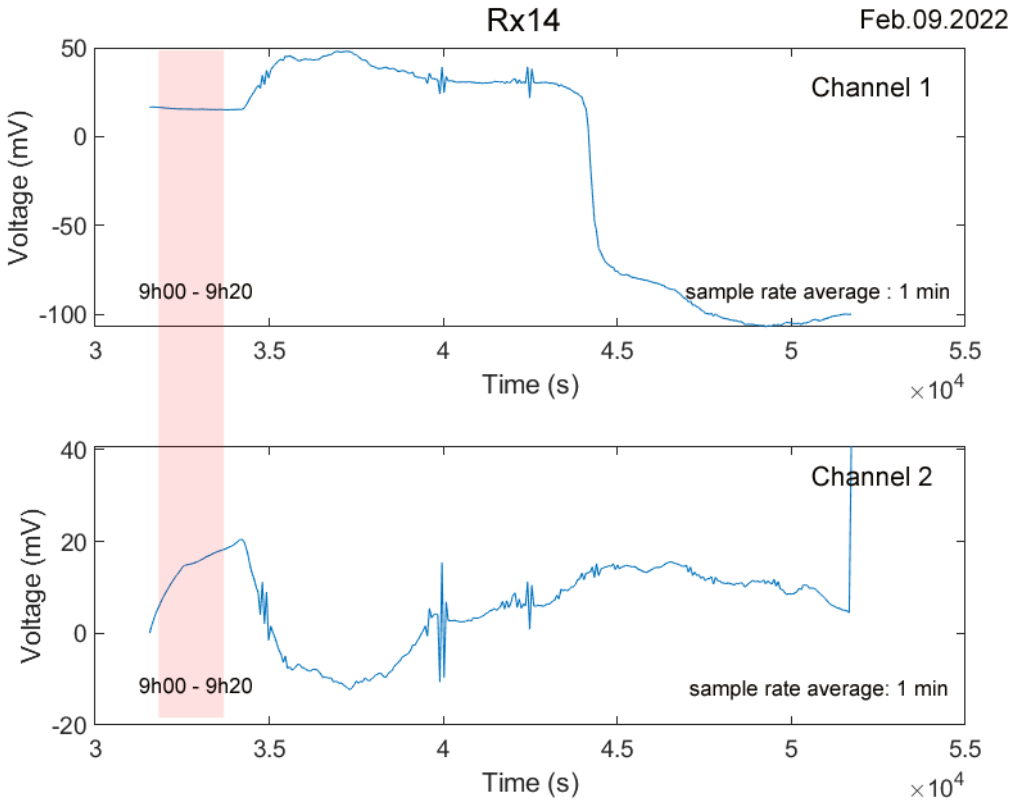

Figure 5.6 - The same daily SP recording presented in Figure 5.5 and the removal of the blue spikes after the application of an anti-spike filter to remove the artificial voltages from the SP time series. Potential sample rate average over a time window of 60 s.

A new moving average filter, operating on a 600 s interval, was then applied to the data resulting in a much cleaner signal (Figure 5.7).

The SP trend in channel 1 shows a clear anomaly with a sudden drop of the potential occurring at about 43800 s (12:10 PM). This type of "hat-shaped" anomaly ("hat anomaly") is outlined by a progressive increase in signal intensity later followed by a sudden decrease of about 100 mV. It is the typical example associated with infiltration or percolation of water as can be observed in Jardani et al. (2009); and Ikard et al. (2012).

Since every unit is considered an independent station, temporal trends can be removed from the data if necessary. The same SP – FW procedure was performed on the data of both days.

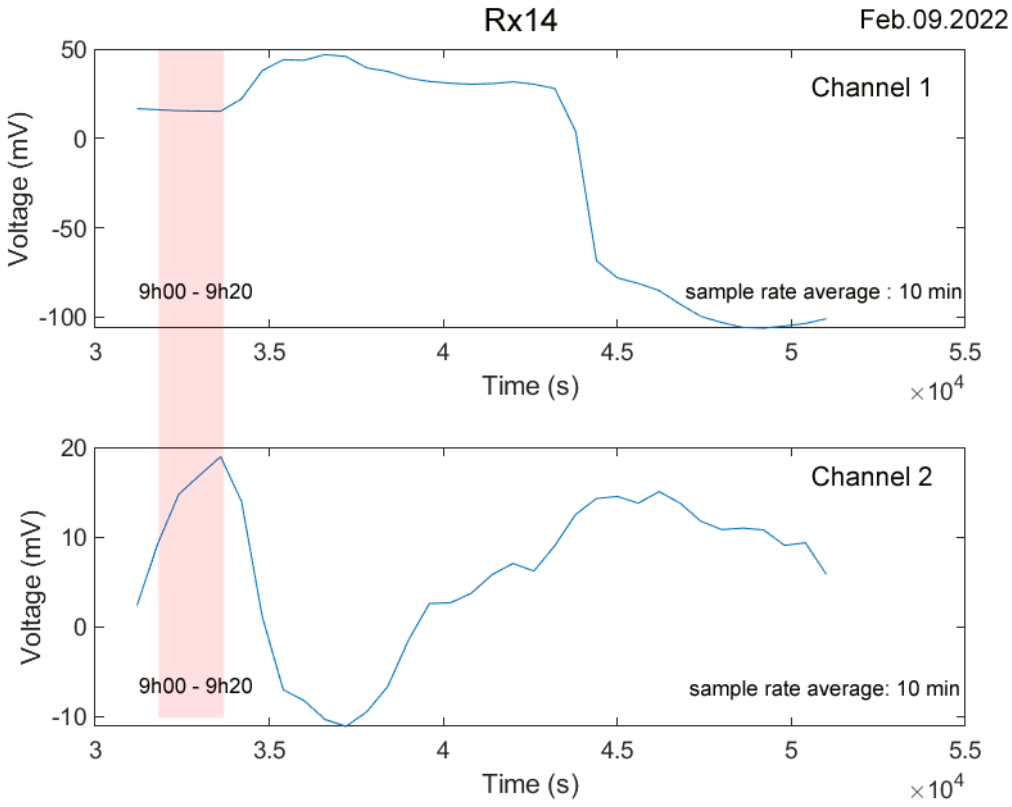

Figure 5.7 - The same daily SP recording presented in Figure 5.5 and Figure 5.6 after a moving filter average operating on 600 s intervals for removing high frequencies. The new sample rate is equal to 600 s.

5.5 RESULTS

SP signals were almost stable after few minutes of recording. In most cases, the substantial SP variation with time is related to the geology below the electrodes, as shown in Figure 5.7.

SP maps from day 1 (11:20 AM - 11:30 AM) and day 2 (9:20 AM – 9:30 AM) are shown in Figure 5.8a and Figure 5.8b respectively. The maps describe the intensity of the self-potential prior to the injection of current in the subsurface. SP values were plotted in the mid-point of the receiving dipole and lately interpolated to generate the final XY maps. Regional SP values are also associated with topography and are usually negative going uphill, probably caused by streaming potential. Both maps show similar results with considerable accumulation of positive SP signal (warm colors) in the lower topography's center going downhill. For this study area, significantly lower negative

values (cold colors) are observed mainly in the vicinity of units Rx3, Rx14, Rx17, and Rx22.

Unlike the usual SP gradient technique, the measured potential was not divided by the electrode separation distance to obtain the potential gradient in "mV/m" nor the cumulative sum of the SP measurement value of each point was performed. Self-potentials were plotted in terms of "mV" positioning the data point in the midpoint of the relative dipole.

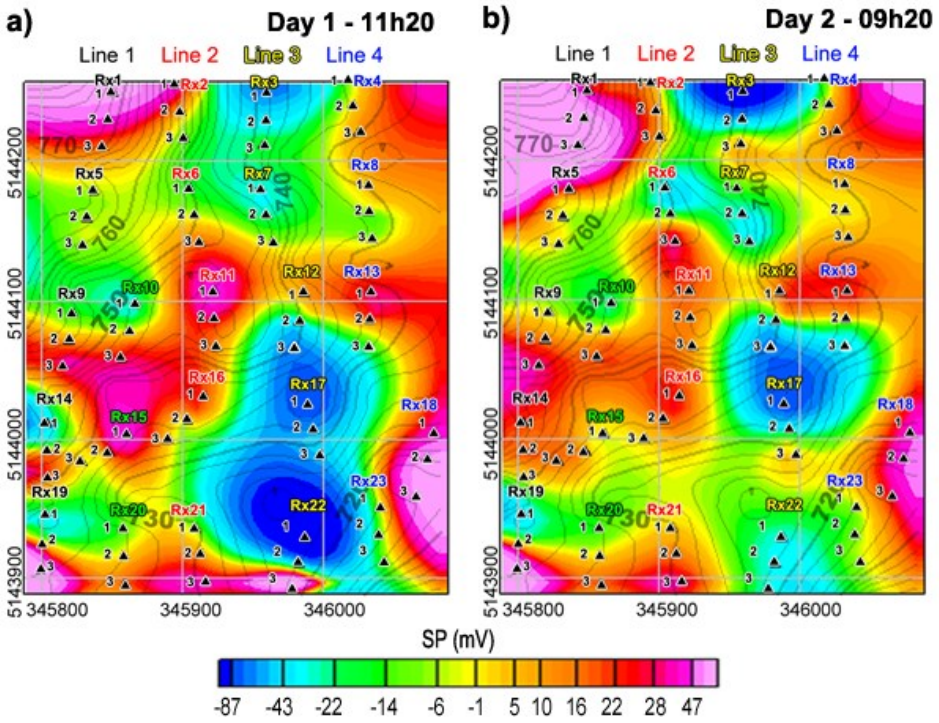

Figure 5.8 - SP maps prior to the injection of electrical current in the subsurface. a) Day 1: SP averaged over a time window of 600 s since 11:20 AM. b) Day 2: SP averaged over a time window of 600 s since 9:20 AM. Elevation contours are spaced of 2.5 m.

We plotted in Figure 5.9 (day 1) and Figure 5.10 (day 2) the SP signal time-lapse from 11:20AM to 12:30 PM.

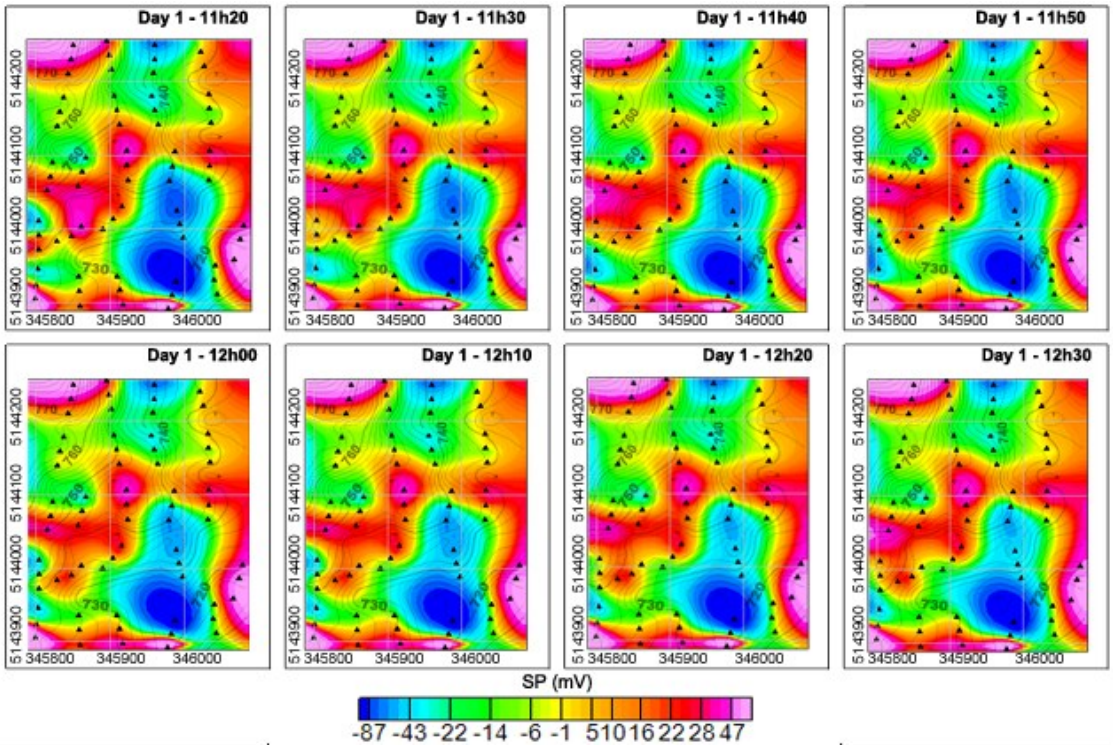

Figure 5.9 - SP maps of Feb 08/2022 with an average sampling interval of 10 min. The black triangles are the electrode positions. Elevation contours are spaced of 2.5 m.

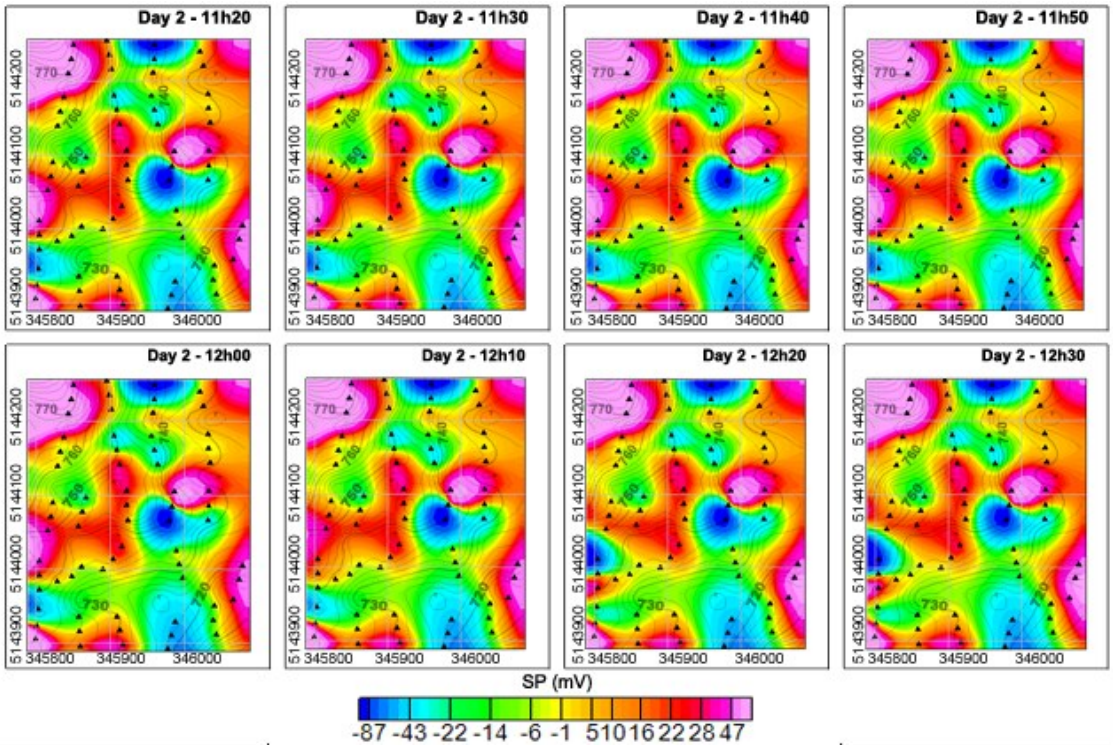

Figure 5.10 - SP maps of Feb 09/2022 with an average sampling interval of 10 min. The black triangles are the electrode positions. The topographic isolines are spaced into 2.5 m.

We observed that the Amplitude Signal Analytic technique, commonly used in Magnetic and Gravimetric methods, can provide useful information for identifying sources of SP. Following Nabighian (1972), and Biswas (2019), the 2-D Analytical Signal Amplitude (ASA) or the Total Gradient of SP anomaly is given as:

$$ASA = \left(V_x^2 + V_y^2\right)^{\frac{1}{2}} \tag{5.1}$$

Where V_x and V_y are the horizontal and vertical derivatives of the SP anomalies, respectively. The ASA tends to show a single peak centered over source, and the gradient measured over small distances is noisy. At the same time, long wavelengths have low signal-noise-ratio.

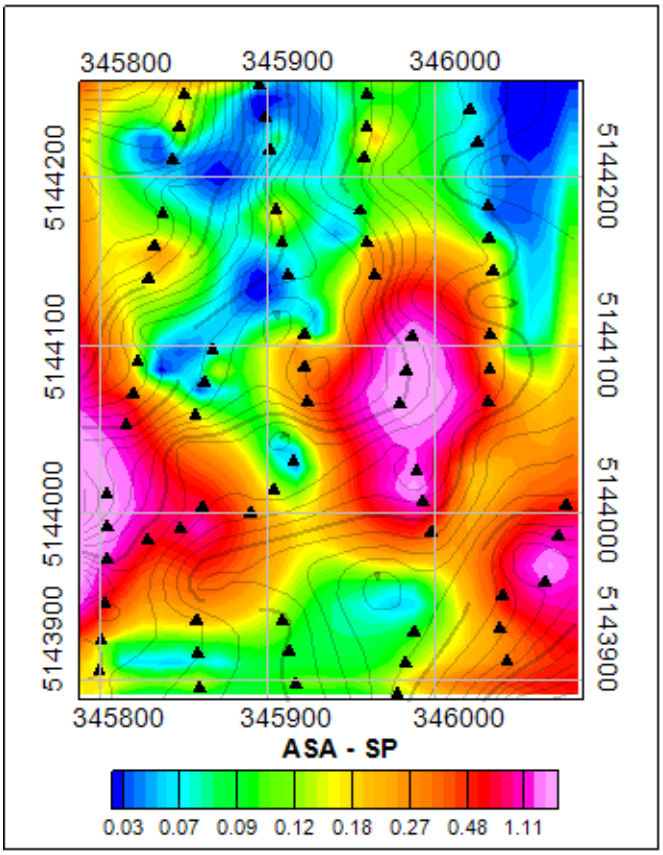

Figure 5.11 - Amplitude Signal Analytic, day 1 – 11:20 AM.

5.6 DISCUSSION

This study was performed in a paleo-landslide in the village of Cazzaso (Municipality of Tolmezzo, Udine, Italy) in the north-eastern Alps. The aim of the study was (1) to present the potentiality for retrieving SP signals from ERT survey based on data loggers georesistivimeters, even using stainless-steel electrodes; (2) to show some procedures for processing and data analysis of SP from ERT survey; (3) to generate SP time-lapse maps in order (4) to recognize groundwater flow pattern based on SP time-lapse monitoring.

As observed in Figure 5.4, verifying a possible electrode swap becomes easy, but only in the case of the current transmission is available. Otherwise, if it is unavailable, it would be unlikely to apply the procedure used. In effect, the SP signal retrieved from the 3D- DERT, as shown in Figure 5.6, is clean and stable in time. For this reason, it is a meaningful SP value and can be helpful in time-lapse map monitoring over a large scale. A range distribution around -127 mV and 127 mV is shown in Figure 5.7. Still, we have

considered the probability distribution around 80% from -75 mV to 65 mV, this aids in choosing the color scale interval for the SP maps and the temperature dependence extrapolation. The color variation seems illusory, but observing the SP values associated with each color, even if not significant, by highlighting trends in the ASA approach, the color outline helps us interpret preferential water paths.

Since we performed the acquisition during the winter, a slight temperature variation of approximately 3°C was observed for the entire day. For a qualitative SP approach, the temperature dependence could be neglected. Few changes are observed when comparing the SP maps before the current injection and post-injections. Those changes or variations are probably associated with infiltration/percolation of water below the measured dipole. Note that the so-called "hat-shaped" anomaly herein registered on the units Rx1, Rx12, Rx14 (Fig.6), Rx17, and Rx22 have similarities with the anomalies presented by Jardani et al., (2009) in pumping/injection tests, and Ikard et al., (2012) in pulse test monitoring.

Indeed, the results show that the measurements are stable along the same day and have few variations on different days. For better comparison results, in Figure 5.12, we showed the SP profiles from every single line (Figure 5.8) against the elevation. The profiles are digitized in 5 m for every line (Figure 5.2), and the data are from the grid profiles (Figure 5.9 and Figure 5.10 at 12:30 PM). As mentioned, the data have very few variations from day 1 to day 2.

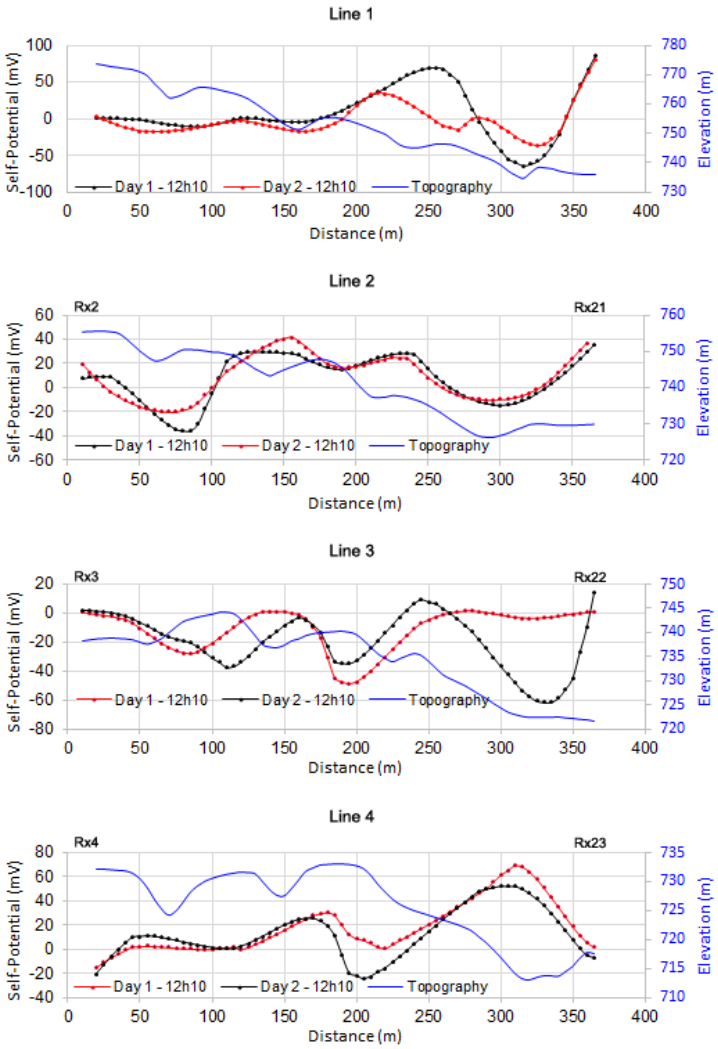

Figure 5.12 - SP profiles of "day 1" and "day 2" measured at 12:30 PM and data digitized at every 5 m from the grid profiles in Figure 5.9 and Figure 5.10 at 12:30 PM.

Even when comparing the data from different days (Figure 5.9 and Figure 5.10), the repeatability of the SP measures is notorious. The profiles in Figure 5.12 also put into evidence this interpretation. In general, we observed an increase in the SP signal in low topography. Instead, a decrease is observed in the urbanized area, some parts of Lines 2 and 3. However, we present a qualitative approach; the presence of high frequencies on the SP signal could be associated with shallow sources with periodic events ("hat-shaped" anomaly). Meanwhile, lower frequencies look to be associated with the regional background or deeper sources. The negative SP signals observed on the units Rx17 and Rx22 are probably related to local anomaly below the electrodes caused due to walls structures in the urbanized area and infiltration process.

On both days, a spatial pattern given by positive SP anomalies can be inferred, delimiting the village of Cazzaso (Figure 5.13), which may be due to drainage structures. Those positive anomalies also correspond to coarse materials observed in the field probably carried into the paleo-landslide and the presence of water. Boreholes close to Rx10 have shown the presence of silty sand with pebbles and gravel up to a depth of 1.5 m, as well as, rubble silty and sandy shale bedding intercalation up 43 m depth. Due to their high permeability, they can provide a preferential flow into the subsurface. From 43 m to 130 m depth, the boreholes presented intercalations of limestones and calcarenites.

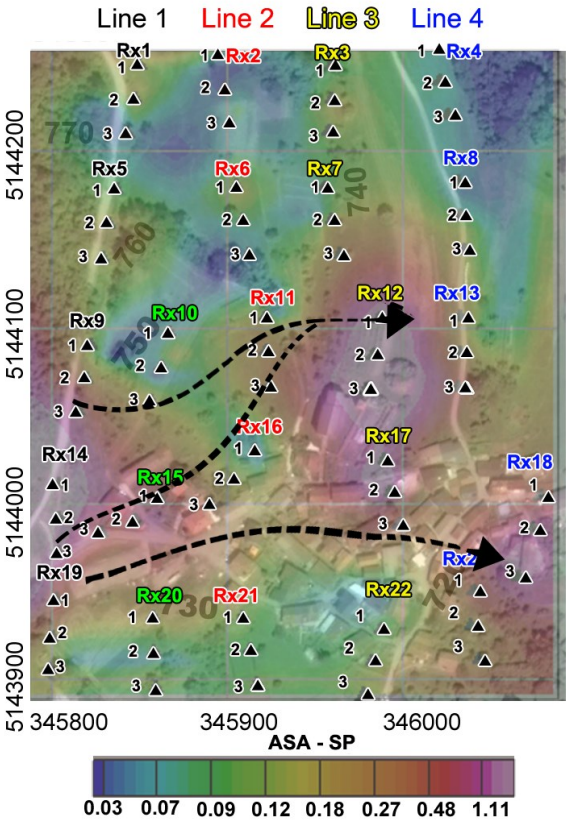

Figure 5.13 - Amplitude Signal Analytic. Black arrows linking high positive anomalies are inferred pathways overlaying Figure 5.2 in Figure 5.11.

As mentioned, there are no water springs, but piezometers in the area have registered the water table variation from -25.4 m to -25.9 m below the ground level during the geophysical survey. The 3D-DERT (Figure 5.14) shows four slices with a plan view at different elevations. In correspondence to the intercalations of limestones and calcarenites, a very conductive zone (30 Ohm.m to 120 Ohm.m), dip in the northeast

direction at different elevations can be a great candidate for the source of the regional background SP, even 100 m below the ground level. The conductive zone correlates well with the SP negative in the urbanized area and the positive peaks in ASA interpretation (Figure 5.13). The resistive (215 Ohm.m to 400 Ohm.m) zone in the southwest portion correspond to the detachment slide.

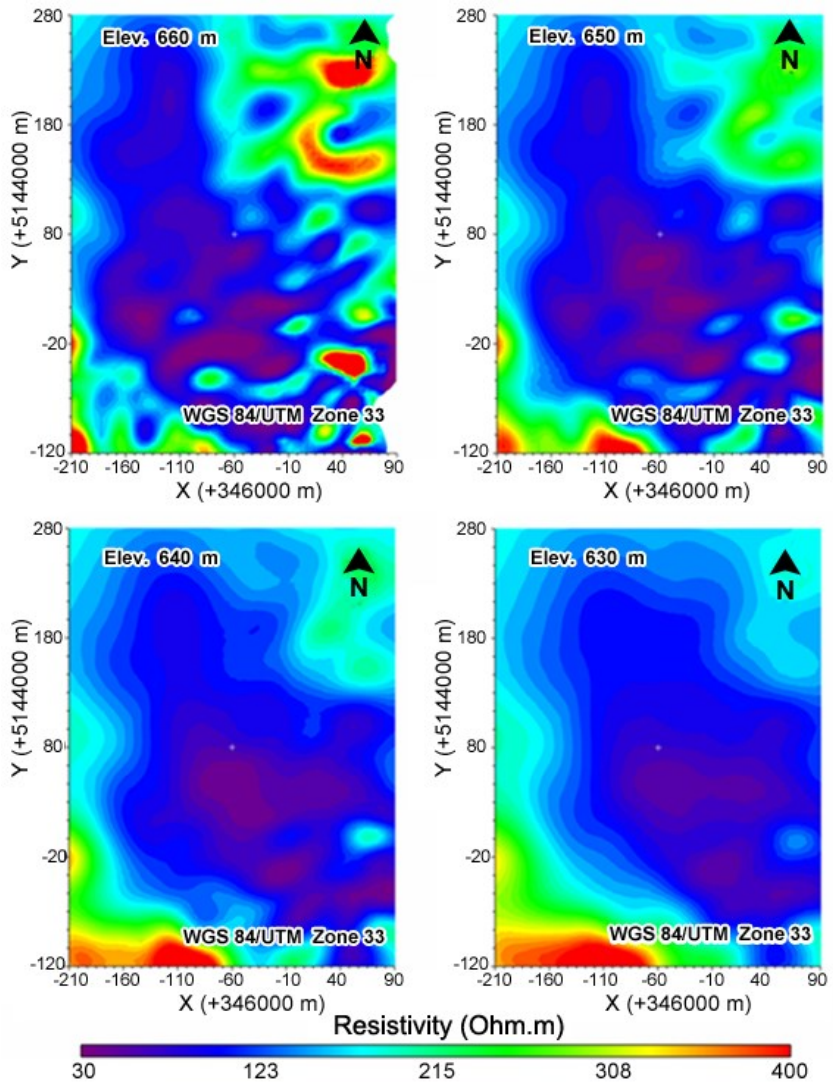

Figure 5.14 - 3D-DERT section in 4 plan view, from the elevation 660 to 630 m.

5.7 CONCLUSIONS

We have presented a practical approach for retrieving self-potential signals from 3D-DERT data. Usually, these signals would be eliminated/discarded because they are considered noise in the ERT model. In our experiment, we have inferred flow pathways

into a landslide. We have assumed that coarse materials carried into the landslide provide a preferential flow due to their high permeability.

The capability of the FW system for monitoring SP changes in time and simultaneous in several dipoles allows us to use simple stainless-steel electrodes to acquire the self-potential in time-lapse during the winter. From the qualitative point of view, the present procedure helps detect zones of possible interest in landslide monitoring. Furthermore, comparing measurements using non-polarizing electrodes and stainless-steel ones for validating a quantitative approach deserves attention.

Although the use of the FW system in 3D -DERT acquisitions and non-traditional SP array are very promising, among the main disadvantages is the low spatial resolution, which could be solved by adding more receiver units and less spacing between the electrodes. On the other hand, this solution increases the acquisition costs.

DERT quality control can be an interesting procedure for validating the reduction of cumulative errors present in traditional gradient SP surveys. If SP signals from FW systems are not from DERT surveys, other strategies must be applied since it becomes more challenging to understand possible electrodes swap.

In order to obtain a better understanding of the contribution of each component of the electric field, future studies are encouraged using non-collinear dipoles on the same receiver unit as it is performed in Magnetotelluric surveys.

The Amplitude Signal Analytic technique applied to the Sparse Gradient array can be useful as a first approach for delineating source SP anomalies in regional scale like geothermal studies.

REFERENCES

Anderson, L. A., & Johnson, G. R. (1976). Application of the self-potential method to geothermal exploration in Long Valley, California. Journal of Geophysical Research, 81(8), 1527–1532.

Barde-Cabusson, S., Finizola, A., & Grobbe, N. (2021). A practical approach for self-potential data acquisition, processing, and visualization. Interpretation, 9(1), T123-T143.

Biswas, A. (2019). Inversion of Amplitude from the 2-D Analytic Signal of Self-Potential Anomalies. Minerals. doi:10.5772/intechopen.79111

Bocchia, F., Francese, R. G., Giorgi, M., Fischanger, F., & Picotti, S. (2021). The impact of multiple transmitters on the signal strength in Deep Electrical Resistivity Tomography data: an experiment in the Vajont valley (north-eastern Italy). Bollettino di Geofisica Teorica e Applicata. Forthcoming.

Carrier, A., Fischanger, F., Gance, J., Cocchiararo, G., Morelli, G., & Lupi, M. (2019). Deep electrical resistivity tomography for the prospection of low-to medium-enthalpy geothermal resources. Geophysical journal international, 219(3), 2056-2072.

Carlini, M., Chelli, A., Francese, R., Giacomelli, S., Giorgi, M., Quagliarini, A., ... & Tellini, C. (2018). Landslides types controlled by tectonics-induced evolution of valley slopes (Northern Apennines, Italy). Landslides, 15(2), 283-296.

Chambers, J. E., Meldrum, P. I., Wilkinson, P. B., Ward, W., Jackson, C., Matthews, B., ... & Gunn, D. (2015). Spatial monitoring of groundwater drawdown and rebound associated with quarry dewatering using automated time-lapse electrical resistivity tomography and distribution guided clustering. Engineering Geology, 193, 412–420.

Colucci, R. R., Monegato, G., & Žebre, M. (2014). Glacial and proglacial deposits of the Resia Valley (NE Italy): new insights on the onset and decay of the last Alpine Glacial Maximum in the Julian Alps. Alpine and Mediterranean Quaternary, 27(2), 85-104.

CNR-GNDCI. Consiglio Nazionale delle Ricerche, Gruppo Nazionale per la Difesa dalle Catastrofi Idrogeologiche. Progetto AVI (Aree Vulnerate Italiane)—Archivio Frane. Scheda di Censimento n. 1300218. 1992. Available online:

http://wwwdb.gndci.cnr.it/php2/avi/frane_tutto.php?numero_frana=1300218&lingua=it (accessed on November 2022).

Embeng, S. B. N., Meying, A., Ndougsa-Mbarga, T., Moreira, C. A., & Amougou, O. U. O. (2022). Delineation and Quasi-3D Modeling of Gold Mineralization Using Self-Potential (SP), Electrical Resistivity Tomography (ERT), and Induced Polarization (IP) Methods in Yassa Village, Adamawa, Cameroon: A Case Study. Pure and Applied Geophysics, 179(2), 795-815.

Eppelbaum, L. V. (2021). Review of processing and interpretation of self-potential anomalies: Transfer of methodologies developed in magnetic prospecting. Geosciences, 11(5), 194.

Gallas, J. D. F. (2020). Self-potential (SP) generated by electrokinesis–Efficiency and low cost dam safety. *Journal of Applied Geophysics*, *180*, 104122.

Gallipoli, M. R., Lapenna, V., Lorenzo, P., Mucciarelli, M., Perrone, A., Piscitelli, S., & Sdao, F. (2000). Comparison of geological and geophysical prospecting techniques in the study of a landslide in Southern Italy.

Gance, J., Leite, O., Texier, B., Bernard, J. & Truffert, C., (2018). The Fullwaver systems: distributed network of autonomous devices for deep 3D electrical resistivity and induced polarization survey, in EGU General Assembly Conference Abstracts, Vol. 20 of EGU General Assembly Conference Abstracts, p. 12569.

Goto, T. N., Kondo, K., Ito, R., Esaki, K., Oouchi, Y., Abe, Y., & Tsujimura, M. (2012). Implications of self-potential distribution for groundwater flow system in a nonvolcanic mountain slope. International Journal of Geophysics, 2012.

Ikard, S. J., Revil, A., Jardani, A., Woodruff, W. F., Parekh, M., & Mooney, M. (2012). Saline pulse test monitoring with the self-potential method to non-intrusively determine the velocity of the pore water in leaking areas of earth dams and embankments. Water Resources Research, 48(4).

Ikard, S. J., Briggs, M. A., & Lane, J. W. (2021). Investigation of Scale-Dependent Groundwater/Surface-water Exchange in Rivers by Gradient Self-Potential

Logging: Numerical Modeling and Field Experiments. Journal of Environmental and Engineering Geophysics, 26(2), 83–98.

Jardani, A., Dupont, J. P., & Revil, A. (2006). Self-potential signals associated with preferential groundwater flow pathways in sinkholes. Journal of Geophysical Research: Solid Earth, 111(B9).

Jardani, A., Revil, A., Santos, F., Fauchard, C., & Dupont, J. P. (2007). Detection of preferential infiltration pathways in sinkholes using joint inversion of self-potential and EM-34 conductivity data. Geophysical Prospecting, 55(5), 749-760.

Jardani, A., Revil, A., Barrash, W., Crespy, A., Rizzo, E., Straface, S., ... & Johnson, T. (2009). Reconstruction of the water table from self-potential data: A Bayesian approach. Groundwater, 47(2), 213–227.

Jouniaux, L., Maineult, A., Naudet, V., Pessel, M., & Sailhac, P. (2009). Review of self-potential methods in hydrogeophysics. Comptes Rendus Geoscience, 341(10-11), 928-936.

Kukemilks, K., & Wagner, J. F. (2021). Detection of Preferential Water Flow by Electrical Resistivity Tomography and Self-Potential Method. Applied Sciences, 11(9), 4224.

LaBrecque, D. J., Morelli, G., Fischanger, F., Lamoureux, P., & Brigham, R. (2013, December). Field trials of the multi-source approach for resistivity and induced polarization data acquisition. In AGU Fall Meeting Abstracts (Vol. 2013, pp. NS34A-03).

Lajaunie, M., Gance, J., Nevers, P., Malet, J. P., Bertrand, C., Garin, T., & Ferhat, G. Structure of the Séchilienne unstable slope from large-scale 3D electrical tomography using a Resistivity Distributed Automated System (R-DAS). Geophysical Journal International.

Marchi, L.; Cazorzi, F.; Arattano, M.; Cucchiaro, S.; Cavalli, M.; Crema, S. Debris flows recorded in the Moscardo catchment (Italian Alps) between 1990 and 2019. Nat. Hazards Earth Syst. Sci. 2021, 21, 87–97.

Minsley, B. J. (2007). Modeling and inversion of self-potential data (Doctoral dissertation, Massachusetts Institute of Technology).

Nabighian M.N. The analytic signal of two-dimensional magnetic bodies with polygonal cross-section, its properties and use for automated anomaly interpretation. Geophysics. 1972; 37:507-517.

Nyquist, J. E., & Corry, C. E. (2002). Self-potential: The ugly duckling of environmental geophysics. The Leading Edge, 21(5), 446–451.

Orellana, E. (1972). Prospección geoeléctrica en corriente continua (Vol. 1). Madrid: Paraninfo.

Perrone, A., Iannuzzi, A., Lapenna, V., Lorenzo, P., Piscitelli, S., Rizzo, E., & Sdao, F. (2004). High-resolution electrical imaging of the Varco d'Izzo earthflow (southern Italy). Journal of Applied Geophysics, 56(1), 17-29.

Poldini, E. (1938). Geophysical exploration by spontaneous polarization methods. Mining magazine, 3–22.

Pondrelli, M., Corradini, C., Spalletta, C., Simonetto, L., Perri, M. C., Corriga, M. G., ... & Schönlaub, H. P. (2020). Geological map and stratigraphic evolution of the central sector of the Carnic Alps (Austria-Italy). Italian Journal of Geosciences, 139(3), 469-484.

Revil, A., & Jardani, A. (2013). The self-potential method: Theory and applications in environmental geosciences. Cambridge University Press.

Revil, A., Titov, K., Doussan, C., & Lapenna, V. (2006). Applications of the self-potential method to hydrological problems. In Applied hydrogeophysics (pp. 255-292). Springer, Dordrecht.

Rizzo, E., Capozzoli, L., De Martino, G., Piscitelli, S., Bellanova, J., Caputo, R., ... & Fischanger, F. (2020). Deep geophysical investigation in urban area: Ferrara city example (No. EGU2020-9294). Copernicus Meetings.

Sato, M., & Mooney, H. M. (1960). The electrochemical mechanism of sulfide self-potentials. Geophysics, 25(1), 226–249.

Thanassoulas, C. P. (1989). Application of the self-potential technique over the Milos geothermal test site. Geothermics, 18(4), 497-505.

The Math Works, Inc. MATLAB. Version 2020a, The Math Works, Inc., 2020. Computer Software.

Troiano, A., Isaia, R., Di Giuseppe, M. G., Tramparulo, F. D. A., & Vitale, S. (2019). Deep electrical resistivity tomography for a 3D picture of the most active sector of Campi Flegrei caldera. Scientific reports, 9(1), 1-10.

Zuliani, D., Tunini, L., Di Traglia, F., Chersich, M., & Curone, D. (2022). Cost-effective, single-frequency GPS network as a tool for landslide monitoring. Sensors, 22(9), 3526.

CHAPTER 6

6. DEEP ELECTRICAL RESISTIVITY TOMOGRAPHY AND UNCONVENTIONAL SELF-POTENTIAL TECHNIQUE APPLIED TO LANDSLIDE

6.1 INTRODUCTION

Tizzano Val Parma, a mountain municipality located on the Apennine chain in the province of Parma (Italy), is prone to landslides due to geological and geomorphological factors. In recent years, the valley hydrogeological instability has increased, causing significant environmental damages and making it essential to monitor potential landslides in the local earth massifs. The Self-Potential (SP) monitoring method is an effective geophysical method for identifying anomalous water flows (i.e., water infiltrations) within landslides (Bogoslovsky and Ogilvy, 1977; Colangelo et al., 2006; Kukemilks et al., 2021; Hu et al, 2024). If the concentration or speed of water flows reaches a critical level, it can trigger erosion or liquefaction processes, leading to subsidence, the movement of materials from the slope massif, and eventually to a partial or complete collapse of the landslide. It is important to understand the different SP source anomalies induced by this degradation process, in order to improve the accuracy of landslide monitoring and to reduce the risk of potential hazards. Revil and Jardani (2013) identified different types of SP source anomalies, such as thermo-potential, electrochemical potential, streaming potential or electrokinetic potential, and geobattery potential. In most cases of landslide application of the SP method, it can be assumed that the SP anomalies are electrokinetic flow potentials induced by underground water flows (Gallas, 2020; Heinze et al., 2019).

According to Perrone et al., (2014) and Lappena and Perrone (2022) the Electrical Resistivity Tomography (ERT) method stands out as one of the mostly employed geophysical techniques in landslide studies. 2D and 3D ERT surveys has been extensively applied to delineate the geometric features of landslide bodies, identifying the sliding surface and pinpointing regions with elevated water content (Pazzi et al., 2019; Bellanova et al., 2018).

Recent advancements in the application of induced polarization (IP) for landslide investigations have significantly enhanced our understanding of subsurface conditions and stability assessments. Marescot et al. (2008) demonstrated the reliability of 2D resistivity imaging in mountain permafrost studies, establishing a foundational approach for using IP in complex terrains. Building on this, Sastry and Mondal (2012) explored the geoelectrical properties of rocks and minerals through the IP method, providing insights into the theoretical underpinnings essential for accurate data interpretation in landslide-prone areas. Gallistl et al. (2018) applied IP to the Reichenkar rock glacier, highlighting the method's capability in detecting variations in frozen ground conditions, which are critical for assessing landslide hazards in alpine regions. Revil et al. (2020) reviewed several low-frequency electrical methods, including IP, emphasizing their importance in hydrogeological characterizations that are pertinent to landslide monitoring. More recently, Orozco et al. (2022) have showcased the latest advancements in IP imaging techniques, presenting case studies that demonstrate improved methodologies for continuous landslide monitoring. These studies collectively underscore the significant role of IP in enhancing the precision and reliability of geophysical surveys aimed at mitigating landslide risks.

Chen et al., (2023) applied the mise-a-la-masse method and tracer tests to map conduits. They found conduits align with faults, cluster near tectonic fractures, and are shaped by lithology and geological structures. This integrated approach effectively maps karst conduits, essential for groundwater management and engineering in similar terrains.

Some studies integrated SP and ERT methods to landslide monitoring with excellent results. Perrone et al., (2004) and Colangelo et., al (2006) for example, applied the SP and ERT methods to the Varco d'Izzo landslide in Italy, allowing the reconstruction of the geometry of the landslide body and to define the possible reactivation areas. Kukemilks and Wagner (2021) applied ERT and SP to a landslide-prone hillslope in Luxembourg for detecting preferential water flows. In this case, the authors noted that the source of the measured SP anomalies was not evident, as it was unclear which preferential flow system was involved. Although the signals were dispersed across a wide area, assumptions were made in the numerical modelling to conceptualize the preferential flow paths, by exploiting ERT and geological data.

Two standard single-channel techniques have been widely reported in the literature for SP data acquisition: the Potential or Fixed-Base and the Gradient (Leapfrog) techniques. Theoretically, under some circumstances, they are somewhat equivalent but, from the practical point of view, they are rather different (Orellana, 1972). This study proposes a new approach called Sparse Gradient Array, which is similar to traditional Gradient and Fixed-Base techniques, but with a significant difference: there are no reference points and potential differences are measured between couples of electrodes deployed on the study area. The originality of our approach consists in using a new-concept Resistivity Distributed System, such as the Fullwaver system (MPT-IRIS — www. iris-instrument.com), to conduct sparse measurements. This passive system is capable of logging both artificial and self-potentials at a frequency of 100 Hz between multiple pairs of electrodes.

6.2 GEOLOGICAL SETTING

Our field investigations took place in the Apennines (Italy), specifically within the scenic Tizzano Val Parma in the Emilia-Romagna region (refer to Fig.6.1). The study area is characterized by the Flyschoid Formation of the Marne Rosate (Ligurian Domain - Caio Unit), overlaid by a thick eluvial alteration blanket. This alteration is likely a result of periglacial environment degradation associated with the late Pleistocene glacial episodes (Federici and Tellini, 1983). The covering matrix is predominantly clayey and contains numerous angular inclusions, primarily calcarenitic and arenaceous.

The water circulation within the detrital mass is complex, and over time, localized water emergence areas may occur, facilitated by the slope of the stratification and related plasticization phenomena. This hydrogeological situation historically predisposes the area to landslide hazards (Almagià, 1907). In a landslide, from the mountaintop to the valley, there are typically three zones: a detachment zone, a zone of movement, and a zone of deposition or accumulation. In Fig.1 only the deposition zones are outlined (thus occupied by terrains that have shown evidence of movement).

Understanding the geological vulnerability of the area is crucial for effective risk management and mitigation strategies. By integrating various methodologies, such as ERT-IP surveys and SP monitoring, we can comprehensively analyze the geology and

track dynamic variations within the landslide-prone terrain. Moreover, given the susceptibility to extreme events, it's imperative to conduct measurements following periods of rainfall to gauge the immediate impact on geological stability. Our research aims to contribute to a better understanding of the geological vulnerability of the site and inform proactive measures for risk reduction and management.

In Fig.6.1, the ERT-IP survey spanned four distinct landslide units, encompassing an active landslide of undetermined type, a quiescent landslide by sliding, a complex active landslide, and possible evolutions of active landslides. The SP monitoring phase focused on the unit identified as a complex active landslide. This integration of different methodologies provided a comprehensive analysis of the geology and facilitated the tracking of dynamic variations within the expansive landslide area.

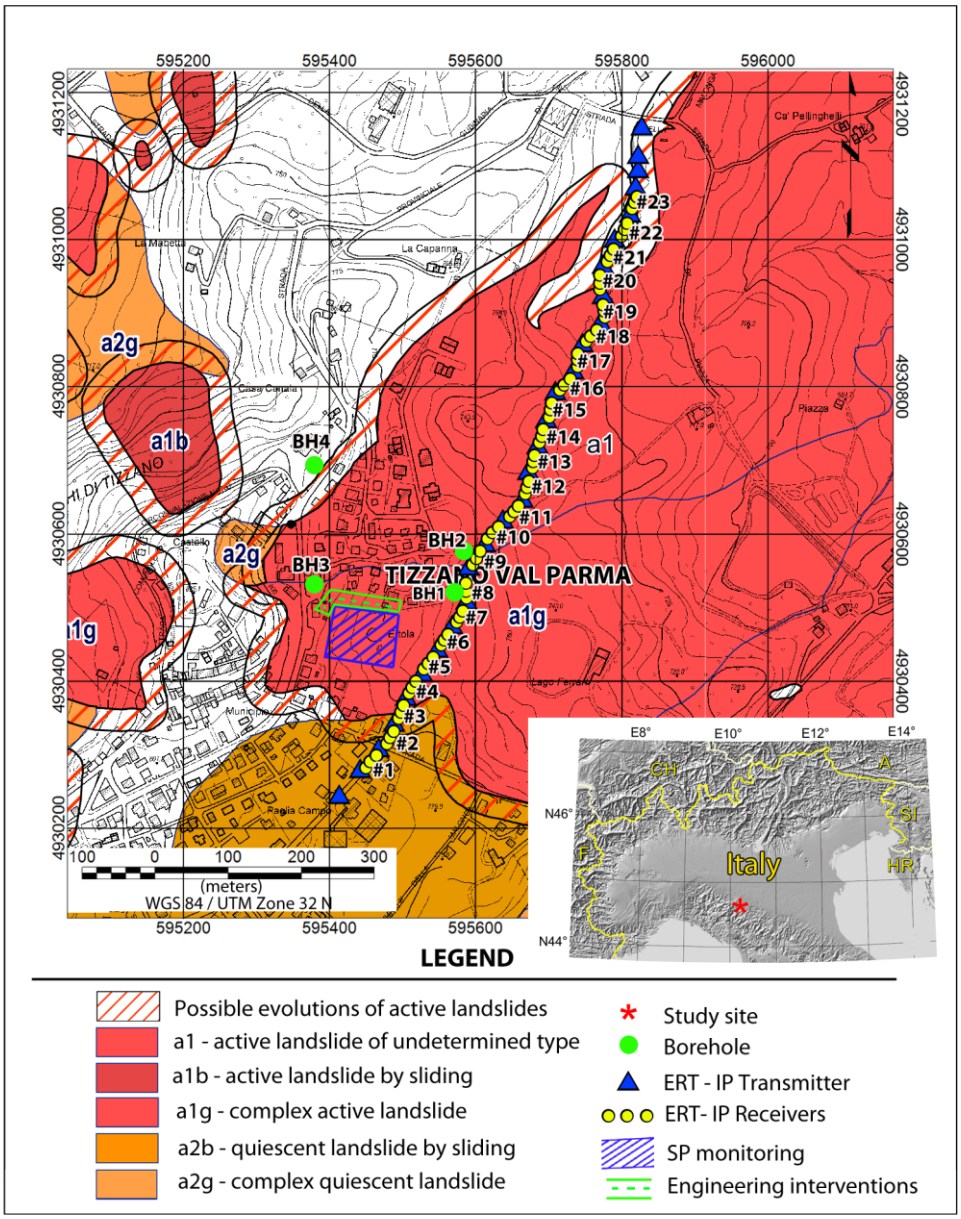

Figure 6.1 – Location map and layout survey. (Modified from Seismic and Soil Geological Service, Emilia-Romagna Region, accessed on January 15, 2024)

6.3 GEOELECTRICAL INSTRUMENTATION – THE FULLWAVER SYSTEM

The FullWaver system is a distributed network of autonomous devices designed for deep 3D ERT and IP surveys (MPT-IRIS — www. iris-instrument.com). The system is composed of multiple autonomous units (V-FullWaver), continuously recording the potential difference through two channels comprised of three electrodes (P1-P2 and P2-P3). The dipoles are arranged in either a regular or adapted irregular layouts based on

field conditions like topography, roads, buildings, and vegetation. By employing such a setup, the system effectively eliminates common drawbacks associated with extensive cable arrangements in large 3D areas, including time consumption, limited accessibility, weight, and electromagnetic induction (Gance et al., 2018). Real-time recording of the injected current on the I-FullWaver enhances the system's efficiency and adaptability. Functioning as independent measuring nodes, the GPS PPS signal ensures synchronization and thus a seamless signal processing. Data retrieval is simplified as information stored in the memory can be directly downloaded to a standard USB stick from all FullWavers (Carrier et al., 2019).

The V-FullWaver is a versatile receiver designed for dual-channel applications in Induced Polarization (IP), Deep Electrical Resistivity Tomography (DERT), and Self-Potential (SP). With a continuous recording capability at a 10ms sample rate, it captures comprehensive waveform records. The FullWaver system also incorporates an induced polarization transmitter (VIP), and a motor generator. The VIP transmitter allows injecting current up to 10 Amps, 5000 W, and 3000 V, at a frequency of 0.5 Hz. External generators supply the required current to the VIP.

6.4 GEOELECTRICAL METHODOLOGIES

Preliminary DERT and IP surveys were conducted in 2022, to assess vulnerable zones within the Tizzano Val Parma landslide (Fig.6.1). Then, SP monitoring was carried out throughout 2022 and 2023, following rain events.

6.4.1 DERT and IP techniques

DERT and IP surveys were performed on March 23rd and 24th, 2022, employing the FullWaver system in time domain. The instrumentation ensemble comprised 23 independent receiving nodes (i.e., the V-FullWavers), 20 m spaced. As explained above, each receiving unit controls two dipoles and was connected to 3 electrodes PbCl/Pb electrodes. The spacing between electrodes was initially set at 10 meters and was then adjusted based on logistical circumstances such as roads, country borders, and highways. The receiving nodes were 20 m spaced, while energizations were performed using large dipoles A-B, where A and B are current injecting electrodes. The entire profile extended over a total length of about 1060 meters. The B electrode remained

fixed at one end of the profile, while the A electrode was systematically moved along the entire acquisition line, by energizing between couples of adjacent receiving nodes. This configuration ensured a 10 m distance between the injection electrode A and the nearest receiver electrode. In the first phase of the acquisition procedure the B electrode was placed at the NE end of the profile and the A electrode was moved towards SW. Subsequently, electrode B was relocated to the SW end of the profile, and electrode A was shifted towards the NE. The number of injections carried out in each direction is 26, resulting in a total of 52 energizations. The injected currents, as measured by the I-FullWaver, ranged from 1.7 to 3.4 A. In order to allow a better evaluation of the signal-to-noise ratio through statistical signal processing, a square-wave current lasting 180 s, with 2 s ON/OFF times. The coordinates of all electrodes were recorded using a high-precision differential GNSS device.

The raw geoelectrical data underwent processing using the FullWaver Viewer software developed by IRIS Instruments, and the ViewLab3D (Geostudi Astier, 2022) software. The automated processing involved the following tasks: realigning potentially desynchronized time series, filtering out spikes and self-potential jumps, stacking different periods after synchronously detecting the fronts, calculating average voltages over a portion of the injection window on the stacked period, computing the average current over a segment of the injection window on the stacked period, and curve analysis of the Cole-Cole model. For data exhibiting low signals and high standard deviations, a manual reprocessing was conducted. Generally, measurements with standard deviation (obtained through multiple measurement stacks) larger than 10 % and receiver potentials lower (in absolute value) than 0.01 mV are eliminated.

6.4.2 Self-Potential techniques

The primary field for Self-Potential (SP) assessments include measuring potentials and gradients (Gallas, 2020). In many scenarios, including the one described in this study, the optimal approach is measuring potential differences. This technique employs two electrodes for data collection. As described above, in our approach one potential electrode remains fixed at a base station, while the other moves along the survey profile.

We employed the conventional Fixed-Base configuration and the unconventional Sparse Gradient array. Numerical modeling has showed that the Fixed-Base and Leapfrog techniques are the best survey choice for SP mapping due to their better accuracy and to their higher resolution in outlining the anomaly sources. The Sparse Gradient also provides excellent and interpretable responses when adopting the Analytic Signal Amplitude approach (Araujo et al., 2024).

As usual in field acquisition, the negative port of the voltmeter remains in the base station, the positive one reveals the potential of the measured point related to the base station. In the V-FullWaver, the connection ports P1, P2, and P3 provide a dual-channel potential difference (Ch1, Ch2) between P1 and P2 (Ch1), and between P2 and P3 (Ch2), where P1 and P3 are the positive ports, and P2 is the negative one. The electrode connected to the negative port is referred to as negative electrode. Therefore, the channel Ch2 provides a negative signal with respect to channel Ch1. Usually the negative electrode remains fixed at the base station during the SP surveys using the Fixed-Base technique, while the other positive ports are connected to the electrodes deployed on the study area. The V-FullWavers measure the potential differences respect to the reference negative electrode.

Figure 6.2 shows the SP arrays techniques used in our monitoring survey. The Fixed-Base technique shown in Figure 6.2a is the one adopted in 2023 and has a reference electrode #Ref in the corner of the study area. All V-FullWaver units (Rx1 to Rx8) have the negative ports (p1.2 to p8.2 in blue) connected to the reference electrode #Ref. As consequence, the central position on the field layout remains uncovered. In this case, an extra Rx unit was used for acquiring the data relative for those positions, using the same reference electrode. The main difference in this case is regarding to the time of acquisition that was of 180s, while the main Fixed-Base acquisition was 2.5 hours of continuous monitoring. The single-channel traditional Fixed-Base technique was used in 2022, by adopting a classic voltmeter. The reference electrode was always the same. As the measured potential difference is a relative value, after the acquisition, any point can be taken as a reference electrode. For this reason, as result we have plotted the values for both years 2022 and 2023 relative to the point position p8.2. We have

considered the positive port #1 for the highest position Y (units #1 to #6), and the positive port #1 for the most minor position X (units #7 and #8).

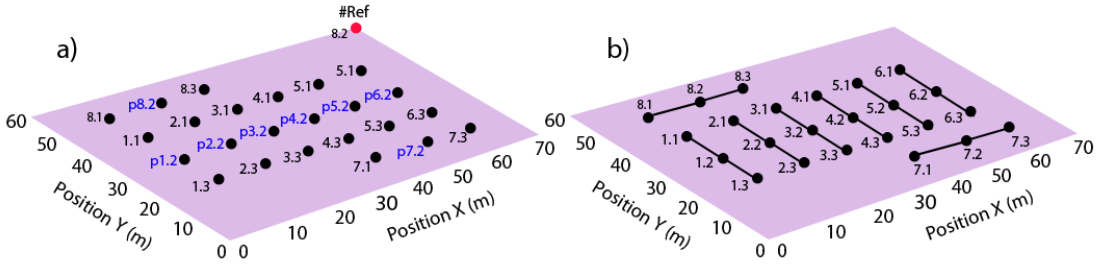

Figure 6.2 – SP arrays techniques, the first number from 1 to 8 represents the V-FullWaver number unit, and the second one, from 1 to 3, represents the unit port. a) Fixed-Base technique with reference electrode #Ref in the corner of the study area; b) Sparse Gradient technique, where electrodes are organized by triplets.

The Sparse Gradient technique is shown in Figure 6.2b. In this case the reference electrode is independent for each single unit (connected to ports p1.2 to p8.2). The main idea of using this kind of configuration is regarding to the possibility of leveraging the available SP data in DERT acquisitions as a reconnaissance of primary anomaly. Although this configuration allows us to record local and suitable SP variations on the ground associated with electrokinetic processes, it would be worth considering deploying the units (#1 to #6) in the X direction, similar to units #7 and #8 (Figure 6.2b), orthogonal to the main expected water flow. Instead, we decided to traverse the topographic variations. The Sparse Gradient technique was monitoring continuously for more than 8 hours, starting at 4 PM, with a temperature around 6 °C on November 30th, 2022, and December 1st, 2022. The same configuration was set for the monitoring on October 23rd, 2023, but the observed temperature was around 13 °C.

It is worth mentioning that, compared to the 2022 monitoring, in 2023 an engineering intervention has been re-installed with more than 11 active vertical wells connected horizontally to each other around the surveyed area, extending beyond the X position of 70, from the highest Y position towards the lowest Y position.

6.4.3 SP data interpretation

Usually, the interpretation of SP maps obtained from conventional techniques is performed as shown in Figure 6.3. In the case of electrokinetic processes, due to the high availability of cations in waters, the flow will always be from a smaller to a higher

potential (Gallas, 2020). Figure 6.3a shows a 1-grid vector map with typical uniform flow (black arrows) without any anomaly overlaying a 2d map of a synthetic SP data. The vector is drawn at each grid node (Golden Software, Inc). The arrow symbol points from the Position Y 60 to 0, representing the “downhill" direction, and the length of the arrow depends on the magnitude. For better visualization, the lengths of the arrows are normalized. In Figure 6.3b the uniform flow is distorted, and an anomalous flow can be observed (blue arrow), also called primary flow lineament. The anomalous flow in blue is interpreted by connecting the arrows directions in convergence.

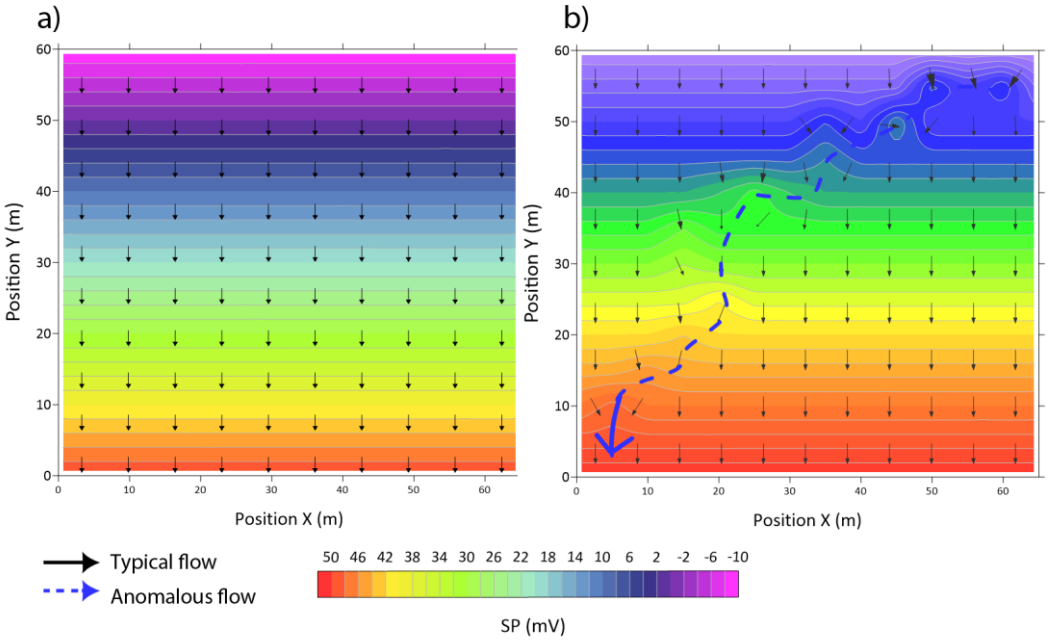

Figure 6.3 - Typical electrokinetic interpretation of SP maps obtained from conventional techniques. a) typical uniform flow (black arrows) without any anomaly; b) anomaly is present generating a primary flow lineament, represented by the blue arrow.

Feasibility studies based on forward modeling, have shown that the Fixed-Base technique is the most effective for SP surveys. However, both the Sparse Gradient and Full Sparse Gradient can be effective for primary source reconnaissance. Nonetheless, it is necessary to pay close attention to the interpretation of maps obtained using non-conventional SP techniques.

As electrokinetic processes generate transient SP anomalies, an initial interpretation can be conducted by analyzing the V-FullWaver curves. The typical shapes of these curves highlight the presence of potential anomalous flow. Interpreting the electric field is one

option, which can be achieved by computing the Analytic Signal Amplitude (ASA) of the potential electric field.

The ASA technique, commonly used in Magnetic and Gravimetric methods, can help to identify the primary source of SP. Following Nabighian (1972), Roest et al. (1992), Biswas (2019), and Sindirgi & Ozyalin (2019), the 3D analytic signal (or ASA) of a potential field is defined as:

$$ASA = \left[\left(\frac{\partial V}{\partial x}\right)^2 + \left(\frac{\partial V}{\partial y}\right)^2 + \left(\frac{\partial V}{\partial z}\right)^2\right]^{1/2}, \quad (6.1)$$

where V represents the measured potential at the surface. In the case of electric potential field, the three derivatives in equation 1 coincide with the three components E_x , E_y and E_z , i.e., the ASA is the modulus of the electric field $\boldsymbol{E}$ or the total gradient magnitude V of the SP anomaly. The ASA technique first calculates the analytic signal of the input profile using a Hilbert transform. Then, local peaks in the analytic signal profile are interpreted as corners of source anomalies, and the shape of the peak contains information about the depth of the corner (Li, 2006; Beiki, 2010; Sunny, 2018). The ASA tends to show a single peak centered over the source anomaly. In absence of aliasing with a sufficient signal-to-noise ratio, ASA allows for an accurate horizontal localization of anomalies.

6.5 RESULTS

6.5.1 DERT, IP and boreholes

There are at least 4 boreholes in the study area. The simplified stratigraphy results of two boreholes, BH1 and BH2, is represented in Figure 6.4 These boreholes are in proximity to V-FullWaver units #8 and #9, respectively. The BH1 stratigraphy reveals a complex lithology dominated by sandstones and clayey marl, starting from a depth of 14.7 m. On the other hand, the BH2 stratigraphy is dominated by coarse material from sand to gravel with clay in the first 18 m depth, after which the clayey marl level begins.

Figure 6.5a shows the DERT section, depicting the positions of boreholes BH1 and BH2. The section reaches a depth of approximately 200 meters and displays high conductivity (color scale ranging from 10 to 80 Ohm.m). At least three distinct domains

are identified by 51-degree dipping discontinuities in the southwest direction. These domains extend to a depth of around 90 meters. The initial conductive zone spans 0 to 400 meters, with a resistivity of approximately 30 - 50 Ohm.m and few blobs of 10 Ohm.m. The central zone, situated between 400 and 600 meters, appears to be the most resistive, ranging from 50 to over 80 Ohm.m. A third zone, stretching from 400 to 950 meters, exhibits an average resistivity of 50 Ohm.m. Below these three zones, starting from 90 meters, a continuous layer is observed with resistivity ranging from 25 to 35 Ohm.m.

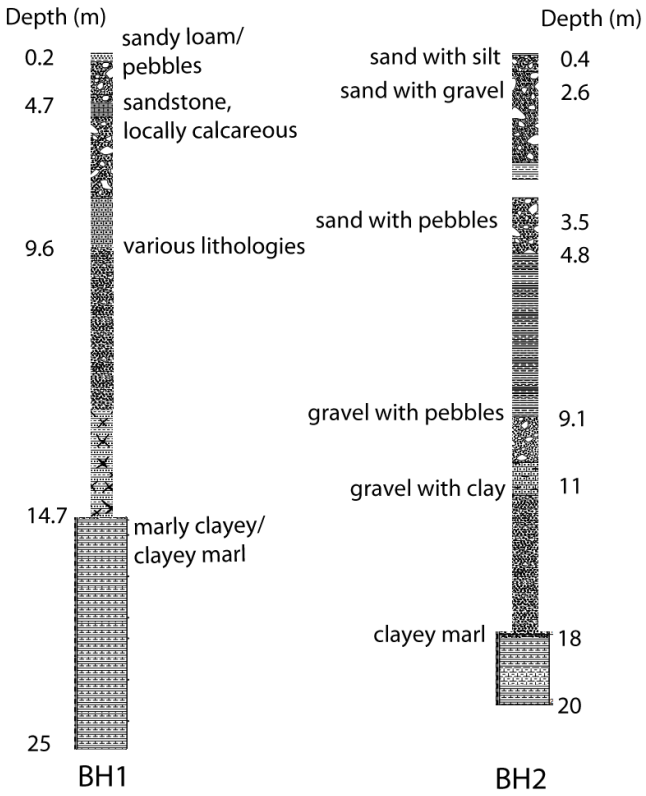

Figure 6.4 – Simplified stratigraphy of the boreholes BH1 and BH2.

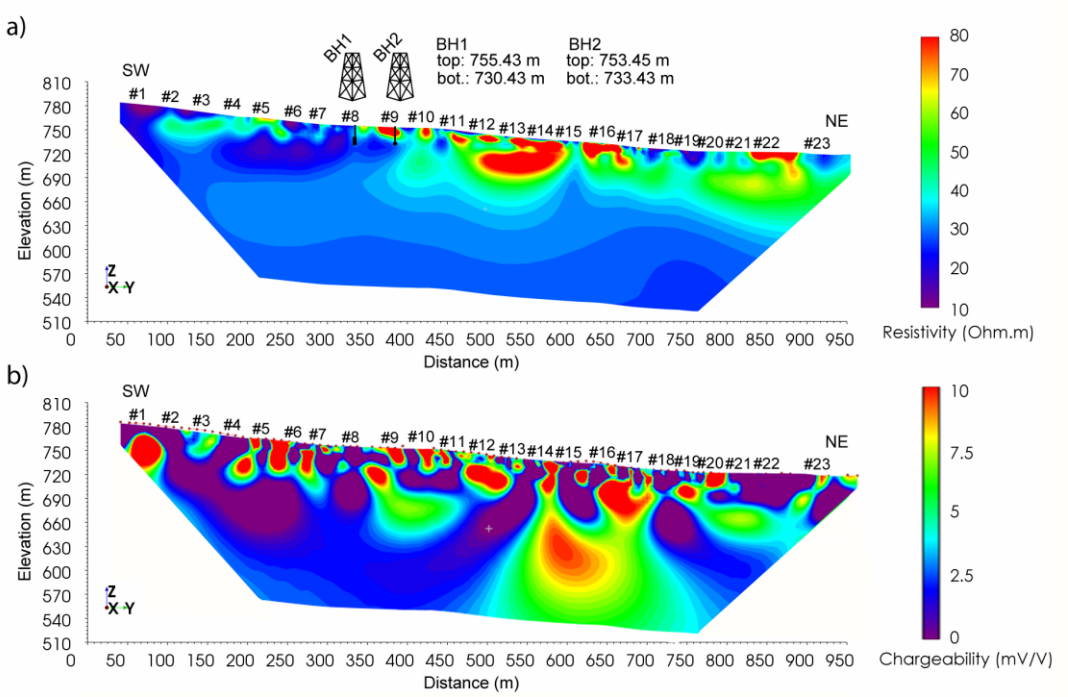

Figure 6.5 - DERT (a) and IP (b) sections versus depth.

The IP section is depicted in Figure 6.5b. It is characterized by an overall low chargeability (0 to 10 mV/V) and it is divided into two main zones. The first zone exhibits an average low chargeability or non-chargeable characteristics (0 to 2.5 mV/V) within a distance range from 0 to 600 meters. The second part, spanning from 600 to 950 meters, shows chargeability varying from 5 to 10 mV/V. A prominently highlighted discontinuity at 600 meters, dipping at 51 degrees in the SW direction, crosses the section from the surface to greater depths.

Similarly to the resistivity section, an interface at about 90 m depth is observed also in the IP section. This interface generally separates low or no chargeability with some high-chargeability zones (10 mV/V). Secondary discontinuities are also observed.

6.5.2 SP monitoring

Figure 6.6 shows the raw SP curves recorded during the night of 30th November 2022, using the Sparse Gradient technique. It represents the V-FullWaver units from #1 to #8 and their respective channels (1 and 2) with a sampling interval of 10 ms.

In geophysical studies employing the SP method, variations in the distribution of electrical potential are often attributed to changes in the electrical conductivity of the subsurface medium. In contexts such as landslides, levees, and dams, temporal

variations in well calibrated SP surveys are frequently driven by electrokinetic processes such as water infiltration or percolation. These processes can substantially alter the distribution of electrical potential due to changes in the conductivity of adjacent materials. The presence of infiltrated water, typically characterized by higher electrical conductivity compared to dry soil, can induce increases or decreases in SP measurements. This phenomenon manifests prominently in vertical profiles or cross-sections, where rapid transitions between layers with differing electrical conductivities produce a distinctive 'hat-shaped' signature in SP data. Such configurations are interpreted as indicative of zones with elevated moisture or saturation levels, often linked to areas susceptible to groundwater recharge processes. A characteristic 'hat-shaped' anomaly associated with water infiltration or percolation, as documented by Jardani et al. (2009), Ikard et al. (2012), and also observed in other SP pumping test experiments (Rizzo et al., 2004; Vasconcelos et al., 2014; Titov et al., 2015; Konosavsky et al., 2017).

Those typical shape anomalies are also observed in channels #1, #3, #7, and #8 in Figure 6.6. This shape likely signifies localized variations in electrokinetic processes over a short temporal interval (approximately 2 hours) relative to the 11-hour monitoring period. A long period of transient SP signal is also observed in all other units, and very well evident in channel 1 of unit #4 and both channels of the unit #1. The largest absolute SP value was recorded by unit #2 (20 mV), while the smallest one was recorded by unit #3 (0.5 mV). In general, the daily SP variation is minimal, with a range of less than 6 mV.

Figure 6.7 shows the raw SP curves acquired on the following night, with 11 hours of monitoring. Subtle characteristic variations of anomalies related to electrokinetic processes are observed in channel 1 of units #1, #5, #7, and #8, as well as in channel 2 of units #3, #4, #6, and #8. Once again, similarly to Figure 6.6, unit #2 exhibits the highest absolute SP value (22 mV), while unit #3 has the lowest absolute value (2 mV). In contrast to the SP curves of November 30th, the signals recorded on December 1st appear more stable and linear, with minimal variations.

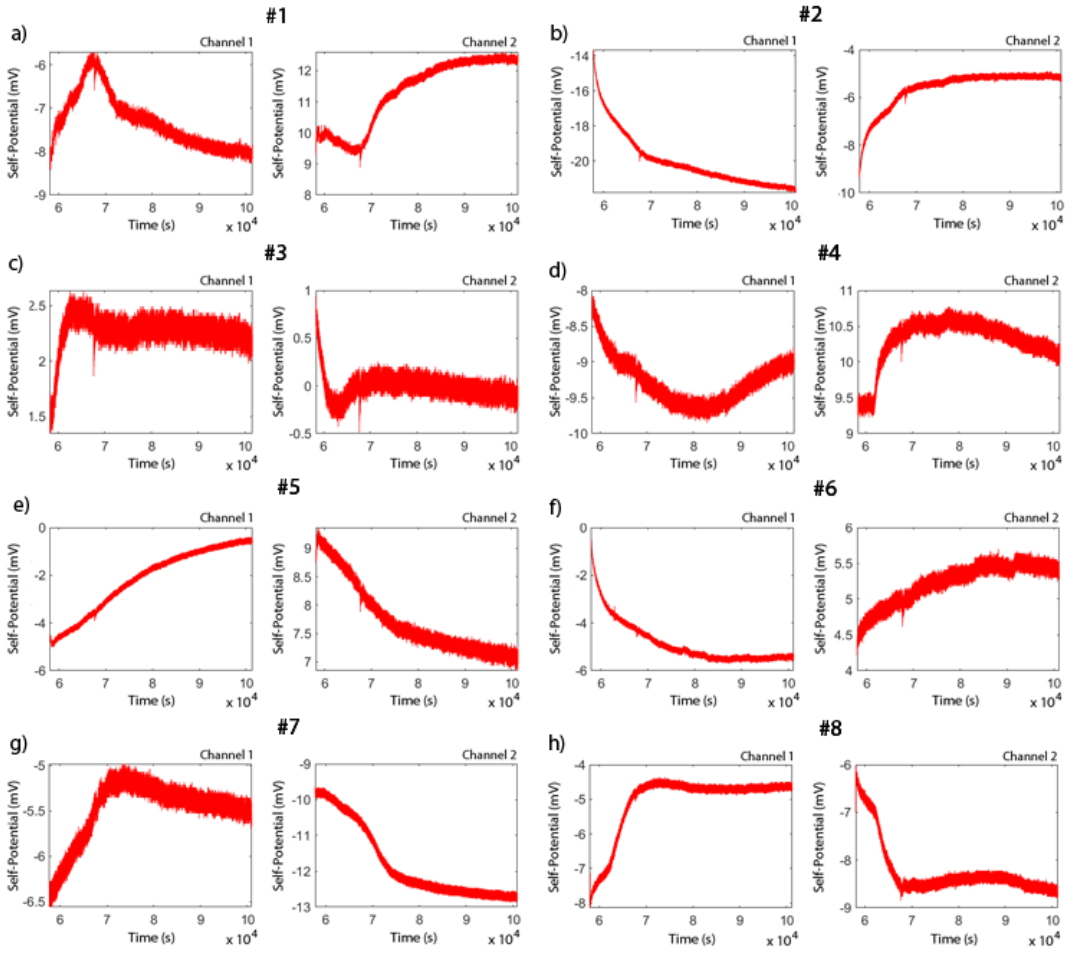

Figure 6.6 - Raw SP curves (30th November 2022), using the Sparse Gradient technique for the V-FullWaver units from #1 to #8.

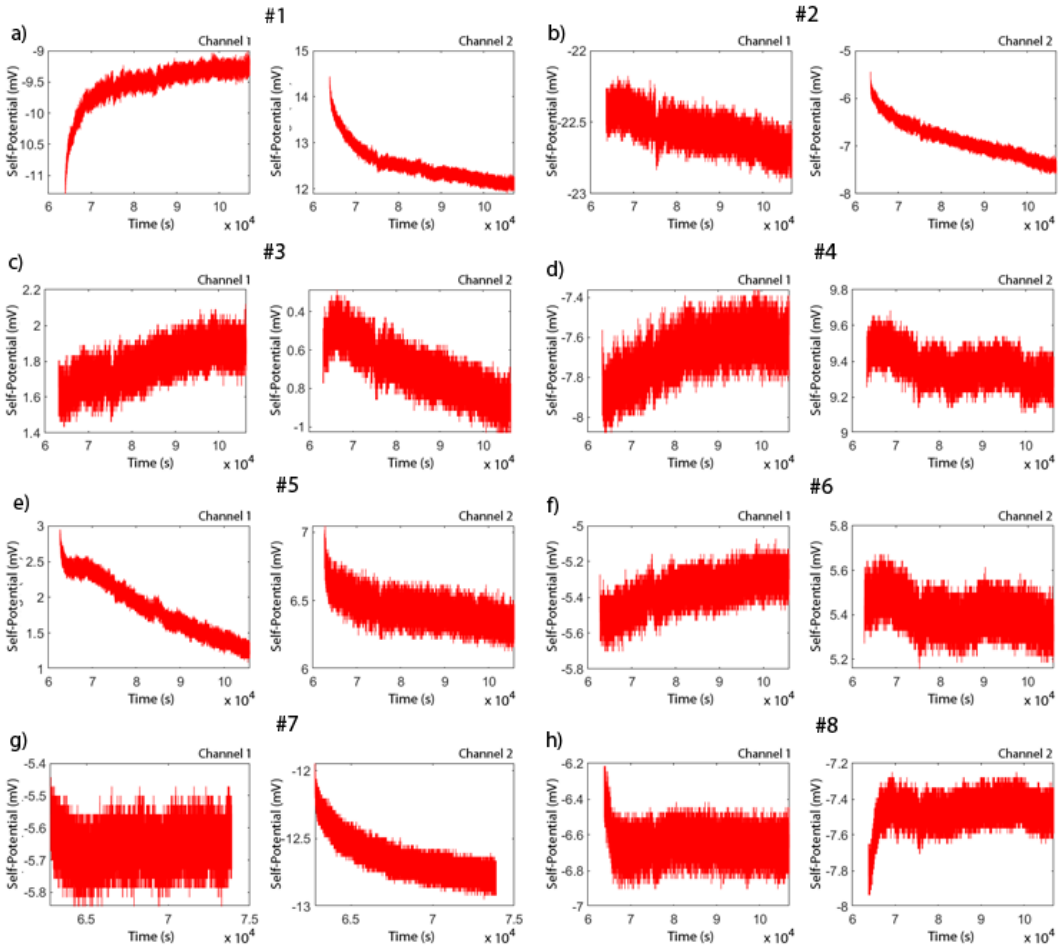

Figure 6.7 - Raw SP curves (1st December 2022), using the Sparse Gradient technique for the V-FullWaver units from #1 to #8.

Figure 6.8 shows the SP monitoring conducted in 2023 compared with the monitoring carried out in 2022, with an average potential sample rate over a 60-second time window, where 6000 SP data points were averaged for every 60 seconds. While the shapes of the curves are quite similar, they differ in amplitude due to higher amplitudes in the year 2023. For example, unit #6 in channel 1 (Figure 6.8j) exhibits an absolute maximum value of 6 mV in 2022 and an absolute value of 14 mV in 2023. The channel 2 of the same unit measured values ranging from 4.6 to 5.6 mV in 2022, and values from 14 to 16.5 mV in 2023.

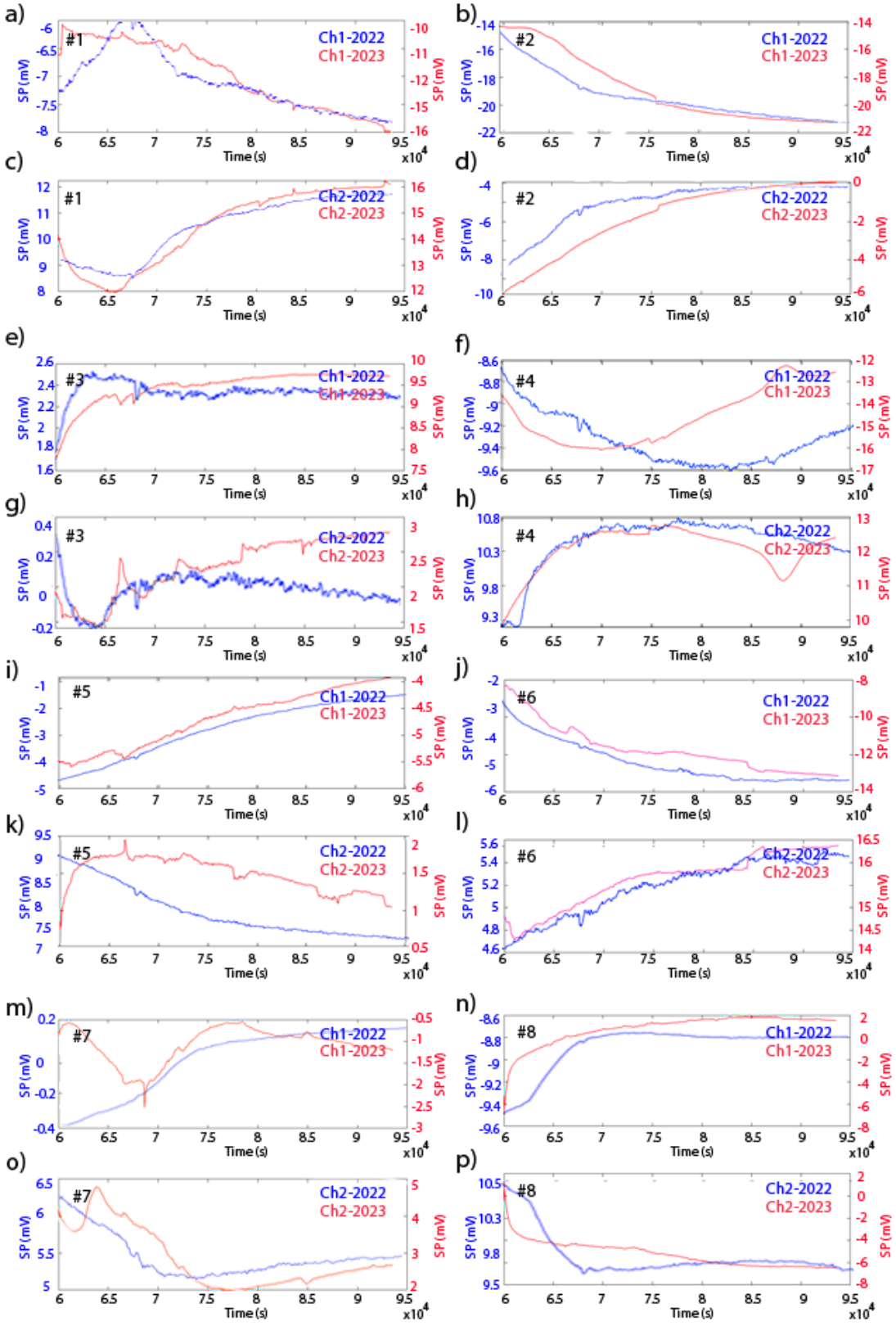

Figure 6.8 - Comparative time-lapse monitoring curves between years 2022 (blue) and 2023 (red).

Features curves of anomalies ("hat shape-like" anomalies) related to electrokinetic processes are well highlighted in Units #1, #3, #4, #7.

Figure 6.9 shows the plots of the raw data of the SP monitoring for three days at 8 PM using the sparse gradient technique. The maps display the values at the midpoint of the electrode couples and show a good repeatability of the measurements. However, the potential differences reflect local and independent variations without a common reference electrode for all of them. When plotting the spatiotemporal variation every 10 min, for instance, anomaly zones can be identified.

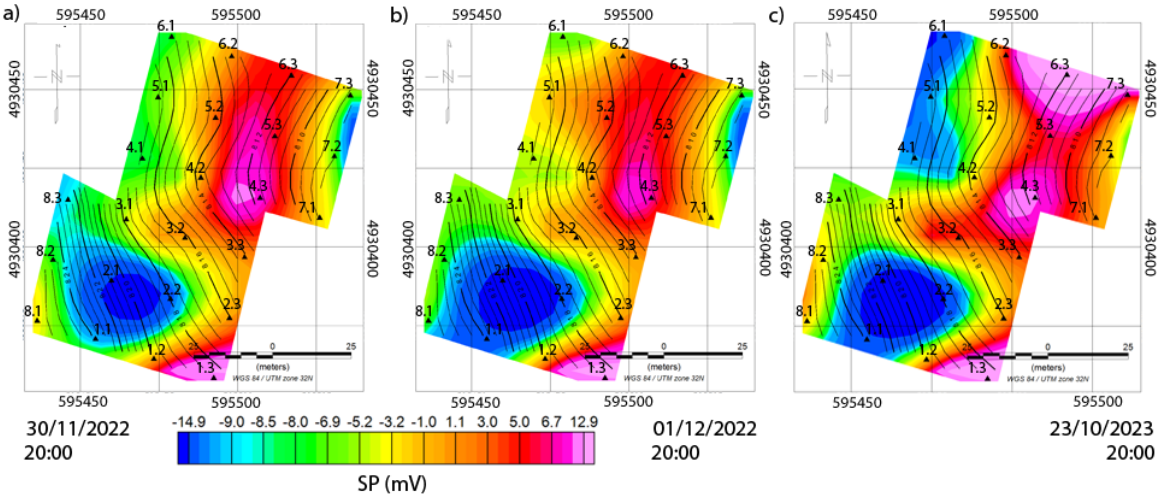

Figure 6.9 - Raw plots of the SP time-lapse monitoring at 8 PM, 30th November 2022 (a); 1st December, 2022 (b); and 23rd October, 2023 (c).

Figure 6.10 shows the raw SP curves using the Fixed-Base technique with an average potential sample rate over a 60-second time window. The position of the common reference electrode #Ref is shown in Figure 6.2a. Channels 1 and 2 provide opposite polarities, as observed in all measurements of Figure 6.10. In absolute values, the SP values range from 40 to 82.5 mV, with a subtle variation of about 2 mV within each curve, except Unit #1 which exhibits a variation of 6 mV for both channels.

Figure 6.11 shows the SP measurements for the central points (see Figure 6.2a) using a V-FullWaver unit, performing one potential measurement at a time with an average sampling rate of about 180 s for stabilized measurements. Again, the signal appears negative due to the use of channel two, which provides inverse polarity. The central point p2.2 yielded the lowest absolute values ranging from 27.5 to 27.6 mV, while the largest variation was observed at the central point p6.2, ranging from 66 to 69 mV. The variations were subtle and stable.

The Fixed-Base time-lapse SP maps can be observed in Figure 6.12. In Figure 6.12a, the reference electrode is positioned at location 8.2, while in Figure 6.12b, it is at position at location #Ref, as depicted in Figure 6.2. To ensure a consistent color scale for plotting, we adjusted the reference electrode in the post-processing phase, adopting the same central point location 8.2 for both maps. After this adjustment, the 2023 Fixed-Base SP measurements values range from -8.6 mV to over 24 mV, while initially were all positive values. Notably, the most negative potential is observed at position 2.1 in Figure 6.12a, whereas it is at position 2.2 in Figure 6.12b. The substantial positive anomaly noted in Figure 6.12b at position 6.3 has shifted to position 7.3 in Figure 6.12a. Nevertheless, the maps agree in delineating a more negative zone in the first half of the area towards the SW, and another more positive zone in the second half towards the NE

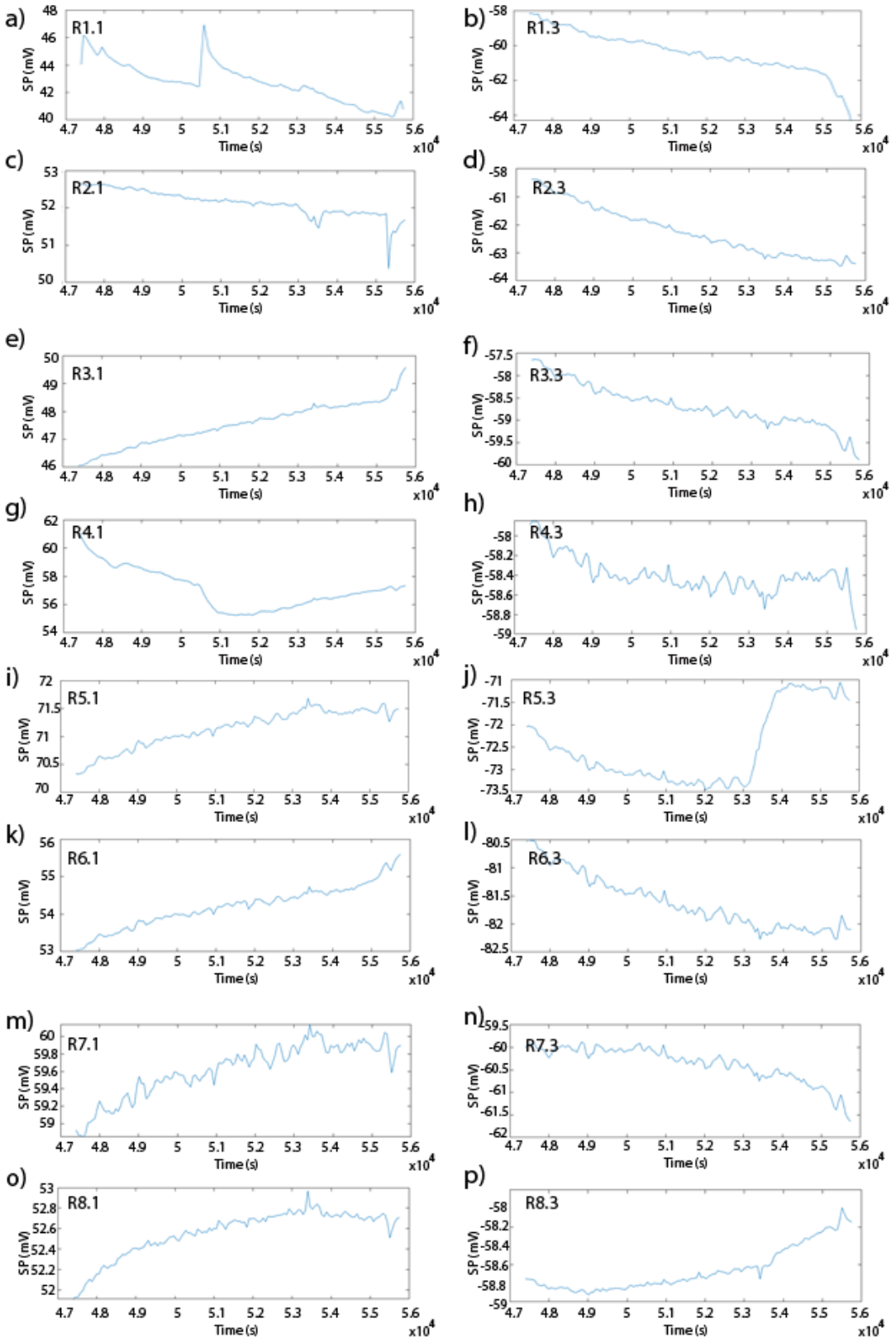

Figure 6.10 – Raw SP curves using the Fixed-Base technique with an average potential sample rate over a 60-second time window.

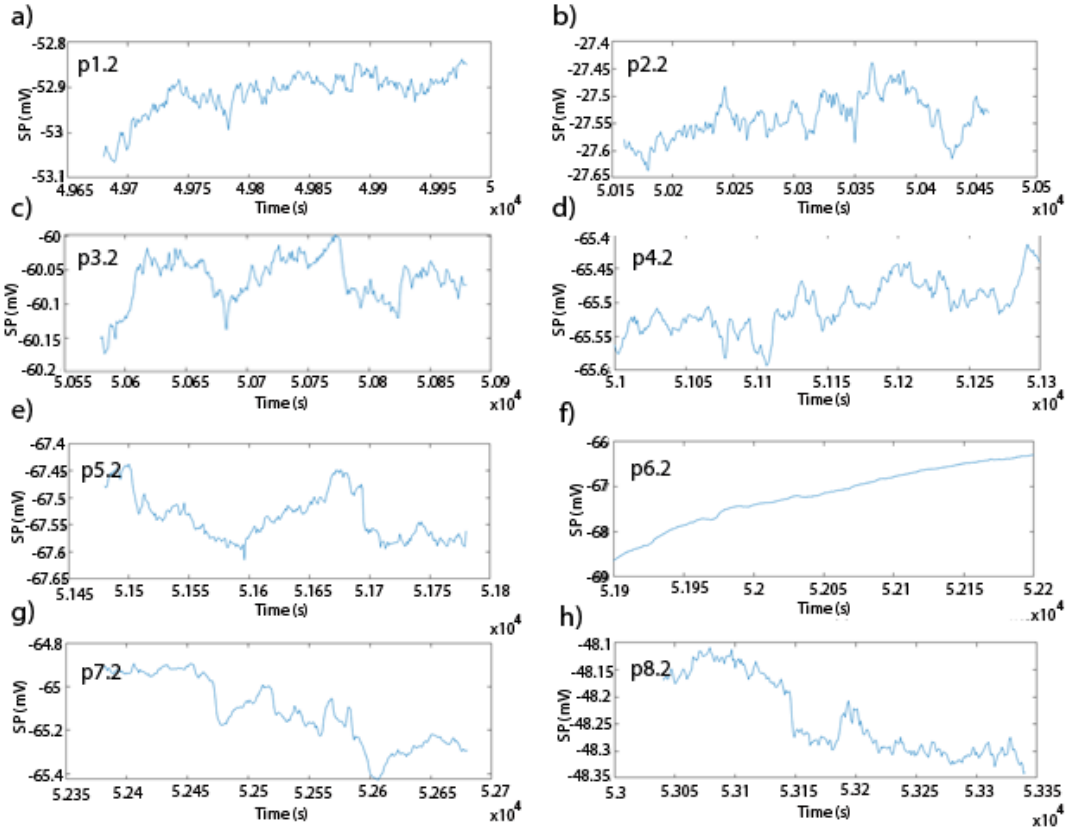

Figure 6.11 – Raw SP curves using the Fixed-Base technique for the central points with an average potential sample rate over a 60-second time window.

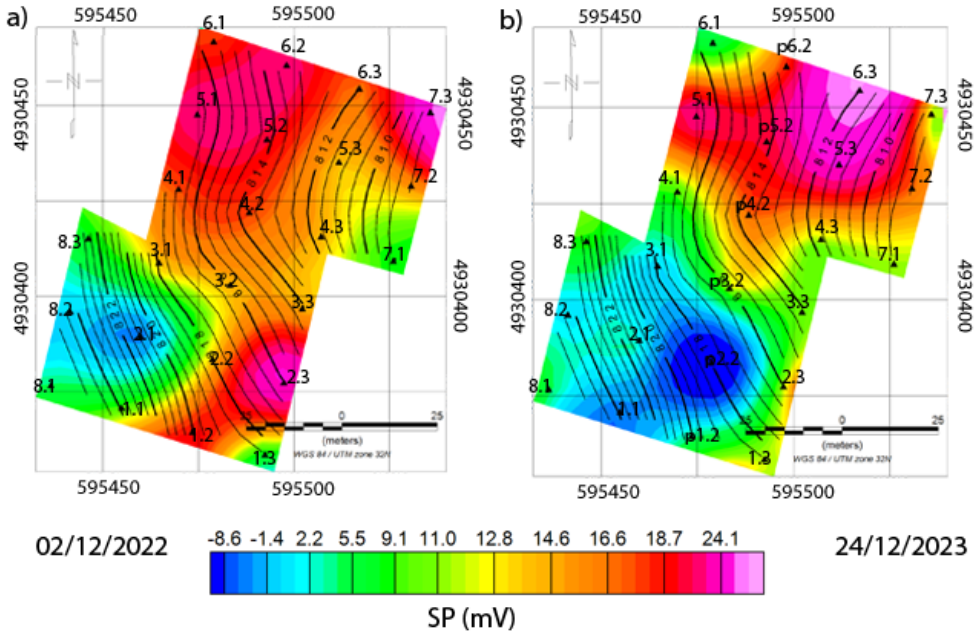

Figure 6.12 - SP Fixed-Base time-lapse monitoring: 2nd December 2022 (a); 24th December, 2023 (b).

Figure 6.13 displays the results of the ASA analysis for the Fixed-Base 2022 (Figure 6.13a), Fixed-Base 2023 (Figure 6.13b), Sparse Gradient 2022 (Figure 6.13c), and Sparse Gradient 2023 (Figure 6.13d) SP techniques. Overall, the results appear similar, with minor differences related to the displacement of anomaly locations represented by peaks or high ASA values. The Sparse Gradient array shows secondary peaks in the central region of the map, not represented by the Fixed-Base arrays. On the other hand, border regions with significant anomalies are present in the 2023 map, but not in the 2022 map. It is worth noting that from 2022 to 2023, the anomalies moved towards the valley.

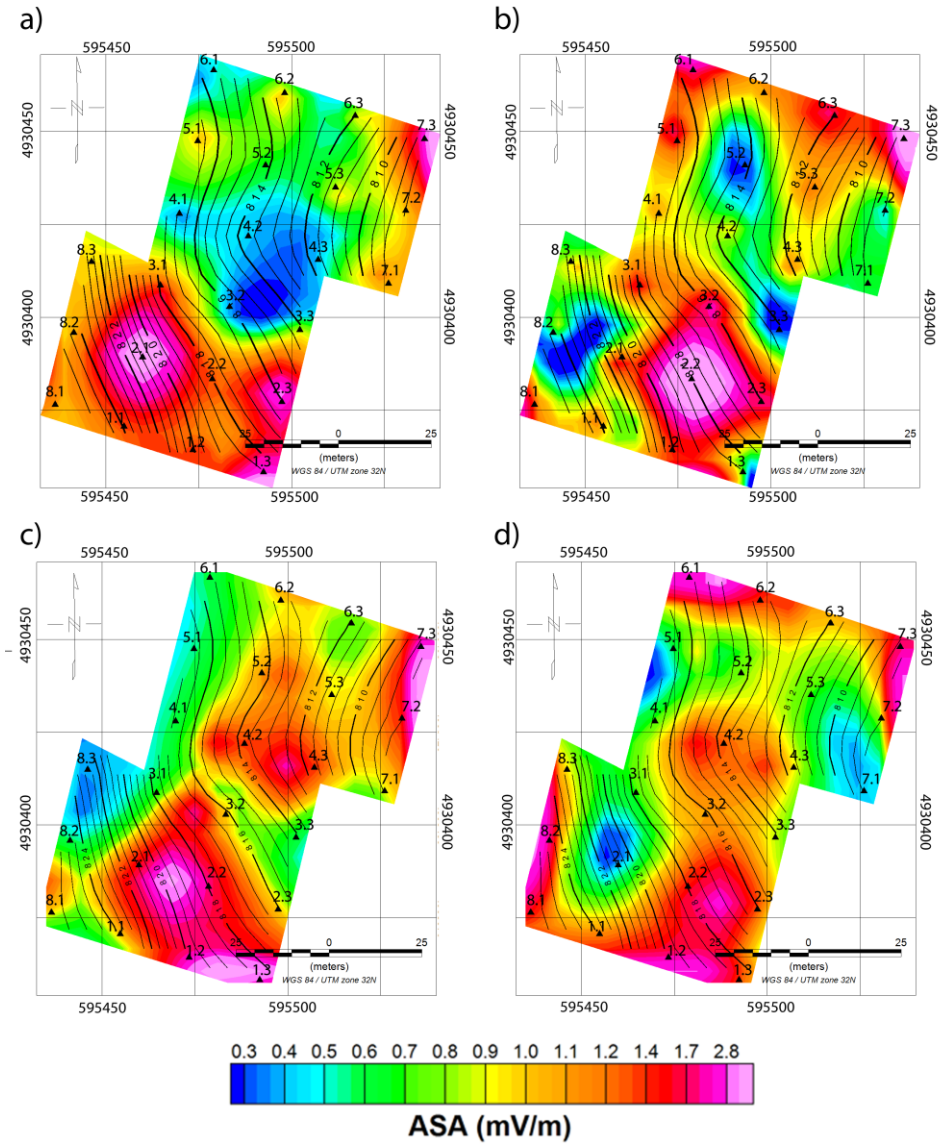

Figure 6.13 – Results of the ASA analysis for different arrays: Fixed-Base 2022 (a); Fixed-Base 2023 (b); Sparse Gradient 2022 (c); Sparse Gradient 2023 (d).

6.6 DISCUSSIONS

This work describes the results of integrated geophysical surveys focused on landslide monitoring in the Tizzano Val Parma region using DERT, IP and SP methods, where a novel approach called Sparse Gradient array has been employed for the latter.

The study area, Tizzano Val Parma, faces hydrogeological instability and recurrent landslides due to geological and geomorphological factors. Hydrogeological instability induces landslides reactivation, leading to severe environmental damages. When reaching critical levels, anomalous water flows can trigger erosion liquefaction, and subsequent landslide reactivation events. The SP monitoring method is deemed effective for identifying anomalous water flows within landslides.

Stratigraphy results from boreholes BH1 and BH2 reveal complex lithology dominated by sandstones, clayey marl, and coarse materials (Figure 6.4).

Although the boreholes are limited to a maximum depth of 25 meters, while the DERT and IP sections extend to a depth of about 200 meters (Figure 6.5), information from the boreholes is essential for understanding the surface dynamics of the landslide. Figure 6.14 shows the interpreted DERT (Figure 6.14 a) and IP (Figure 6.14 b) sections, where the main geological features are inferred from discontinuities observed in the geophysical parameters. A first layer of about 30 meters tick is interpreted as composed by fine and coarse materials (Figure 6.14 b). The first part of both sections, from the beginning on the SW to a distance of about 400 meters, shows low resistivity and high chargeability values, attributable to fine and saturated materials, confirmed by the boreholes BH1 and BH2. In particular, the presence of clayey marls at the bottom of the two boreholes is in according with the low resistivity. The second part of the sections exhibit characteristics attributable to coarse materials with high resistivity and chargeability, leading us to infer that this zone, containing complex lithologies, may also contain disseminated and saturated clays. Three domains labelled as a2b, a1g, and a1 are identified in the sections (Figure 6.14 a), represented in the geological map of Figure 6.14 a complex quiescent landslide by sliding, a complex active landslide, and an active landslide of undetermined type, respectively.

The active landslide evolution is also observed at the edges of the profile. Around unit #10 there is a transition zone between domains a1g and a1 the presence of highly saturated marly clayey in a1g masks the contact response of higher resistivity in the a1 domain. The discontinuity interpreted around unit #14 is quite evident in the resistivity section up to a depth of about 90 meters, while in the IP section it extends until the base of the section. As the domain a1 is an active landslide of undetermined type, these abrupt changes in resistivity and chargeability deserve attention as potential detachment risk zones.

Beneath 100 meters depth, a single homogeneous layer with characteristics of clayey marl material is observed in the resistivity section, while the IP section exhibits high chargeability values in depth starting from a distance of about 600 meters. One possible explanation is that while the first part of the section presents a thick and less chargeable clay package, the second part contains more coarse material with disseminated clay, which has a low resistivity but a higher likelihood of chargeability.

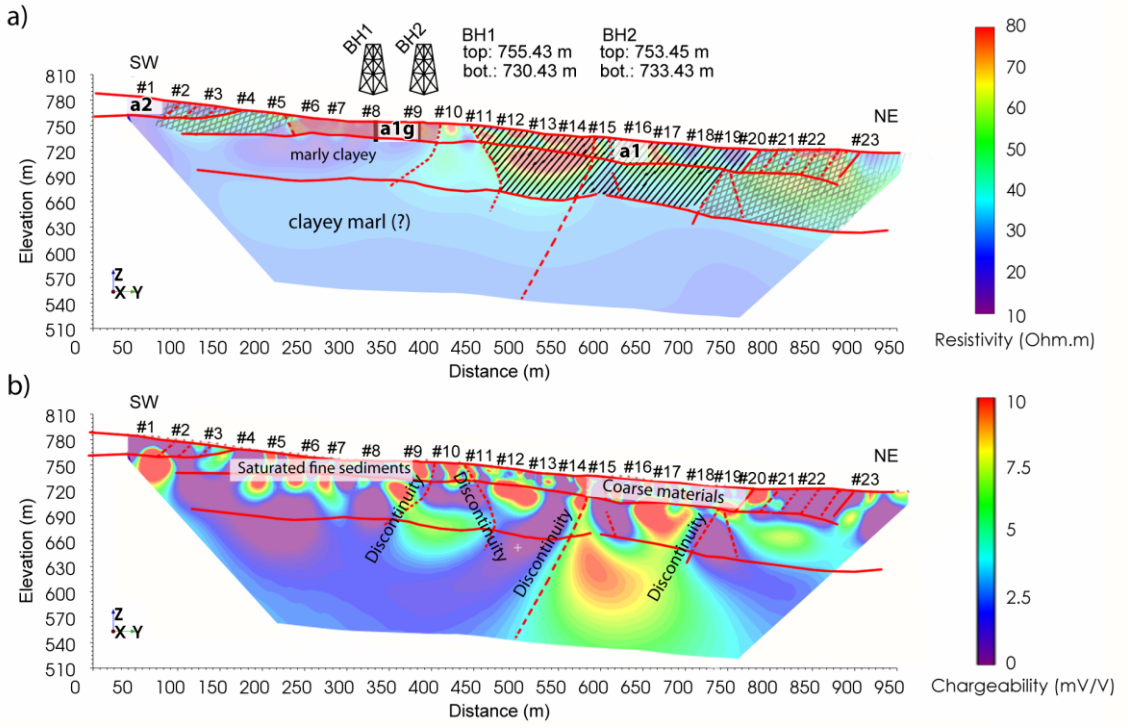

Figure 6.14 - DERT (a) and IP (b) sections versus depth. Three domains are identified in the sections, represented in the geological map of Figure 6.1: a2 is a complex quiescent landslide by sliding, a1g a complex active landslide, the hachured a1 is active landslide of undetermined type.

Analyzing the SP curves obtained with the Sparse Gradient array, typical SP anomalies associated with short-term electrokinetic processes, as well as long-term variations, were observed. The monitoring was conducted from late afternoon throughout the night on different days during years 2022 and 2023. Beyond checking repeatability over time, this dataset allows us to perform a robust time-lapse analysis of transient SP.

Indeed, cyclic processes were observed, even after engineering works involving the reinstallation of interconnected boreholes to divert groundwater flow. Although such transient anomalies were observed in various FullWaver units, unit #2 exhibited one of the highest absolute SP values.

Overall, all V-FullWaver units were able to monitor subtle variations, often associated with percolation and water infiltration processes in the soil, confirmed by visual inspection in the study area during acquisitions carried out in days following rainfall events. The SP variations with the Sparse Gradient array were very stable and accurate, as demonstrated in the plot of Figure 6.9 with similar responses in 2022 and 2023.

On the other hand, the results obtained with the Fixed-Base technique showed some similarities but also significant differences, as presented in Figure 6.12. In 2022, Fixed-Base monitoring showed a negative anomaly at position #2.1 and subtle positive anomalies at the northeast edge of the map, while in 2023, the negative anomaly appeared displaced to position #2.2.

This shift is confirmed by the ASA, displayed in Figure 6.13. Indeed, the primary anomaly source is observed at position #2.1 for the Fixed-Base 2022 (Figure 6.13a) and Sparse-Gradient 2022 (Figure 6.13b), while in 2023, it shifts to position #2.2. This leads us to the hypothesis that the difference in the location of the primary SP anomaly underwent a displacement toward the valley. This suggests that the origin of the anomaly within the landslide is shifting towards the valley, possibly due to engineering interventions altering the internal flow dynamics within the landslide.

Figure 6.15 presents an interpretation of preferential water flow overlaying the Fixed-Base SP map. Secondary flows, represented by the black arrows, also known as typical flow, follow a preferential direction represented by the cyan arrows. Comparing this

with the maps obtained in Figure 6.13, the applicability of using ASA in recognizing primary SP anomaly sources is evident.

Even on the same ASA map, with caution and discretion, it would be possible to infer preferential flows by connecting peak amplitudes. However, the main idea with the use of unconventional SP arrays, through datalogger instruments like the V-FullWaver, lies in the feasibility of recognizing SP anomaly sources, especially regional ones, allowing the delineation of areas of interest for the application of traditional techniques.

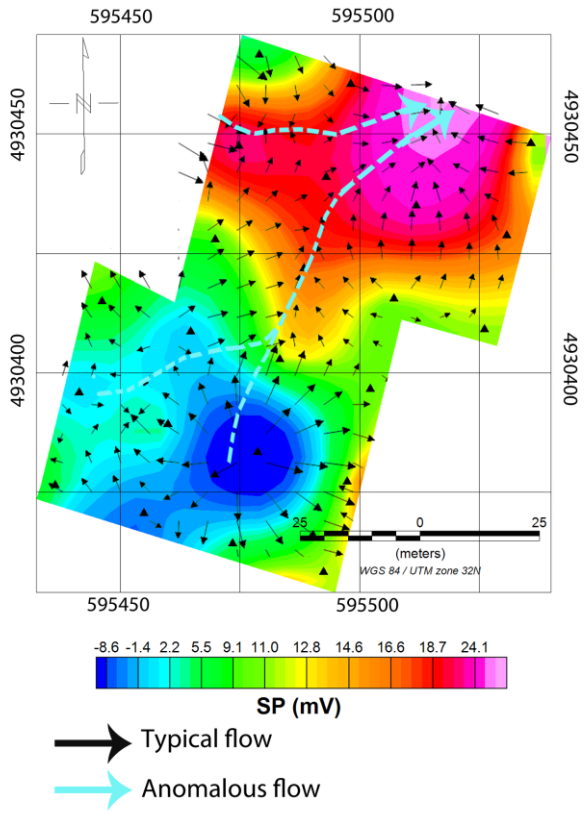

Figure 6.15 - Preferential water flow paths observed on the Fixed-Base SP map.

As the engineering interventions have been carried out on the northern edge of the map in 2023, capturing water that would tend to migrate to the preferential flow zone, continuous monitoring of the anomaly zones indicated by the ASA map deserves attention. Given the validity of the mentioned hypothesis with the gradual displacement of the anomalous zone of the primary source, there is a potential risk of catastrophes during intense rainfall events.

6.7 CONCLUSIONS

The study presents a comprehensive approach to landslide monitoring in Tizzano Val Parma, combining traditional and novel geophysical approaches, including Deep Electrical Resistivity Tomography (DERT), Induced Polarization (IP), and Self-Potential (SP) methods. The results highlight the importance of continuous SP monitoring for early detection of potential landslide hazards in the region. We have emphasized the need for ongoing risk assessment, especially considering the dynamic nature of landslide-prone areas.

Non-conventional SP arrays are not panaceas for the SP method, as it still requires improvements in the quantitative approach. On the other hand, insights are valuable in revealing repeatability and stability in measurements over different years, raising concerns about potential landslide movement, as well as their applicability to risk assessment. The SP monitoring method has proven effective in identifying anomalous flows on landslides, and the use of non-conventional SP arrays has been valuable for primary anomaly reconnaissance.

Integration of DERT-IP results with borehole information provided insights into subsurface characteristic, showing notable geological discontinuities from the surface to the section bottom. It was possible to identify different landslide domains up to a depth of 200 m. The first 30 meters show more complex and diversified lithological structures. Abrupt changes in resistivity and chargeability, identified in the active landslide of undetermined type, suggest potential detachment risk zones. Therefore, techniques such DERT and IP play a central role in understanding and mitigating landslide instabilities. Soil heterogeneity can be characterized by mapping abrupt changes in electrical resistivity and chargeability, locating and following the evolution of potential risk zones over time. These insights are crucial for landslide dynamics evaluation, to plan geotechnical interventions aimed to reduce the damage risks to infrastructure and communities.

Ultimately, the application of these techniques significantly contributes to a more effective approach in managing areas prone to landslides, promoting safety and sustainability in land use planning.

REFERENCES

Beiki, M. (2010). Analytic signals of gravity gradient tensor and their application to estimate source location. *Geophysics*, 75(6), I59-I74. https://doi.org/10.1190/1.3493639

Bellanova, J., Calamita, G., Giocoli, A., Luongo, R., Macchiato, M., Perrone, A., ... & Piscitelli, S. (2018). Electrical resistivity imaging for the characterization of the Montaguto landslide (southern Italy). *Engineering geology*, *243*, 272-281. https://doi.org/10.1016/j.enggeo.2018.07.014

Biswas, A. (2019). Inversion of Amplitude from the 2-D Analytic Signal of Self-Potential Anomalies. *Minerals.* https://doi.org/10.5772/intechopen.79111

Carrier, A., Fischanger, F., Gance, J., Cocchiararo, G., Morelli, G., & Lupi, M. (2019). Deep electrical resistivity tomography for the prospection of low-to medium-enthalpy geothermal resources. *Geophysical journal international*, 219(3), 2056-2072. https://doi.org/10.1093/gji/ggz411

Chen, Y., Dong, W., Ren, H., & Li, X. (2023). Mise-a-la-masse method, tracer tests and cave detection analysis of underground-river karst-conduit distribution and structure: a case study of the Dafengdong conduits in Guizhou Province, China. Hydrogeology Journal, 31(3), 589-600.

Colangelo, G., Lapenna, V., Perrone, A., Piscitelli, S., & Telesca, L. (2006). 2D Self-Potential tomographies for studying groundwater flows in the Varco d'Izzo landslide (Basilicata, southern Italy). *Engineering Geology*, *88*(3-4), 274-286. https://doi.org/10.1016/j.enggeo.2006.09.014

Gallas, J. D. F. (2020). Self-potential (SP) generated by electrokinesis–Efficiency and low cost dam safety. *Journal of Applied Geophysics*, *180*, 104122. https://doi.org/10.1016/j.jappgeo.2020.104122

Gallistl, J., Schrott, L., Otto, J. C., & Dietrich, A. (2018). Applicability of electrical resistivity tomography to study variations in frozen ground conditions at the

Reichenkar rock glacier (Stubai Alps, Austria). Earth Surface Processes and Landforms, 43(12), 2384-2398. https://doi.org/10.1002/esp.4417

Gance, J., Leite, O., Texier, B., Bernard, J. & Truffert, C., (2018). The Fullwaver systems: distributed network of autonomous devices for deep 3D electrical resistivity and induced polarization survey, in EGU General Assembly Conference Abstracts, Vol. 20 of EGU General Assembly Conference Abstracts, p. 12569.

Geostudi Astier (2022). ViewLab3D v.2.3.7. www.geostudiastier.it, Livorno, Italy.

Heinze, T., Limbrock, J. K., Pudasaini, S. P., & Kemna, A. (2019). Relating mass movement with electrical self-potential signals. *Geophysical Journal International*, *216*(1), 55-60. https://doi.org/10.1093/gji/ggy418

Konosavsky, P., Maineult, A., Narbut, M., & Titov, K. (2017). Self-potential response to periodic pumping test: a numerical study. Geophysical Journal International, 210(3), 1901-1908.

Kukemilks, K., & Wagner, J. F. (2021). Detection of preferential water flow by electrical resistivity tomography and self-potential method. *Applied Sciences*, *11*(9), 4224. https://doi.org/10.3390/app11094224

Lapenna, V., & Perrone, A. (2022). Time-lapse electrical resistivity tomography (TL-ERT) for landslide monitoring: Recent advances and future directions. *Applied Sciences*, *12*(3), 1425. https://doi.org/10.3390/app12031425

Li, X. (2006). Understanding 3D analytic signal amplitude. *Geophysics*, 71(2), L13-L16. https://doi.org/10.1190/1.2184367

Nabighian M.N. The analytic signal of two-dimensional magnetic bodies with polygonal cross-section, its properties and use for automated anomaly interpretation. *Geophysics*. 1972; 37:507-517. https://doi.org/10.1190/1.1440276

Orellana, E. (1972). Prospección geoeléctrica en corriente continua (Vol. 1). Madrid: Paraninfo.

Orozco, A. F., Mewes, B., & Lin, Y. (2022). Advances in induced polarization imaging for landslide monitoring: Case studies and methodologies. Journal of Applied Geophysics, 201, 104477. https://doi.org/10.1016/j.jappgeo.2022.104477

Pazzi, V., Morelli, S., & Fanti, R. (2019). A review of the advantages and limitations of geophysical investigations in landslide studies. *International Journal of Geophysics*, *2019*. https://doi.org/10.1155/2019/2983087

Perrone, A., Iannuzzi, A., Lapenna, V., Lorenzo, P., Piscitelli, S., Rizzo, E., & Sdao, F. (2004). High-resolution electrical imaging of the Varco d'Izzo earthflow (southern Italy). *Journal of Applied Geophysics*, *56*(1), 17-29. https://doi.org/10.1016/j.jappgeo.2004.03.004

Perrone, A., Lapenna, V., & Piscitelli, S. (2014). Electrical resistivity tomography technique for landslide investigation: A review. *Earth-Science Reviews*, *135*, 65-82. https://doi.org/10.1016/j.earscirev.2014.04.002

Rizzo, E., Suski, B., Revil, A., Straface, S., & Troisi, S. (2004). Self-potential signals associated with pumping tests experiments. Journal of Geophysical Research: Solid Earth, 109(B10).

Revil, A., & Jardani, A. (2013). The self-potential method: Theory and applications in environmental geosciences. Cambridge University Press.

Revil, A., Karaoulis, M., Johnson, T., & Kemna, A. (2020). Review: Some low-frequency electrical methods for subsurface characterization and monitoring in hydrogeology. Hydrogeology Journal, 28, 1687-1701. https://doi.org/10.1007/s10040-020-02141-8

Roest, W. R., Verhoef, J., & Pilkington, M. (1992). Magnetic interpretation using the 3-D analytic signal. *Geophysics*, 57(1), 116-125. https://doi.org/10.1190/1.1443174

Sastry, R. S., & Mondal, S. (2012). Induced polarization method for the study of geoelectrical properties of rocks and minerals. Journal of Applied Geophysics, 84, 25-34. https://doi.org/10.1016/j.jappgeo.2012.05.005

Sindirgi, P., & Özyalin, Ş. (2019). Estimating the location of a causative body from a self-potential anomaly using 2D and3D normalized full gradient and Euler deconvolution. *Turkish Journal of Earth Sciences*, 28(4), 640-659. https://doi.org/10.3906/yer-1811-14

Sunny, A. A. (2018). Derivatives And Analytic Signals: Improved Techniques for Lithostructural Classification. *Malaysian Journal of Geosciences*, 2(1), 01-08. https://doi.org/10.26480/mjg.01.2018.01.08

Seismic and Soil Geological Service, Emilia-Romagna Region: https://mappegis.regione.emilia-romagna.it/gstatico/documenti/dissesto/pdf/psr/Frane_tav_34039_3_di_3.PDF accessed on January 15, 2024

Titov, K., Konosavsky, P., & Narbut, M. (2015). Pumping test in a layered aquifer: Numerical analysis of self-potential signals. Journal of Applied Geophysics, 123, 188-193.

Vasconcelos, S. S., Mendonça, C. A., & Silva, N. (2014). Self-potential signals from pumping tests in laboratory experiments. Geophysics, 79(6), EN125-EN133.

CHAPTER 7

7. FREQUENCY DOMAIN ELECTROMAGNETIC CALIBRATION FOR IMPROVED DETECTION OF SAND INTRUSIONS IN RIVER EMBANKMENTS

7.1 INTRODUCTION

Levee failures occurring during floods cause severe damages to agriculture, industry, buildings and infrastructures. In the last few years in Europe, as well as in many other regions of the world, have been observed several unexpected events with maxima of rainfall intensity of hundreds of mm in few hours (Jongman et al., 2014). A rainfall peak of more than 250 mm in less than 24 hours was recorded during the recent flood of May 2023 that affected part of the Emilia-Romagna region in northern Italy. More than twenty levee failures were reported during this flood that resulted in a disastrous situation with many casualties and billions of Euros of damages. The social costs of these events, worsened by climate change, could be then very high.

River levees were constructed using a variety of methods and during different times, some structures date back to the mediaeval period. The materials forming the embankment determine the effective protection from floods. Different methods along with different available materials cause the internal composition of embankments to be very heterogeneous as for textures and water content (Huisman et al., 2010). For this reasons levee monitoring represents a great technological challenge. Effective monitoring allows the assessment of the degree of vulnerability and instability of river levees preventing failure.

Integration of geophysical and geotechnical data is vital to fully characterize the inner and deep structure of river embankments. Geotechnical investigation alone could be the better choice in case of well-defined problems when precise and extremely localized data are requested. However, because of its restricted validity, geotechnical testing must be often extrapolated by integrating results from non-invasive indirect methods (e.g., geoelectric and seismic techniques). In addition, geotechnics is time-consuming,

invasive, and expensive compared to geophysical methods (Cosenza et al., 2006). On the other hand, geophysical surveys are non-destructive and they rapidly provide physical information over large areas (e.g., Francese and Santos, 2014). For this reason, indirect methods are the first choice to identify potential critical segments, while geotechnical testing allows for interpretation and validation of geophysical results. The two methods are complementary and their joint application is the best survey choice for mapping levee instability.

Among the available geophysical methods used for levee investigations, the Electrical Resistivity Tomography (ERT) technique is the most popular (Johansson and Dahlin, 1996; Hennig et al., 2005). The seismic method is sometimes used (Karl et al., 2011) to integrate the resistivity models and to infer petrophysical properties of the subsoil (Accaino et al., 2023). The Electro-Magnetic Induction (EMI) technique rapidly delivers information about the subsurface conductivity distribution, by processing and inversion of the recorded EM field components. To our knowledge, the EMI method is probably the fastest geophysical mapping technique (Doll et al., 2014) for surveying long levee segments, while ERT is the most accurate to correlate geophysical results to geotechnical and hydraulic data (Weller et al., 2006; Hen-Jones et al., 2017). However, because of costs and logistics, ERT is suitable to investigate limited levee segments. Although the basic physical principles are different (induction versus galvanic phenomena), under certain assumptions both methods could measure similar electrical conductivity (inverse of resistivity) values. If low-frequency signals ($f < 10^5$ Hz) are adopted and if there are no metallic objects in the subsoil, ERT and EMI methods should theoretically provide comparable results, although ERT is more sensitive to strong resistors and EMI more sensitive to strong conductors.

Among the EMI systems, due to their multi-array arrangement, the DUALEM (DUAL-geometry Electro-Magnetic) and the CMD-Explorer systems are fairly popular (e.g., Monteiro Santos et al., 2010) and particularly effective for the investigation of river levees.

EMI instruments deliver apparent conductivity values that reflect cumulative resistivity distribution over a specific depth range (Lavoué et al., 2010). Inversion of EMI data provides only qualitative values of electrical conductivity because of instrument

calibration difficulties (Lavoué et al., 2010; Minsley et al., 2012). In addition, EMI measurements are very sensitive to different factors, namely: ground coupling, thermal drifts, EM noise, etc. For all these reasons, resistivity fields obtained from ERT and from EM data inversion cannot be directly compared. A reliable quantitative approach requires calibration of EMI measurements. A good calibration approach is based on the simultaneous acquisition of EMI and ERT data (e.g., Lavoué et al., 2010; von Hebel et al., 2019; McLachlan et al., 2021).

We report here about a joint EMI and ERT survey carried out along a levee near Venice, in north-eastern Italy, where the presence of sand boils indicates the occurrence of water seeping underneath and throughout the levee during floods. Aerial image analysis and soil mapping suggested the presence of a large sandy paleochannel. The embankment was built right on top and almost parallel to the sandy paleochannel causing major concerns for the levee stability during floods. ERT was adopted for local imaging of the sand body while multi-array EMI (CMD-Explorer) was used to scan extensively the entire levee segments located above the paleochannel. Being the main target of the survey, the sand body was exploited as a benchmark to validate EMI inversion and assist interpretation. The poor correlation between EMI and ERT, right on top of the sand body, suggested the adoption of a more rigorous approach. A second multi-array EMI, with larger coil spacing (DUALEM 642S), was then tested and results were compared to ERT. Although this second EMI device provided a better subsurface image results were still not satisfactory and we devised a calibration strategy to better constrain EMI inversion.

First, we describe and overview the EMI method and comment on the ERT and EMI responses of the internal levee structure. Secondly, we describe step by step the calibration procedure. Finally, we discuss how this calibration affects EMI data in view of a reliable geophysical imaging of sand intrusions within levees.

7.2 GENERAL SETTINGS

The geophysical survey targeted is a segment of the right levee of the Brenta River, a major river located in the vicinity of the Venice Lagoon (Figure 7.1a and Figure 7.1b). The terrain stratigraphy, down to a depth of about 15 m below the surface, was

reconstructed by means of three boreholes drilled on the levee crest (BH1 and BH2) and on the upper landside berm (BH3). Stratigraphy mainly consists of alternations of clayey silt, sandy silt with silty clay levels of 0.5-1.5 m thick and some layers of sandy silt of 0.15-0.35 m thick. A medium to coarse sand lens (namely the sand intrusion) spans the lower portion of the levee and the underneath layers. This lens, exhibiting a maximum thickness of 8 m, is probably a major unit of the depositional system of a large paleochannel (Figure 7.1c). The levee crest is at approximately 10.8 m above sea level (a.s.l.) while its toe is at about 4.1 m a.s.l. The elevation of the top of the sand intrusion is more or less similar in the three boreholes and it is located at about 2 m a.s.l. In the cohesive levels, the resistance to the pocket penetrometer varies between 35 kPa and 275 kPa and the resistance to the Torvane varies between 13 kPa and 70 kPa. The laboratory tests indicate water content between 21.7% and 26.7%, with liquidity limits W_L between 29.0% and 42.2%, and plasticity index I_P between 4.5% and 21.0%. Triaxial compression test on a sample of loamy sand and clayey silt (taken at 5 m a.s.l.) resulted in undrained shear strength values C from 35 kPa to 40 kPa. The granulometry of a sample of a silty sand with silt showed a percent passing at the 0.075 mm sieve equal to 27.7%. In general, the cohesive layers could be classified as inorganic silts of low compressibility and inorganic clays of low to medium plasticity.

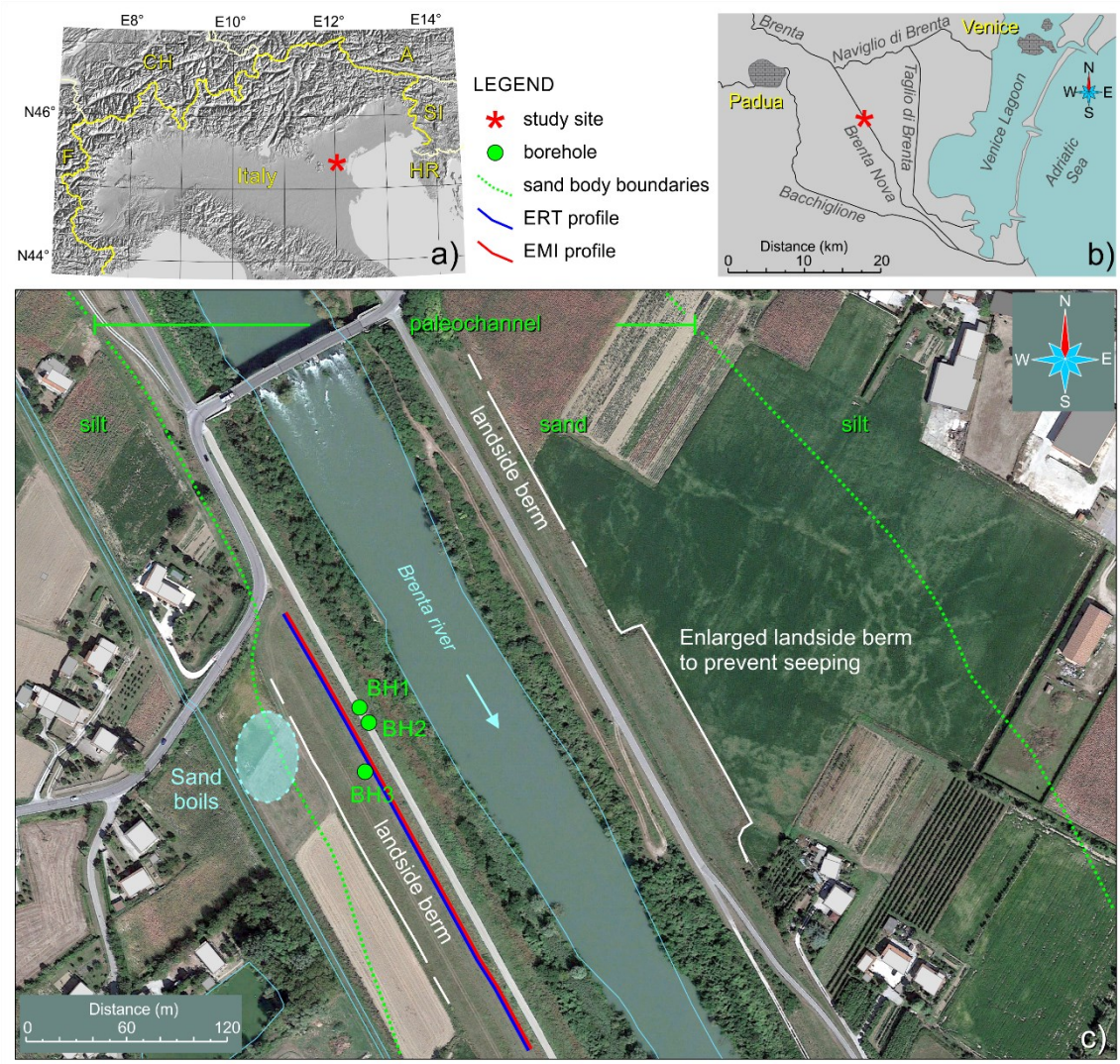

Figure 7.1 - Map of the study area. (a) Location map. (b) Sketch map of the river network showing the artificial fluvial diversion, dating to the 17th century, outside the Venice Lagoon. (c) Satellite image (map data: Google, 2019) of the Brenta River with the geophysical profiles (ERT and EMI in blue and red solid lines, respectively), the boreholes, and the pattern of the sandy paleochannel outlined.

7.3 ELECTRO-MAGNETIC INDUCTION – BASIC CONCEPTS

The EMI technique aims to reconstruct the electrical conductivity of the subsurface by measuring the magnetic fields using pairs of small coils on the surface. In general, the electrical conductivity σ (the reciprocal of resistivity) of ordinary soils is weakly dependent on frequency for $f < 10^5$ Hz. When working with ERT, the distribution of σ at the zero frequency limit is obtained. Let us consider an EM field generated by an alternating current in a small loop. The EM induction effect, encoded in Maxwell's first-

order differential equations, produces eddy currents in the ground, which in turn induce secondary EM fields. At a low frequency ($f < 10^5$ Hz, quasi-static regime) and in the absence of metallic objects in the ground, the displacement currents are much smaller than the conduction currents, and the complex wave number can be approximated as $k \approx \sqrt{-i\mu\sigma\omega}$, where $\omega = 2\pi f$ and μ is the magnetic permeability of the vacuum $\mu_0 = 4\pi 10^{-7}$ H/m ($\mu \approx \mu_0$ for most materials in the subsurface). Under the above conditions σ can be determined from the measured magnetic fields at the surface by considering μ as a constant. Moreover, the conductivity fields determined by the two considered techniques, ERT and EMI, must be similar.

7.3.1 Loop configurations

Typical source-receiver coil orientations in EMI instruments (Figure 7.2) are Horizontal Coplanar loops - HCP (or Vertical Magnetic Dipole -VMD) configuration where both transmitter and receiver coils are oriented horizontally; Perpendicular loops (PRP) where the transmitter coil is oriented horizontally and the receiver coil is oriented vertically; Vertical Coplanar loops - VCP (or Horizontal Magnetic Dipole - HMD) configuration where both transmitter and receiver coils are oriented vertically; Vertical Coaxial loops (VCX) where both transmitter and receiver coils are oriented vertically and the magnetic dipoles are coaxial. The VCX configuration was not considered in this work.

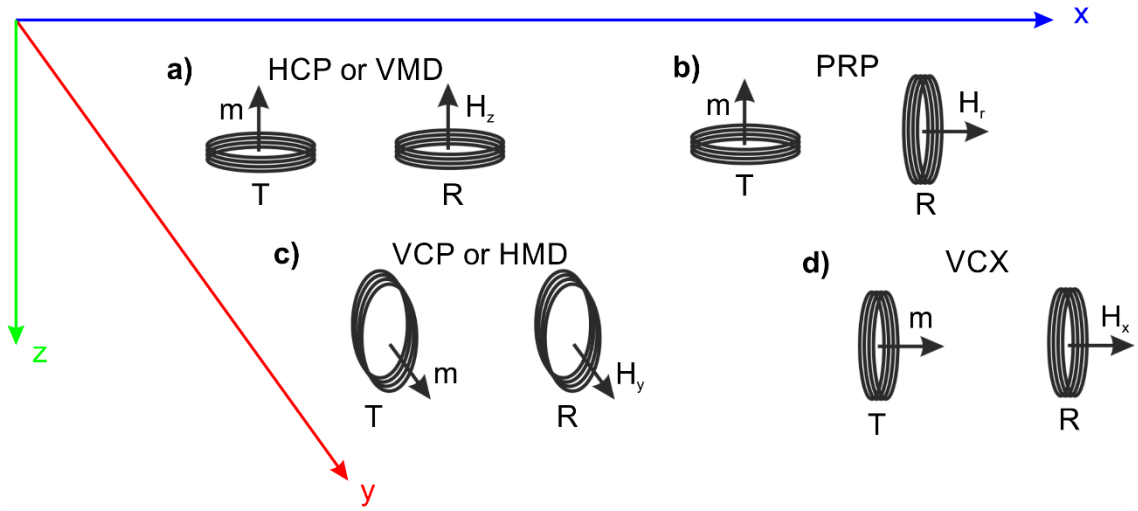

Figure 7.2 - Transmitter (T) and receiver (R) coil configurations of a general EMI instrumentation, where m is the magnetic moment of the transmitter loop: (a) horizontal coplanar loops, or vertical magnetic dipole (HCP, VMD); (b) perpendicular loops (PRP); (c) vertical coplanar loops, or horizontal magnetic dipole (VCP, HMD); (d) vertical coaxial loops (VCX). The measured magnetic field at the receiver coil is indicated by Hz , Hr , Hy , and Hx, respectively.

7.3.2 Induction number and apparent conductivity

Considering two small loops over an inhomogeneous half-space: an alternating current in the transmitter loop emits a primary magnetic field H_p, which is defined as the field in the absence of the half-space (i.e., as if the coils were in free space). The measured magnetic fields at the receiver coils are: the vertical H_z, the radial H_r and the horizontal H_y components in the HCP (or VMD), PRP and VCP (or HMD) configurations, respectively (Figure 2.2). The induction number is defined as $B = d/D$, where $d = \sqrt{2/\omega\mu\sigma}$ is the skin depth and D is the source-receiver distance (offset).

In a layered subsurface, the electrical conductivity of the equivalent homogeneous medium is defined as the apparent conductivity σ_a. At low induction numbers (LIN), $B \ll 1$, McNeill (1980, eq. (6) of the appendix) obtained the following approximation for the apparent electrical conductivity:

$$\sigma_a = A \cdot Im\left(\frac{H_s}{H_p}\right), \qquad A = \frac{4}{\omega\mu D^2} \tag{7.1}$$

where the measured magnetic field H_s can be H_z, H_r or H_y, respectively. The primary magnetic field H_p depends on the orientation of the transmitter coil. Most field EMI experiments for soil exploration take place at the LIN approximation conditions. Commercial EMI equipment for these applications generally uses equation (7.1) to convert measured magnetic field components in the form of apparent conductivity. As we will show in this work, the concept of apparent conductivity can be used to calibrate EMI data.

7.3.3 Sensitivity and depth of investigation

Considering a subsurface discretized with N layers, where the N^{th} layer is of infinite extent and the vertical coordinate is z. The LIN approximation is equivalent to assume that the frequency is low ($f < 10^5$ Hz, quasi-static regime), and that the current flow at any point is independent of the current flow at any other point since the magnetic coupling between all induced current loops is negligible (McNeill, 1980). Therefore, the secondary magnetic field H_s measured at the receiver can be expressed as the sum of the independent fields from each individual current loop induced in the ground (Wait, 1962; 1982). Under these assumptions, it is possible to show that the response of a layered medium can be approximated as:

$$\left(\frac{H_s}{H_p}\right)_G = 1 + \frac{i}{A}\sum_{j=1}^{N} \sigma_j \left(R_G(z_{j-1}) - R_G(z_j)\right) \tag{7.2}$$

(e.g., McNeill, 1980), where the coefficients R_G are geometric factors (also called EMI cumulative response coefficients), which depend upon the coil configuration G. HCP (VMD), PRP and VCP (HMD) coil configurations were considered for implementing and testing the calibration procedure. Their geometric factors have the following expressions:

$$R_{HCP} = \frac{1}{\sqrt{1+4\xi^2}}, \quad R_{PRP} = 1 - 2\xi R_{HCP}, \quad R_{VCP} = \frac{1}{R_{HCP}} - 2\xi, \tag{7.3}$$

(McNeill, 1980; Fitterman and Labson, 2005), where $\xi = z/D$. The sensitivity of a coil configuration depends on the offset and on the depth of investigation (DOI), i.e., it represents the differential response of the dipole for a particular value of ξ. An estimation of the sensitivity can be obtained under the LIN assumption by simply differentiating the geometric factors (7.3) with respect to ξ. Figure 7.3a shows the normalized sensitivity of the considered dipole configurations.

The VCP (HMD) and PRP arrays show a high sensitivity to the near surface materials, and it drops to 1/10 of the maximum value for $z \approx D$. On the other hand, the HCP (VMD) array shows low sensitivity to the near surface materials, but it increases to the maximum value for $\xi = 0.3$. Then, the sensitivity does not drop to 1/10 of the maximum value until $z < 2.5D$. Thus, the HCP geometry shows a DOI larger than the DOI of the other arrays. By employing HCP (VMD), PRP and VCP (HMD) array geometry, DUALEM-642S and CMD-Explorer ensure a high sensitivity in the near surface and at larger depths.

Under the LIN assumption, the maximum DOI depends only on the offset and not on the frequency or σ (Kaufman and Keller, 1983). The effective DOI is defined as the depth to which a coil configuration accumulates 70% of its total sensitivity. Figure 2.3b shows the cumulative sensitivity of the considered dipole configurations. The sensitivity of PRP and VCP (HMD) arrays accumulates rapidly with depth, while the sensitivity of an HCP (VMD) array accumulates more gradually. The maximum DOI is about $D/2$ for PRP and $2D/3$ for VCP (HMD) arrays, while it increases to about $3D/2$ for the HCP (VMD) array.

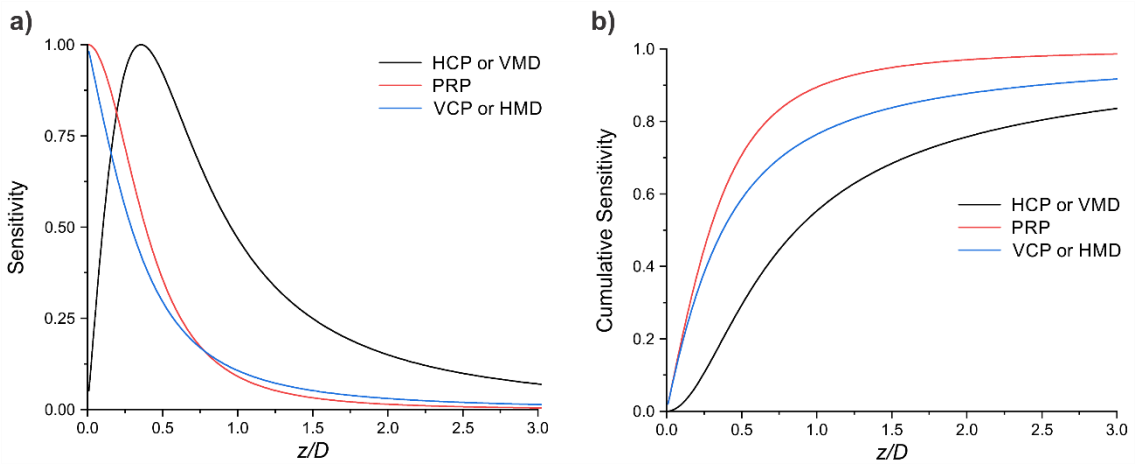

Figure 7.3 - (a) Normalized sensitivity and (b) cumulative sensitivity of the considered dipole geometries under the LIN assumption. The cumulative sensitivity of a coil configuration corresponds to its geometric factor R_G , while the differential response is computed as the normalized derivative (i.e., as $dR_G/d\xi$).

This method is effective in environments with moderate resistance. However, in structures with high conductivity, the instrument response deviates from linearity due to the invalidity of the LIN approximation. As a result, utilizing the cumulative function leads to the generation of biased models. In this case sensitivity and maximum DOI depend also on conductivity and frequency (e.g., Christiansen and Auken, 2012; Baasch et al., 2015).

7.4 DATA ACQUISTION AND PROCESSING

We acquired one ERT line, and two EMI profiles, with different EM induction instruments, on the same transect (Figure 7.1).

The ERT line was collected using a 48-electrode IRIS SYSCAL Pro georesistivimeter (IRIS Instruments, 2001) and using the Wenner Alpha and the Pole-Dipole configurations. Electrode spacing was set to 2 m and a roll-along scheme was adopted resulting in a profile length of 286 m and in a maximum nominal DOI of about 30 m. The ERT dataset is comprised of 6720 measurements. Particular attention was devoted to the coupling of the electrodes with the ground. Each electrode was watered using a brine to reduce the contact resistance and improve data quality. Contact resistance check was performed before every session of data acquisition. Measured resistance,

after watering, was less than 1.5 kOhm for all adjacent electrode couples, indicating good operational conditions.

The first EMI profile was collected using the CMD-Explorer (GF Instruments, 2011), consisting of a transmitter coil and a single receiver coil, placed at different distances from the transmitter coil, typically 1.5, 2.8, and 4.5 m. The transmitter-receiver coil configurations can be set to VMD or to HMD geometry, respectively. The CMD-Explorer operates at a frequency of 10 kHz, providing three simultaneous conductivity-sounding depths and a reference theoretical maximum DOI of about 6.7 m.

The second EMI profile was collected with the DUALEM-642S (DUALEM Inc, 2008), consisting of a transmitter coil and two closely spaced receiver coils (i.e., dual coils) placed at different distances from the transmitter coil, typically 2, 4 and 6 m. The dual coil configurations (also called modes) are HCP and PRP. The DUALEM-642S technology operates at a frequency of 9 kHz, providing six simultaneous conductivity-sounding depths and a reference theoretical maximum DOI of about 9 m.

The length of the EMI profiles was about 180 m, and a 2 s sampling rate was adopted. The average measurement spacing is 1.8 m for DUALEM and 1.1 m for CMD-Explorer. The equipment was hosted on a non-magnetic cart in order to avoid interferences and keep the sensors at a constant height of 0.5 m with respect to the ground surface.

7.4.1 Electrical Resistivity Tomography

Resistivity measures were quality controlled prior to perform the inversion. Approximately 0.37% of the quadrupoles were removed using the following criteria: removal of the reciprocal measurements; elimination of data with instrumental standard deviation (obtained through multiple measurement stacks) larger than 10%; removal of the receiver potentials lower (in absolute value) than 0.01 mV and filtering out of negative apparent resistivity values. The average injected current was 340 mA, while the average apparent resistivity was about 40 Ohm.m, which is a quite low value, reflecting the fact that the levee is mainly composed by clayey silt and silty clay materials partially saturated by water. Filtered data were inverted using the ERTLab-3D Studio processing package (e.g., Accaino et al., 2023).

The three-dimensional inversion parameters were the following:

- mesh size in the x, y, and z directions: 1 m, equal to half electrode spacing;

- noise level of 1%.

Initial homogeneous resistivity was set equal to the average apparent resistivity value. The inversion converged after a maximum of 8 iterations, when the χ^2 equals the number of measurements of the whole dataset.

7.4.2 EM modeling and data inversion

EM4Soil is a software package (EMTOMO, 2013) developed to perform forward EM modeling and to invert EM induction measurements using a 2-D smoothness constraint approach (Monteiro Santos, 2004). As described in details by Monteiro Santos et al., (2010), the algorithm can either derive the Full-Solution of the EM induced field in a layered earth, or an approximated solution using the cumulative function approach. When dealing with structures exhibiting moderate to high conductivity, the instrument response becomes non-linear, and using the cumulative function approach may introduce bias to the models, i.e., the resistivity of deeper layers is underestimated if covered by highly conductive layers. Because the studied levee presents quite low-resistivity layers and the latter approach is only valid for fairly resistive environments, forward modeling (and the inversion) was computed using the Full-Solution. Further details about improvements in EM inversion in case of highly-conductivity layers could be found in Triantafilis and Santos (2013) and in Huang et al., (2016; 2017).

A moving average filter was applied to improve the signal-to-noise ratio of the time/space sequences. The window size was set to 5 samples to smooth out the few high-frequency peaks present in the data. No additional data processing was required. Inversion parameters were a damping factor of 0.07 and a noise level of 1%. The same initial conductivity of 20 mS/m (the average apparent conductivity) was used for both instruments. The bottom of the model depends on the maximum DOI, i.e., 9 m for the DUALEM and 6.7 m for the CMD-Explorer. Therefore, to have a similar vertical resolution, the model was uniformly discretized with 8 layers for the former and with 7 layers for the latter, respectively. The thicknesses of the layers are free to change during inversion.

Inversion of EMI data was carried out using many different homogeneous starting models. The same initial conductivity was adopted for both instruments. These inversions lead to very similar results. Among the various outcomes, we selected the tomographic models showing the lowest root mean square error (RMSE), which corresponds to homogeneous starting models with conductivity equal to the average apparent conductivity of 20 mS/m. The inversion was performed simultaneously, for all the sensor configurations, and converged after 10 iterations.

7.5 RESULTS AND CALIBRATION PROCEDURE

The ERT resistivity model was used to calibrate EMI data. Figure 7.4 shows the tomographic resistivity model, down to a depth of 27 m below the surface, along with the geotechnical logs of the three boreholes (BH1, BH2 and BH3). A prominent resistive layer, in the elevation range from 7.5 m a.s.l. to 5.0 m a.s.l., is visible below some near-surface heterogeneities and it is comprised of sand and sandy silt. Two conductive zones (15-40 Ohm.m) are observed in the elevation ranges from 5.0 m a.s.l. to 2.5 m a.s.l. and from –5.0 m a.s.l. to -21.5 m a.s.l. A deep anomalous resistive zone (with resistivity ranging from 60 Ohm.m to 120 Ohm.m) is visible between 2.5 m a.s.l. and -5 m a.s.l., located at horizontal distances between 30 m and 120 m. This resistive zone clearly correlates to the geotechnical logs evidencing the presence of a sand body in the same depth range, as displayed in Figure 2.4. EMI data calibration was thus undertaken using the ERT response of the prominent resistive layer (black dashed rectangle in Figure 7.4) avoiding the sides of the resistivity model affected by higher uncertainty.

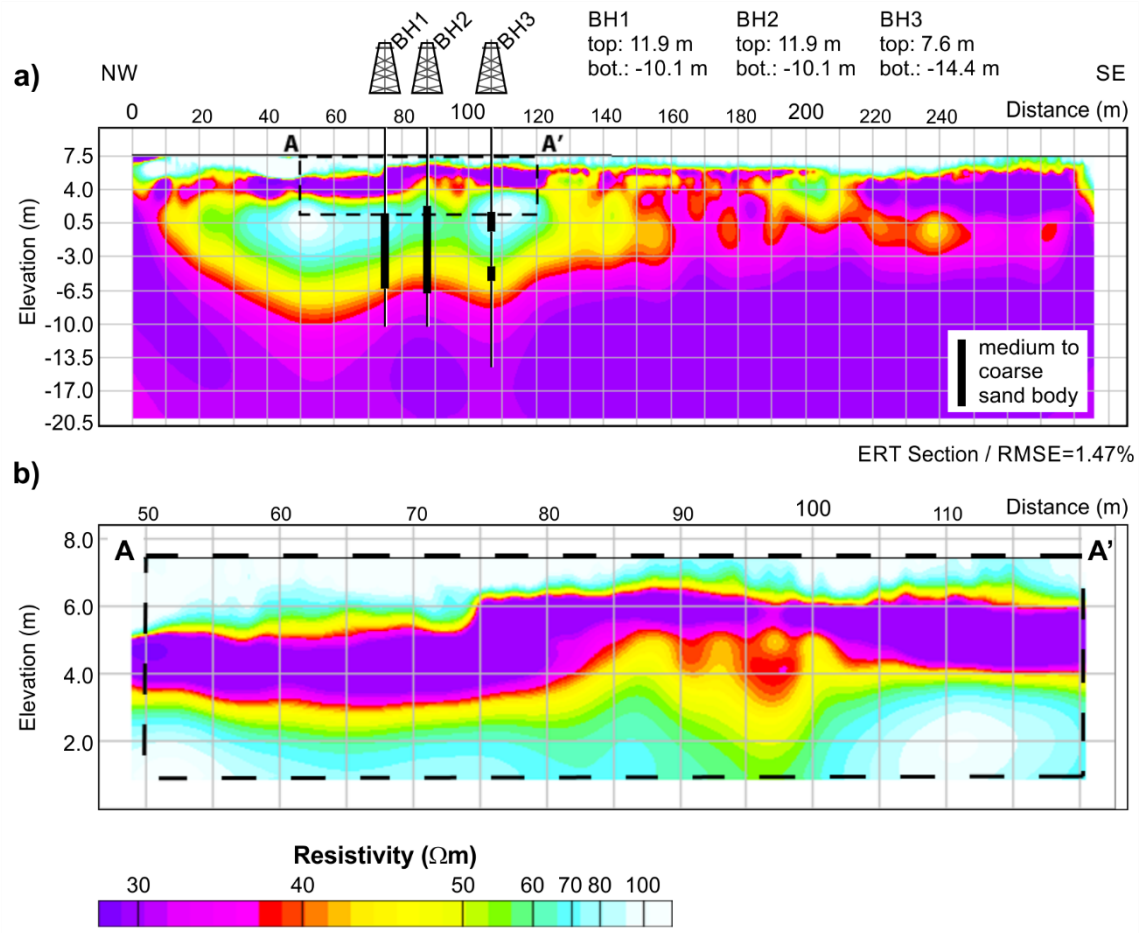

Figure 7.4 - (a) Resistivity section from ERT data with superimposed borehole stratigraphy. The RMSE is equal to 1.47%. The black dashed rectangle corresponds to (b) the portion of the resistivity model selected for EM data calibration.

Inversion of EMI data was carried out as previously described. Figure 7.5 shows the results of DUALEM-642S and CMD-Explorer inversions. A quantitative comparison between ERT and EMI suggests that EM inverted models are shifted towards higher resistivity for the CMD-Explorer (Figure 7.5a), and towards lower resistivity for the DUALEM-642S (Figure 7.5b). Moreover, the CMD-Explorer, because of the reduced spacing, has a limited maximum DOI (6.7 m) compared to the DUALEM–642S (9 m). In other words, the secondary EM field generated in the resistive layer could not be detected by the receiver at largest offset of the CMD-Explorer. It is a geometry issue, the shorter offsets of the CMD-Explorer compared to the DUALEM–642S result in a consistent decrease of sensitivity versus depth. Another reason making the detection of

the deep resistive layer particularly challenging is the masking effect of the overlying conductive layer (less than 35 Ohm.m), between 4 m a.s.l. and 6 m a.s.l., which limits the EM field penetration. This hiding effect could be observed also for the DUALEM–642S but the lower decrease of sensitivity versus depth (see Figure 7.3) guarantees a maximum DOI of around 9 m (Figure 7.5b).

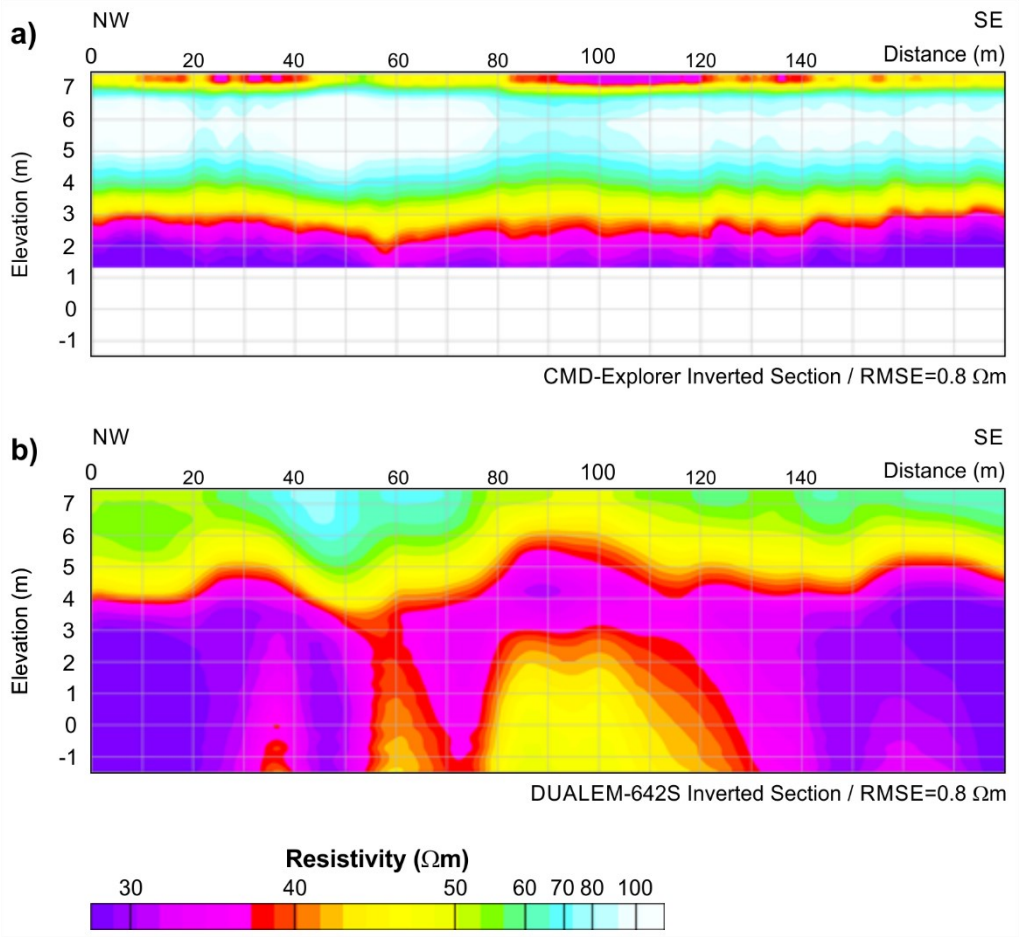

Figure 7.5 - Electromagnetic inverted sections: (a) CMD-Explorer and (b) DUALEM–642S. The RMSE is 0.8 Ωm for both inversions.

The cumulative function algorithm for highly conductive structures produces biased models, underestimating the resistivity of deeper layers covered by conductive layers. In the current case the inverted resistivity of the deeper zones seems to be underestimated and non-calibrated despite the Full-Solution algorithm was preferred to the cumulative function approach.

CMD-Explorer inversion (Figure 7.5a) shows a high resistive layer (>80 □.m) ranging from the elevation of 7 m a.s.l. to the elevation of 4 m a.s.l., while DUALEM-642S inversion (Figure 7.5b) shows the same layer with resistivity of 45 Ohm.m and also an anomalous resistive zone (45 Ohm.m) in the mid portion of the profile just below 3 m a.s.l.

The selected portion of the ERT resistivity section (black dashed rectangle in Figure 7.4) was imported into the EM4Soil package, to derive a synthetic model of apparent conductivity for each EMI system. This procedure consists in performing forward modeling, i.e., an EMI data acquisition is simulated, Calibrations of EMI measurements are obtained by comparing, in terms of Pearson's correlation coefficients (e.g., Kai-Feng et al., 2020), the synthetic apparent conductivity values with the corresponding experimental ones, i.e., those resulting from equation (7.1) and the measured magnetic fields. The calibration procedure is schematized in Figure 7.6.

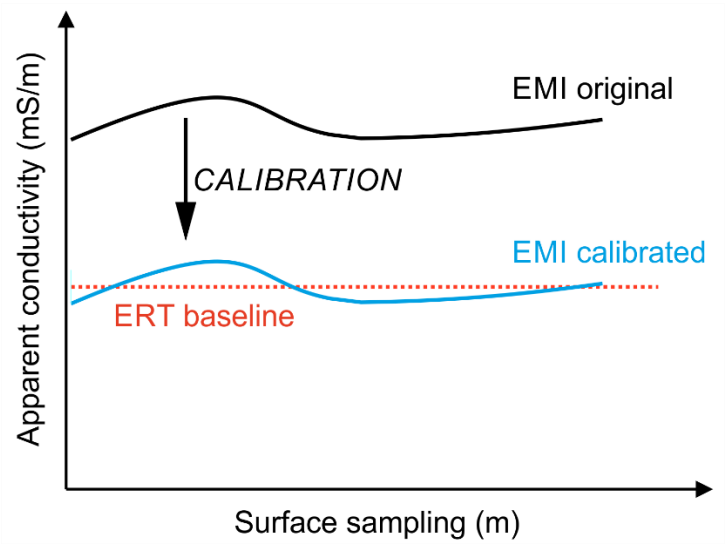

Figure 7.6 - Scheme of the calibration procedure based on the best fitting of an experimental apparent conductivity curve over a synthetic baseline obtained via EM modeling of ERT data.

Figure 7.7 shows a comparison between the synthetic apparent conductivity data and the corresponding measured data, for both the DUALEM–642S and the CMD-Explorer. A qualitative analysis of Figure 7.7 shows consistency in the shapes of the calculated and measured curves. Table 7.1 shows the quantitative analysis in terms of Pearson's

correlation coefficients. In this case, the PRP responses from the DUALEM–642S show higher correlations than those corresponding to the HCP configuration. Similarly, the HMD responses from CMD-Explorer show a better correlation than the VMD. However, the HMD modes show limited cumulative responses and a poor vertical resolution respect to VMD modes. In fact, while the synthetic curves are well separated, the experimental curves corresponding to the HMD modes for the different offsets are very close to each other. This effect might be due to instrumental calibration problems. In contrast, the VMD modes could better resolve different layers. For all configurations, correlation decreases as coil spacing (offset) increases.

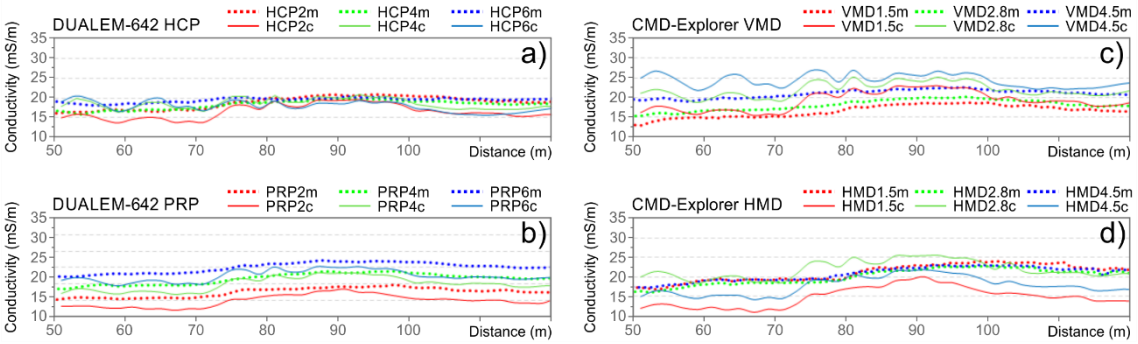

Figure 7.7 - Comparison between the modeled apparent conductivities and the experimental apparent conductivities, measured by (a) and (b) the DUALEM–642S and (c) and (d) by the CMDExplorer, respectively. The suffixes "c" and "m", appended to the mode, indicate calculated and measured apparent conductivity.

Correlation analysis suggests a global bias of the experimental apparent conductivities towards lower values for the CMD-Explorer and towards higher values for the DUALEM–642S, in according to results of the inversions (Figure 7.5). The calibration coefficients shown in Table 7.1 indicate an increase or a decrease of conductivity for values higher and lower than 1, respectively. Considering the synthetic model as baseline for each mode, calibration consists in shifting the original apparent conductivity data toward the corresponding synthetic baseline until the best fit is achieved, as schematized in Figure 7.6. The best fitting is obtained by maximizing the correlation based on Pearson's coefficients. Figure 7.8 displays a flow-chart outlining the main steps of the calibration procedure.

Table 7.1 - Correlation coefficients between measured and calculated EM data.

DUALEM-642S			CMD-Explorer		
Mode	Pearson's correlation coefficient	Calibration coefficient	Mode	Pearson's correlation coefficient	Calibration coefficient
HCP-2	68 % - Moderate	0.89	VMD-1.5	76 % - High	1.18
HCP-4	34 % - Low	0.98	VMD-2.8	52 % - Moderate	1.21
HCP-6	21 % - Low	0.85	VMD-4.5	13 % - Negligible	1.13
PRP-2	86 % - Very High	0.83	HMD-1.5	82 % - High	0.72
PRP-4	82 % - High	0.93	HMD-2.8	77 % - High	0.90
PRP-6	69 % - Moderate	0.88	HMD-4.5	65 % - Moderate	1.06

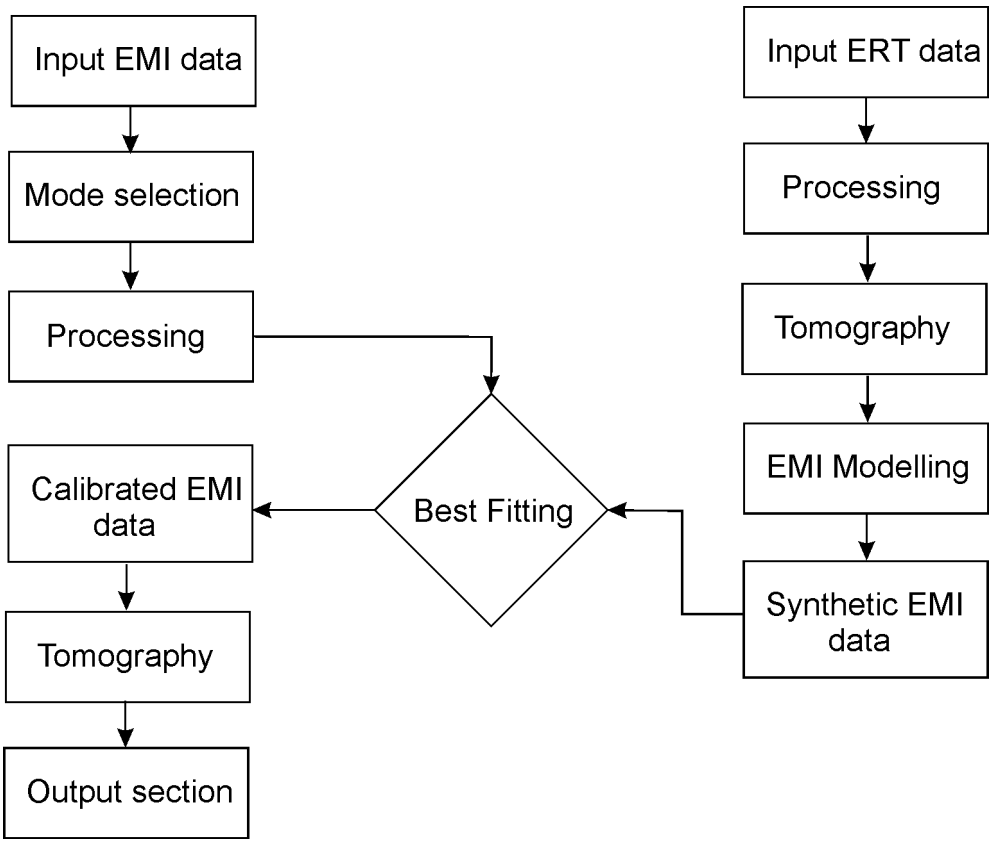

Figure 7.8. Flowchart describing the main steps of the calibration procedure.

Calibration of EMI measured data for all the coil configurations is performed using the EM4Soil software. Figure 7.9 shows the results of EM inversion of calibrated EMI data (Figure 7.9b and Figure 7.9c). The selected portion of the resistivity section, corresponding to the black dashed rectangle in Figure 7.4, is shown in Figure 7.9a, together with the EMI inversions. After calibration, the inverted EMI inversions (Figure 7.9b and Figure 7.9c) nicely correlate with the ERT section (Figure 7.9a). Vertical resolution is greatly improved after calibration and the resistivity contrast between different layers is also enhanced.

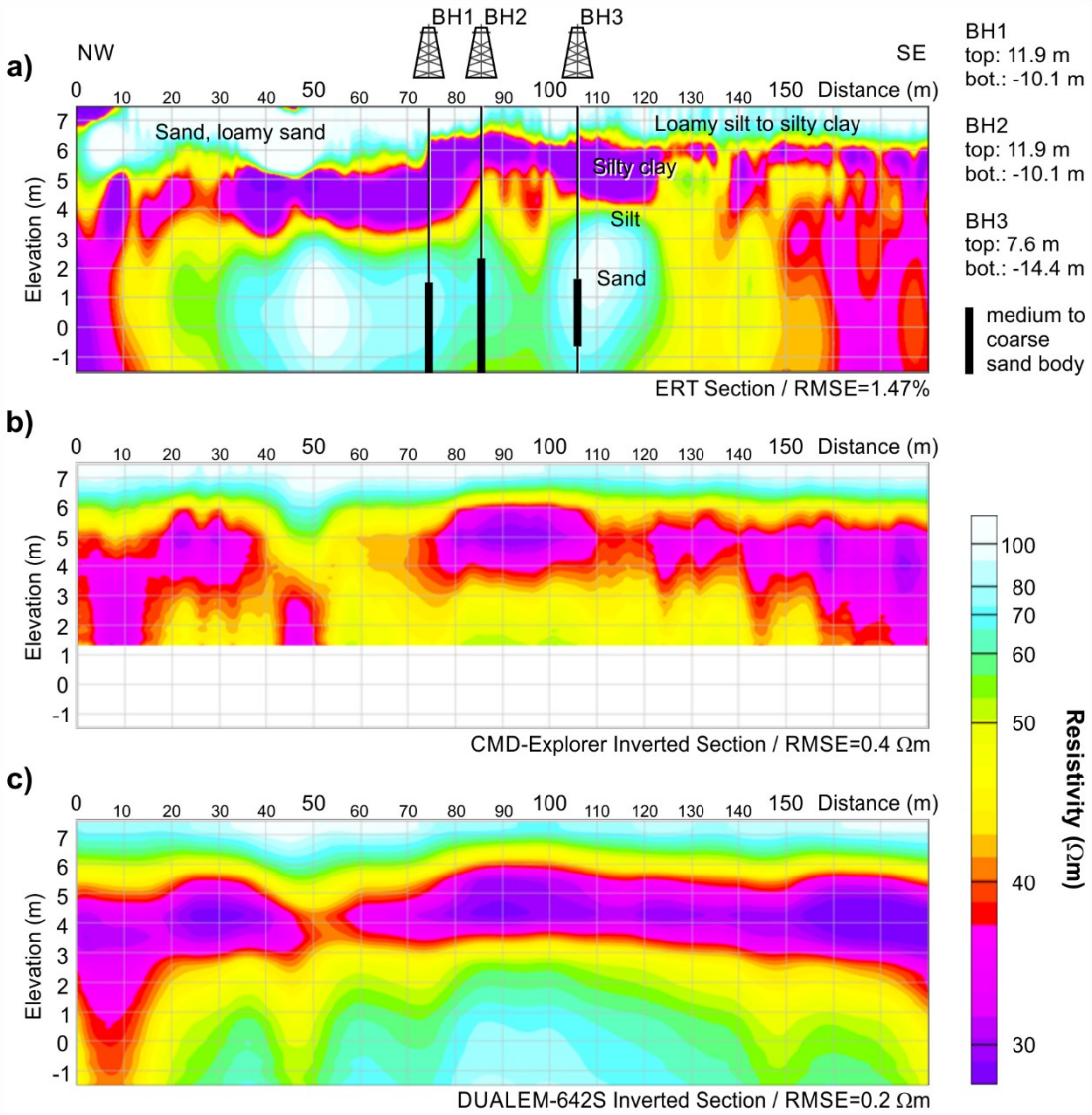

Figure 7.9 - Data comparison on top of the sand intrusion after calibration. (a) Segment of the ERT section selected for calibration (see Figure 2.4) with superimposed borehole stratigraphy; (b) inverted section from the CMD-Explorer calibrated data; (c) inverted section from the

DUALEM–642S calibrated data. The RMSE is equal to 0.4 Ωm and 0.2 Ωm for the CMD-Explorer and DUALEM–642S, respectively.

7.6 DISCUSSION

Being based on different physical phenomena, ERT and EMI methods probe the ground in different ways. While ERT generates direct currents connecting different electrodes, EMI induces alternating currents circulating in closed loops in the subsoil. Thus, the volume of ground excited by the two methods is different. Indeed, the differences in the current paths are implicitly described in the equations governing the physics of the two phenomena that are implemented in the modeling and inversion codes adopted (i.e., Maxwell's equations for EMI and Poisson's law for ERT). The final results are two resistivity distributions that must be similar because EMI operates in a quasi-static regime. Therefore, based on these considerations, the data from one of the two methods can be used to calibrate those from the other method. Despite ERT does not provide the true resistivity distribution of the subsoil (no indirect method can do that) it represents one of the best and most reliable methods to image the earth interior, as proved by its large application and its validation with borehole data and surface geology.

In the inverted models, according to borehole stratigraphy, conductive zones (resistivity lower than 60 Ohm.m) could be interpreted as partially saturated silt loam, silty clay, and clay. Resistive zones (resistivity larger than 60 Ohm.m) are to be associated with sand and loamy sand. In the study case, geotechnical logs and ERT results are rather comparable, as shown by borehole stratigraphy superimposed to subsurface resistivity distribution (Figure 7.4 and Figure 7.9). In particular, it is possible to appreciate the good match between the resistive zone and the sand body. Offering ERT a much higher coverage than EMI, it is absolutely reasonable to take an ERT inversion as a local reference model to which the EMI inversion should approach. The different current paths generate only modest discrepancies in the geometry of the underground structures reconstructed by tomography, as clearly shown in Figure 7.9.

The sand intrusion within the levee is much better imaged in the EMI inversions after data calibration, but mostly for the DUALEM-642S, given its higher DOI with respect

to the CMD-Explorer. A discontinuity in the conductive zone is visible in the EMI sections at distances comprised between 50 m and 60 m. This discontinuity is probably due to the different current paths of EMI and ERT respectively, as mentioned above. Geotechnical tests showed an increase in grain size at increasing depth, and measured water contents in a range between 21.7% and 26.7%. As expected, the ERT section (Figure 7.4) shows that low resistivity values are influenced by the clay content and they are associated with fine sediment with relevant moisture saturation.

The correlation coefficients for the DUALEM–642S, in HCP mode, decrease from moderate to negligible as coil spacing increases. Differently, correlation coefficients in PRP mode decrease from very high to moderate. The better performance of the PRP sensor compared to HCP occurs because HCP mode is more sensitive to depth structures but returns values that reflect cumulative electrical conductivity distribution over a large depth range.

On the other hand, the correlation coefficients for the CMD-Explorer, in VMD mode, decrease from high to negligible as coil spacing increases, while the correlation coefficients in HMD mode decrease from high to moderate. Similarly to the HCP mode of the DUALEM–642S, the VMD delivers more depth of investigation, but the accuracy decreases due to the large depth range from the cumulative electrical conductivity distribution. Moreover, as shown by Figure 7.7d, instrumental calibration problems might affect the measured EMI data.

Shallow vertical heterogeneities have caused more perturbations in the signal of the HCP mode than in the VMD mode. Similarly, shallow lateral heterogeneities have caused more perturbations in the signal of the HMD mode than in the PRP mode. However, in this second case, it is essential to consider that the HMD mode of the CMD-Explorer cannot be compared directly with the PRP mode of the DUALEM–642S, as they are oriented differently.

After the calibration, the resistive layer close to the surface and the conductive layer from 5 m a.s.l. to 2 m a.s.l. are clearly distinguishable in both EMI inversions (Figure 7.9b and Figure 7.9c). At the same time, a hidden resistive layer below the conductive layer became more evident (Figure 7.9c). Table 7.2 shows the absolute mean errors

between the experimental EMI data and the synthetic data computed from the ERT model, for both DUALEM–642S and CMD-Explorer. The error values computed before (measured original data) and after calibration show an improvement of about 103% and 123% for the two instruments, respectively.

Table 7.2 - Absolute mean errors between the experimental EM and the synthetic data computed from the ERT model, both for DUALEM–642S and CMD-Explorer instruments. The error values are computed before (measured original data) and after calibration.

	HCP-2 (mS/m)	PRP-2 (mS/m)	HCP-4 (mS/m)	PRP-4 (mS/m)	HCP-6 (mS/m)	PRP-6 (mS/m)	HCP&PRP (mS/m)
DUALEM–642S measured	2.34	2.46	1.31	1.53	2.10	2.36	2.02
DUALEM–642S calibrated	1.17	0.92	1.37	1.01	1.81	1.08	1.23
	VMD-1.5	HMD-1.5	VMD-2.8	HMD-2.8	VMD-4.5	HMD-4.5	VMD&HMD
CMD-Explorer measured	2.76	6.06	4.24	2.30	4.12	1.99	3.58
CMD-Explorer calibrated	1.39	1.66	1.41	1.62	1.98	1.74	1.63

DUALEM-642S, due to the larger transmitter-receiver offsets, performed overall better than the CMD-Explorer in identifying the sand intrusion, because of the higher cumulative sensitivity at larger depths. In addition, the CMD-Explorer requires two distinct surveys to acquire data for VMD and HMD modes separately. On the other hand, the DUALEM-642S can provide measurements for both sensors (HCP and PRP) in a single acquisition. This fact might reduce the accuracy of the CMD-Explorer, because of the difficulty of aligning the two distinct sets of measurements.

These results demonstrate that, in the particular context of river levees, the use of ERT data to assist calibration of EMI data is particularly effective to identify a sand body underneath a conductive silty clay layer. In this case, being the EMI method more sensitive to strong conductors, it benefits the higher sensitivity of ERT to strong resistors (e.g., Francese and Santos, 2014).

7.7 CONCLUSIONS

The presence of sand boils nearby the levee of a major river in northern Italy suggested geotechnical and geophysical investigations to get proper insight on water filtration underneath and within the embankment. Borehole stratigraphy confirmed the presence of a paleochannel and outlined a thick sand body lately better defined via ERT imaging. Multi-array EMI (CMD-Explorer) scanning was also deployed to investigate nearby levee segments and evidence further possible compositional anomalies. Unfortunately, EMI validation right on top of the spotted was not successful. An additional profile collected with another multi-array EMI device (DUALEM-642S) was still not satisfactory although the resistivity image was improved mostly because of the larger coil spacing.

A calibration procedure based on Pearson's coefficients was then tested and implemented. Calibration coefficients were computed by comparing experimental ERT and modeled apparent conductivities. Calibration was successful and both the inverted EMI profiles converged to a resistivity image comparable with the ERT inversion.

EMI measurements are very sensitive to different factors, namely: ground coupling, thermal drifts, EM noise, etc. For this reason, calibration of EMI measurements, prior to carry out inversion, is mandatory to guess the real texture of the subsurface materials. This is particularly true when targeting the internal structure of river levees to prevent water filtration and potential failures. The textural anomaly causing the failure is typically characterized by resistive sand bodies embedded in conductive silty and clay backgrounds. Such resistivity distribution induces a relevant shift between EMI and ERT because of the masking effect of the shallow conductive layers, reducing the EMI imaging capability.

The ultimate goal of this experiment was to obtain a procedure capable of correcting multi-array EMI data in such a way to obtain cost-effectively information similarly to standard ERT imaging. Calibration could be done on one or more segments of the levees to be investigated with multi-array EMI and then the entire survey could be transposed onto "ERT-like" images making textural anomaly interpretation more reliable.

The experiment also revealed the importance of calibrating EMI measurements, collected with different equipment, to obtain absolute electrical resistivity values. EMI data inversion, after calibration, made results obtained with different equipment comparable and greatly improved the horizontal and vertical resolution. In particular the deep portion of the DUALEM-642S dataset showed an almost one-to-one correspondence with the ERT section.

The devised procedure could be exported and validated in large-scale surveys where there is no availability of geotechnical data and hazard assessment is within the survey goals. This experiment confirmed how the integration of different geophysical methods should be always considered to obtain reliable results. Geophysical surveying based on fast multi-array EMI scanning, assisted and integrated by ERT imaging, is a solid methodology to identify failure-prone levee segments and mitigate flood hazards.

REFERENCES

Accaino, F., F. Da Col, G. Böhm, S. Picotti, M. Giorgi, F. Meneghini, and A. Schleifer, 2023, *Petro-physical characterization of the shallow sediments in a coastal area in NE Italy from the integration of active seismic and resistivity data*. Surveys in Geophysics, 1-28, doi: 10.1007/s10712-023-09776-x.

Baasch, B., H. Müller, F. K. J. Oberle, and T. von Dobeneck, 2015, *Inversion of marine multifrequency electromagnetic profiling data: a new approach to resolve surficial sediment stratification*. Geophysical Journal International, 200, 439-451. doi: 10.1093/gji/ggu406.

Christiansen, A. V. and E. A. Auken, 2012, *Global measure for depth of investigation*. Geophysics, 77, WB171–177, doi: 10.1190/geo2011-0393.1.

Cosenza, P., E. Marmet, F. Rejiba, Y. J. Cui, A. Tabbagh, A., and Y. Charlery, 2006, *Correlations between geotechnical and electrical data: A case study at Garchy in France*. Journal of Applied Geophysics, 60, 3-4, 165-178.

Doll W. E., J. Norton, T. J. Gamey, D. T. Bell, J. S. Holladay, 2014, *Benefits of Joint Magnetic and Electromagnetic Surveying with Boom-mounted Helicopter*

Systems. 20th European Meeting of Environmental and Engineering Geophysics, Athens, Greece, 14-18 September 2014, We Verg 08.

DUALEM, 2008, *DUALEM 421s User's Manual*. Milton, Ontario, Canada: DUALEM Inc.

EMTOMO, 2013, *EM4Soil: Software for Electromagnetic Tomography, V.2*. <http://emtomo.com/ > (accessed June 25, 2020).

Fitterman, D. V., and V. F. Labson, 2005, *Electromagnetic induction methods for environmental problems*. In: Butler, D.K., (editor), Near surface geophysics. Society of Exploration Geophysicists, Tulsa, Oklahoma, 301–355.

Francese, R. G., and F. A. Monteiro Santos, 2014, *Towards a global approach to scan earthen levees*. In SEG Technical Program Expanded Abstracts 2014, 2099-2103, Society of Exploration Geophysicists.

GF Instruments, 2011, *CMD Electromagnetic conductivity meter user manual V.1.5*. Geophysical Equipment and Services, Czech Republic.

Huang, J., T. Koganti, F. Monteiro Santos, and J. Triantafilis, 2017, *Mapping soil salinity and a fresh-water intrusion in three-dimensions using a Quasi-3d joint-inversion of DUALEM-421S and EM34 data*. Science of the Total Environment, 577, 395-404.

Huang, J., F. A. Monteiro Santos, and J. Triantafilis, 2016, *Mapping soil water dynamics and a moving wetting front byspatiotemporal inversion of electromagnetic induction data*. Water Resource Research, 9131-9145, doi: 10.1002/2016WR019330.

Huisman, J.A., J. Rings, J.A. Vrugt, J. Sorg, and H. Vereecken, 2010, *Hydraulic properties of a model dike from coupled Bayesian and multi-criteria hydrogeophysical inversion*. Journal of Hydrology, 380, 62–73, doi:10.1016/j.jhydrol.2009.10.023.

Hen-Jones, R. M., P. N. Hughes, R. A. Stirling, S. Glendinning, J. E. Chambers, D. A. Gunn, D. A., and Y. J. Cui, 2017, *Seasonal effects on geophysical–geotechnical relationships and their implications for electrical resistivity tomography monitoring of slopes*, Acta Geotechnica, 12, 5, 1159–1173, doi:10.1007/s11440-017-0523-7.

Hennig, T., A. Weller, and T. Canh, 2005, *The effect of dike geometry on different resistivity configurations*, Journal of Applied Geophysics, 57, 4, 278–292, doi:10.1016/j.jappgeo.2005.03.001.

IRIS Instruments, 2001, *Syscal switch V.11.4. User's manual*, Orleans, France.

Johansson S., and T. Dahlin, 1996, *Seepage monitoring in an earth embankment dam by repeated resistivity measurements*. European Journal of Engineering and Geophysics, 1, 229-247.

Jongman, B., S. Hochrainer-Stigler, L. Feyen, J. C. J. H Aerts, R. Mechler, W. J. W. Botzen, L. M. Bouwer, G. Pflug, R. Rojas, and P.J. Ward, 2014, *Increasing stress on disaster-risk finance due to large floods*. Nat. Clim. Change, 4, 264–268.

Kai-Feng, M., Y. Chang-Chun, L. Yun-He, R. Xiu-Yan, S. Si-Yuan, M. Jia-Jia, and X. Bin, 2020, *Inversion of time-domain airborne EM data with IP effect based on Pearson correlation constraints.* Appl. Geophys., 17, 589–600. doi:10.1007/s11770-020-0832-8.

Karl L., T. Fechner, M. Schevenels, S. Francois, and G. Degrande, 2011, *Geotechnical characterization of a river dyke by surface waves*. Near Surface Geophysics, 9, 515–527.

Kaufman, A. A. and G. V. Keller, 1983, *Frequency and transient soundings*. Methods in Geochem. and Geophys, 16, Elsevier, New York.

Lavoué, F., J. van der Krak, J. Rings, F. André, D. Moghadas, J. A. Huisman, H. Vereecken, 2010, *Electromagnetic induction calibration using apparent electrical conductivity modeling based on electrical resistivity tomography*. Near Surface Geophysics, 8, 6, 553-561.

McLachlan, P., Blanchy, G., & Binley, A. (2021). EMagPy: Open-source standalone software for processing, forward modeling and inversion of electromagnetic induction data. Computers & Geosciences, 146, 104561

McNeill, J. D., 1980, *Electromagnetic terrain conductivity measurement at low induction numbers.* Geonics Technical Note TN-6.

Minsley, B. J., B. D. Smith, R. Hammack, J. I. Sams, and G. Veloski, 2012, *Calibration and filtering strategies for frequency domain electromagnetic data*. Journal of Applied Geophysics, 80, 56–66, doi: 10.1016/j.jappgeo.2012.01.008.

Monteiro Santos, F. A., 2004, *1-D laterally constrained inversion of EM34 profiling data*. Journal of Applied Geophysics, 56, 2, 123-134.

Monteiro Santos, F. A., J. Triantafilis, K. E. Bruzgulis, and J. A. E. Roe, 2010, *Inversion of multiconfiguration electromagnetic (DUALEM-421) profiling data using a one-dimensional laterally constrained algorithm.* Vadose Zone Journal, 9, 1, 117-125.

Triantafilis, J., and F. A. Monteiro Santos, 2013, *Electromagnetic conductivity imaging (EMCI) of soil using a DUALEM-421 and inversion modelling software (EM4Soil).* Geoderma, 211–212, 28–38.

von Hebel, C., J. van der Kruk, J. A. Huisman, A. Mester, D. Altdor, A. L. Endres, E. Zimmermann, S. Garré, and H. Vereecken, 2019, *Calibration, Conversion, and Quantitative Multi-Layer Inversion of Multi-Coil Rigid-Boom Electromagnetic Induction Data*. Sensors, 19, 4753, 1-25.

Wait, J. R., 1982, *Geo-electromagnetism*, Academic Press.

Wait, J. R., 1962, *A note on the electromagnetic response of a stratified Earth*. Geophysics, 27, 382–385.

Weller, A., T. Canh, K. Breede, and N. Trong, 2006, *Multi-electrode measurements at Thai Binh dikes (Vietnam).* Near Surface Geophysics, 4, 135-143, doi: 10.3997/1873-0604.2005039.

CHAPTER 8

8. FINAL CONSIDERATIONS

This thesis integrates diverse methods and geophysics arrays. The approach through the investigation of levees in northern Italy, numerical simulations of self-potential (SP), and the application of SP monitoring in landslide-prone regions, unfolds a narrative of innovation, challenges, and solutions that collectively contribute to the broader landscape of geological risk management.

Going into the numerical simulations of self-potential (SP) data using COMSOL software, it was modeled a homogeneous background with spherical, cylindrical, and blocky targets, evaluating different summation techniques and array strategies. The Fixed-Base and Leapfrog summation techniques excelled for their equivalency and excellent resolution in defining source anomalies. On the contrary, the responses of Leapfrog without summation and Sparse Gradient techniques posed challenges in interpretation, particularly in the presence of noisy data. The recommendation of the summation procedure in the Leapfrog technique echoed the importance of refining acquisition techniques for optimal SP data interpretation. The use of the Amplitude Signal Analytic (ASA) technique showcased its utility in enhancing the Full Sparse Gradient response, especially in the presence of random noise, as well as, the high accuracy and high resolution provided by the Fixed-Base in delineating source anomalies.

Deep Electrical Resistivity Tomography (DERT) surveys and their potential integration with SP monitoring opened avenues for a more comprehensive geoelectric site characterization. The comprehensive approach to landslide monitoring in Tizzano Val Parma and Cazzaso provided a nuanced perspective on the dynamic nature of landslide-prone regions. Traditional and novel geophysical methods, including DERT, Induced Polarization (IP), and SP, were integrated to offer a holistic understanding of potential landslide hazards.

Non-conventional SP arrays were recognized for their valuable insights, albeit with a note on the ongoing need for improvements in the quantitative approach. The study

shed light on the repeatability and stability of measurements over different years, raising concerns about potential landslide movements and the applicability of non-conventional SP arrays in risk assessment.

The exploration of the FullWaver system's application in retrieving SP signals from 3D-DERT data showcased its potential for landslide monitoring. The procedure introduced the capability of using simple stainless-steel electrodes for time-lapse SP monitoring during the winter, aiding in the detection of zones of possible interest in landslide monitoring. While the FullWaver system and non-traditional SP arrays exhibited promise, challenges such as low spatial resolution and increased acquisition costs were recognized.

The introduction of innovative technologies, particularly the FullWaver system, marked significant advancements in geoelectrical data acquisition.

The development and utilization of specialized tools, such as the SPViewer takes an important role in streamlining data analysis, eliminating noise, and enabling precise anomaly identification. The SP monitoring exemplified through a field example from San Martino di Venezze and Boara Polinese have emphasized its effectiveness in detecting infiltration-related anomalies.

The investigation into the levees along the Brenta river in northern Italy commenced with the identification of sand boils, indicating potential water percolation concerns beneath and within the embankment. To gain insights into this geotechnical challenge, a combination of borehole stratigraphy, Electrical Resistivity Tomography (ERT) imaging, and multi-array Electromagnetic Induction (EMI) scanning was employed. The incorporation of diverse methodologies allowed for a comprehensive understanding of the subsurface conditions, particularly in relation to the presence of a paleochannel and a significant sand body. The calibration procedure emerged as a crucial step to address the challenges associated with EMI profiling. Calibration aimed to reconcile multi-array EMI data with standard ERT imaging, offering a cost-effective approach to transposing the entire survey onto "ERT-like" images. This calibration procedure not only improved the accuracy of EMI profiles but also showcased its potential for large-scale surveys lacking geotechnical data.